

UNIVERSIDAD POLITÉCNICA DE MADRID

E.T.S.I. de CAMINOS, CANALES Y PUERTOS



Climate change impact on floods assessment at different spatial scales

TESIS DOCTORAL

Marco Lompi

Environmental Engineer

2022

Acknowledgements

My first gratitude goes to my supervisors for their guidance and support during the research activities. I want to thank Prof. Enrica Caporali, who gave me the basic knowledge of hydrology during my Bachelor's and Master's degree studies and allowed me to carry out my PhD research at the Department of Civil and Environmental Engineering (DICEA) of the University of Florence (Italy). I want to thank Prof. Luis Mediero, who accepted me as a PhD student at the Universidad Politecnica de Madrid (Spain), who shared with me part of his knowledge and work and helped me better understand how to conduct research.

I want to thank the Doctoral school of Florence, the Erasmus Traineeship, and the project 'SAFERDAMS: Assessment of the impact of climate change on hydrological dam safety' (PID2019-107027RB-I00) of the Spanish Ministry of Science and Innovation for supporting my research with fundings.

I wish to thank all the people I met during these three (four) years of research, the entire staff, and the colleagues of the DICEA. I want to thank my family, who supported me during my studies, without which I would not be the person I am today. Finally, I would like to thank my partner and my friends, who supported me during these years, listening to and encouraging me in the most challenging moments.

Abstract

Climate change is increasing the frequency and magnitude of precipitation and flood extremes events. Increasing peak discharges in the future can lead to underestimating hydraulic risk in urban areas, which could affect the current hydraulic safety of critical infrastructures, such as dams. Climate change impacts on floods can be assessed at different spatial scales, from the global to the river basin scale, with varying objectives, applications, and methodologies. Therefore, new tools are required to assess climate change impacts at each spatial scale.

This thesis evaluates climate change impacts on floods at three spatial scales: regional, river basin, and infrastructure scale. Particularly, it proposes two different methodologies. First, a methodology to assess climate change impact on design floods (river basin scale) and hydrological dam safety (infrastructure scale). Second, a methodology to adapt the design floods at the regional scale to consider uncertainty and climate change impacts on floods in small river basins in a given area.

The first part of this thesis proposes a methodology to assess hydrological dam safety in the future considering the combined impact of climate change on both inflow hydrographs and initial reservoir water levels at the beginning of flood events. The methodology is based on the analysis of climate projections supplied by an ensemble of 12 climate models and also incorporates uncertainty. The Arga River and the Eugui Dam (Spain) are selected as case studies. The quantification of expected changes in flood quantiles considers two emission scenarios (RCP 4.5 and RCP 8.5), three time windows in the future (2011-2040, 2041-2070, and 2070-2100), and seven return periods. The RIBS distributed and event-based hydrological model is used to simulate rainfall-runoff processes in the catchment at sub-daily time scale in flood events. The impact of climate change on initial reservoir water levels expected at the beginning of flood events is assessed by integrating the HBV continuous hydrological model, to simulate the catchment response at a daily time step, with a reservoir operation model, to simulate daily water balance in the reservoir. A stochastic procedure is developed to obtain the frequency curves of maxima reservoir water levels and outflow discharges in flood events for each scenario, assessing the expected changes in the exceedance probability of dam overtopping and quantifying the uncertainty chain in the methodology. Expected future floods in the city of Pamplona show a decrease in design peak discharges for return periods smaller than ten years and an increase for the 500- and 1000-year floods for both RCPs in the three time windows. The emission scenario RCP 8.5 usually provides greater increases in flood quantiles of peak discharges, almost 10-30% higher than in RCP 4.5. Change magnitudes for the most extreme events could be related to the greenhouse gas emission predictions in each RCP, as the greatest expected changes are found in 2040 for the RCP 4.5 and in 2100 for the RCP 8.5. The impact of climate change on hydrological dam safety at the Eugui Dam show expected increases both in the maximum reservoir water level for the most extreme events and the probability of dam overtopping, especially in the 2071-2100 period for the RCP 8.5. Moreover, the maximum outflow discharge frequency also increases in all the time windows for the RCP 8.5, exacerbating the hydraulic risk for the downstream population in Pamplona city. Uncertainty has a key role in estimating changes in future risk, as the exceedance probability of dam overtopping, maximum reservoir water levels, and maximum outflow discharges are underestimated for almost all the scenarios when uncertainty is not considered.

The second part of the thesis presents the adaptation of design floods in small river basins at the regional scale in northern Tuscany (Italy). The work is developed within an agreement with the District River Basin Authority of Northern Apennine. In this case, a simple approach based on rainfall scaling and stochastic storms transposition of occurred events is presented to identify areas where design discharges underestimate flash flood risk. A Flash Flood Design Adaptation index is introduced to adapt the design discharges. Design floods of small river basins in Northern Tuscany, with an area generally less than 30 km², underestimate the flash flood risk. Therefore, their design discharges should be adapted.

Resumen

El cambio climático está aumentando la frecuencia y la magnitud de las precipitaciones extremas y las inundaciones. El aumento de la magnitud de los caudales punta en el futuro puede llevar a subestimar los riesgos de inundación en áreas urbanas, lo que podría afectar el diseño de infraestructuras, como las presas, que se construyeron en su día considerando las avenidas de diseño estimadas en el momento de la construcción. Los impactos del cambio climático sobre las inundaciones pueden evaluarse a diferentes escalas espaciales, desde estudios a escala global hasta la escala de cuenca. Cada escala tiene sus objetivos, aplicaciones y metodología. Por lo tanto, se requieren nuevas herramientas para evaluar los impactos del cambio climático considerando diferentes escalas espaciales.

Esta tesis implica la evaluación de los impactos del cambio climático en las inundaciones a escala de cuenca, a escala de infraestructura hidráulica y a escala regional. En particular, la evaluación del cambio climático sobre las inundaciones se realiza a escala de cuenca, para evaluar las futuras avenidas de diseño, así como a escala de infraestructura hidráulica, para evaluar la futura seguridad hidrológica de las presas. A continuación, se define la adaptación de las crecidas de diseño a escala regional para considerar la incertidumbre y los impactos del cambio climático en las crecidas súbitas en pequeñas cuencas de un área determinada.

En la evaluación de la seguridad hidrológica de las presas, se debe evaluar el impacto del cambio climático tanto en los hidrogramas de entrada como en la frecuencia inicial del nivel del agua en el embalse. Las probabilidades de sobrevertido en la presa están asociadas a avenidas extremas de alto período de retorno, las cuales se ven afectadas por una gran incertidumbre en la estimación de los cuantiles de precipitación. Además, la incertidumbre también aumenta debido a los errores residuales de los modelos hidrológicos tras su calibración.

La primera parte de esta tesis presenta una metodología para evaluar la seguridad hidrológica de las presas en el futuro considerando el impacto del cambio climático en los hidrogramas de entrada y los niveles iniciales de agua en el embalse al comienzo de los eventos de avenida, cuantificando la incertidumbre en las estimaciones. La cuenca del río Arga y la presa de Eugui se seleccionan como casos de estudio. La presa se utiliza para la gestión de los recursos hídricos y la mitigación de inundaciones en la ciudad de Pamplona, situada aguas abajo. La cuantificación de los cambios esperados en los cuantiles de caudal punta se realiza mediante un conjunto de 12 modelos climáticos, siete periodos de retorno, dos escenarios de emisión (RCP 4.5 y RCP 8.5) y tres periodos de tiempo (2011-2040, 2041-2070 y 2070-2100). El modelo hidrológico distribuido RIBS se utiliza para simular el proceso lluvia-escorrentía en eventos de avenida a escala de cuenca. El impacto del cambio climático en los niveles de agua en el embalse al inicio de los eventos de avenida se evalúa integrando el modelo hidrológico continuo HBV con un modelo de operación del embalse. El modelo HBV simula los caudales de entrada diarios en el embalse de Eugui utilizando las proyecciones de lluvia y temperatura como datos de entrada. El modelo de operación del embalse se ha desarrollado para obtener los niveles diarios del agua en el embalse, utilizando los caudales de entrada simulados por HBV como datos de entrada y considerando las reglas de operación del embalse, como los caudales de suministro de agua, los caudales ecológicos y los caudales máximos de vertido en función del nivel de embalse. También se ha desarrollado un procedimiento estocástico para obtener las curvas de frecuencia del nivel máximo de agua en el embalse y del caudal máximo de salida para cada escenario, evaluando los cambios esperados en la probabilidad de excedencia de sobrevertido de la presa, así como cuantificando la cadena de incertidumbre en la metodología. Las futuras inundaciones esperadas en la ciudad de Pamplona muestran una disminución de los caudales punta de diseño para periodos de retorno inferiores a 10 años y un aumento para las avenidas de 500 y 1000 años de periodo de retorno para los dos RCP considerados en los tres periodos de tiempo. El escenario de emisión RCP 8.5 suele proporcionar mayores aumentos en los cuantiles de caudal punta. El aumento en los caudales de diseño es un 10-30% mayor en el RCP 8.5 que en el RCP 4.5. Las magnitudes de cambio de los eventos más extremos podrían estar relacionadas con las predicciones de emisión de gases de efecto invernadero en cada RCP, ya que los mayores cambios esperados se encuentran en 2040 para el RCP 4.5 y en 2100 para el RCP 8.5. Los resultados sobre la seguridad hidrológica de la presa en la presa de Eugui en situación de cambio climático muestran un aumento en la frecuencia esperada del nivel máximo de agua en el embalse alcanzado durante la laminación de las avenidas y en la probabilidad de sobrevertido de

la presa, especialmente en el período 2071-2100 para el RCP 8.5. Además, la magnitud de los caudales de vertido por la presa también aumenta en todos los periodos de tiempo para el RCP 8,5, aumentando el riesgo de inundación para la población situada aguas debajo de la presa en la ciudad de Pamplona. La incertidumbre tiene un papel clave en la estimación del riesgo en el futuro, ya que la probabilidad de excedencia de sobrevertido en la presa, los niveles máximos de agua en el embalse durante la laminación de las avenidas y los caudales punta de salida se subestiman sin su consideración en casi todos los escenarios.

La segunda parte de la tesis presenta la adaptación de las avenidas de diseño a escala regional en pequeñas cuencas fluviales sujetas a inundaciones súbitas en el norte de la Toscana. En este caso, se presenta un enfoque simple basado en el reescalado de la precipitación y la transposición estocástica de tormentas de eventos ocurridos para identificar áreas donde los caudales de diseño subestiman el riesgo de inundación para crecidas súbitas. Se introduce el índice Delta Flash Flood Design para adaptar los caudales de diseño. Las avenidas de diseño en pequeñas cuencas fluviales en el norte de la Toscana, con un área generalmente inferior a 30 km², subestiman el riesgo de inundaciones para avenidas súbitas. Por lo tanto, sus caudales de diseño deberían ser adaptados.

Contents

Acknowledgements	iii
Abstract	v
Resumen	vii
List of Figures	xiii
List of Tables	xv
List of Acronyms	xvii
1 Introduction	1
1.1 Motivation.....	3
1.2 Objectives.....	6
1.3 Thesis structure	7
2 Literature Review	9
2.1 Climate change and floods methodologies	11
2.1.1 Climate Projections in the Euro-Cordex Domain.....	12
2.1.2 Flood frequency analysis in climate change.....	13
2.2 Uncertainty in flood risk assessment at different spatial scales	14
2.3 Impact of climate change on floods at different spatial scales	16
2.3.1 Global scale	16
2.3.2 European scale.....	17
2.3.3 River basin scale.....	18
2.4 Impact of climate change on hydrological dam safety	20
2.5 Impact of climate change on flash floods	21
2.6 Knowledge gaps.....	22
2.6.1 Impacts of climate change on river floods (Chapter 4).....	22
2.6.2 Impact of climate change on hydrological dam safety (Chapter 5)	22
2.6.3 Uncertainty in hydrological dam safety and climate change studies (Chapter 6)	23
2.6.4 Improve flash floods hazard assessment at the regional scale (Chapter 7).....	23
3 Methodology	25
3.1 General Methodology	27
3.2 Case studies.....	30
3.3 Software and tools.....	31
3.3.1 RIBS model.....	32
3.3.2 HBV model.....	33
3.3.3 HEC-HMS	34

4 Future design floods in the Arga river basin (Spain)	35
4.1 Introduction	37
4.2 Methodology	37
4.2.1 Calibration of the RIBS model	37
4.2.2 Current Scenario	38
4.2.3 Climate change scenario	39
4.2.4 Quantification of expected changes in flood quantiles	40
4.3 Data and Case Study	40
4.4 Results	43
4.4.1 RIBS model calibration and validation	43
4.4.2 Flood quantile changes expected in the future	48
4.4.3 Influence of the GCMs and RCMs in the flood quantile determination	51
4.5 Discussion and Conclusion	55
5 Stochastic methodology to assess climate change impacts on hydrological dam safety	57
5.1 Introduction	59
5.2 Methodology	59
5.2.1 Observed data analysis	59
5.2.2 HBV model: calibration and hydrological modelling of the climate change scenarios	59
5.2.3 Reservoir operation model	60
5.2.4 Stochastic procedure to combine floods and initial water levels frequencies	62
5.2.5 Volumetric Evaluation Method (VEM)	64
5.2.6 Overtopping probability and delta changes estimates	65
5.3 Data and Case Study	65
5.4 Results	67
5.4.1 Statistical analysis of observed data	67
5.4.2 Reservoir water levels and peak inflows in the future	68
5.4.3 Statistical analysis of climate variables: projections and HBV model output	70
5.4.4 Changes in maximum reservoir water levels	73
5.4.5 Changes in maximum outflow discharges	76
5.4.6 Overtopping probability in the future	79
5.5 Discussion	80
5.6 Conclusions	81
6 Uncertainty chain assessment for the future hydrological dam safety	83
6.1 Introduction	85
6.2.1 Uncertainty on rainfall delta changes	86

6.2.2 Uncertainty due to the RIBS model errors	87
6.2.3 Uncertainty associated with the HBV model	88
6.2.4 Uncertainty chain	89
6.2.5 Delta changes with uncertainty	90
6.3 Results	90
6.3.1 Changes in maxima reservoir water levels after the incorporation of uncertainty	91
6.3.2 Changes in maxima outflow discharges after the incorporation of uncertainty	94
6.3.2 Overtopping probability after the incorporation of uncertainty	97
6.4 Discussion	99
6.5 Conclusions	99
7 Improving flash floods risk assessment at the regional scale	101
7.1 Introduction	103
7.2 Methodology	104
7.2.1 Selection of the most intense Short-Duration Events (SDEs)	104
7.2.2 Rainfall spatial distribution of the selected events assessment	105
7.2.3 Areal Reduction Factors computing	106
7.2.4 Hydrological Modelling	108
7.2.5 Comparison of the design and short-duration events	109
7.3 Application of the SDE hyetographs on Northern Tuscany	110
7.3.1 Dataset and Short-Duration Events – SDEs identification	110
7.3.2 Hydrological models: comparison between design and SDE hyetographs	112
7.4 Results	114
7.5 Discussion	117
7.6 Conclusions	118
8 Conclusions and Outlook	119
8.1 Conclusions	121
8.1.1 Impact of climate change on river floods and hydrological dam safety	121
8.1.2 Improve flash flood risk assessment at the regional scale	122
8.2 Original Contributions	123
8.3 Future developments	125
Reference	129
Appendix A.	139
Appendix B.	151
Appendix C.	157
Appendix D.	169

Appendix E.	181
------------------	-----

List of Figure

- Figure 1.1.** Number of total people affected by floods per decade in the world
Figure 1.2. Number of total people affected by floods per decade in Europe
Figure 1.3. Thesis Outline
Figure 2.1. Approaches to analyse the impact of climate change on floods
Figure 2.2. Global drivers of future flood risk
Figure 2.3. Trend analysis and climate change projections on the 100-year flood in Europe
Figure 3.1. General methodology of the thesis
Figure 3.2. Flow chart of the thesis methodology on the climate change impacts on floods
Figure 3.3. Flow chart of the thesis methodology on the adaptation of design floods
Figure 3.3. Case Studies: Arga river basin (Spain), Eugui Dam (Spain) and Northern Tuscany (Italy)
Figure 4.1. Rainfall spatial distribution in the future
Figure 4.2. Digital elevation model (DEM), Soil types and location of streamflow and rain gauges
Figure 4.3. Floods selected in the A323 hydrometer by using a Peak Over Threshold
Figure 4.4. Objective function results for the five flood events considered in the RIBS calibration
Figure 4.5. NSE objective function for the five flood events considered in the RIBS calibration
Figure 4.6. Comparison between observed and simulated hydrographs in the RIBS calibration
Figure 4.7. Boxplots of rQT values for the 12 climate models considered in the study (RCP 4.5)
Figure 4.8. Boxplots of rQT values for the 12 climate models considered in the study (RCP 8.5)
Figure 4.9. Hydrographs for the current and climate change scenarios (CNR-CCL climate model)
Figure 4.10. Median values of expected flood changes in the climate change scenarios
Figure 4.11. Median values of rQT for the climate change scenario grouped by GCMs and RCMs
Figure 4.12. Median values of rQT for each combination of GCM and RCM
Figure 5.1. No correlation between observed daily peaks and initial water levels
Figure 5.2. Random generation of inflow peak discharges and initial water levels
Figure 5.3. Arga river basin upstream to the Eugui reservoir in northern Spain
Figure 5.4. Frequency curves of the current scenario
Figure 5.5. Results of the calibration of the HBV model
Figure 5.6. Results of the calibration of the reservoir operation model
Figure 5.7. Inflow discharge and reservoir water levels in the future for MPI-CCL in the RCP 4.5
Figure 5.8. Reservoir water level frequency curves and design inflow discharge for ICH-CCL
Figure 5.9. Exceedance Probability (EP) of some future climate variables under the ICH-CCL
Figure 5.10. Current and future maximum water level frequency for IPS-WRF
Figure 5.11. Delta changes of maxima water levels with the ensemble of all the climate models
Figure 5.12. Current and future maximum outflow discharge frequency for MPI-RCA
Figure 5.13. Delta changes of maxima outflow discharges with the ensemble of all the climate models
Figure 5.14. Overtopping probability in each scenario
Figure 6.1. Uncertainty chain assessment in future hydrological dam safety
Figure 6.2. Uncertainty in the rainfall delta changes for MPI-RCA
Figure 6.3. Comparison between the modelled and observed peak discharges at the Eugui dam
Figure 6.4. Dependency of the HBV model errors with the simulated discharge magnitude
Figure 6.5. Mean water level frequency curve associated with the control period of the MOH-RCA

Figure 6.6. Stochastic procedure to incorporate uncertainty in the inflow hydrographs estimation

Figure 6.7. Expected maxima reservoir water levels for IPS-WRF considering uncertainty

Figure 6.8. Maxima reservoir water levels in the current scenario and delta changes accounting uncertainty

Figure 6.9. Expected maxima outflow discharges for MPI-RCA considering uncertainty

Figure 6.10. Maxima outflow discharges in the current scenario and delta changes accounting uncertainty

Figure 6.11. Overtopping Probability with the ensemble of the climate models accounting uncertainty

Figure 7.1. Possible combinations of submatrices with a given dimension within a rainfall raster

Figure 7.2. Maximum average rainfall depth H_a to calculate the Areal Reduction Factors for river basins with an area of 4 cells

Figure 7.3. Rain gauge network and spatial distribution of the 200 years rainfall depth with a three hours duration in the study area.

Figure 7.4. Rain Gauges and rainfall raster of CSDE4 (coastal short-duration event)

Figure 7.5. ISDE1 (internal short-duration event) hyetograph and Areal Reduction Factors associated with the event

Figure 7.6. Carza river basin mode and ISDE1 (internal short-duration event) hyetograph

Figure 7.7. Areal Reduction Factors associated with the internal Short-Duration Events and the coastal Short-Duration Events

Figure 7.8. Results of all Short-Duration Events occurred inland in the set of internal river basins.

Figure 7.9. Results of all Short-Duration Events occurred near the coast in the set of coastal river basins.

Figure 7.10 Flash Flood Design Adaptation index with respect to the river basin area for the internal river basins and the coastal river basins

List of Tables

Table 2.1. Global Climate Models (GCM) considered in this study

Table 2.2. Regional Climate Models (GCM) considered in this study

Table 2.3. Review of the studies on climate change impacts on floods at the river basin scale

Table 3.1. Ensemble of the 12 climate models considered in the analysis

Table 4.1. Summary about the rain- and streamflow-gauge stations considered in the study

Table 4.2. Hydraulic characteristics of the soil classes belonging to the soil raster

Table 4.3. Summary of the flood events considered in the calibration process of the RIBS model

Table 4.4. Ranges of the RIBS model parameter values used in the calibration procedure

Table 4.5. Weighted values of the objective function values in the three hydrometers considered in the study for the events used in the calibration and validation phases.

Table 4.6. RIBS parameter values for the best combination identified in the calibration process

Table 5.1. Flow coefficient associated with each ecological condition and month in the Variable Monthly Flow method.

Table 5.2. Instruments of the current scenario data

Table 5.3. Monthly environmental flows used in the reservoir operation model

Table 5.4. Overtopping Probability in each scenario for all the climate models.

Table 6.1. Overtopping probability associated with the 50th percentile after the incorporation of uncertainty for all the climate models in the different scenario.

Table 6.2. Difference between the overtopping probability associated at the 50th percentile after the incorporation of uncertainty and the overtopping probability without the evaluation of the uncertainty for all the climate models in the different scenario.

Table 7.1. Short-Duration Events – SDEs for the inner part of the Region.

Table 7.2. Short-Duration Events – SDEs for the coastal part of the Region.

Table 7.3. Set of the river basins in the inner parts of Tuscany

Table 7.4. Set of the river basins near the Tyrrhenian Sea

List of Acronyms

AMC	Antecedent soil Moisture Condition
AMS	Annual Maxima Series
ARF	Areal Reduction Factor
CCL	CCLM4-8-17 (Regional Climate Model)
CNR	CNRM-CM5 (Global Climate Model)
CSDE	Coastal Short-Duration Event
DEM	Digital Elevation Model
EP	Exceedance Probability
GCM	Global Climate Model
GEV	Generalized Extreme Value
HBV	Hydrologiska Byrans Vattenbalansavdelning model
ICH	ICHEC-EC-EARTH (Global Climate Model)
IDW	Inverse Distance Weighting
ISDE	Internal Short-Duration Event
IPS	IPSL-CM5A-MR (Global Climate Model)
MAE	Mean Absolute Error
MAF	Mean Annual Flow
MMF	Mean Monthly Flow
MOH	MOHC-HadGEM2-ES (Global Climate Model)
MP	Magnitude of the Peak
MPI	MPI-ESM-LR (Global Climate Model)
NEP	Not Exceedance Probability
NSE	Nash-Sutcliffe model Efficiency
PDF	Probability Distribution Function
POT	Peak Over Threshold
RAC	RACMO22E (Regional Climate Model)
RCA	RCA4 (Regional Climate Model)
Reff	Efficiency of the Model
RIBS	Real-time Interactive Basin Simulator

RCM	Regional Climate Model
RCP	Representative Concentration Pathways
RMSE	Root Mean Squared Error
RP	Return Period
SST	Stochastic Storm Transposition
SDE	Short-Duration Event
STA	Stochastic Transposition Area
TP	Time to Peak
VEM	Volumetric Evaluation Method
WRF	WRF331F (Regional Climate Model)

Chapter 1

Introduction

1.1 Motivation

Floods are the most frequent natural disaster and occur when water submerges usually dry land (Flood Directive 2007/60/EC). Floods can be caused mainly by rainfall storms, rapid snowmelt, and storm surges in coastal areas. Nevertheless, rainfall represents the main driver of floods. Rainfall storms can generate either pluvial or fluvial floods. Fluvial floods occur when streamflow exceeds the maximum capacity of a river cross section, flooding surrounding areas. A historical review of flood events (Doocy et al., 2013) shows how floods are the leading cause of natural disaster deaths worldwide, with more than a half-million fatalities caused by rain-induced floods from 1980 to 2009. The number of people affected by floods increases over time. This relates to the intensification of extreme events in a warmer climate (IPCC 2012, IPCC 2014) and increasing urbanisation (Mahmoud & Yew Gan, 2018). According to the World Health Organization, floods affected more than two billion people worldwide between 1998-2017. The increased number of people affected by floods over time can be seen in the estimates of the International Disaster Database (Guha-Sapir et al., EM-DAT), shown in Figure 1.1.

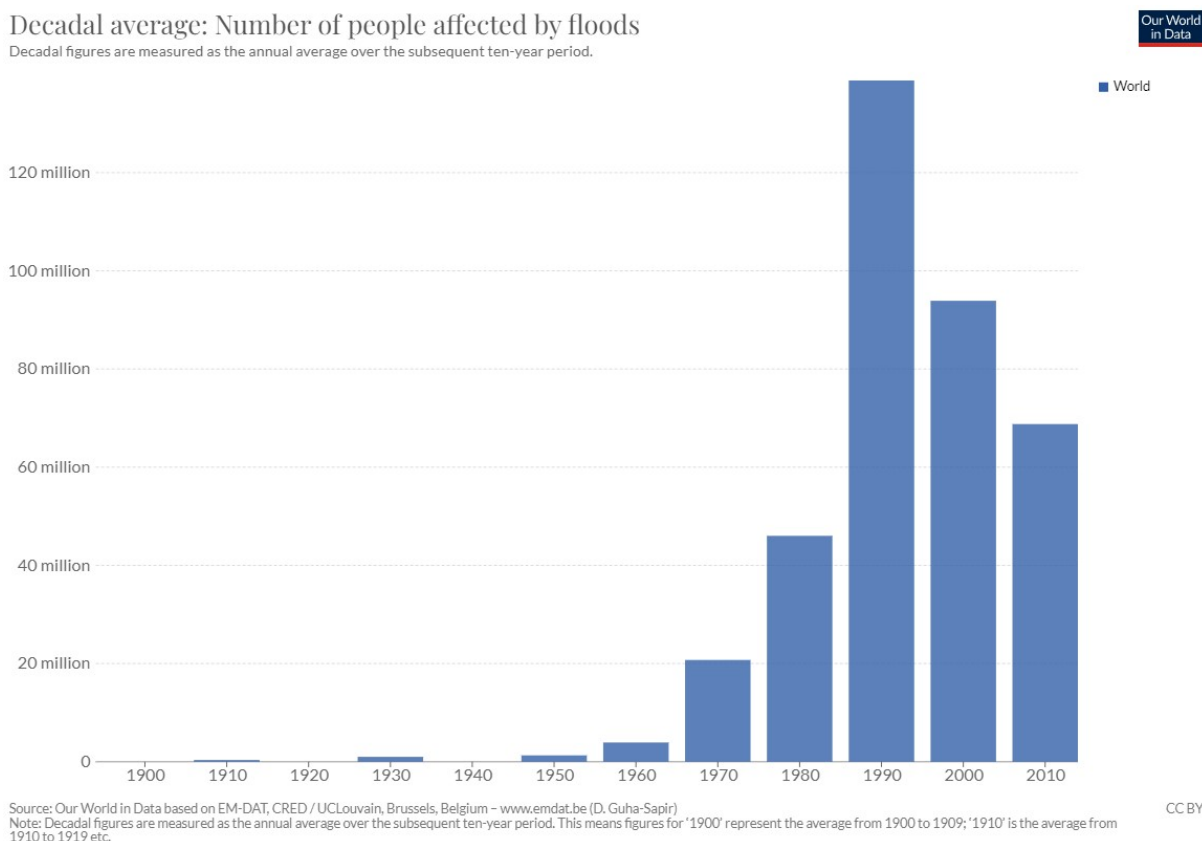


Figure 1.1. Number of total people affected by floods per decade in the world. (Source: The International Disaster Database <http://www.emdat.be/>).

Figure 1.1 shows the mean annual number of people affected by floods averaged globally. However, this number seems to decrease in the last two decades (2000 and 2010). This could be associated with the increasing capabilities of hydrological and forecasting models, the application of adaptation and mitigation measures, or the drafting of directives and technical regulations on flood mitigation. Nevertheless, when the point of view (or spatial scale) changes from the entire globe to Europe only, the average number of people affected by floods does not seem to decrease abruptly in the last two

decades (Figure 1.2). In this case, Europe worked considerably in the last years to cope with flood risks by requiring European countries to adhere to the Floods Directive 2007/60/EC principles.

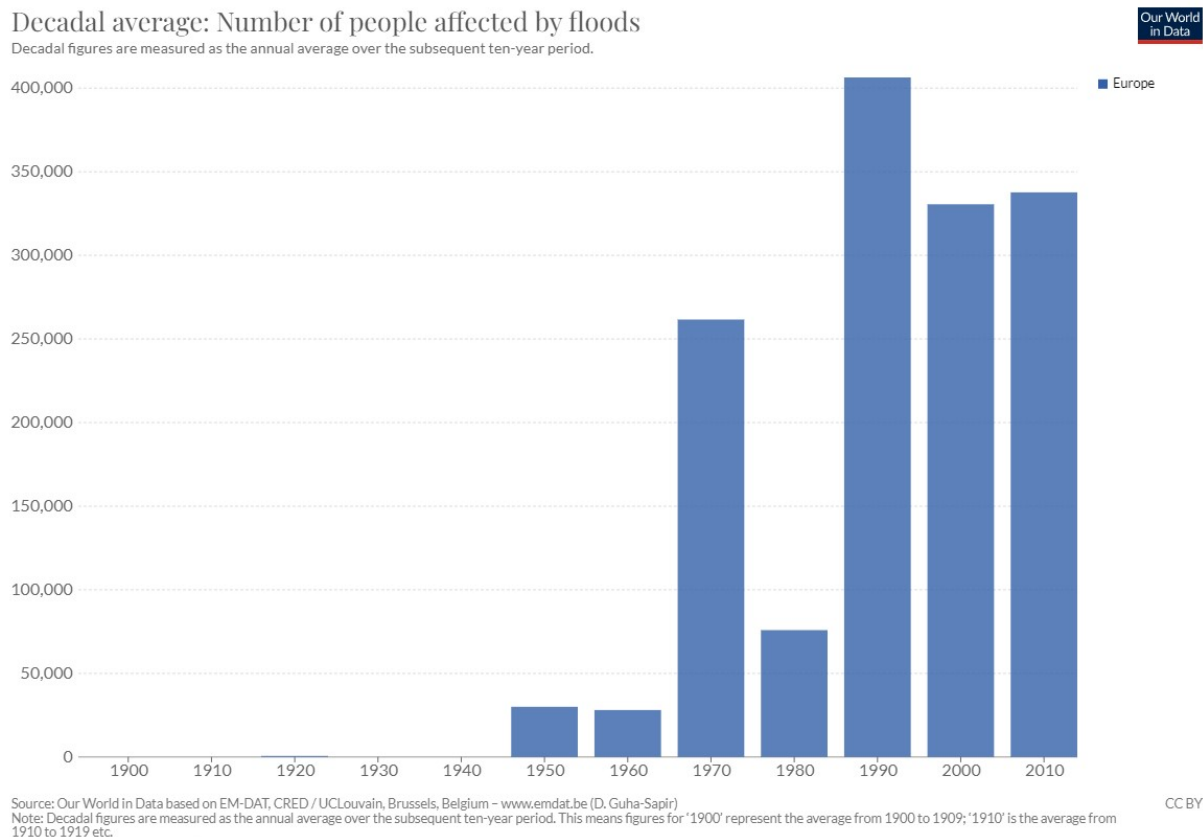


Figure 1.2. Number of total people affected by floods per decade in Europe. (Source: *The International Disaster Database* <http://www.emdat.be/>).

Despite all the efforts done by research studies on climate, hydrology, and fluvial hydraulics, which have increased the application of engineering practices and adaptation and mitigation measures over time, floods still represent a big deal for societies. Moreover, people affected by floods are also expected to rise worldwide in the future under some climate change scenarios (Alfieri et al., 2016). Therefore, studies that continue investigating flood occurrence and magnitude are fundamental to improve the knowledge about flood risks and mitigate the hydraulic risk and its impact on people.

Floods can occur at varying spatial and temporal scales. Different scales in flood risk assessment call for different methods and uses, with future research that needs to improve flood risk assessments at different scales (Moel et al. 2015). For instance, greater rivers have response times that allow the use of forecasting models and real-time applications to reduce the risk of extreme rainfall events. On the contrary, real-time flood warning systems are less efficient in small and intense short-duration events in small river basins. For this reason, flash floods, characterised by high-velocity flows and short warning times in small river basins, have the highest average mortality rates per event and are responsible for most flood deaths in developed countries (Jonkman & Kelman, 2005).

Flood risk assessment studies usually estimate potential damages associated with given events. The typical risk formula combines the hazard, which indicates the probability of a certain event magnitude, with information regarding the exposure and vulnerability of the elements that can be exposed and subjected to the hazard. Therefore, flood risk relates to the frequency associated with a

given flood event magnitude (hazard) and with the presence of potentially exposed subjects in urban areas (exposure and vulnerability) either located close to a river or subject to pluvial floods.

Several studies have focused on the impact of climate change on the hydrological cycle to understand a possible relationship between a warmer climate and the intensification of extreme events (hazard). An increase in precipitation intensity and frequency has been detected in a warmer climate (Donat et al. 2016; Prein et al. 2017; Li et al. 2019; Myhre et al. 2019). Therefore, flood risks are also expected to increase in urban areas (Zhou et al. 2016; Miller & Hutchins, 2017), imposing high costs on aquatic and terrestrial ecosystems, human societies, and the economy (Tabari, 2020). Nevertheless, such increasing frequency and magnitude of extreme rainfall events do not imply that long-term statistical trends of flood peaks will also increase (Hall et al. 2014). Therefore, there is a need to directly analyse the effect of climate change on flood magnitude trends using rainfall projections as input of hydrological models.

Krysanova et al. (2018) analysed the performance of hydrological models in estimating changes driven by climate change by using climate projections. They grouped the methodologies into two categories: i) studies that provide their results using a multi-model ensemble without calibrating or validating the hydrological models; ii) studies with model performances evaluated with observations in the historical period. The study confirms how the second approach provides reliable results for impact assessment studies. Indeed, good performances of the hydrological models in the current scenario also decrease the uncertainty in the description of the climate projections. In addition, several variables can impact the model performances, such as a good representation of the soil and land use characteristics or the description of the rainfall spatial distribution. Segond et al. (2007) conducted a sensitivity analysis to detect which variables influence the goodness of model performances. The results showed how rainfall spatial variability was the most sensitive parameter in the calibration of rainfall-runoff models. However, the use of fully distributed hydrological models in climate change and flood impact assessment studies is scarcely investigated, although they are needed to consider the spatial distribution of rainfall. Indeed, a multi-model ensemble mean approach with lumped or semi-distributed hydrological models is more frequent. Nevertheless, the use of a fully distributed hydrological model can better describe the spatial distribution of rainfall fields, increasing the model performance in simulating flood events in the current and future scenarios.

Assessing the impact of future climate on river flood risks and water resources is essential to plan effective adaptation strategies to cope with the expected changes in extreme event risks (IPCC 2012; IPCC 2014). This is particularly true for cities with significant potential damages and large hydraulic infrastructures, such as dams, with a higher hydraulic risk related to their efficiency. Indeed, statistical methods commonly used in traditional flood frequency analysis usually assume independency and stationarity in time series of extreme events. However, several studies have identified significant trends in annual floods (Mediero et al., 2014). Therefore, the stationarity assumption may be questioned (Milly et al., 2008; Sraj et al., 2016). Also, for long-term dam safety management, stationary climatic baselines seem no longer appropriate (USACE, 2016). Moreover, large dams located upstream of population centres are often designed for downstream flood-control purposes, but they were designed and built to handle flood risks known at the time of the construction (Chen & Hossain, 2019). In addition, the impact of climate changes on hydrological dam safety is also related to other variables apart from the expected changes in inflow hydrographs. Indeed, assessing the impact of climate change on the initial reservoir water level expected at the beginning of flood events is crucial. Furthermore, evaporation is also expected to increase in a warmer climate (Konapala et al., 2020), lowering initial reservoir water levels at the beginning of flood events in the future, implying that a given inflow hydrograph will have a lower hydraulic risk for dams.

Uncertainty is crucial in climate change impact assessment studies, as there are several sources of uncertainty in the methodologies used in this kind of studies. Uncertainty is generally deeply

connected with flood risk assessment also if no climate projections are involved. Indeed, uncertainties in design rainfall estimates and hydrological models cannot be neglected. In addition, high return periods are required in hydrological dam safety studies. Design rainfall and flood estimates for high return periods usually have greater uncertainties. Therefore, uncertainty quantification is necessary to assess the reliability of the estimates. In addition, Global Climate Models (GCMs) and Regional Climate Models (RCMs) are used to estimate the expected changes in rainfall quantiles in the future (Garijo and Mediero, 2019). Consequently, uncertainties associated with such delta changes must also be assessed. Therefore, a complete procedure to evaluate the impact of climate change on hydrological dam safety that also account for uncertainty is needed.

On the other hand, due to their short response times, flood risk management in small river basins is more critical than in medium-size or large catchments. Indeed, river basins without streamflow gauging sites prevent the possibility of calibrating hydrological models, increasing uncertainties. Moreover, small river basins are susceptible to flash flood phenomena, as their response times are comparable with the duration of intense short-duration storms. Kendon et al. (2018) state that “*there are very few studies examining the detection of changes in sub-daily rainfall given the high cost of very high-resolution climate models needed to capture hourly rainfall extremes and to a lack of sufficiently long, high-quality, sub-daily observational records*”. For this reason, projections for short-duration rainfall are not available everywhere. Nevertheless, tools that can consider possible changes in flash flood magnitudes are needed, even without sub-daily or sub-hourly rainfall projections. Methodologies should be in favour of safety to also consider possible underestimates of design rainfalls with short durations. Indeed, uncertainty has a significant role in this case due to the short time series length of sub-daily precipitation.

Therefore, understanding the current and future hydraulic flood hazards in urban areas and hydrological dam safety is essential to adapt design floods or develop new strategies for the management and adaptation to the expected changes. Moreover, uncertainty should be considered in the proposed methodologies, if possible, as it can supply valuable information about their reliability and be used in decision-making.

1.2 Objectives

This thesis aims to improve the knowledge about the impact of climate change on floods, assessing the expected changes in hydraulic hazards at different spatial scales. Indeed, this work focuses on the impacts of climate change on fluvial floods (*river basin scale*), hydrological dam safety (*infrastructure scale*), and flash-flood events at the *regional scale*.

A detailed analysis of the research questions based on the literature review and knowledge gaps that have been identified are included in the next chapter (Section 2.6). The objectives underlying the research are:

1. Assess the impact of climate change on floods at the river basin scale, considering the spatial distribution of the future rainfall fields.
2. Evaluate the usefulness of distributed hydrological models to improve the characterisation of catchment response in flood events by considering the spatial distribution of rainfall.
3. Analyse how greenhouse gas emission scenarios can be related to the expected flood frequency changes by using an ensemble of climate projections.
4. Assess the impact of climate change on hydrological dam safety, considering the expected changes in both future inflow hydrographs and initial reservoir water levels at the beginning of flood events.

5. Evaluate the sources of uncertainty in methodologies used to assess the expected changes in hydrological dam safety driven by climate change.
6. Develop a straightforward methodology to improve flash flood risk assessment in small river basins with data scarcity at the regional scale.

The first objective is also connected with the fourth goal of the thesis, which is the analysis of the impact of climate change on hydrological dam safety. The fifth objective of the thesis aims to evaluate the role of uncertainty in climate change impact assessment studies, focusing on hydrological dam safety analyses. The sixth goal of this work is to provide and develop a simple tool to improve the design flood discharges at the regional scale, to face the intensification of extreme events and the uncertainty of their estimates.

1.3 Thesis structure

The literature review is presented in Chapter 2, summarising the research questions based on the gaps highlighted after reviewing the literature. Chapter 3 describes the general methodology of the thesis, i.e. how the single case studies are connected. The thesis has six main objectives, some of which have their dedicated chapter (from Chapter 4 to Chapter 7), where the methodology and results in each part are also shown. Finally, Chapter 8 summarises the main conclusions of the thesis.

Therefore, the thesis has eight chapters, detailed below and schematised in Fig. 1.3:

- Chapter 2 - Literature Review
- Chapter 3 - Methodology
- Chapter 4 - Future design floods in the Arga river basin (Spain): First, second and third objectives
- Chapter 5 - A stochastic methodology to assess the climate change impact on hydrological dam safety: Fourth objective.
- Chapter 6 - Uncertainty chain assessment of the future hydrological dam safety: Fifth objective
- Chapter 7 - Adaptation of the design floods of small river basins at the regional scale: Sixth objective
- Chapter 8 - Conclusions and Outlook

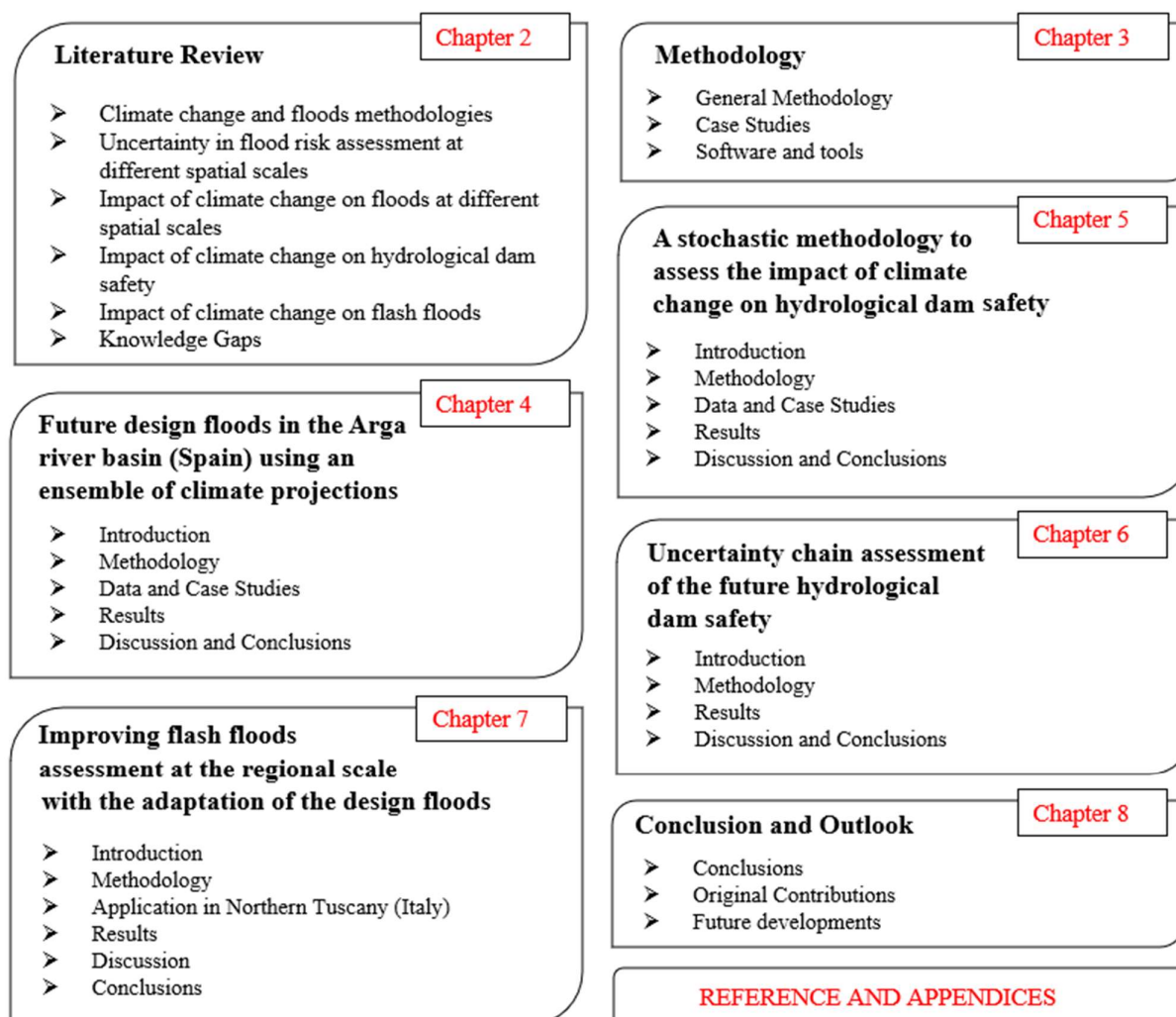


Figure 1.3. Thesis Outline.

Chapter 2

Literature Review

The literature review is divided into six parts: the main methodologies to approach the climate change and floods topic are shown in Section 2.1; the uncertainty associated with the flood risk assessment at different spatial scales is described in Section 2.2; findings on climate change impacts on floods are then presented at different spatial scales (global scale, European scale, and river basin scale) in Section 2.3; the methodologies and findings on climate change and hydrological dam safety topic are reported in Section 2.4; the role of climate change and uncertainty on the flash floods risk assessment is described in Section 2.5; the knowledge gaps that have been found studying literature are discussed in Section 2.6.

2.1 Climate change and floods methodologies

The expected impact of climate change on the water cycle can be analysed using two approaches, as shown in Figure 2.1. First, trend analyses of observations recorded in the past with a set of statistical models can predict what will happen in the future. Second, rainfall-runoff models that use climate projections as input data can extract the flood change signal predicted by climate models (Quintero et al., 2018).

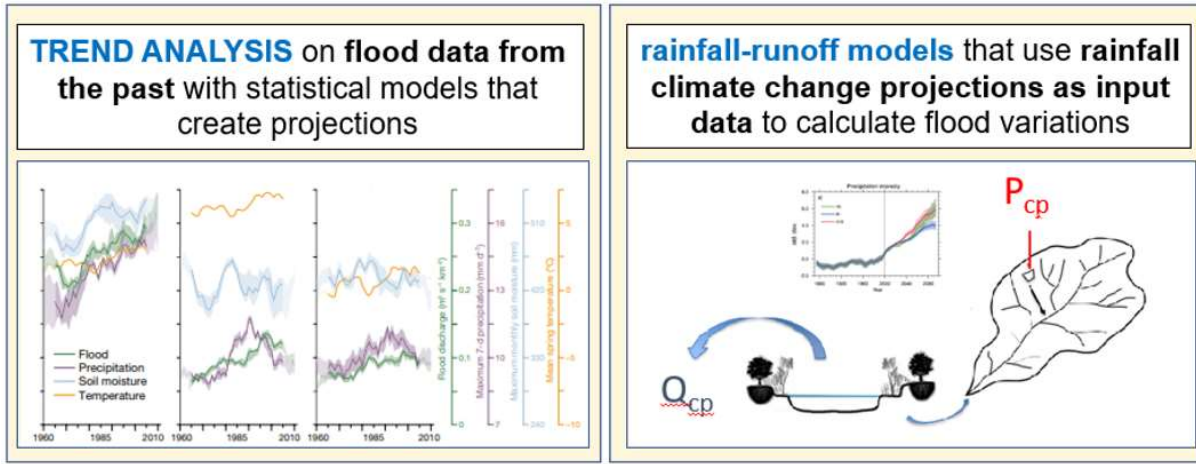


Figure 2.1. Approaches generally implemented to analyse the impact of climate change on floods: on the left, the trend analysis (adapted from Blöschl et al., 2019); on the right, the use of rainfall-runoff models with climate projections as input data.

Regarding the spatial scales, while the first approach is usually applied to large-scale studies, the second usually regards either large or small and finer spatial resolutions, such as catchment scales.

In this thesis, the impact of climate change is evaluated using the second approach, and the rainfall and temperature projections represent the input data of the hydrological models used to do impact assessment studies. These input data consist of a combination of Global Climate Models (GCMs) and Regional Climate Models (RCMs). GCMs simulate the climate behaviour under a set of given Representative Concentration Pathways (RCPs), which are hypothetical future greenhouse gas emissions (Meinshausen et al., 2011). RCMs downscale such climate projections on a finer spatial scale. Indeed, it is necessary to reproduce rainfall projections with adequate spatial and temporal scales, especially to force hydrological models for small and medium catchment areas (Tofiq et al., 2014). An ensemble of RCMs and GCMs is preferred to a single climate model to remove potential biases in the outputs of RCMs or GCMs (Pechlivanidis et al., 2017). In climate change impact assessment studies, the most used emission scenarios are the RCP 4.5, with the peak of greenhouse gas emissions that occur around 2040 and with a stabilisation of the radiative forcing at the end of the

century (Thomson et al., 2010), and the RCP 8.5, with increasing greenhouse gas emissions throughout the 21st century (Riahi et al., 2011) and these two scenarios are also used in this thesis.

2.1.1 Climate Projections in the Euro-Cordex Domain

A great part of the information in this section is taken by Jacob et al. (2020). The Coordinate Regional climate Downscaling Experiment (CORDEX) was created in 2009 primarily with three main objectives: understanding the changes in climate phenomena at the regional and local scale with the downscaling, increasing models downscaling capability, and producing regional projections worldwide. In the European domain, the EURO-CORDEX project provides open-source projections data based on several institutions' voluntary work. For this reason, giving the voluntary effort, each institution chooses the GCM to run the climate projection, even if this approach can introduce some inconsistency in the climate signal (Turco et al., 2013). The projections are supplied by several combinations of GCMs and RCMs provided by more than 30 modelling groups. The projections considered in this study are provided by the GCMs shown in Table 2.1, after the downscaling of their information by the RCMs in Table 2.2.

Table 2.1. *Global Climate Models (GCM), whose projections in the Euro-CORDEX domain are considered in this study*

GCM	Institution	Country	website
CNRM-CERFACS-CM5	Centre National de Recherches Météorologiques	France	http://www.umr-cnrm.fr/
ICHEC-EC-EARTH	Irish Centre for High-End Computing	Ireland	https://www.ichec.ie/
IPSL-CM5A-MR	Institut Pierre-Simon Laplace	France	https://www.ipsl.fr/
MOHC-HadGEM2-ES	Met Office Hadley Centre	UK	https://www.metoffice.gov.uk/
MPI-M-MPI-ESM-LR	Max Planck Institute for Meteorology	Germany	https://mpimet.mpg.de/

Table 2.2. *Regional Climate Models (RCM) considered in this study*

RCM	Institution	Country	website
CLMcom-CLM-CCLM4-8-17	Climate Limited-area Modelling Community	EU	https://clmcom.scrollhelp.site/clm-community/
IPSL-WRF331F	Institut Pierre-Simon Laplace	France	https://www.ipsl.fr/
KNMI-RACMO22E	Koninklijk Nederlands Meteorologisch Instituut	Netherlands	https://www.knmi.nl/
SMHI-RCA4	Sveriges Meteorologiska och Hydrologiska Institut	Sweden	https://www.smhi.se/

In the EURO-CORDEX, simulations are divided into three periods: 1989-2008, which is used to evaluate the model's performance with ERA-Interim data (Dee et al., 2011), which is a global atmospheric re-analysis that provided meteorological information with an 80 km² resolution globally; 1951-2005, that represent the Control period and 2006-2100 that is the period of the climate Scenarios. The projections are available with two spatial resolutions: EUR-44 with a grid of 0.44° degree spacing and EUR-11, in which the same domain is divided into a grid with a finer spatial scale of 0.11° degree. This latter spatial resolution can guarantee a good description of meteorological phenomena, especially of extreme events (storms and droughts), to do impact assessment studies in

Europe. Indeed, the projections have been demonstrated to perform well in describing extreme precipitation (Luu et al., 2018; Garijo and Mediero, 2019).

2.1.2 Flood frequency analysis in climate change

First, this section aims to provide some basic knowledge of flood (or rainfall) frequency analysis. Then, some methodologies used in literature to also consider the possibility of a changing climate, i.e. frequency of extreme events in non-stationary time series, are described. [Madsen et al. \(2013\)](#) is a review article that describes all the methods used in Europe regarding the flood-frequency analysis in a changing environment. Therefore, part of the following information is taken by this report. The main methodologies are described in this subsection, while further details about studies that used these approaches in Europe can be found in the report.

The design of hydraulic infrastructures is based on design floods that are usually evaluated with univariate frequency analysis. In the univariate frequency analysis, the magnitude of the design flood, i.e. the peak discharge of the hydrograph, is connected with a given probability of occurrence, which is determined by analysing the observed discharge time series. Particularly, the Annual Maxima Series (AMS) of rainfall (or discharges) is extracted by the observed time series to obtain the empirical frequency of the extreme events. The frequency of a given event x is usually expressed with its Exceedance Probability (EP) or Not Exceedance Probability (NEP), which relate to the Return Period (RP) concept as in the following equations.

$$P[X < x] = NEP = 1 - \frac{1}{RP} \quad (2.1)$$

$$P[X > x] = EP = \frac{1}{RP} \quad (2.2)$$

The Return Period (RP) can be seen as the mean interarrival time between two events with the same magnitude x . For instance, if the EP of a given event x is 0.2 in each year, the RP associated of that event is 5 years. Design events with a given RP , i.e., flood quantiles, are used in engineering and hydrological applications. Flood quantiles for different RP s are determined fitting a Probability Distribution Function (PDF) to the observed cumulative distribution function $F(x) = P[X < x] = NEP$. In this case, the assumption is that the observed time series is stationary. Therefore, the analysed variable is assumed to be identically distributed over time and the flood quantile with a given RP , x_{RP} , is obtained with the inverse distribution: $x_{RP} = F^{-1}(NEP)$. There are several PDFs that use a different number of parameters θ to describe the flood quantiles for a given return period, . For instance, the Gumbel (Eq. 2.3) is a two-parameters distribution, while the Generalized Extreme Values (Eq. 2.4), GEV, uses three parameters:

$$x_{RP} = u - \alpha \cdot \ln \left[-\ln \left(1 - \frac{1}{RP} \right) \right] \quad (2.3)$$

$$x_{RP} = u + \frac{\alpha}{k} \left\{ 1 - \left[-\ln \left(1 - \frac{1}{RP} \right) \right]^k \right\} \quad (2.3)$$

Where u , α , and k are the location, the scale and the shape parameters (θ) and in the stationary flood frequency analysis are assumed to be constant over time. The parameters can be obtained with several methods: the maximum likelihood, the method of moments or L-moments ([Hosking and Wallis, 1997](#)).

Nevertheless, in a changing climate, stationarity may be questioned (Milly et al., 2008; Sraj et al., 2016), and different approaches must be considered to extract flood quantiles. The Non-stationary flood frequency analysis is based on time-dependent parameters $\theta(t)$. Therefore, the probability associated with an event with a magnitude x change over time. This methodology is rarely used in hydrological practice, as the shortness of the observed time series affects this approach with significant uncertainty.

For this reason, other methodologies are available to consider the flood frequency in a changing climate and are usually based on climate projections supplied by GCMs or RCMs.

One of the most common approaches is the “delta change” method. This methodology is a direct statistical downscaling method which provides adjustments that can be applied to the observed time series. Since the entire future time series provided by the GCM and RCM is not stationary, the delta change method analyses smaller time windows, in which the time series can assume to be stationary. This methodology is widely used as it is simple and provides adjustment factor for the flood quantiles determined with the observed data. Particularly, a delta change of rainfall (or discharge) represents the ratio between a given quantile in the future, $x_{RP,fut}$, and in the current scenario with historical observations, $x_{RP,cur}$. Nevertheless, uncertainty has a crucial role also in this approach, as the determination of the future flood quantiles $x_{RP,fut}$ for high RPs is based on the time series length of the future time windows, which is usually very short (30 years).

A second approach is based on the use of weather generators to describe the changes in climate variables supplied by the climate models. This indirect downscaling method has been proven to obtain reliable results in the description of extreme precipitation and flood frequency. Some weather generators seem to evaluate changes in extremes better than delta change methods (Sunyer et al., 2012). Nevertheless, many weather type approaches don't generate future precipitation greater than the observed one in the historical period. This aspect represents an important limitation of this approach, as the intensity of extreme events in the future climate may increase.

A third approach is the bias correction method. In this case, the output of the GCMs and RCMs are not directly used as in the previous approaches. Indeed, the model output is previously adjusted to fit with the observations. In this case, the corrected time series of the climate models have some climate variables closer to the observed ones. For instance, some methodologies correct just the mean of the model output (Graham et al., 2007) and others that also correct the standard deviation (Engen-Skaugen, 2007) or some quantiles (Déqué, 2007). The limit of the bias correction method is that the correction alters some statistical properties of GCM model outputs.

2.2 Uncertainty in flood risk assessment at different spatial scales

The uncertainty evaluation is made to consider all the sources of error in a procedure in a stochastic way. Several tools and methodologies are available to account for uncertainty (Refsgaard et al., 2007; Matott et al., 2009) and guidance to identify the most suitable uncertainty assessment tool (Van der Keur et al., 2010).

There are different sources of uncertainty in flood risk assessment studies: design rainfalls estimation and hydrological model errors are the relevant factors that impact the goodness of the analysis. Moreover, the nature of uncertainty can be different as it can be divided into two main categories: aleatory and epistemic uncertainty.

Aleatory uncertainty refers to the natural variation of the system in the environment, such as the variability of the rainfall frequency or the transformation of some parameters that are used in the

hydrological models, such as the hydraulic conductivity of the soil. Therefore, aleatory uncertainty cannot be reduced by calibrating the hydrological models. The hydrological models are a representation of a natural phenomenon that is meant to be reproduced with laws and parameters. The epistemic uncertainty relates to a partial description of the model or to the assumptions that describe the complexity of how the system works partially in a simpler way. For this reason, epistemic uncertainty can be reduced with an increased knowledge of the system.

Part of the following information in this subchapter is taken from a review by [de Moel et al. \(2015\)](#), which analysed the different sources of uncertainty in hydrological assessment studies at different spatial scales. There are many differences between flood risk assessment at different spatial scales as different scales imply different uses, data, and results reliability. The review distinguishes four different spatial scales that are used in flood risk assessment: the supra-national scale, in which the hydrological domain is the globe or a continent; the macro-scale or national scale; the meso-scale or regional scale and micro-scale, which refers to a certain province or a given small river basin.

The applicability and interest in supra-national scale studies are increased with the improvement of the computational speed of the hydrological models. Continental scale studies are useful especially in Europe to support climate change adaptation policies ([Van Renssen, 2013](#)) or to understand how public disaster relief funds must be allocated ([Hochrainer et al., 2010](#)). Nevertheless, the reliability of their results represents the most significant limitation since the scale of the events used to calibrate the models is often much smaller than the cell size in their domain. When climate change is considered in the risk assessment at these spatial scales, global scale studies usually consider GCMs without using RCMs to downscale the projections. In contrast, regional assessment studies use a combination of GCMs and RCMs and impact assessment studies. Therefore, also [Krysanova et al. \(2018\)](#) state that the use of “*hydrological models for climate impact assessment at a large (global or continental) scale without checking their performance can be useful for obtaining global/continental overviews and motivating regional- and basin-scale studies, but zooming information from large-scale maps into regions should be restricted*”.

Moreover, studies that analyse the same region can have different results for a given scenario (time window and Representative Concentration Pathways) as they use different climate models, downscaling techniques, or bias correction methods ([Kundzewicz et al., 2017](#)). For this reason, there is a need to harmonise information on flood defences derived from global or continental scale studies. Some effort in this direction is made in the next section, where an overview of global scale studies results is shown.

National scale (or macro-scale) studies, such as supra-national flood assessment studies, present the same problem regarding validating their results. Indeed, records and observations of flood events within a given country can be largely uneven, and part of the results can be unverified. For this reason, several states have undertaken the evaluation of flood hazards at the river basin authorities (meso-scale or regional scale), as at this spatial scale it is also possible to evaluate the effects of given management measures used for the mitigation of flood events.

In flood impact assessment studies at the river basin scale (micro-scale), uncertainty can usually be evaluated and managed since rain and stream flow data can provide information on past flood events. These data can be used to calibrate and validate hydrological models. At this spatial scale, [de Moel et al. \(2015\)](#) state that there is a need to improve the understanding of floods on critical infrastructures. Nevertheless, this consideration is more often valid for medium-sized river basins, as very small ones can be ungauged. In these very small spatial scales (river basins with an area generally less than 100 km²), it can often be impossible to verify the hydrological models, as the information density of the gauging network does not guarantee measurements in all these small river basins.

2.3 Impact of climate change on floods at different spatial scales

The studies that have analysed the impact of climate change on floods are divided in this chapter into three different groups: global scale studies (Section 2.3.1), European scale studies (Section 2.3.2), and river basin scale studies developed in Europe (Section 2.3.3).

2.3.1 Global scale

Global scale studies have a coarse spatial resolution because of the computational cost in such a large domain. For this reason, only the biggest rivers in the world can be considered in these studies. For instance, [Winsemius et al. \(2015\)](#) only analyse rivers with a catchment area over 10000 km², as shown in Figure 2.2. In this study, an increase in the future damages caused by floods in almost all the main river basins in the world is detected. Indeed, the circles in the figure represent the damages as a percentage of the Gross Domestic Product of each country: the left grey part represents the damages in the current scenario, while the coloured right part the damages in 2080 under the RCP 8.5 scenarios. The results of the future damages are divided into two categories, climate change impacts (purple) or socio-economic changes (green), and they describe the damages without applying Flood Protection Standard. Except for the Murray-Darling in Australia and the Volga River (Russia), all the main rivers in the world have an increase in future flood damages. All the increased damages are driven by climate change, except for the Mekong and Yangtze rivers, where the main drivers are socio-economic changes.

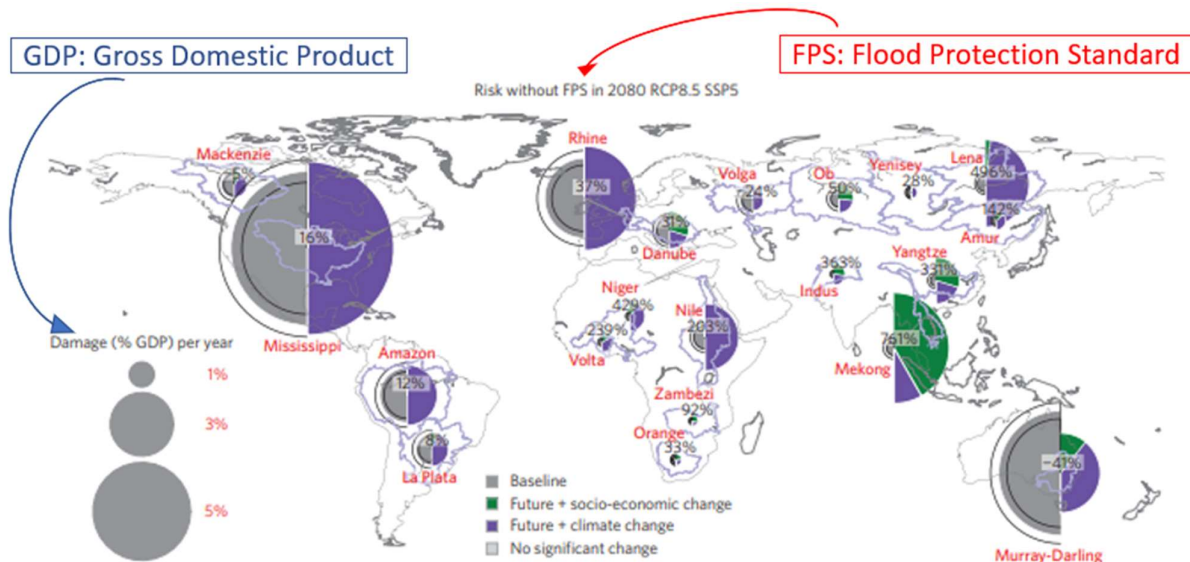


Figure 2.2. Global drivers of future flood risk (adapted from [Winsemius et al., 2015](#)).

Even if increasing flood damages are not strictly related to an increase in the flood hazard, [Hiribashi et al. \(2013\)](#) found different results, using an ensemble of 11 climate models to investigate changes in flood frequency of the 100-year flood at the global scale. In this study, a general increase in flood risk almost all over the world is not detected, as in [Winsemius et al. \(2015\)](#). Indeed, the multi-model median design flood is expected to increase in Southern and Eastern Asia, India, Africa, and a great part of South America, while a decreasing frequency is shown almost all over Europe, except for the Northern-west part. The Murray-Darling in Australia has a greater flood risk in the future than in the current scenario in this study, showing how harmonising the findings between different studies is difficult. [Hiribashi et al. \(2013\)](#) also found that global exposure to floods would increase depending

on the degree of warming. Moreover, the interannual variability of the exposure may imply the necessity of adaptation before significant warming. Similar results are found by [Alfieri et al. \(2016\)](#), which analyse the impact of different degrees of warming (+1.5°C, +2°C and +4°C) on floods at the global scale. The increasing frequency of floods in this study is directly proportional to the degree of warming all over the world. The most significant expected changes in floods at the global scale are found in the RCP 8.5 also in [Arnell and Lloyd-Hughes \(2014\)](#). The impacts of climate change on floods have not only been investigated by analysing their magnitude but also their duration. [Najibi and Devineni \(2018\)](#) use the global flood database of the Dartmouth Flood Observatory (DFO) to analyse the presence of trends in flood duration during 1985–2015 at global and latitudinal scales. Their results show a significant increasing trend in the annual median of flood durations globally. Summarising all these results, a clear increase of the design floods almost all over the world is detected in the RCP 8.5 with some discrepancies only in Europe, which is further analysed in the next section, and Australia.

2.3.2 European scale

Many studies have analysed expected flood risk changes in Europe using trend analyses or hydrological models with climate projections. Recent studies to identify large-scale trends in observed time series have shown that a changing climate in the last decades both increases and decreases European river floods ([Hall et al., 2014](#); [Blöschl et al., 2019](#)). [Blöschl et al. \(2019\)](#) investigate trends in the mean annual flood, and the results depend mainly on which part of Europe is considered. While Southern and Eastern Europe show negative trends in river floods, the Northern part of Europe has increasing trends. The authors explain that since mean annual floods are usually correlated with the 100-year flood discharge, similar trends could also be expected for the design flood, which represents the key design criterion in flood risk management.

Trends of 100-year flood discharge frequency are shown in Figure 2.3 on the left. The red dots (or red areas) represent the parts of Europe in which the 100 y-flood of 1960 is associated with a return period of over 100 years in 2010, i.e. where decreasing trends in the magnitude of the design flood have occurred. Nevertheless, trends in observed data from the past differ in some areas from the 100-year flood obtained with hydrological models and climate projections in some RCP scenarios. Indeed, [Alfieri et al. \(2015\)](#) use climate projections in the RCP 8.5 as input of the Lisflood hydrological models and point out that, on average, flood peaks with return periods above 100 years can double their frequency within three decades in Europe, as it is shown in the right part of Figure 2.3. The two studies agree on increasing design floods (100-year flood) in the North-West of Europe and decreasing design floods in eastern Europe. Still, their findings are very different in the Mediterranean area, especially in Italy, Northern Spain, Southern France and the Balkans (black ovals in the figure). For this reason, the case studies chosen in this thesis are within these areas.

Even if the two studies are not directly comparable, as they use different approaches, the results have opposite directions in the Mediterranean area. In this area, several other studies found contrasting results. For instance, future design discharge (100-year flood) in Spain will decrease in the future for [Dankers et al. \(2009\)](#) and [Rojas et al. \(2012\)](#) and will increase for [Roudier et al. \(2016\)](#). Nonetheless, some of these latter studies agree with [Alfieri et al. \(2015\)](#) on the increasing trend for the 100-year flood in western and eastern Europe, especially on the decreasing trends in north-eastern Europe ([Dankers et al., 2009](#); [Rojas et al., 2012](#)). As a matter of fact, there is not a clear pattern of the future hydraulic risk for Southern Europe because all the studies consider different climate models, downscaling techniques, or bias correction methods ([Kundzewicz et al., 2017](#)), as also explained in the previous section. Nevertheless, the results of future design floods in Europe can be summarised

as an increase in the north-western part and a decrease in the northeast, while the Mediterranean area is affected by more uncertainty, as the studies show discrepancies in this region.

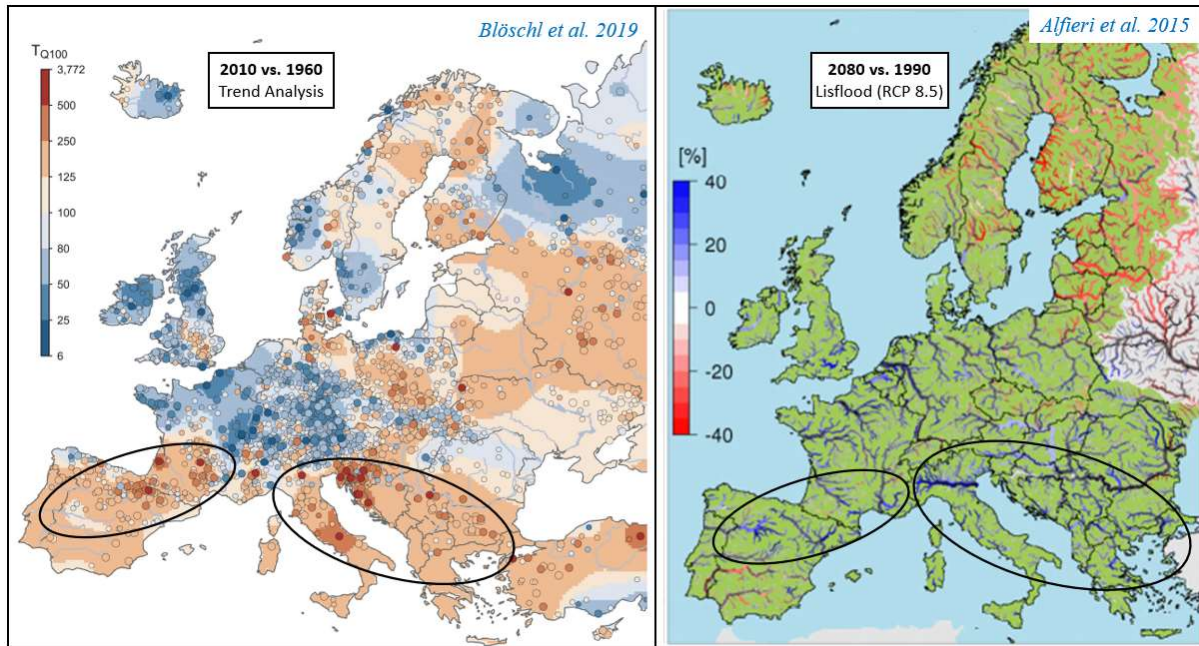


Figure 2.3. Comparison of the 100-year flood between trend analysis and climate change projections on flood in Europe. The black ovals show the regions in which the trend analysis on observed data has a different pattern from the rainfall-runoff model with projections (adapted from Blöschl et al., 2019 and Alfieri et al., 2015).

2.3.3 River basin scale

Several studies have considered the impact of climate change in smaller river catchments, avoiding extrapolating the results from large-scale studies. They evaluate the climate change impact on the water cycle with different objectives, as climate change can have implications for sustainable management of ecosystem services (Pham et al., 2019), daily, monthly, and yearly streamflow patterns (Zhang et al., 2016) or engineering hydraulic design (Quintero et al., 2018). Findings in flood quantile changes in small-scale studies either can differ from the results obtained in the same zone by large-scale studies or can have different change signals for all the considered climate models. In this latter case, statistically significant changes could not be obtained using an ensemble of climate models (Osuch et al., 2012). Table 2.3 shows the results of some climate change impacts on flood assessment studies at the river basin scale in Europe. The information in the table is obtained by extrapolating and updating a review on this topic (Madsen et al., 2014). Table 2.3 shows how all the studies focused on the impact of climate change on floods at the river basin scales are conducted with lumped or semi-distributed hydrological models. The use of a fully distributed hydrological model in climate change impact assessment studies is less investigated, even if the description of the flood routing process can usually be better described in such models. Indeed, fully distributed hydrological models are demonstrated to perform better in flood detection as they can include more information on the spatial heterogeneity in terrain, soil texture, land cover and meteorological conditions (Zang et al., 2013). Moreover, Table 2.3 also shows how any information on extreme floods with high return periods can be found, such as, for instance, the 1000-year flood. Indeed, studies in literature are usually focused on the mean annual flood or the design discharges

with lower return periods. Even if high return periods can be strongly uncertain, hydrological dam safety assessment requires the definition of very extreme floods.

Table 2.3. Review of the climate change impacts on flood studies at the river basin scale in Europe (Adapted from [Madsen et al., 2014](#)).

Reference	River Basin	Region	Model	Key findings
Hlavcova et al. (2007)	Hron	Slovakia	Slovak University of Technology Lumped rainfall–runoff model	Increases in discharge up to 80% in 2030 and up to 140% in 2075
Kriauciuniene et al. (2008)	Nemunas	Lithuania	SWIM	Significant decreases in spring flood magnitude.
Ducharne et al. (2010)	Seine and Somme	France	WSFS	10-year flood magnitudes do not change significantly.
Lawrence and Haddeland (2011)	Flaksvatn, Masi, Nybergssund, Viksvatn	Norway	HBV	Large decreases in annual flood in the northern and inland catchments; moderate increases in the southern and western catchments by 2100
Osuch et al. (2012)	Wetna and Orla	Poland	HBV	different directions of change or lack of statistically significant changes
Iulii Didovets et al. (2019)	Tisza and Prut	Romania Ukraine Moldova	SWIM	30-year flood increase in the RCP4.5, huge uncertainty in the RCP 8.5
Soriano et al. (2020)	Douro	Northern Spain	HBV	large increase in the flood quantiles by 2100 obtained for the RCP 8.5

2.4 Impact of climate change on hydrological dam safety

The impact of climate change on hydrological dam safety is described in this subsection separately because the impact at the infrastructure scale requires methodologies that are different from the quantification of expected changes in flood quantiles only. Several aspects relate to future dam safety and there are both climatic and not climatic drivers that can generate different failure modes, such as overtopping, piping or sliding. This thesis focuses only on hydrological dam safety, and overtopping hazard is assessed only. Overtopping occurs when the water level in the reservoir reaches the dam crest and starts spilling over the downstream face of the dam. Over the last century, almost 30% of all dam failures worldwide have been caused by overtopping (Jandora et al., 2008), and floods represent the main driver of this phenomenon (Costa, 1985). A detailed analysis of overtopping requires comprehensive information on hydrology; hydraulics; characteristics of the dam, spillways, and reservoir; and the use of routing methods (Michailidi and Bacchi, 2017). For this reason, only studies at the river basin scale can properly assess the impact of climate change on future dam safety, even if tools to assess overtopping probabilities in more dams at the regional scales are available (Fluixa-Sanmartin et al., 2019a).

Stationary climatic baselines seem to be no longer appropriate for long-term dam safety management (USACE, 2016). Moreover, larger dams upstream of population centres are often designed for downstream flood-control purposes. Still, they were designed and built assessing flood risks known at the time of the construction (Chen and Hossain, 2019). For this reason, several studies proposed different methodologies to evaluate if dams are still safe nowadays or if their risk is changed over time. At the same time, future dam safety can also be assessed considering climate change projections. Fluixa-Sanmartin et al. (2019b) analyse the future dam safety of a dam in Western Spain with 21 climate projections and three RCP scenarios and found a significant uncertainty in the risk given by the climate projection inputs for the RCP 8.5, while an increase in both the social and economic risks is detected for the RCP4.5 scenarios. Lee and Gene Jiing-Yun (2013) combined the effect of climate change with the increased risk due to the reduction of the flood control volume caused by sedimentation. The conclusion is that the major source of risk is the magnitude of extreme hydrological conditions. Nevertheless, this study has two main limits: no projections supplied by climate models are used, while time-dependent Gamma distribution is used; overtopping is not analysed directly by assessing changes in reservoir water levels, but the 2000-year flood is considered the event threshold that causes overtopping.

A recent review on climate change impact on dam safety (Fluixa-Sanmartin et al., 2018a) explains that most studies tend to focus only on the projections of the future hydrological loads (Bahls and Holman, 2014; Chernet et al., 2014; Novembre et al., 2015), i.e., the variations of the inflow hydrograph, neglecting other aspects, such as the future variations on the initial water level in the reservoir. Indeed, climate change is expected to affect future water availability because of the increased precipitation variability and potential evapotranspiration (IPCC, 2014), impacting the water level frequency in the reservoirs. Moreover, reservoir storage volumes reduction are expected in the future also because of the decrease in catchment runoff or the increase of evapotranspiration rates (Konapala et al., 2020; Fluixa-Sanmartin et al., 2019b; Bukac et al., 2017). In fact, global annual mean reservoir evaporation rates are expected to increase by 16% by 2100 (Woolway et al., 2020). A decrease of reservoir water levels in the future will increase the hydrological dam safety, as flood will encounter a lower volume in the reservoir at the beginning of the event. Nevertheless, it is essential to account for both the variation of the inflow hydrographs and the water level frequency to obtain reliable results. A reservoir operation model able to estimate outflow discharges in the future is needed to assess expected changes in water level frequency between the future and the current scenario. In literature, HEC-ResSim (Klipsch and Hurst, 2007) represents a tool that can do this kind of analysis, even if it is more suitable for managing a reservoir network on a given river rather than

modelling a single dam. Indeed, the software also evaluates inflow discharge in the reservoirs, modelling the upstream watershed and preventing the use of other hydrological models for estimating the inflow volumes. Dam risk analysis is usually correlated to floods with high return periods, and their estimation is affected by significant uncertainty. Therefore, evaluating uncertainty due to hydrological and climate modelling must be accounted for to provide scientifically based advice to decision makers (Prudhomme and Davies, 2008).

2.5 Impact of climate change on flash floods

Flash floods are considered in this subsection because the temporal scale of these events relates to sub-daily precipitation in often small ungauged river basins. Indeed, all the studies described in the previous sections are done with projections of daily precipitation, and this temporal scale is insufficient to describe the flash flood phenomena. Flash floods are among the worst natural hazards, as they are characterised by sudden, short-duration heavy rains and unpredictable peak discharges (Ali et al., 2017). Flash floods are generated by rainfall events, mainly of convective origin, that occur locally and usually impact small river basins with response times of a few hours or less (Marchi et al., 2010). In the last three decades, the number of significant flood events in the world has increased. This is related to the impact of climate change on extreme precipitation and the land use change connected with the increasing urbanisation (Kourgialas and Karatzas, 2011). Climate change is leading to the intensification of extreme rainfall. High precipitation quantiles of short durations generally increase with temperature as this is possibly related to an increase in convective origin precipitation (Lenderink and Van Meijgaard, 2008; Berg et al., 2013). Moreover, flash floods are expected to increase in the future in frequency and magnitude under some climate change scenarios (Dougherty and Rasmussen, 2021; Zhang et al., 2019), and an increasing trend of flash flood events have been detected in the Mediterranean area (Llasat et al., 2016; Esposito et al., 2018). Consequently, there is a need for practical approaches and methods for flash flood management under such changing circumstances (Dawod et al., 2011). However, changes in urban flash flooding may not be detected this century in some regions, as there is a lack of sufficiently long, high-quality, sub-daily observational records (Kendon et al., 2018). For this reason, a strategy to obtain information on sub-daily rainfall projections can be the use of an hourly weather generator to temporal disaggregate the daily projections, as in Zhang et al. (2021). In this study, the authors calibrate the weather generator in the historical period and then evaluate the future flash flood occurrence with 13 GCMs in the RCP 4.5. The results identify a unanimous increase in flash flood frequency due to the increase of short extreme rainfall.

Southern Europe is vulnerable to flash flood events because their intensity is greater in magnitude in the Mediterranean countries and decreases moving inland (Gaume et al., 2009). At the same time, this region is the most affected by uncertainty when projections of the future design floods are considered (section 2.3). In this context, decision-makers need a simple and useful approach to take the right measures against the impacts of these events. Nevertheless, observed data about flash floods are scarce, as such events often occur in small ungauged river basins (Blöschl et al., 2019).

The risk associated with a flash flood can be reduced with forecasting models that work in real-time to give a forewarning, such as the Flash Flood Guidance (Mogil et al., 1978), which is based on rainfall thresholds. Nevertheless, such a method is more suitable for river basins with response times greater than three hours. Even if it is possible to forecast rainfall and establish a given alert threshold previously, the uncertainty behind the procedure (forecasting, rainfall-runoff model, initial soil moisture condition) prevents the possibility of a system with a high degree of reliability, especially in ungauged river basins. For this reason, flash flood risk pre-assessment, i.e. identifying the prone areas to flooding, can support decision-making and reduce the hazard of these events (Saharia et al., 2017; Cao et al., 2016).

2.6 Knowledge gaps

This section includes the research questions that emerged from the literature review. In some cases, the knowledge gaps do have not a research “question” properly, but they express with a sentence something that is missing and that it is necessary to be done for the study. This section is further divided into four parts according to the structure of this thesis, i.e. each part represents a given chapter. The research questions will have answers in each chapter's discussion or conclusion section. Moreover, the conclusion will also be summarised in the final chapter of the thesis (Chapter 8).

2.6.1 Impacts of climate change on river floods (Chapter 4)

The lack of agreement between global and European scale assessment studies cannot be read easily by decision-makers. Furthermore, large-scale studies on climate change impact on floods cannot provide information on each catchment within their study area. However, quantifying flood quantile changes is crucial in urban areas and municipalities, especially for urban planners. Moreover, large-scale studies are mainly conducted for the 100-year flood and are focused on time windows close to the end of the century. Indeed, other return periods are not usually considered in these studies, and they don't provide information in time windows close to nowadays. Moreover, Southern Europe is an area where studies are particularly conflicting with contrasting signals of future floods changes. In addition, fully distributed hydrological models are rarely used to assess impact of climate change in flood quantiles. Therefore, the first section (Chapter 4) considers the spatial distribution of future design rainfall fields to address the following questions:

- *Will climate change impact floods with a homogeneous pattern regardless of flood frequency or with a varying pattern in return periods?*
- *Is there any relationship between RCP scenarios and expected changes in floods depending on their frequency or return period (RP)?*
- *Do delta changes in flood quantiles show different patterns depending on the time window considered in the future?*
- *Do expected changes in flood quantiles depend more on the results supplied by GCMs or on the downscaling techniques (RCMs)?*

2.6.2 Impact of climate change on hydrological dam safety (Chapter 5)

There are several climate change studies at the river basin scale in the literature. However, the impact of climate change on hydrological dam safety is less investigated. Particularly, there is a lack of studies that evaluate the expected changes in reservoir water level frequency at the beginning of a flood event in the future. Moreover, the few available studies that assess the impact of climate change on dams are mainly focused on dam stability and overtopping probability. Nevertheless, they usually neglect the impact of climate change on the outflow discharge released by the dam. The outflow discharges can vary in the future due to the flood routing processes of more extreme events in the reservoir. Quantifying the future outflow discharge frequency is essential to assess the downstream population hydraulic risk properly. Therefore, the knowledge gaps are:

- *A complete procedure for the evaluation of hydrological dam safety in climate change is needed.*

- *Which are the impacts of climate change on reservoir water level frequency in different time windows and emission scenarios?*
- *How will climate change impact the reservoir outflow hydrographs?*
- *Will overtopping probability increase or decrease in the future?*

2.6.3 Uncertainty in hydrological dam safety and climate change studies (Chapter 6)

There are many sources of uncertainty in assessing future hydrological dam safety. The uncertainty of the future inflow hydrographs represents the most important part, as hydrological dam safety is associated with high return periods. Indeed, design rainfalls with high return periods are affected by significant uncertainty. In addition, errors in hydrological model simulations that remain after their calibration and validation must be quantified to consider the uncertainty in their estimates. The errors of the hydrological models can also affect the evaluation of the initial reservoir water level at the beginning of a flood event. Therefore, the procedure proposed for evaluating hydrological dam safety should include an uncertainty assessment. For this reason, the knowledge gaps are:

- *The methodology to assess the impact of climate change on hydrological dam safety must include an uncertainty chain assessment.*
- *The methodology for assessing all the sources of uncertainty in rainfall quantiles, inflow peaks discharge, and reservoir water levels is missing.*
- *How does uncertainty affect the future hydrological dam safety assessment?*

2.6.4 Improve flash floods hazard assessment at the regional scale (Chapter 7)

The southern part of Europe represents two main questions unsolved. As already said, the impact of climate change on future floods is less clear here than in other zones. Moreover, flash floods are more frequent and extreme in this area due to the vicinity of the Mediterranean Sea. Flash flood risk cannot be easily managed, as floods often occur in ungauged river basins, where models cannot be calibrated and uncertainty cannot be assessed. In addition, climate projections of short duration are not available everywhere. Therefore, new methodologies are required to increase the reliability of design discharges in small ungauged river basins, especially to face the intensification of extreme short-duration rainfall. Moreover, a simple methodology could guarantee its use in the river basin authority at the regional scale.

- *A methodology to improve flash flood hazard assessment at the regional scale is necessary.*
- *Are design floods usually underestimated or overestimated in small ungauged river basins with respect to the flash flood risk?*

Chapter 3

Methodology

The general methodology adopted in the thesis is described in this chapter. An overview of the relations and connections between each case study is shown, that is how the output of a given case study represents the input of another one. A more detailed methodology of each case study is then deeply presented in each chapter of the thesis (see thesis outline in Figure 1.3). Three cases are selected to test the methodologies proposed in this thesis work and are described in section 3.2. At the same, three software are used in the methodology and are described in section 3.3. The first part of the thesis regards the assessment of the impact of climate change on floods and hydrological dam safety. This part uses both observed data and climate projections (yellow circle in Figure 3.1), and it is deeply described in Figure 3.2. The second part involves flash floods in ungauged basins. Hence, the same methodology cannot be applied at these spatial scales, as hydrological models cannot be calibrated, uncertainty cannot be assessed and climate projections for short-duration rainfall are unavailable. Nevertheless, a methodology to face the impact of climate change on short-duration rainfall and flash flood occurrence is needed. Therefore, this part has a methodology based only on observed data (blue circle in Figure 3.1), further described in Figure 3.3.

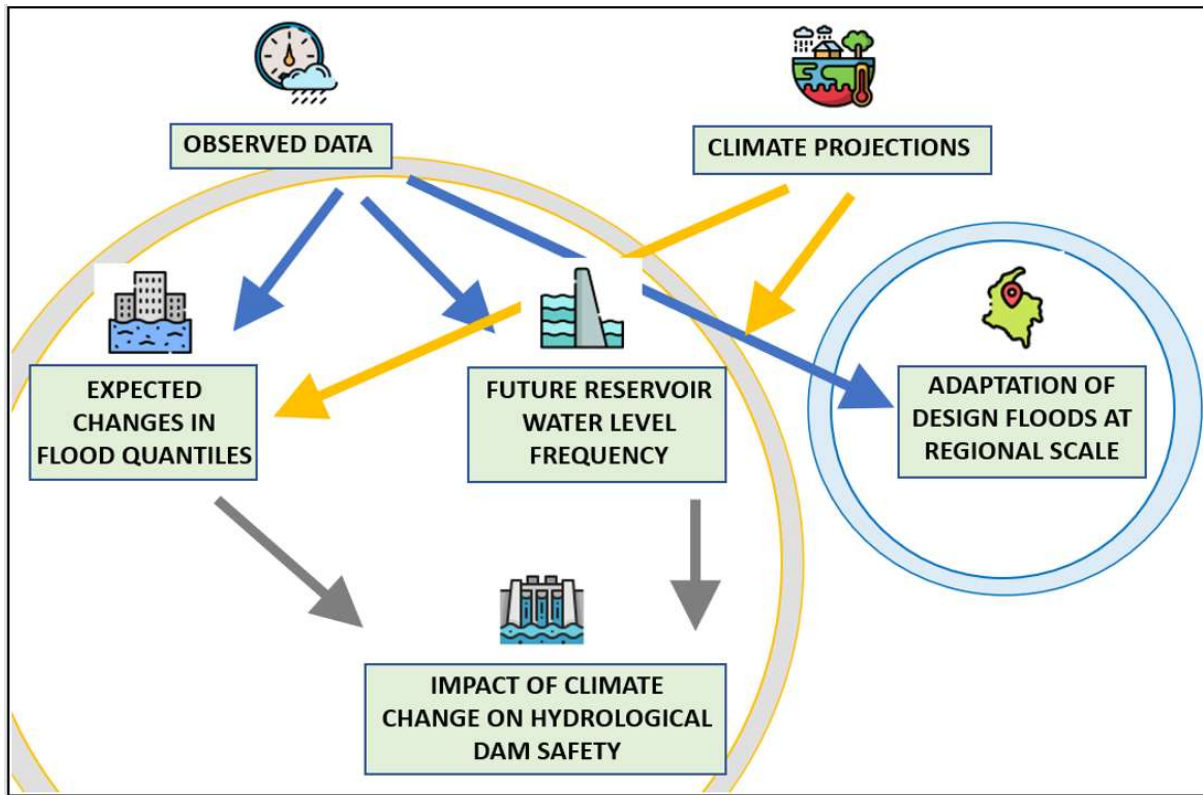


Figure 3.1. General methodology of the thesis: observed data and climate projections are used to assess the impact of climate change on floods and reservoir water levels to characterise the future hydrological dam safety; only observed data are used in the methodology to adapt design floods of small river basins at the regional scale.

3.1 General Methodology

The two proposed methodologies are shown in this section: the assessment of climate change on floods is done at the river basin scale to evaluate the future design floods, and at the infrastructure

scale to assess future hydrological dam safety (Figure 3.2); the adaptation of the design floods of small river basins is made to account uncertainty and climate change impacts on floods at the regional scale (Figure 3.3).

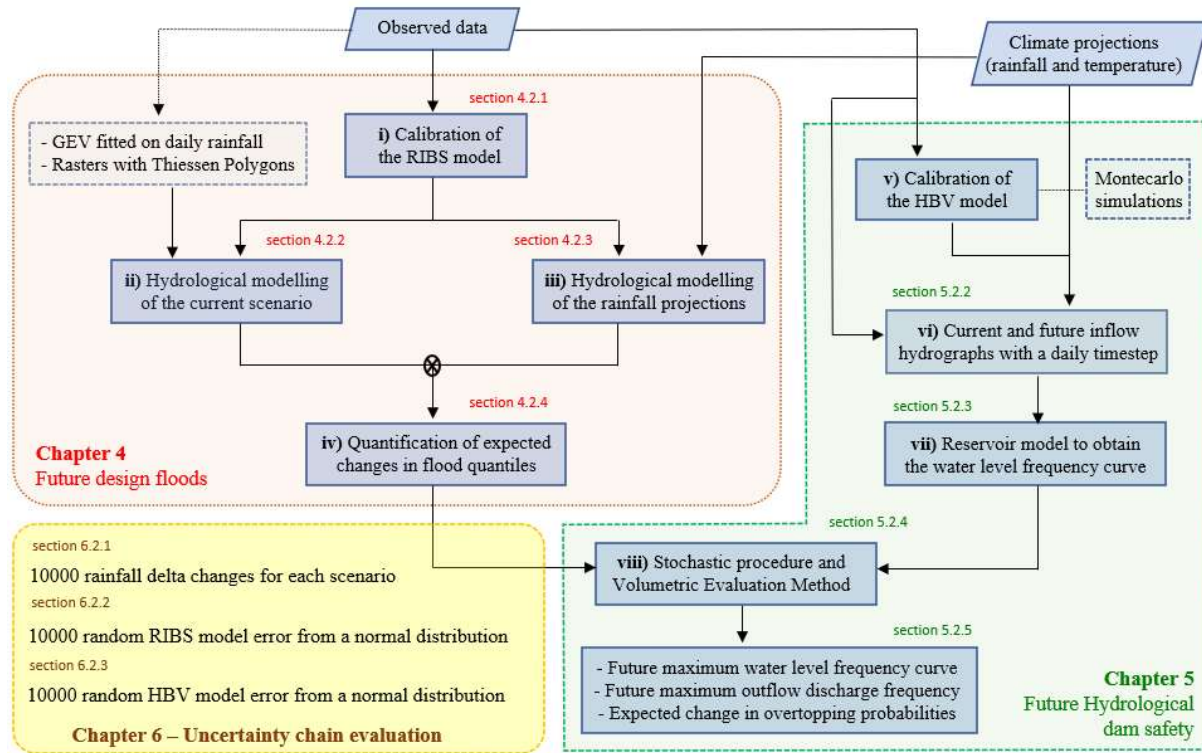


Figure 3.2. Flow chart representing the methodology of the thesis related to the assessment of climate change on floods at the river basin scale and on hydrological dam safety.

Expected changes in flood quantiles must be determined to evaluate the impact of climate change on hydrological dam safety. The evaluation of the expected changes in flood quantiles (Section 4.2.4) is done in Chapter 4 by comparing the flood quantiles of the current scenario (Section 4.2.2) with the ones obtained using rainfall projections as input data (Section 4.2.3). This comparison is made with the Real time-Interactive Basin Simulator (RIBS) fully distributed hydrological model (Section 3.3.1) after its calibration (Section 4.2.1). The observed data in Figure 3.2 represents observations of rainfall, temperature, and discharge. To calibrate the RIBS model just rainfall and discharge data are required. Daily rainfall data are used to estimate the design rainfalls of the current scenarios with a Generalized Extreme Values (GEV) distribution. Then, they are spatially distributed with the Thiessen Polygon Technique.

The climate projections are the input data to estimate the future design floods. Daily precipitation quantiles in the future are extracted from rainfall climate projections supplied by 12 climate models of the EURO-CORDEX program for the Iberian Peninsula (Garijo and Mediero, 2019). The climate models are combinations of GCMs and RCMs (Table 3.1). The “delta change” approach is used in this study to assess the flood frequency in the future, as bias corrections methods alter statistical properties of GCM model outputs to fit GCM outputs to observations in the control period. Therefore, the expected changes predicted in the future could also change, modifying change signals predicted by GCMs. A delta change of rainfall represents the expected variation of a given rainfall quantile between the future and the current scenario (see Section 2.1.2). Delta changes are provided for each combination of return period, climate model, time window and RCP scenario. Particularly,

they are supplied for seven return periods (RP = 2, 5, 10, 50, 100, 500 and 1000 years), two representative concentration pathways (RCP 4.5 and RCP 8.5) and three time windows in the future (2011-2040, 2041-2070, 2071-2100). More information regarding the climate models (GCMs and RCMs) that provide the projections and the delta change methodology can be found in sections 2.1.1 and 2.1.2, respectively.

Table 3.1. Ensemble of the 12 climate models considered in this thesis.

Code	Acronym	GCM	RCM
1	ICH-CCL	ICHEC-EC-EARTH	CLMcom-CCLM4-8-17
2	MPI-CCL	MPI-ESM-LR	CLMcom-CCLM4-8-17
3	MOH-RAC	MOHC-HadGEM2-ES	KNMI-RACMO22E
4	CNR-CCL	CNRM-CERFACS-CM5	CLMcom-CCLM4-8-17
5	ICH-RAC	ICHEC-EC-EARTH	KNMI-RACMO22E
6	MOH-CCL	MOHC-HadGEM2-ES	CLMcom-CCLM4-8-17
7	IPS-WRF	IPSL-CM5A-MR	IPSL-WRF331F
8	IPS-RCA	IPSL-CM5A-MR	SMHI-RCA4
9	MOH-RCA	MOHC-HadGEM2-ES	SMHI-RCA4
10	ICH-RCA	ICHEC-EC-EARTH	SMHI-RCA4
11	CNR-RCA	CNRM-CERFACS-CM5	SMHI-RCA4
12	MPI-RCA	MPI-ESM-LR	SMHI-RCA4

The impact of climate change on the reservoir water level frequency curves is evaluated in Chapter 5, where the HBV continuous hydrological model (Section 3.3.2) is integrated with a reservoir operation model. HBV is calibrated with Montecarlo simulations and 13 years of precipitation, temperature, and reservoir inflow discharge observations. HBV simulates daily inflow discharges in the Eugui reservoir (see next section) using rainfall and temperature projections as input data (Section 5.2.2). The reservoir operation model is developed to obtain daily reservoir water levels (Section 5.2.3). It uses HBV inflow discharges as input data and considers reservoir operation rules, such as water supplies and environmental releases. Expected changes in daily reservoir water levels at the Eugui dam are assessed for each time window and emission scenario, including the control period using the same ensemble of climate models (Table 3.1).

A stochastic procedure is then used to combine the future design discharge obtained in Chapter 4 with the variation in the water level frequency (Section 5.2.4). A set of 10,000 peak inflow discharges are randomly generated from several GEV distribution functions fitted to the outputs of the RIBS model. Given hydrograph shapes and initial reservoir water levels are assigned to each peak flow. The Volumetric Evaluation Method (VEM) simulates flow routing processes in the reservoir. The frequency curves of maximum reservoir water levels and maximum outflow discharges are obtained for each scenario, assessing the expected changes in the probability of exceedance of dam overtopping. In addition, the uncertainty chain of the methodology is evaluated in a stochastic way in Chapter 6. Particularly three sources of uncertainty are considered: uncertainty in rainfall delta changes estimation (Section 6.2.1), uncertainty associated with the inflow hydrographs related to RIBS model error (Section 6.2.2) and the uncertainty in the initial reservoir water level estimation due to the HBV model (Section 6.2.3). Each scenario is modelled within the stochastic procedure 10,000 times to provide percentiles of the future maximum water levels and the future maximum outflow discharges.

The second part of the thesis, which relates to the adaptation of the design rainfalls at the regional scale, follows the methodology shown in Figure 3.3, which is then deeply described in Chapter 7.

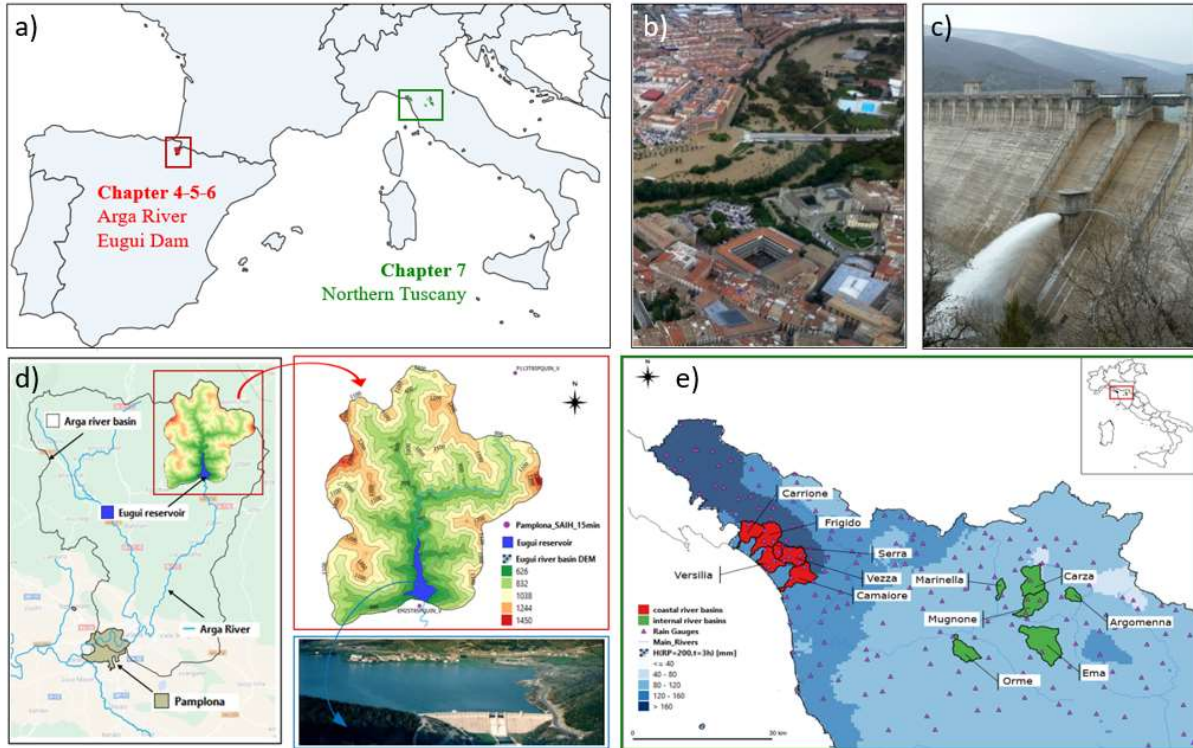


Figure 3.4. a) Case studies of the thesis: in red Argave river basin (river basin scale) and Eugui Dam (infrastructure scale) located in Northern Spain; in green Northern Tuscany (regional scale); b) photo of the fluvial flood occurred in Pamplona in June 2013 (source: https://elpais.com/politica/2013/06/10/album/1370888219_774560.html); c) Eugui dam (source: <https://mapcarta.com/24884700>); d) Argave river basin upstream to the city of Pamplona and Eugui river basin upstream to the dam e) River basins analysed in Northern Tuscany for the procedure applied at the regional scale to improve flash flood assessment.

Northern Tuscany is the case study where the methodology of design floods' adaptation in small river basins is tested since this region is vulnerable to flash flood events. Indeed, flash floods have been proven to be more intense in Mediterranean countries (Gaume et al., 2009), especially along the coast. Northern Tuscany, such as near Liguria, has a mountain range very close to the Tyrrhenian Sea. The proximity of this orography to the coast causes lots of convective storms. For this reason, many flash floods have occurred in recent years near the Tyrrhenian Sea, along the coasts of Liguria and Tuscany (Arrighi and Castelli, 2020; Faccini et al., 2015; Faccini et al., 2018; Faccini et al., 2021).

3.3 Software and tools

The choice of the most appropriate hydrological model depends on the spatial and temporal scale of the phenomenon intended to be presented. The thesis requires both hydrological models at the single-event temporal scale and long-term continuous hydrological modelling.

Fully distributed hydrological models at the single-event temporal scale can usually better describe the flooding process in a river basin associated with high rainfall quantiles than semi-distributed or lumped models. On the other hand, a continuous model that works with long-term simulation is needed to calculate the expected variation of reservoir water levels since future scenarios have a time series length of almost 100 years. Moreover, since many river basins must be modelled at the regional scale, a fully distributed hydrological model would require high computational cost, even if the single event temporal scale is involved.

For all these reasons, the fully distributed hydrological model RIBS (Garrote and Bras 1995a,b) is used to assess the impact of climate change on floods in the Arga river (river basin scale and single event temporal scale); HBV (Bergstrom, 1976; Bergstrom, 1992) is used for long term modelling at the river basin scale; HEC-HMS (USACE, 2013) is used to model design and short-duration events to adapt the design floods against the flash flood hazards (regional scale and single event temporal scale).

3.3.1 RIBS model

The Real-time Interactive Basin Simulator (RIBS) (Garrote and Bras 1995a,b) is a distributed hydrological rainfall-runoff model typically used for real-time application on medium-size river basins. RIBS requires the information in a raster format, in this case with a cell size of 50 meters. A Digital Elevation Model (DEM) is used to determine the flow direction and flow accumulation in each cell of the domain. The soil information is used to estimate the parameters in the Brooks-Corey equation (Eq. 3.1) to calculate the part of the rainfall depth that is transformed into runoff in each cell.

$$K_s(y) = K_{0n} e^{-fy} \left(\frac{\theta - \theta_r}{\theta_s - \theta_r} \right)^\varepsilon \quad (3.1)$$

where $K_s(y)$ is the saturated hydraulic conductivity (mm/h), K_{0n} is the saturated hydraulic conductivity at the soil surface in the normal direction (mm/h), f is the saturated hydraulic conductivity decay in depth (mm^{-1}), y is the soil depth (mm), θ is the soil moisture content, θ_r is the residual soil moisture content, i.e. the minimum value under which capillary forces cannot extract the humidity, θ_s is the saturated moisture content, and ε is the index of soil porosity (Cabral et al., 1992). The Brooks-Corey equation assumes that $K_s(y)$ has a maximum value at the soil surface (K_{0n}), and then decrease exponentially in the normal direction in the soil depth y with the parameter f . Ten different antecedent soil moisture conditions (AMC) at the beginning of the flood event simulation can be considered in the RIBS model. The AMC are characterised based on the water table depth from the terrain surface.

When rainfall intensity exceeds the soil infiltration capacity, surface runoff is generated. Runoff is propagated in the domain through Eqs. 3.2 and 3.3. The catchment is divided into two parts based on a given flow accumulation threshold. Cells with flow accumulation values under such a threshold represent hillslopes in the model and have a runoff velocity equal to v_h . Cells with flow accumulation values over the threshold represent streams with a water velocity equal to v_s . It is assumed that v_s depends on the discharge in the catchment outlet with respect to a reference flow rate Q_{ref} (Eq. 3.2).

$$v_s(t) = C_v \left[\frac{Q(t)}{Q_{ref}} \right]^r \quad (3.2)$$

where v_s is the water velocity in streams (m/s), C_v is a model parameter (m/s), $Q(t)$ is the discharge at the catchment outlet in time step t (m^3/s), Q_{ref} is a reference discharge (m^3/s), and r is a model parameter. If r equals 0, v_s equals C_v , remaining constant throughout the simulation. If r is greater than 0, v_s is greater than the parameter C_v when the discharge at the catchment outlet is higher than Q_{ref} . At a given time step, the velocity in hillslopes, v_h , is related to the velocity in streams, v_s , with the dimensionless parameter K_v (Eq. 3.3).

$$K_v = \frac{v_s(t)}{v_h(t)} \quad (3.3)$$

Both velocities can be considered uniform in all the stream and hillslope cells at a given time step, as v_s depends only on the discharge at the catchment outlet. More information about the RIBS model can be found in [Mediero et al. \(2011\)](#), [Garrote and Bras \(1995a\)](#) and [Garrote and Bras \(1995b\)](#). The parameter r in Eq. 3.2 has been set equal to 0 to reduce the computational cost of the model, as the number of simulations with climate change scenarios is high. Therefore, velocity in streams (v_s) is always equal to C_v in all the time steps. The model parameters that are considered during the calibration procedure are reduced to three: f (Eq. 3.1), C_v (Eq. 3.2) and K_v (Eq. 3.3).

3.3.2 HBV model

Hydrologiska Byråns Vattenbalansavdelning (HBV) is a semi-distributed conceptual continuous rainfall-runoff model ([Bergstrom, 1976](#); [Bergstrom, 1992](#)) widely used in long-term hydrological modelling. The catchment is divided into sub-catchments, which can be further divided into a set of elevation and vegetation zones. The data required by the model are daily temperature, precipitation, and potential evapotranspiration (PET), which must be calculated externally to the model. The model structure is divided into three modules (snow and glacier routine, soil routine, and response function routine). Runoff (Q) is obtained with Eq. 3.4, which represents a mass balance equation.

$$P - AET - Q = \frac{d}{dt}(SNP + SM + SUZ + SLZ + lakes) \quad (3.4)$$

Where P is precipitation, AET is the actual evapotranspiration, SNP is the snowpack, SM is the soil moisture, SUZ and SLZ are the upper and lower groundwater zones, and lakes represent the storage volume of lakes ([Devi et al., 2015](#)).

In the snow routine, precipitation data are distributed over the river basin: precipitation is converted into snow accumulation with a snowfall correction factor SFCF where the temperature is under the temperature threshold TT ; precipitation is rain where the temperature is above TT . Indeed, the temperature varies within the elevation zones of the river basin with $TALT$ [$^{\circ}C/100$ m], while the temperature input data are associated with the zones with the same altitude of the instrument. In the same way, also precipitation intensity varies with the altitude with $PCALT$ [%/100 m]. Moreover, temperature also varies each month with respect to a seasonal parameter SP . The snow already present in the SNP melts with a degree-day method, in which a parameter $CFMAX$ reflects the equivalent melted snow as a function of the difference between the temperature and TT . On the contrary, water can also refreeze into snow with a refreezing coefficient CFR . Meltwater and rainfall represent the liquid part in the SNP , and they are retained within it until they do not exceed the water holding capacity CWH . Once CWH is exceeded, the liquid portion is divided into surface runoff Q and infiltration in the soil routine. The infiltrated water fills the soil box, recharging the groundwater depending on the ratio between the content already present in the soil box SM [mm] and its largest possible value FC [mm]. The soil is characterised by two reservoirs: upper (SUZ) and lower (SLZ). Groundwater recharge is firstly added to the upper groundwater box SUZ [mm] and then arrives in the lower groundwater box SLZ . The maximum percolation rate $PERC$ [mm/day] defines the underground flow between the two reservoirs. Both rain and snow contribute to runoff. A $BETA$ parameter determines the relative contribution to runoff from rain or snowmelt. In the soil routine, the actual evaporation (AET) depends on the soil moisture SM . When the soil moisture is above a given threshold ($LP*FC$), AET is equal to the potential evaporation (PET), which is calculated externally and is an input of the model. Otherwise, AET is reduced linearly from its maximum value (PET) to zero with respect to the SM .

Runoff from the two groundwater boxes SUZ and SLZ is simulated as a release from two linear reservoirs with parameters K1 and K2. A further contribution from the upper box is considered only if the SUZ is above a threshold UZL [mm]. After the runoff generation, the response routing determines the discharge using a triangular weighting function characterised by the parameter MAXBAS (Seibert and Vis, 2012).

3.3.3 HEC-HMS

HEC-HMS (USACE, 2013) is a widely known and used semi-distributed hydrological model. For this reason, just a few details are given in this section. Further information can be easily found in the software user manual, especially in the Technical Reference Manual (available at: <https://www.hec.usace.army.mil/software/hec-hms/documentation.aspx>). HEC-HMS is a rainfall-runoff model that describes the river basin hydrology by dividing it into hydrological units as subbasins, reaches, junctions and reservoirs. In each hydrological unit, several models can be implemented. For instance, in each subbasin, canopy surface, baseflow, transform, and loss method can be chosen between a plethora of available methodologies: for instance, Green and Ampt, SCS Curve Number, Soil Moisture Accounting for the Loss method; Kinematic Wave, ModClark, SCS Unit Hydrograph as transform method. Therefore, the model is very flexible and can be adapted based on the available data.

Chapter 4

Impact of climate change on floods at the river basin scale

Future design floods in the Arga river basin (Spain) using an ensemble of climate projections and a distributed hydrological model

4.1 Introduction

This chapter presents a study that aims to quantify expected changes in flood quantiles in Pamplona (Spain) using a distributed rainfall-runoff model (Lompi et al., 2021) and an ensemble of climate projections. Expected variations in precipitation quantiles are extracted from a recent study (Garijo and Mediero, 2019) and are used as input data of the RIBS model (Garrote and Bras, 1995a; Garrote and Bras, 1995b). This study also aims to analyse the results of each climate model to identify which projection provides the greatest or smallest flood quantile changes in the future.

The structure of this chapter is: Section 4.2 presents the methodology; Section 4.3 shows the data collected in the Arga River catchment to apply the methodology; Section 4.4 reports the results of the hydrological model calibration and the quantification of the expected changes in flood quantiles. Finally, the discussion and conclusion of this research line are included.

4.2 Methodology

The methodology proposed to identify flood quantile modifications driven by climate change is divided into four parts: calibration methodology of the RIBS model (Section 4.2.1), hydrological modelling to quantify flood peaks in the current scenario (Section 4.2.2), spatial distribution of the future design storms (Section 4.2.3), and flood quantile change quantification (Section 4.2.4).

4.2.1 Calibration of the RIBS model

The description of the RIBS model is given in Section 3.3.1. The calibration procedure aims to find the model parameter values that minimise the errors between the model results and the observations of the real system that it is intended to represent (Gupta et al., 1998). Such errors in model simulations can be represented with Eq. 4.1 (Beven, 2006).

$$Q(x, t) = M(\theta, x, t) + \varepsilon(\theta, x, t) \quad (4.1)$$

where $Q(x, t)$ is the measured discharge in a given location x at the time step t , $M(\theta, x, t)$ is the modelled discharge that is obtained using a set of parameters θ , and $\varepsilon(\theta, x, t)$ is the error in the same location and time step with a set of parameters θ .

The model calibration can be based on optimisation methods, seeking to minimise model errors. Model errors can be quantified by using different objective functions. A set of objective functions are needed to consider a set of aspects in the hydrograph, such as the hydrograph shape, the timing and magnitude of the peak and the magnitude of errors in low flows, among others.

This study uses five objective functions to calibrate the RIBS model. Three of them quantify the errors considering the complete hydrograph duration: mean absolute error (MAE), root mean square error (RMSE) and the Nash-Sutcliffe efficiency coefficient (NSE) (Eqs. from 4.2 to 4.4). Two additional parameters are considered to assess the fitting in the upper part of the hydrograph: Time to Peak (TP) and the magnitude of the peak (MP) (Eqs. 4.5 and 4.6).

$$MAE(\theta) = \frac{1}{N} \sum_{k=1}^N |q_t - q'_t(\theta)| \quad (4.2)$$

$$RMSE(\theta) = \sqrt{\frac{1}{N} \sum_{k=1}^N (q_t - q'_t(\theta))^2} \quad (4.3)$$

$$NSE(\theta) = 1 - \frac{\sum_{k=1}^N (q_t - q'_t(\theta))^2}{\sum_{k=1}^N (q_t - \bar{q})^2} \quad (4.4)$$

$$TP(\theta) = |t(\max(q_t)) - t(\max(q'_t(\theta)))| \quad (4.5)$$

$$MP(\theta) = |\max(q_t) - \max(q'_t(\theta))| \quad (4.6)$$

where q_t is the measured discharge at a given time step t ; $q'_t(\theta)$ is the simulated discharge with a set of model parameters θ at the time step t , and \bar{q} is the mean value of the observed discharges.

The NSE objective function (Nash and Sutcliffe, 1970) quantifies the improvement of using the simulated hydrograph compared with the average discharge of the observed hydrograph. The best value of all the objective functions is zero, except for NSE, which supplies a value equal to one in a perfect match between the simulated and measured hydrographs. Indeed, MAE and RMSE values equal to zero and NSE values equal to one mean that there are no biases between the measured and the simulated discharge. A TP value equal to zero means that the peak discharge of the simulated hydrograph occurs in the same time step as in the observed hydrograph. An MP value equal to zero means that there is no difference between the magnitude of simulated and observed peaks. AMC is assumed to be the average condition of the RIBS model for all the events, as any AMC information in the flood events used in the calibration is retrieved.

4.2.2 Current Scenario

The current scenario represents the period in which observed historical data are available, as current design floods are usually based on time series of observations recorded in recent decades. The design floods in the current scenario have been obtained using the RIBS distributed and event-based hydrological model with a set of design hyetographs as input data obtained through extreme frequency analysis. Daily observations at eight rain gauge stations have been considered. The GEV and the Gumbel distribution functions have been used to fit a frequency curve to the Annual Maximum Series (AMS). A set of homogeneous regions were identified in Spain at the national scale by the Centre for Hydrographic Studies of CEDEX (*Centro de Estudios Hidrográficos*, in Spanish), recommending a given probability distribution function (PDF) in each region. The parameters of each PDF are estimated using the L-moments method (Hosking and Wallis, 1997), as this method has been proven to obtain the best results in Spain (Jimenez et al. 2013), as well as in most European countries (Castellarin et al., 2012). The use of a regional shape parameter in the regions where the GEV distribution function is recommended is also suggested, combining a regional value of the L-coefficient of skewness (L-CS) with local values of the mean and the L-coefficient of variation (L-CV). The return periods of 2, 5, 10, 50, 100, 500 and 1000 years are considered.

An Areal Reduction Factor (ARF) is considered to reduce the mean areal precipitation in the catchment obtained from the precipitation quantiles estimated at rain gauge locations, as annual maximum rainfalls in the eight rain gauge stations are unlikely to occur on the same day in all the years. The mean rainfall intensity for a given sub-daily duration is obtained from the intensity-duration-frequency curve in the region. A storm duration of 24 hours is considered. The 24-hour design rainfall for a given return period is obtained by scaling a dimensionless hyetograph by the T-year daily rainfall multiplied by ARF. Therefore, the design hyetographs in the Arga River catchment have a fixed shape with the peak intensity in the central part of the event regardless of the return period. Finally, at-site design hyetographs obtained in the eight gauging sites are spatially distributed in the catchment, obtaining the spatial distribution of precipitation in each time step. Indeed, RIBS requires precipitation input in a raster format. Each time step is with a different cumulative rainfall,

as the hyetograph has a peak of intensity in the central part, instead of a uniform distribution of precipitation. The Thiessen polygon technique is used to obtain the precipitation fields in each time step. Therefore, 24 precipitation fields are obtained for each design event in the catchment, one for each time step of the hyetograph.

4.2.3 Climate change scenario

As already mentioned, the expected changes in daily precipitation quantiles in the future under climate change conditions were extracted from rainfall climate projections supplied by 12 combinations of GCMs and RCMs (Table 3.1 in Chapter 3) of the EURO-CORDEX program (Garijo and Mediero, 2019). Delta changes (see section 2.1.2) in daily precipitation quantiles are supplied for seven return periods (RP = 2, 5, 10, 50, 100, 500 and 1000 years), two representative concentration pathways (RCP 4.5 and RCP 8.5) and three time windows in the future (2011-2040, 2041-2070, 2071-2100). In this case, a delta change represents the expected variation in rainfall quantiles for each combination of return period, climate model, time window and RCP scenario with respect to the current scenario. The delta changes are provided in a grid with a cell resolution of 0.11° . Hence, the Arga River catchment is covered mainly by three points that have the greatest influence on the design rainfall variation, though additional seven points are also considered, as they cover minor parts of the river catchment (Figure 4.1). Each cell considers 504 values of delta changes, as this is the number of the analysed scenarios given by the combination of seven return periods, two emission scenarios, three time windows and 12 climate models considered in the study. The delta changes are spatially distributed with the 50-m grid cell size that is used in the RIBS hydrological model simulations. Though the best geostatistical method depends on each case characteristics, ordinary kriging has been proven to provide better results than the Inverse Distance Weighting (IDW) method in several studies regarding precipitation fields (Luo et al., 2011). Nevertheless, the IDW technique has been used with a high exponent in this case study to maintain the same original squared shape of the delta changes. Furthermore, the use of the kriging method is not possible with these data as a fitting model cannot be determined for the semivariogram. Indeed, all the points have a fixed reciprocal distance. Therefore, for the same distance in the x-axis, there are several semivariance values in the y-axis that prevent any model from being able to converge (gaussian, exponential, spherical). The spatial distributions of the future design precipitations are obtained by combining the spatial distributions of the current design rainfalls and the delta changes.

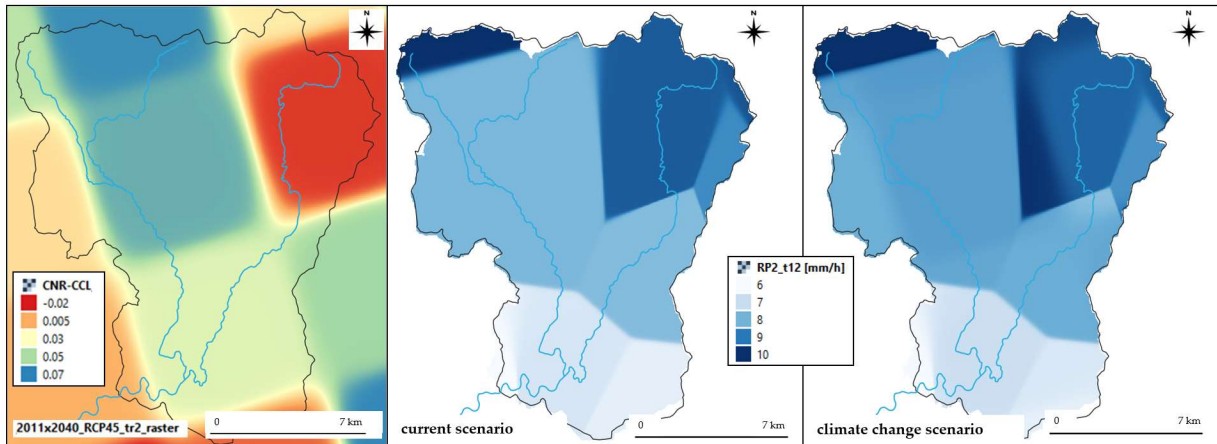


Figure 4.1. Combination of the delta changes with the design rainfall to obtain the rainfall spatial distribution in the future.

Figure 4.1 shows the spatial distribution of the peak intensity in the 2-year hyetograph and the delta changes for the CNR-CCL climate model for the same return period in the 2040 time window.

Considering the 504 combinations in each cell described above and the 24-time steps of the design hyetographs, 12,096 rainfall spatial distributions have been considered as input data in the RIBS model.

4.2.4 Quantification of expected changes in flood quantiles

The expected changes in flood quantiles due to climate change are obtained by comparing flood quantiles in the future periods and the current period for each climate model. The flood quantile change supplied by a given climate model and return period (rQ_T) are obtained using the ratio between the hydrograph peak discharge in the climate change scenario $(Q_{p,T})_{fut}$ and the hydrograph peak discharge in the current scenario $(Q_{p,T})_{curr}$ (Eq. 4.7). rQ_T quantifies the change between a future time window and the current period, extracting the signal change supplied by a climate model forced with a given emission scenario, regardless of the flood frequency curve obtained from observations. Therefore, the potential biases between the model simulations and observations do not influence the results.

$$rQ_T = \frac{(Q_{p,T})_{fut}}{(Q_{p,T})_{curr}} \quad (4.7)$$

where $(Q_{p,T})_{fut}$ is the hydrograph peak magnitude for the return period T in the future period, $(Q_{p,T})_{curr}$ is the hydrograph peak magnitude for the return period T in the current period, and rQ_T is the expected change in the flood quantile for the return period T . If rQ_T is greater than one, flood quantiles are expected to increase in the future. If rQ_T is smaller than one, flood quantiles are expected to decrease in the future. A value of one means that no changes in flood quantiles are expected in the future.

4.3 Data and Case Study

Pamplona is crossed by the Arga River, which has a catchment area of 510 km² upstream to the city. The Arga River is in the Navarre region and rises in the Urquiaga pass, located in the Paleozoic Quinto Real massif, one of the rainiest areas in Northern Spain. It is a tributary of the Aragón River with a total drainage area of 2759 km². In this study, the catchment outlet is in Pamplona city, where the A323 streamflow gauging station is placed, as shown in Figure 4.2.

Two types of rain-gauge stations are used in the study. For the RIBS model calibration procedure, six 15-min rain-gauge stations are used (purple circles in Figure 4.2). For estimating the design rainfall hyetographs, daily rain-gauge stations with longer time series are used (green triangles in Figure 4.2). Therefore, a time step of 15 min has been considered in the RIBS model simulations for both the calibration and the calculation with current and future design rainfalls. Table 4.1 contains a summary of the streamflow- and rain-gauge station network. The soil data were supplied by the Spanish National Geographic Institute (IGN, ‘Instituto Geográfico Nacional’, in Spanish) in a shapefile format. The DEM was also provided by IGN in a raster format.

All the data in the RIBS model are provided in a raster format with a cell size of 50 m. Therefore, the soil raster in Figure 4.2 was obtained by sampling the shapefile with a 50-m grid. Table 4.2 reports the Brooks-Corey parameter values (see Section 3.3.1) for each soil class.

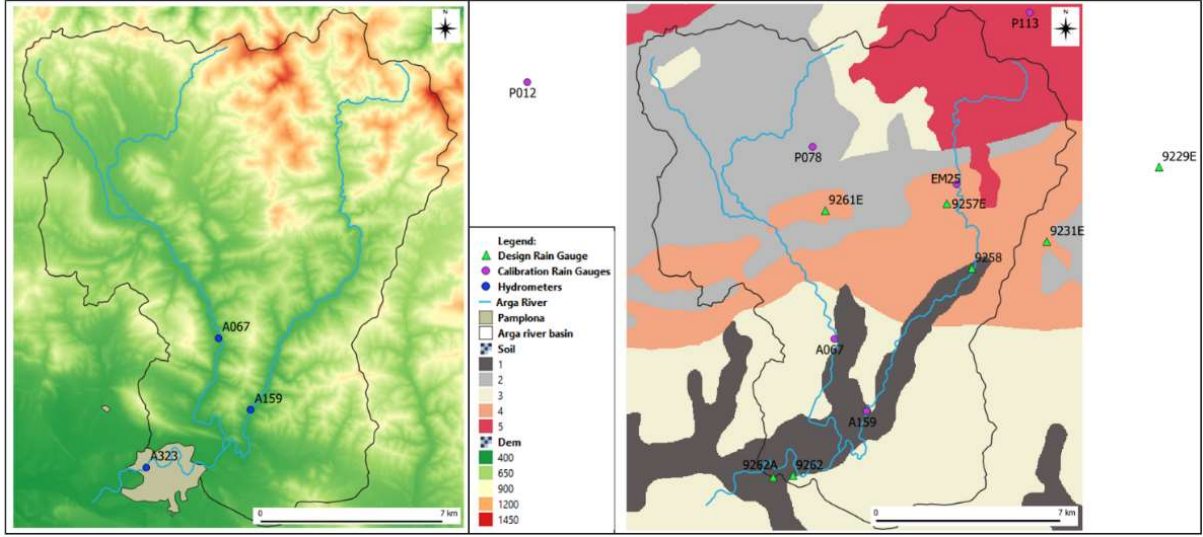


Figure 4.2. (a) Digital elevation model (DEM) and location of streamflow gauges. (b) Soil types and rain gauges location.

Table 4.1. Summary of the rain- and streamflow-gauge stations considered in the study.

Code	Name	Instrument	use	x (UTM)	y (UTM)	z (m asl)
A067	ULZAMA in OLAVE	Rain Gauge & Hydrometer	calibration	613772	4749604	468
A159	ARGA in HUARTE	Rain Gauge & Hydrometer	calibration	615717	4745302	454
A323	ARGA in PAMPLONA	Hydrometer	calibration	609434	4741851	413
EM25	EMA DE EUGUI	Rain Gauge	calibration	621072	4758771	628
P012	BERUETE	Rain Gauge	calibration	595526	4764847	752
P078	LANTZ	Rain Gauge	calibration	612505	4761016	645
P113	VALLE DE BAZTÁN	Rain Gauge	calibration	625416	4768978	906
9229E	ESPINAL-AUZPERRI	Rain Gauge	design	633099	4759795	870
9231E	ERRO	Rain Gauge	design	626428	4755379	688
9257E	EUGUI ESTERIBAR	Rain Gauge	design	620494	4757618	615
9258	ZUBIRI	Rain Gauge	design	621945	4753786	536
9261E	OLAGUE	Rain Gauge	design	613259	4757216	545
9262	PAMPLONA OBSERVATORIO	Rain Gauge	design	611315	4741479	442
9262A	PAMPLONA INSTITUTO	Rain Gauge	design	610148	4741399	441
9263I	ILUNDAIN	Rain Gauge	design	620048	4736998	572

Table 4.2. Hydraulic characteristics of the soil classes belonging to the soil raster.

Soil classes	K_{0n} [mm/h]	θ_s	θ_r	ε
1	50	0.5	0.04	3.5
2	1	0.35	0.04	3.5
3	25	0.25	0.03	3.5
4	15	0.3	0.03	3.5
5	30	0.25	0.01	6

The greatest flood events in the Arga River in Pamplona in the last decade have been selected to calibrate the RIBS hydrological model. A peak-over-threshold (POT) analysis has been applied to the streamflow time series recorded at the A323 hydrometer located at the catchment outlet. A threshold of $300 \text{ m}^3/\text{s}$ has been considered, as floods that exceed such a threshold usually drive significant direct losses in Pamplona city (Figure 4.3). Eight flood events have been selected for the calibration and validation methodology of the RIBS hydrological model. They are named from EPI01 to EPI08 in chronological order.

However, EPI01 has been removed from the calibration process, as two rain-gauge stations were out of service for this event. Hence, five events were used in the calibration procedure (EPI02, EPI03, EPI04, EPI05 and EPI06) and two in the validation (EPI07 and EPI08). A summary of the selected flood events is included in Table 4.3.

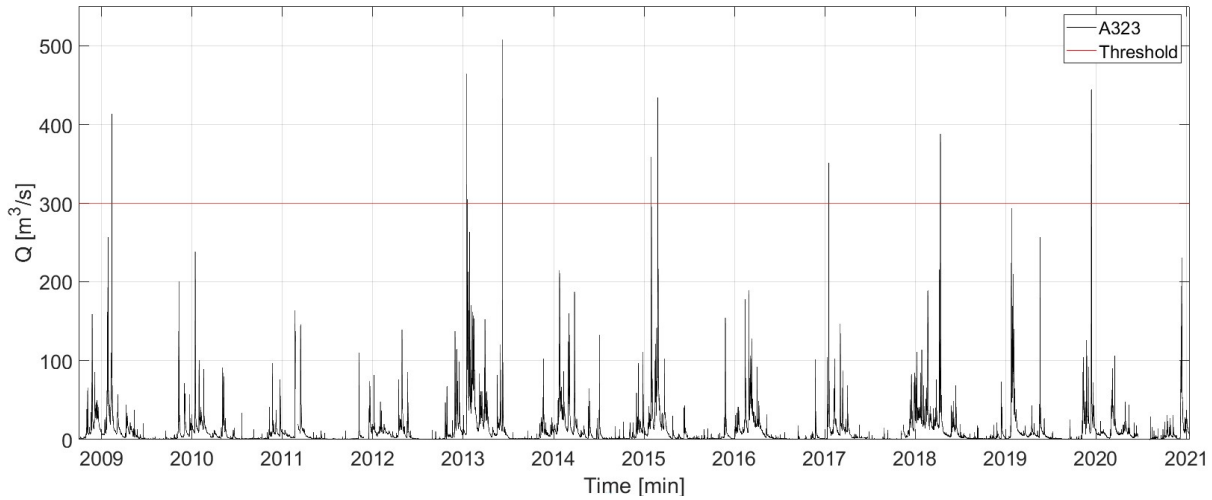


Figure 4.3. Floods selected in the A323 hydrometer by using a POT analysis with a threshold of $300 \text{ m}^3/\text{s}$.

Table 4.3. Summary of the flood events considered in the calibration process of the RIBS model. Maximum intensity refers to the mean rainfall intensity in the catchment.

Code	Date	Flood duration (h)	Maximum Intensity (mm/15min)	Peak flow [m^3/s]
EPI02	12-17 January 2013	105	7.2	464.5
EPI03	7-10 June 2013	53	13.2	507.9
EPI04	29 January - 3 February 2015	110	5.4	359.3
EPI05	23-27 February 2015	95	4.9	434.2
EPI06	12-17 January 2017	101	6.0	351.1
EPI07	10-12 April 2018	53	6.1	388.3
EPI08	11-13 December 2019	64	6.9	444.3

4.4 Results

This section shows the results of the hydrological simulation with the RIBS model. First, the results of the calibration and validation methodology are reported. Second, the expected changes in flood quantiles in the future are compared with the design peak discharges in the current scenario.

4.4.1 RIBS model calibration and validation

A set of 100 parameter value combinations generated randomly with a uniform distribution in the range of parameter values shown in Table 4.4 has been considered in the calibration procedure. The five objective functions selected in Section 4.2.1 have been calculated for the five flood events considered in the calibration process in the three hydrometers located in the Arga River catchment (A067, A159 and A323).

Table 4.4. Ranges of the RIBS model parameter values used in the calibration procedure.

Parameter	Lower Limit	Upper Limit
$f \text{ (mm}^{-1}\text{)}$	10^{-4}	1.5×10^{-3}
$C_v \text{ (m/s)}$	1.0	2.0
K_v	0.5	12

The model errors in the three streamflow-gauge stations have been combined using a weighted mean to summarise the results of the calibration with a unique value for each flood event in the catchment. The results of the calibration process are shown in Figure 4.4. The 100 black circles in each subplot represent the simulations with the 100 combinations of parameter values. The red-filled circle indicates the model error of the best set of parameters used after the calibration in the flood quantile calculation.

Figure 4.4 shows that the parameter value combinations with the smallest values of the MAE and RMSE objective functions agree with the greatest values of the NSE objective function. However, a higher variability can be found in the MP objective function, indicating that a good fit for the flood peak magnitude does not imply a good fit in the flood hydrographs shape. The results of the TP objective function suggest that the identification of the best model parameter value combinations with this objective function is not possible.

Nevertheless, the best combination of parameter values that minimises errors has been selected from the results of all the five objective functions. The set of parameter values that minimise the error has been identified for each flood event and each objective function. Since there are five events in the calibration procedure and five objective functions to evaluate the model error, 25 combinations of events and objective functions are available. These combinations can be seen in blue in Table 4.5. For each combination (event and objective function), only one set of parameters minimises that objective function. The best combination of parameter values has been selected by looking at the set that minimises more combinations. The objective function results for both the calibration and validation flood events, evaluated with the chosen combination of parameters, are shown in Table 4.5.

Most flood events show an NSE result higher than 0.8, representing a good fitting. The RMSE and MAE objective functions have small values when the NSE objective functions has high values, indicating that the three objective functions can identify the best parameter values. Regarding the TP objective function, most flood events show values below 1.5 hours that can be considered a good fit.

Table 4.5. Weighted values of the objective function values in the three hydrometers considered in the study for the events used in the calibration (in blue) and validation phases (in black). The results correspond to simulations with the RIBS model parameter values obtained in the calibration process.

Objective functions	CALIBRATION					VALIDATION	
	EPI02	EPI03	EPI04	EPI05	EPI06	EPI07	EPI08
RMSE [m ³ /s]	45.7	40.4	27.0	34.6	32.2	37.0	37.2
MAE [m ³ /s]	33.0	32.7	19.1	24.2	28.1	24.8	30.6
TP [min]	75	90	330	60	90	195	75
MP [m ³ /s]	108.9	61.3	47.2	68.9	19.3	67.4	43.4
NSE	0.60	0.85	0.87	0.86	0.74	0.82	0.87

The mean value of the observed flood peaks in the calibration is 420 m³/s, and the mean value of the MP objective function is 50 m³/s which corresponds to an error of 12%.

Figure 4.5 shows the relationship between the NSE objective function and the RIBS parameter values. The parameter values selected in the calibration and used for model validation are shown in red. NSE shows a higher sensitivity to the parameter f . Indeed, different values of f correspond to different values of flood volume, and only one value is optimal for the model.

The RIBS model is less sensitive to the parameters K_v and C_v , as the catchment time of response depends on water velocities in hills and streams that can be obtained with several combinations of K_v and C_v . Nevertheless, the best set of parameter values identified in the calibration process is always in the upper part of the graphs, indicating its goodness of fit. The parameter values selected in the calibration process are included in Table 4.6.

Table 4.6. RIBS parameter values for the best combination identified in the calibration process.

Parameter	f (mm ⁻¹)	C_v (m/s)	K_v
Optimal value	$1.4 \cdot 10^{-3}$	1.17	11.9

Figure 4.6 shows the comparison between the observed and simulated hydrographs, considering the set of model parameter values selected in the calibration process. The calibration results show that the simulated hydrographs are closer to the observed ones at the A067 streamflow-gauging station than in the other hydrometers. The location of such a hydrometer pointed to higher reliability in discharge estimations from water level measurements. Therefore, the results of the calibration process confirm the higher reliability of the A067 streamflow-gauging site. Errors in the A159 hydrometer can be driven by flood control processes in the Eugui reservoir located upstream in the Arga River. Underestimation in the RIBS model simulations in the EPI07 event could be explained by flood control processes and flow releases in such a reservoir, as the second rising limb of the observed hydrograph seems not to be forced by rainfall.

The flood events used for the validation (EPI07 and EPI08) show a good fitting between the observed and simulated hydrographs, mainly in the A067 hydrometer and in the A159 and A323 streamflow-gauging stations for the EPI08 flood event. In the EPI07 flood event, the simulated hydrograph underestimates the observed hydrograph in the A159 gauging site, which could be due to the Eugui dam. Therefore, the simulation also underestimates the observed hydrograph in the A323 gauging stations located downstream of the A159.

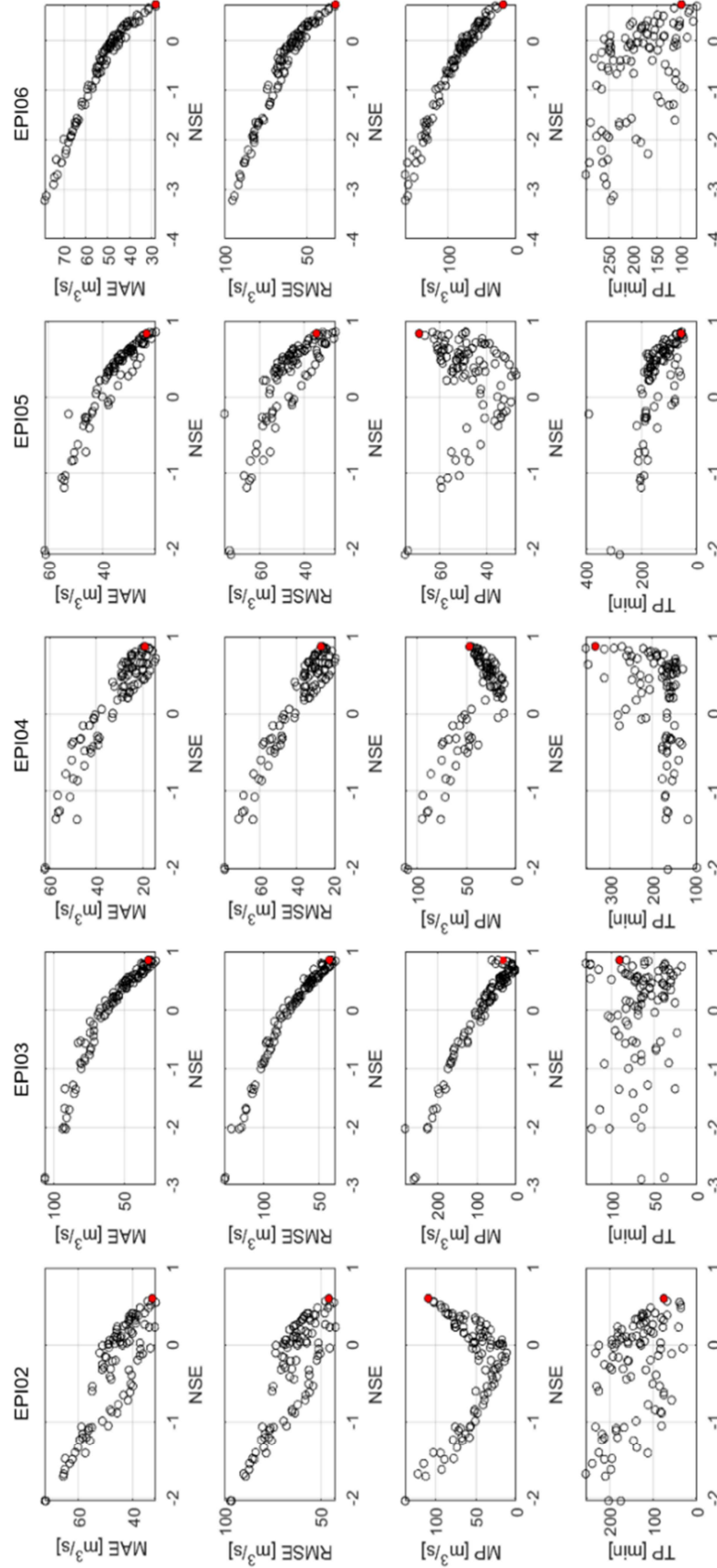


Figure 4.4. Objective function results for the five flood events considered in the calibration process. Columns show flood events. Rows show the relationship between each objective function and NSE. Red circles represent the combination of parameter values selected for the validation procedure.

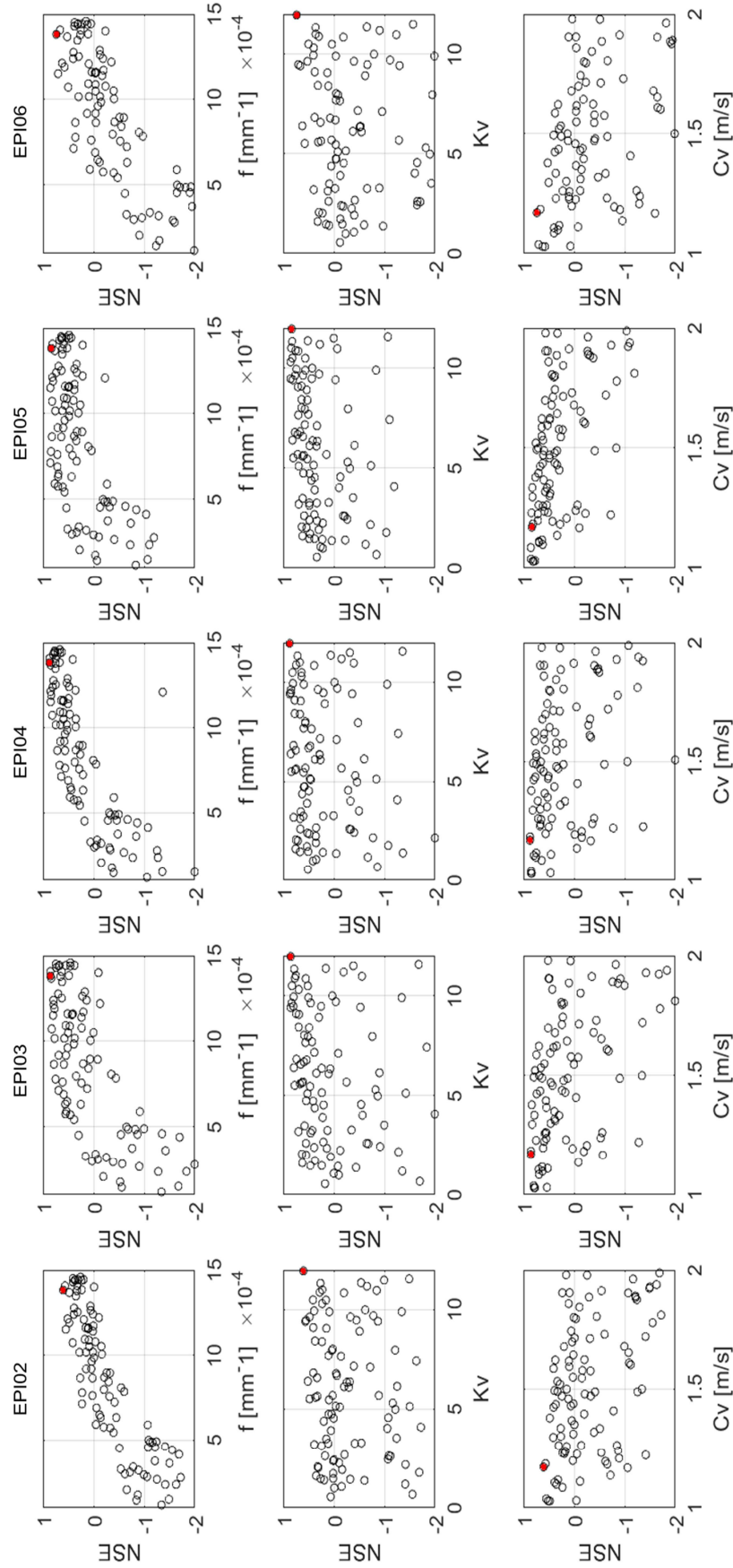


Figure 4.5. NSE objective function results for the five flood events considered in the calibration process. Columns show flood events. Rows show the three parameters used to calibrate the model: f , K_v , C_v . Red circles represent the combination of best combination of parameter values identified in the calibration process.

CALIBRATION

VALIDATION

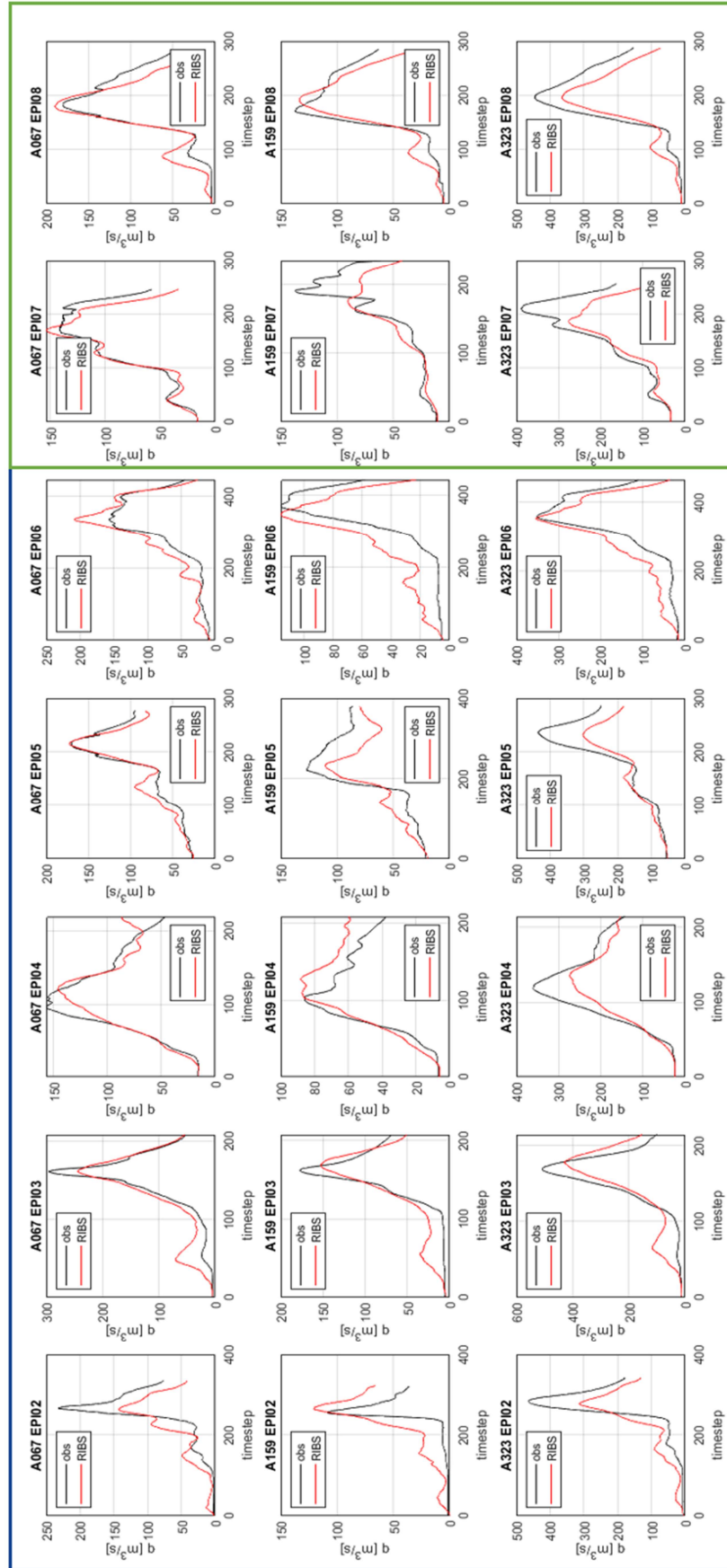


Figure 4.6. Comparison between observed (black) and simulated (red) hydrographs for the calibration and validation flood events with the parameter values selected in the calibration process. Columns show flood events. Rows show streamflow gauging-sites.

4.4.2 Flood quantile changes expected in the future

Flood quantile changes are quantified in the streamflow-gauging site A323, located at the river basin outlet of the Arga River catchment in Pamplona. The flood quantiles in the current scenario agree with the flood frequency curve obtained in the A323 hydrometer in the CAUMAX study (Jiménez et al., 2013), confirming the goodness of the model calibration. A comparison between flood quantiles in the future periods and the current period for each climate model has been carried out. Figure 4.9 shows the results for the CNR-CCL climate model. The figures for the rest of the climate models are provided in Appendix A (from Figure A1 to Figure A11).

The results for the CNR-CLL show a general increase in the flood quantiles in all the return periods, time windows and emission scenarios. Nevertheless, the results for all the climate models considered in the study are summarised to reduce potential biases in future flood quantile estimates.

Expected changes in flood quantiles (rQ_T) are quantified for each climate model and return period with Eq. 4.10. The results of the 12 climate models are summarised in a box plot for each return period, emission scenario and future period (Figure 4.7 and Figure 4.8).

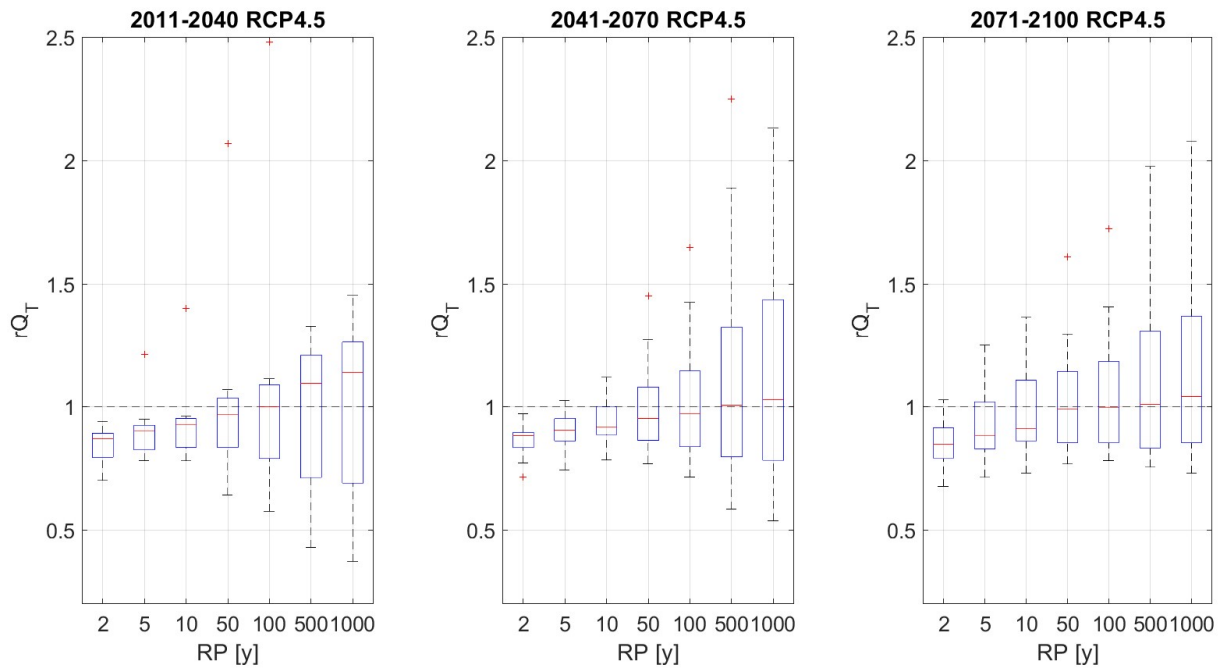


Figure 4.7. Boxplots of rQ_T values for the 12 climate models considered in the study. The results for the RCP 4.5 are shown: the first column shows the results for the 2011-2040 period, the second for the 2041-2070 period and the third for the 2071-2100 period.

In the boxplots, the median value for the 12 climate models is highlighted by a red line; the horizontal black dashed line represents a value of one for rQ_T that separates the figure between the upper part with increasing flood quantiles and the lower part with decreasing flood quantiles. Figure 4.7 and Figure 4.8 use the same vertical scale in each subplot. Therefore, the results for the three time windows and two RCPs can be compared. In RCP 4.5, a clear decrease in flood quantiles for the most frequent floods (2-, 5- and 10-year return periods) is found for the three time windows in the future. The same signal of change for the most frequent floods is also visible in RCP 8.5 (Figure 4.8). The dispersion of the results for the 12 climate models increases with the return period, showing the increasing uncertainty associated with the highest return periods. Nevertheless, the uncertainty for return periods greater than 50 years is smaller in the 2041-2070 and 2071-2100 time windows than

in the period 2011-2040, with an evident increase in the design discharges. For return periods higher than 100 years, increasing flood quantiles are only found in the time window 2011-2040 for RCP 4.5. For RCP 8.5, higher positive changes are expected in the three time windows with flood quantiles increases higher than 25 % for the 500- and 1000-year return period in the three time windows.

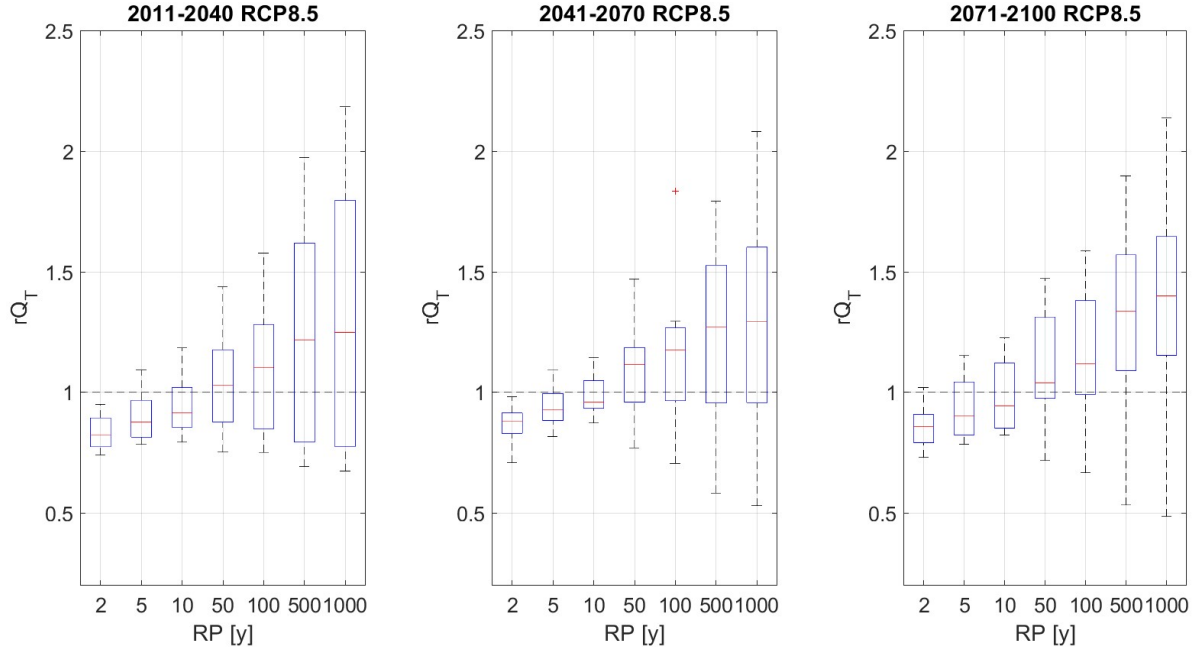


Figure 4.8. Boxplots of rQ_T values for the 12 climate models considered in the study. The results for the RCP 8.5 are shown: the first column shows the results for the 2011-2040 period, the second for the 2041-2070 period and the third for the 2071-2100 period.

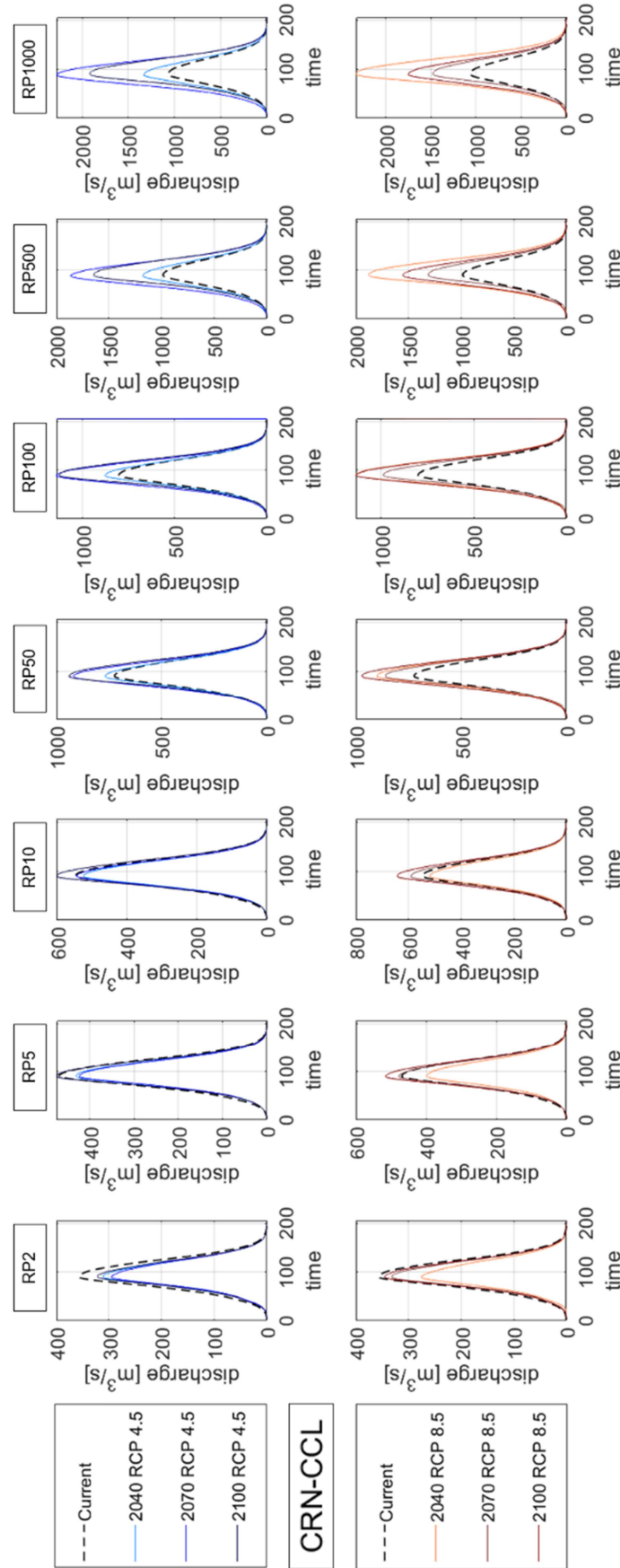


Figure 4.9. Hydrographs for the current (dashed black) and climate change (colored) scenarios for the CNR-CCL climate model in the 3 periods. Columns show return periods. The upper row shows results for the RCP 4.5 and the lower row for the RCP 8.5.

In addition, Figure 4.10 shows the results for the two RCP scenarios, reporting only the median values of the boxplots in Figure 4.7 and Figure 4.8. A given colour is used for each time window: cyan for 2011-2040, blue for 2041-2070 and black for 2070-2100. Dotted lines represent the results for the RCP 4.5 scenario and solid lines for the emission scenario RCP 8.5.

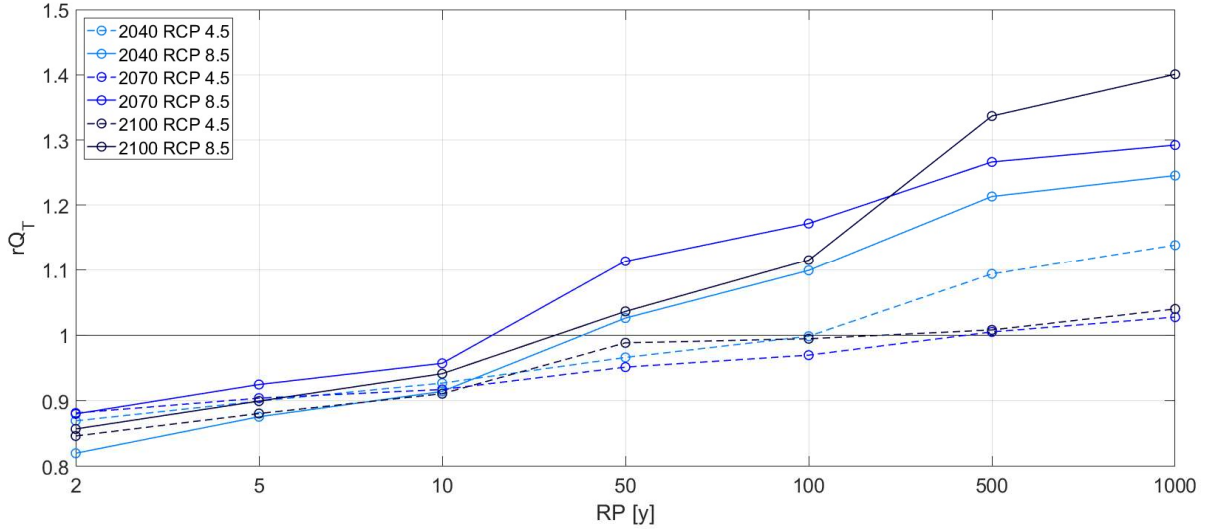


Figure 4.10. Median values of expected flood changes in the three time windows and two emission scenarios.

Figure 4.10 shows the results for the median values of rQ_T for each return period. The decrease in flood quantiles for the most frequent flood peaks (return periods smaller than 10 years) is also evident in this figure in the three time windows and both RCPs. Nevertheless, in this case, a slight increase in the higher return periods (500 and 1000 years) is also evident for the RCP 4.5 in the three time windows, especially for the 2011-2040 period. For the highest return periods, RCP 8.5 leads to an increase in the 1000-year flood quantile 35% greater than in the RCP 4.5. In addition, RCP 8.5 points to 1000-year flood quantile increases of 40% compared with the current period.

However, the most interesting findings in Figure 4.10 are:

- the 100-year flood quantiles are expected to increase 10% in the RCP 8.5 already in the 2011-2040 time window;
- flood quantile increases are generally greater in the scenario with higher emissions (RCP 8.5) than in the scenario with smaller emissions (RCP 4.5), except for the most frequent floods (2, 5 and 10 years) in the time window 2011-2040;
- flood quantile increases of the most extreme events (500 and 1000 years) seem to agree with the greenhouse gas emission trend, as flood quantile increases in the RCP 4.5 scenario are expected to have their peak around 2040 with a subsequent decline, similar to the emission temporal evolution, and flood quantiles increase throughout the century with highest values in 2100, similar to the emission temporal evolution in RCP 8.5.

4.4.3 Influence of the GCMs and RCMs in the flood quantile determination

Figure 4.11 shows the median values of rQ_T for different return periods considering the three periods in the future and the two RCPs, grouped by GCMs and RCMs, to understand how given global or regional climate models influence the results. The results for a given GCM (left part of the figure)

include all the climate projections that consider this GCM, regardless the RCM that is used. Therefore, the plot for GCMs does not reveal information about RCMs used to downscale their results. For instance, the results of ICH (blue line in Figure 4.11) are obtained with the median values of the results that involve this global climate model: ICH-CCL, ICH-RAC and ICH-RCA. At the same, the results for a given RCM (right part of the figure) include all the climate projections that consider such RCM, regardless the GCM that is downscaled. For instance, the results of CCL are obtained with the median values of these climate projections: ICH-CCL, MPI-CCL, CNR-CCL and MOH-CCL. Moreover, the delta changes of flood quantiles for the three time windows and two RCP scenarios are combined in a unique plot with a median value for each climate model. Therefore, at least six rQ_T values for a given return period are considered (two emission scenarios and three time windows). In the figure the GCMs are represented with a given colour, while the RCMs with a given label.

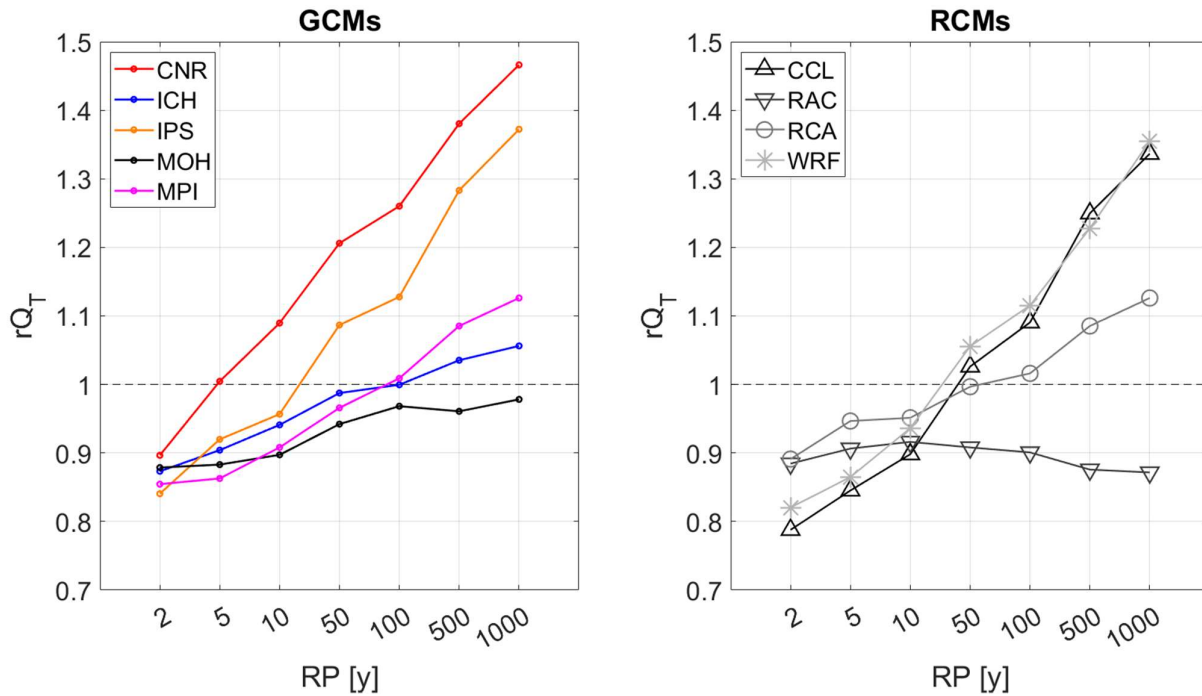


Figure 4.11. Median values of rQ_T for the three periods in the future and two RCPs. The results are shown for each return period grouped by GCMs (left) and RCMs (right). GCMs are represented with a given colour, while RCMs are illustrated with a label.

While the ICH and MOH GCMs have been used three times, the rest of the GCMs have been used twice. Therefore, in the left part of Figure 4.11, ICH and MOH medians are calculated with 18 values and the rest with 12 values. Regarding the RCMs, RCA points represent 30 values, CCL 24 values, RAC 12 values, and WRF just six values.

Figure 4.11 shows that climate models show differing influences on the results. GCMs may have a greater impact on the results compared with RCMs. While the CNR and IPS climate models point to a clear general increase of peak flow quantiles in the future, a similar tendency is shown only by the CCL RCM. Though the results of WRF seem to lead to a clear increase in the higher return periods, it is used only once to downscale the IPS climate model. Therefore, the increase is driven by the IPS GCM. On the contrary, CCL has a clear increasing tendency of peak flow quantiles for large return periods, and the results are more reliable than for the WRF RCM. In this case, the increasing trend is not driven by a given climate model, as it is used to downscale four different GCMs.

Figure 4.12 shows the median value of rQ_T for each combination of GCM and RCM, considering the three future time windows and the two RCPs. Therefore, also in this case, each climate model has six values. Each combination of GCM-RCM is represented with a unique combination of the colours and labels used in Figure 4.11. The variability around the median values increases with the return periods, as shown in the boxplots of Figure 4.7 and Figure 4.8. Nevertheless, variability patterns differ among climate models, and they seem to be driven by the GCMs.

For instance, Figure 4.12 shows that the greatest increases are obtained with the CNR-RCA climate model, though RCA RCM does not show an increasing trend in Figure 4.11. Moreover, the influence of GCMs in the results can be seen by analysing the 1000-year flood results for the combinations that use the RCA RCM. The results vary depending on the GCM that is downscaled: CNR-RCA has a large variability and increase (red squares), MPI-RCA shows no significant changes (purple squares), and ICH-RCA presents an evident decrease in flood quantiles (blue squares).

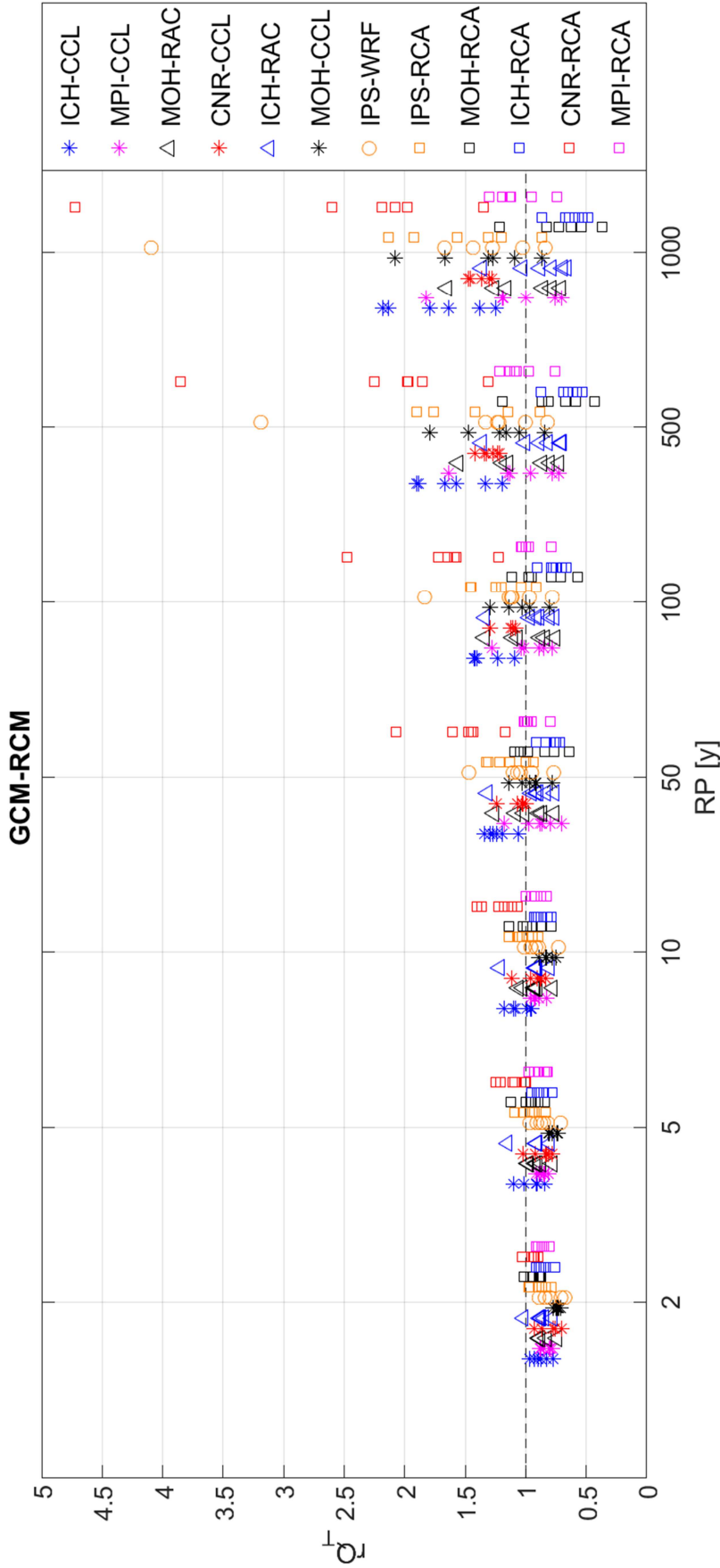


Figure 4.12. Median values of rQ_T for each combination of GCM and RCM

4.5 Discussion and Conclusion

An analysis of the expected changes in flood quantiles in the future for the Arga River in the city of Pamplona has been carried out using precipitation projections supplied by 12 climate models of the EURO-CORDEX program. Delta changes in daily rainfall quantiles obtained in a previous study have been used as input data in the RIBS distributed hydrological model to transform the expected changes in precipitation quantiles into changes in flood quantiles.

The RIBS hydrological model has been calibrated with the seven greatest flood events in the city of Pamplona in the last decade. The results of calibration and validation show that the simulated hydrographs have a good fit with the observations, obtaining acceptable residual model errors both in terms of hydrograph shape (RMSE, MAE, NSE) and flood peak (TP, MP).

The results point to a decrease in the design peak discharges for both RCPs in the three time windows for return periods below 10 years. On the contrary, flood quantiles for return periods greater than 50 years are expected to increase for the three time windows in the RCP 8.5 scenario. In addition, the 100-year flood quantile will not change in the future if environmental policies cut greenhouse gas emissions (RCP 4.5). On the contrary, design peak discharges above 50 years are expected to increase 10-40% in the emission scenario RCP 8.5, especially for the time windows 2041-2070 and 2071-2100. GCMs could have more influence on the results than RCMs. The greatest increases are predicted by the results obtained with climate models that downscale from the CNRM-CM5 and IPSL-CM5A-MR GCMs.

The results of this work agree with [Alfieri et al. \(2015\)](#), that show an increase of 100-year floods across Europe in the RCP 8.5 on average. The changes in flood quantiles in the Arga River could also be a signal for northern Spain, where a downtrend in annual maximum flows was found by [Mediero et al. \(2011\)](#) and [Bloesch et al. \(2019\)](#). The results of this work also agree with the findings of [Sharma et al. \(2018\)](#), that found a similar increase in the more extreme floods, analysing climatic areas completely different from the Mediterranean area. All these findings could be summarised together, pointing out that without a greenhouse gas emission abatement, a generalised increase of the hydraulic risk for greater return periods could also be expected in the areas where the mean annual precipitation is decreasing.

The results show how policies that aim to reduce greenhouse gas emissions could lead to a reduction in future flood risks. This could reduce costs related to flood damages of more extreme events and costs associated with oversized defence infrastructures.

However, the results and considerations of this study cannot be easily extrapolated to other geographical contexts. Nonetheless, they show the importance of the future hydraulic risk assessment for small and medium river basins. Indeed, small river catchments could have differing results from those obtained in large-scale studies that can only analyse the largest river basins in which they are contained.

The results also underline how important it could be to consider the expected increase in future hydraulic risks due to climate change as soon as possible, especially for high return periods and emission scenarios in which environmental policies do not aim to reduce emissions. Considering the expected increases in hydraulic risks for the 1000-year return period, decision-makers could design structures such as dams avoiding spillway underestimates in the future. Similarly, the use of flood risk maps with underestimated 100-year floods could also underestimate the areas prone to flooding in urban cities.

Chapter 5

A stochastic methodology to assess the impact of climate change on hydrological dam safety

The Eugui Dam Case Study

5.1 Introduction

This chapter proposes a stochastic methodology to assess hydrological dam safety, including the impact of climate change on floods and reservoir water levels. The methodology is applied to the Eugui Dam in the River Arga catchment (Spain). The impact of climate change on floods in the River Arga catchment is quantified in Chapter 4 using delta changes in precipitation quantiles extracted from climate projections at the national scale in Spain (Garijo & Mediero, 2019). The RIBS distributed hydrological model has been used to quantify the expected changes in flood quantiles at the Eugui Dam for three time windows (2011-2040, 2041-2070, and 2071-2100), two Representative Concentration Pathways (RCP 4.5 and RCP 8.5) and seven return periods (2, 5, 10, 50, 100, 500 and 1000 years) and an ensemble of 12 climate models (Lompi et al., 2021). The HBV continuous hydrological model is used with a daily time step to simulate inflow discharges in the Eugui reservoir. HBV uses rainfall and temperature climate change projections as input data. A reservoir operation model is developed to obtain reservoir water levels using inflow discharges of HBV as input data and considering reservoir operation rules. The Volumetric Evaluation Method (VEM) simulates flow routing processes in the reservoir, as the Eugui Dam has a gated spillway. The frequency curve of maximum reservoir water levels and maximum outflow discharge is obtained for each scenario, assessing the expected changes in the exceedance probability of dam overtopping.

5.2 Methodology

The methodology used to determine the impact of climate change on the future initial water level at the beginning of a flood event is divided into four parts and used daily data: observed data analysis (Section 5.2.1); calibration of the HBV model, and hydrological modelling of the climate projections (Section 5.2.2); reservoir operation model that describes dam operations and evaluates the outflow discharge from the reservoir in the future (Section 5.2.3). After obtaining the future water level frequency curve for each scenario, i.e., for all the combinations given by a different climate model, emission scenario and time window, a stochastic procedure (Section 5.2.4) is made to obtain the maximum water level frequency and the maximum outflow discharge from the dam. Random inflow hydrographs and random initial water levels are combined in a Volumetric Evaluation Method (VEM). The VEM describes the flood routing process in the reservoir (Section 5.2.5) with a 15-minute timestep. The results are expressed with the Overtopping Probability, the delta changes of maxima reservoir water levels and the delta changes of maxima outflow discharges (Section 5.2.6).

5.2.1 Observed data analysis

The analysis of the observed data is made to identify the water level frequency curve, i.e. the probability associated with a given pool level inside the reservoir in the control period, and to obtain the Generalized Extreme Values (GEV) distribution on the Annual Maxima Series (AMS) of the inflow discharge. These two frequency distributions are used in the stochastic procedure (see Section 5.2.4) to generate random inflow discharges in the reservoir associated with random initial water levels to assess the hydrological dam safety of the current scenario. Moreover, the water level frequency curve is also used for the calibration of the reservoir model (Section 5.2.3).

5.2.2 HBV model: calibration and hydrological modelling of the climate change scenarios

The HBV model description is in the third chapter (Section 3.3.2). HBV requires daily data of precipitation, temperature, and potential evapotranspiration PET, which must be calculated externally. First, PET is calculated from temperature projections using the Hargreaves equation

(Hargreaves, 1981; Hargreaves et al., 1985). In the current scenario all the data required by the Penman-Montieth are available, though climate change data do not include humidity and wind speed projections. Therefore, the Hargreaves equation is also used to calibrate the HBV model in the current scenario

$$PET = 0.0022 \cdot R_A \cdot \delta_T^{0.5} \cdot (T + 17.8) \quad (5.1)$$

Where R_A is the mean extra-terrestrial radiation that depends on the latitude of the case study; δ_T is the difference between the mean monthly maximum temperature and the mean monthly minimum temperature; T is the daily temperature.

The HBV model has been calibrated using Monte Carlo simulations with a single objective function to evaluate model errors, considering 11 parameters for each vegetation zone (TT, CFMAX, FC, LP, BETA, PERC, UZL, K0, K1, K2, MAXBAS) that have been varied within given ranges to find the optimal combination of parameter values for the case study (the description of the parameters is in the Section 3.3.2). The objective function that has been chosen to evaluate the model error is the HBV efficiency of the model (R_{eff}), which represent the NSE, as it can be seen comparing Eq. 5.2 with Eq. 4.4 in Section 4.2.1.

$$R_{eff} = 1 - \frac{\sum (Q_{sim}(i) - Q_{obs}(i))^2}{\sum (Q_{obs}(i) - \overline{Q_{obs}})^2} \quad (5.2)$$

Where $Q_{sim}(i)$ is the simulated discharge at the i -th day; $Q_{obs}(i)$ is the mean daily observed discharge at the i -th day and $\overline{Q_{obs}}$ is the mean value of the observed daily discharge time series. The optimum value of R_{eff} is one when there are no biases between simulation and observations. The calibration target in this study consists of obtaining an efficiency of the model of at least 0.85.

Moreover the last part of the time series is used to validate the model. Therefore, this part is not used for the determination of the model parameters. The validation is done analysing the objective functions R_{eff} and MAE are evaluated.

After the calibration and validation of the HBV model, the climate projections of rainfall, temperature and PET are used as input data to obtain the future inflow discharge time series in the reservoir with a daily time step ($Q_{in,d}$). However, the first four years are skipped for the sake of model stabilisation. Therefore, the remaining part of the time series (2010-2100) is used as input data of the reservoir operation model (Section 5.2.3) to obtain daily water levels at the Eugui Dam.

5.2.3 Reservoir operation model

A reservoir operation model has been developed to simulate dam operations to obtain the expected daily time series of reservoir water levels in the future. The model has been developed in MATLAB and has a daily time step. Daily outflow discharges ($Q_{out,d}$) released by spillways and outlet works depend on dam operations, such as environmental flows released to sustain ecosystems in the downstream river; water supply to meet municipal, industrial and agricultural water demands; and flood control operations to minimise downstream flooding. The Eugui Dam has an outlet work composed of two pipelines and gated spillways. The maximum outflow discharge that can be released by both outlet works and spillway at a given time step i ($Q_{max,i}$) depends on the reservoir water level

at the time step i (WL_i). Maxima daily water releases by the spillway ($Q_{spill,i}$) are assumed to be equal to the inflow water volume that cannot be stored in the reservoir. $Q_{max,i}$ will be equal to the sum of the releases from both the outlet works and the spillway when WL_i is greater than the elevation of the spillway gates upper limb (h_{gate}). $Q_{max,i}$ will be equal to the maximum release by the outlet works, considering that they are completely open, when WL_i is between the elevation of the outlet work inlet (h_{out}) and h_{gate} . $Q_{max,i}$ is equal to zero when WL_i is below h_{outlet} .

$$\left\{ \begin{array}{ll} Q_{max,i} = A_{outlet} \sqrt{\frac{2g(WL_i - h_{outlet})}{\left(1.5 + \frac{\lambda_i L_{outlet}}{D_{outlet}}\right)}} + Q_{spill,i} & \text{if } WL_i > h_{gate} \\ Q_{max,i} = A_{outlet} \sqrt{\frac{2g(WL_i - h_{outlet})}{\left(1.5 + \frac{\lambda L_{outlet}}{D_{outlet}}\right)}} & \text{if } h_{outlet} < WL_i \leq h_{gate} \\ Q_{max,i} = 0 & \text{if } WL_i \leq h_{outlet} \end{array} \right. \quad (5.3)$$

Where A_{outlet} , L_{outlet} , D_{outlet} , and h_{outlet} are the area, length, diameter and intake elevation of the outlet work, respectively; λ_i is the Darcy friction coefficient at the time step i that considers the energy loss in a closed pipe (obtained in this study with the Colebrook-White equation); the coefficient 1.5 considers the energy loss at both the intake and outtake of the closed conduit; and $Q_{spill,i}$ is the maximum discharge that the spillway can release at the time step i . Nevertheless, the values of Q_{max} imply that both the spillway gates and the outlet works are completely open, though this is not always true. Therefore, the outflow discharge at the day i $Q_{out,i}$ is calculated by Eq. 5.4:

$$\left\{ \begin{array}{ll} Q_{out,i} = \alpha_m \cdot EF_m + K(\beta_m \cdot Q_{in,i} + \gamma_m) & Q_{out,i} < Q_{max,i} \\ Q_{out,i} = Q_{max,i} & Q_{out,i} \geq Q_{max,i} \end{array} \right. \quad (5.4)$$

Where EF_m is the environmental flow in the m -th month; $Q_{in,i}$ is the daily inflow discharge in the reservoir at the day i ; α_m , β_m , γ_m are three parameters for each month of the year ($m = 1, \dots, 12$) that are used to calibrate the reservoir operation model; K is a parameter that depends on WL_i that considers flood control magnitudes of the inflow discharges of the most extreme events. Particularly, K is zero when WL_i is below from the maximum reservoir water level. Therefore, in this case, $Q_{out,i}$ only depends on the environmental flow. When WL_i is close to the maximum reservoir water level, K equals one and $Q_{out,i}$ also depends on $Q_{in,i}$ to obtain outflow releases by the spillway, which are obtained from a linear relationship that depends on $Q_{in,i}$. In addition, if $Q_{out,i}$ exceeds the value of $Q_{max,i}$ in a given time step, $Q_{out,i}$ will be equal to $Q_{max,i}$ as the reservoir cannot release $Q_{out,i}$ at that time step given the reservoir water level WL_i (Equation 5.3). In the reservoir operation model, $Q_{in,i}$ is the HBV output for both the current scenario and the climate projections (Section 5.2.1).

Environmental flow (EF_m) is estimated in each month with a revised variable monthly flow (RVFM) (Yu et al., 2021), combining the Variable monthly Flow Method (VFM) (Pastor et al., 2014), with the Tennant method (Tennant, 1976). RVFM assumes that the environmental flow is a percentage of the Mean Monthly Flow (MMF) given by Eq. 5.5.

$$EF_m = \varphi \cdot MMF_m \quad (5.5)$$

where EF_m is the environmental flow in the m -th month, MMF_m is the mean monthly flow in the m -th month; and φ is the flow coefficient, that is a parameter that can vary increase from 0 to 1 considering six different ecological conditions of the river (poor, fair, good, excellent, outstanding, and optimum). The coefficient φ also depends on the month that is considered, as in VFM. Indeed, a given month can be defined as a high-flow month if MMF_m is higher than 80% of the mean annual flow (MAF), and as a low-flow month if MMF_m is lower than 40% of the MAF. Otherwise, it will be an intermediate-flow month (Table 5.1).

Table 5.1. Values of the flow coefficient (φ) associate with each ecological condition (poor, fair, good, excellent, outstanding, and optimum) and hydrological seasons (high-flow, intermediate flow and low-flow months) in the Revised Variable Monthly Flow method. Extracted from [Yu et al. \(2021\)](#).

Months	Poor	Fair	Good	Excellent	Outstanding	Optimum
High-flow	0.10	0.30	0.40	0.50	0.60	0.70
Intermediate-flow	0.15	0.45	0.55	0.65	0.75	0.85
Low-flow	0.20	0.60	0.70	0.80	0.90	1.00

MMF and MAF have been obtained from the observed daily inflow discharge time series at the Eugui reservoir. EF_m does not change in the future, as it is assumed that EF_m is the minimum discharge that is required to sustain freshwater ecosystem downstream the dam. Water supply demands have been calculated and it represent a percentage of EF_m . Therefore, a further contribution is not included to consider the water resource management, and the discharge for the downstream population water supply is considered in the ecological flow. In each day, $Q_{out,i}$ is quantified. A mass balance is applied to the reservoir with $Q_{in,i}$ as input and water volume that directly evaporates from the reservoir and $Q_{out,i}$ as output volumes, obtaining the reservoir water level in the next day (WL_{i+1}). Indeed, water volumes stored at the reservoir in each day are also calculated, benefiting from the one-to-one correspondence between reservoir water levels and water volumes stored in the reservoir. The 36 parameters of the reservoir operation model (α_m , β_m , γ_m) are calibrated by comparing the observed and modelled mean daily reservoir water levels in the current scenario (2008-2021). In addition, even if observed daily inflow discharges are available in the current scenario, $Q_{in,i}$ obtained by the calibrated HBV model is used to calibrate the reservoir operation model. The calibrated reservoir operation model simulates the future period with $Q_{in,i}$ simulated by the HBV model as input, obtaining time series of future daily reservoir water levels in the time window 2010-2100. Such a period is divided into three time windows (2011-2040, 2041-2070, 2071-2100). A reservoir water level frequency curve is obtained for each time window to generate random initial reservoir water levels in a stochastic procedure (Section 5.2.4).

5.2.4 Stochastic procedure to combine floods and initial water levels frequencies

In the previous sub-sections, the methodology to characterise the frequencies of expected reservoir water levels at the beginning of flood events and inflow flood peaks are presented. In this sub-section, a methodology to combine both frequencies is presented to assess hydrological dam safety, considering the expected changes of initial reservoir water levels and flood peaks. Therefore, the objective of this section is to assign a given initial reservoir water level to each flood event generated stochastically to keep the statistical properties of the frequency curves of flood peaks and initial reservoir water levels.

A stochastic procedure is used to generate a large set of inflow hydrographs with random inflow peaks (Q_{peak}) and initial reservoir water levels (WL_{ini}). Two random probability vectors are generated

independently, as no clear correlation has been detected in the pairs of Q_{peak} and WL_{ini} in the observations, as shown in Figure 5.1, where the observed peaks in the Eugui reservoir (obtained with a POT3) are associated with the observed water level at the beginning of flood event 10,000 values of Q_{peak} and WL_{ini} are generated for each of the 72 scenarios considered in the study, given by 12 climate models, three future time windows and two RCPs. The two vectors are the non-exceedance probability (NEP) of Q_{peak} inflow hydrographs and the exceedance probability (EP) of WL_{ini} . The two vectors are randomly combined as in Figure 5.2 to describe all the possible combinations of the pairs $Q_{\text{peak}}-WL_{\text{ini}}$ in the feasible space of NEP-EP. Each scenario will have a different space of probabilities (EP-NEP).

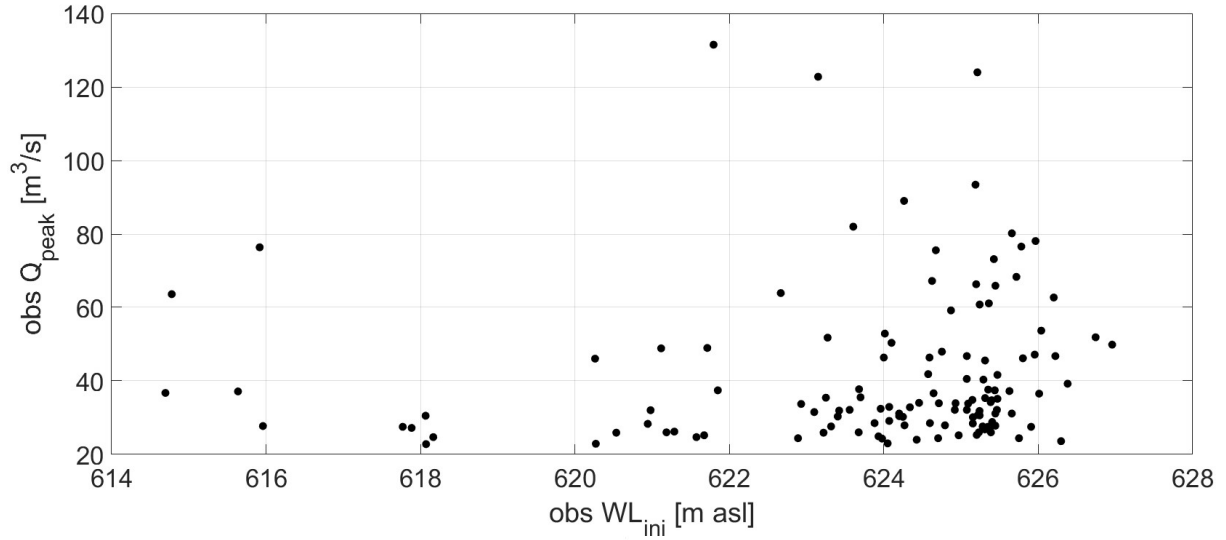


Figure 5.1. No correlation is detected between the observed daily peaks and initial water levels at the beginning of flood events.

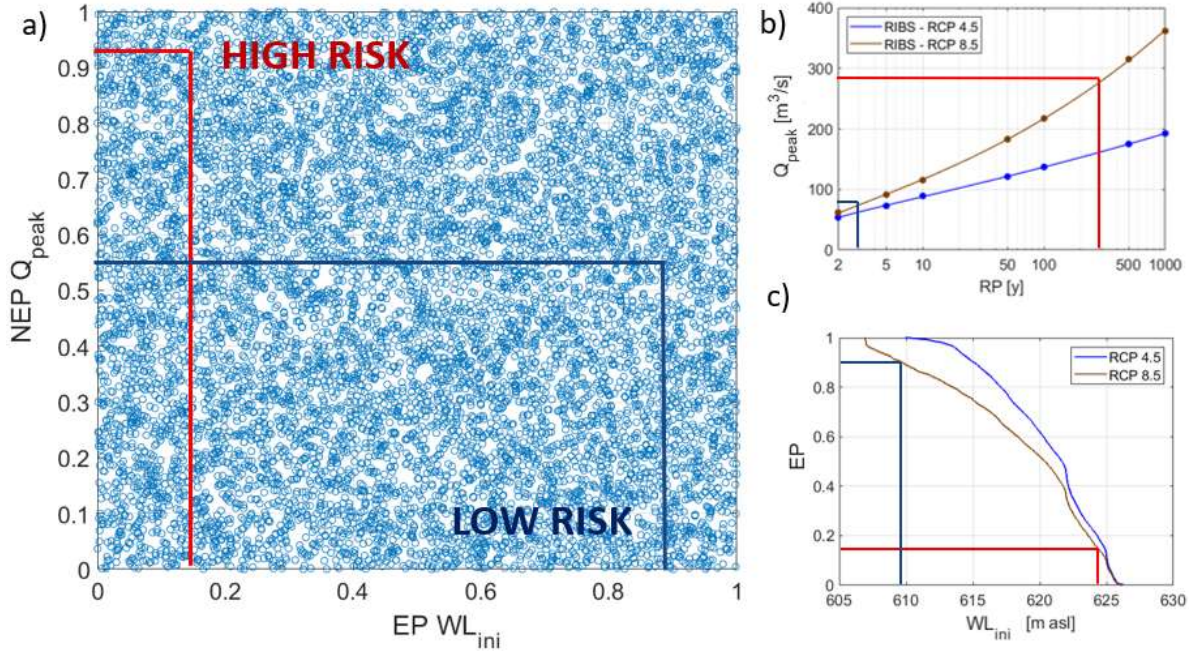


Figure 5.2. Random generation of $Q_{\text{peak}}-WL_{\text{ini}}$ pairs. a) Feasible space of $Q_{\text{peak}}-WL_{\text{ini}}$ pairs; b) non-exceedance probabilities (NEPs) associated with Q_{peak} represented with return periods (RPs); c) exceedance probabilities (EP) of WL_{ini} .

While a low EP is associated with a high initial reservoir water level (red line in Figure 5.2c), a value close to one represents the small reservoir water levels (dark blue line in Figure 5.2c). High NEP values of Q_{peak} correspond to inflow hydrographs with high return periods (RP) (red line in Figure 5.2b).

The relationship between NEP or RP and Q_{peak} is characterised with a GEV distribution function fitted to the RIBS model outputs of [Lompi et al. \(2021\)](#) (Chapter 4). The hydrograph shape supplied by the RIBS model is associated with each value of Q_{peak} . Each EP value of WL_{ini} is associated with a given reservoir water level using the empirical reservoir water level frequency curve obtained by coupling the HBV and the reservoir operation models (Section 5.2.2 and Section 5.2.3). Reservoir water levels are not sampled by an extreme frequency distribution as flood events can found any initial water level in the reservoir. Indeed, the model assumption is that maxima water levels with a given return period are the results of flood events already occurred in the reservoir, while they are not likely to be initial water levels at the beginning of a flood event.

5.2.5 Volumetric Evaluation Method (VEM)

The Volumetric Evaluation Method (VEM) is a flood routing reservoir model that can simulate outflow discharges from gated dam spillways during a flood event ([Gir6n, 1988](#)). The main difference between the VEM and the reservoir operation model (Section 5.2.3) regards on the time step. The reservoir operation model that simulates water balance at a daily time step, considering daily outflow discharges by the dam as a function of daily reservoir water levels, EF_m , daily inflows and some characteristics of the dam (Eq. 5.3 and Eq. 5.4). However, it cannot simulate flood control processes at sub-daily time scales. Instead, the VEM determines how spillway gates are operated in flood events using sub-hourly timesteps. Outflow discharge at each time step is determined considering inflow discharges, spillway gate operations, reservoir water level and outflow discharge variations at a higher temporal resolution. Therefore, the VEM is used to simulate flood control processes in the reservoir in flood events. In this study, inflow hydrographs with a 15-min time step are used.

VEM assumes that, considering constant inflow $Q_{in,t}$ and outflow discharges $Q_{out,t}$, if $Q_{in,t}$ is greater than $Q_{out,t}$, the number of remaining time steps N_t before the maximum reservoir storage capacity (V_{max}) will be reached is:

$$N_t = \frac{V_{max} - V_t}{(Q_{in,t} - Q_{out,t}) \cdot \Delta t} \quad (5.6)$$

Where V_t is the reservoir storage volume at time t ; $Q_{in,t}$ is the inflow discharge at time t ; $Q_{out,t}$ is the outflow discharge at time t ; and Δt is the inflow hydrograph time step. When the reservoir is filled, inflow and outflow discharges must be the same to avoid overtopping. Therefore, VEM is based on a linear increasing of $Q_{out,t}$, to reach $Q_{in,t}$ in the N_t time steps. Therefore, $Q_{out,t}$ must increase $\Delta Q_{out,t}$ in each time step (Eq. 5.7).

$$\Delta Q_{out,t} = \frac{Q_{in,t-1} - Q_{out,t}}{N_t} = \frac{(Q_{in,t-1} - Q_{out,t})^2}{V_{max} - V_t} \Delta t \quad (5.7)$$

Outflow discharge is obtained in each time step with Eq. 5.7, obtaining outflow hydrographs. VEM uses the 10,000 different inflow hydrographs associated with the 10,000 random initial reservoir water volumes in each scenario to obtain the 10,000 maxima outflow discharges $Q_{out,max}$ and the 10,000 maxima water levels WL_{max} . After that, RP quantiles of $Q_{out,max}$ and WL_{max} are estimated from the empirical frequency curve of $Q_{out,max}$ and WL_{max} for each scenario.

5.2.6 Overtopping probability and delta changes estimates

The impact of climate change on hydrological dam safety is assessed using the overtopping probability and delta changes of both maxima reservoir water levels and maxima outflow discharges.

Delta changes of maxima reservoir water level (ΔWL) are obtained with Eq. 5.8.

$$\Delta WL(RP_i) = WL_{fut}(RP_i) - WL_{cur}(RP_i) \quad (5.8)$$

Where $WL_{fut}(RP_i)$ is the maximum reservoir water level expected in the future associated with a given return period RP_i and $WL_{cur}(RP_i)$ is the maximum reservoir water level in the current scenario for the same return period RP_i . If ΔWL is greater than zero, the maximum reservoir water level expected in the future will be greater than the in the current scenario. If ΔWL is lower than zero, the maximum reservoir water level expected in the future will decrease. ΔWL is obtained as the difference between the future and control periods, as all delta changes would be close to one if the ratio between water levels above sea level is considered.

Delta changes of maxima outflow discharges, rQ , are expressed as:

$$rQ_{out}(RP_i) = \frac{Q_{out,fut}(RP_i)}{Q_{out,cur}(RP_i)} \quad (5.9)$$

where $Q_{out,fut}(RP_i)$ is the maximum outflow discharge expected in the future for a given return period RP_i and $Q_{out,cur}(RP_i)$ is the maximum outflow discharge for the same return period RP_i in the current scenario. If rQ is greater than one, the future maximum outflow discharge will be greater than in the current scenario. If rQ is lower than one, maximum outflow discharges will decrease in the future.

The overtopping probability is the EP of the reservoir water level that corresponds to the maximum reservoir storage at the dam crest. In addition, potential waves height generated by wind is also considered, as it is usually done in dam design. The wave height is obtained with the Stevenson formula (Stevenson et al., 1981) (Eq. 5.10), which can be used when no wind data are available (as in future scenarios). Therefore, overtopping is assumed to occur when the reservoir water level equals the dam crest altitude minus the wave height h_w .

$$h_w = 0.76 + 0.34 \cdot \sqrt{F} - 0.26 \sqrt[4]{F} \quad (5.10)$$

In the previous equation, h_w is the wave height [m], and F is the fetch [km], the longest path over water from the dam to any point in the reservoir. The wave height considered in the study is four-thirds of h_w , as two-thirds of h_w is above the reservoir water level for a given wave, and the water jumps until two-thirds of h_w above the wave crest when it hits the dam upstream face.

5.3 Data and Case Study

The methodology is applied to the Eugui Dam in the Arga River catchment in Northern Spain. In Lompi et al. (2021), the quantification of the future design discharges is especially focused on the flood hazard in the city of Pamplona (Chapter 4). Nevertheless, since the RIBS model is a fully distributed hydrological model, future design flood results are also available at the Eugui dam. While the drainage area to the city of Pamplona is 510 km², the catchment area of the Eugui reservoir is 69 km² (Figure 5.3a). The Eugui dam has gated spillways (Figure 5.3c) with the crest at the elevation of

625 m a.s.l. The conservation pool has a storage capacity of 21.8 hm³ at 628 m a.s.l. The dam crest is at 630 m a.s.l.

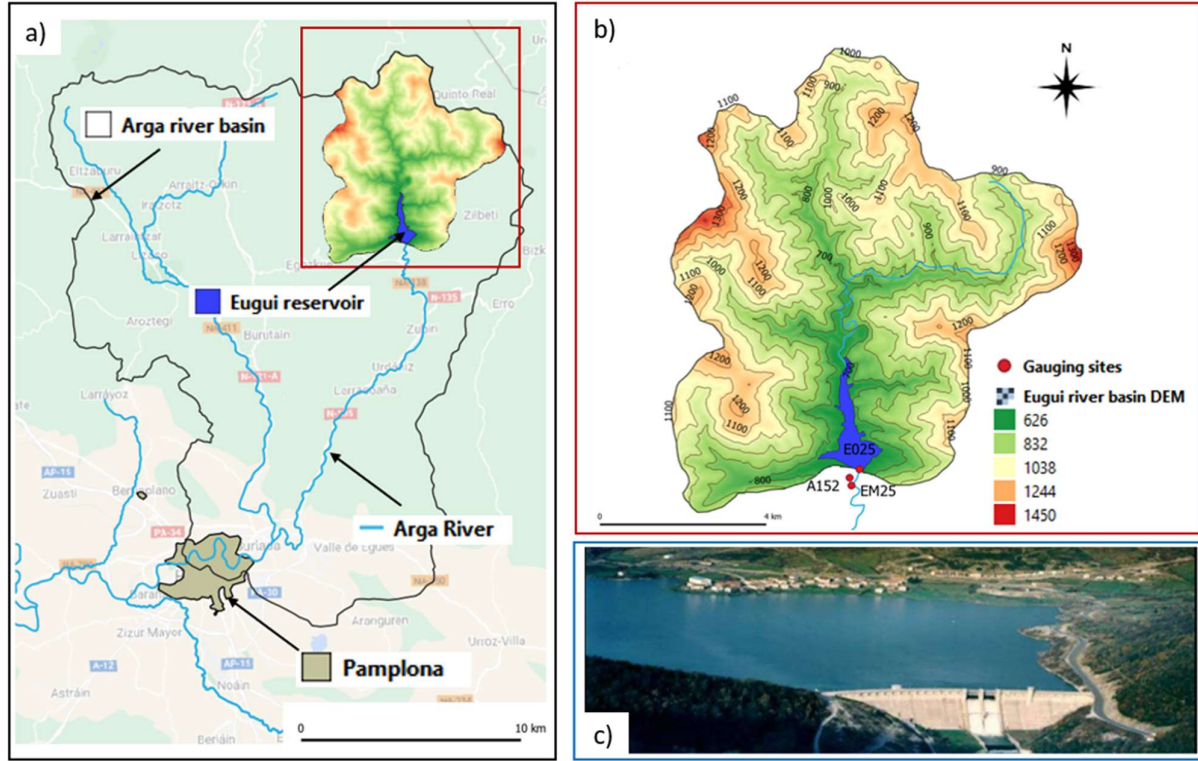


Figure 5.3. a) Location of the Eugui reservoir within the Argu river basin b) Argu river catchment upstream the Eugui reservoir in northern Spain with gauging site location and Digital Elevation Model; c) Eugui Dam and reservoir (source: <https://www.iagua.es/data/infraestructuras/presas/eugui>). E9825 and EA025 gauging sites have the same location. Therefore, only the position of the newest instrument is shown in Figure 2b.

The observed data consist of precipitation, temperature, water levels (or storage volumes) at the reservoir, and outflow discharge released by the dam outlets (Table 5.2). Two data sources of reservoir water levels are available for a total period of 42 years. Daily data are available for 40 years (1978–2018) at the E9825 gauging site. The last part of the time series has a 15-min time resolution for a period of 23 years (1998–2021) recorded at the E025 gauging site.

Table 5.2. Observed data used in the study.

Name	Measured variable	Period	Time resolution
E9825	water level	1978–2018	daily
E025	water level	1998–2021	15 minutes
A152	outflow discharge	1998–2021	15 minutes
EM25	rainfall & temperature	2008–2021	15 minutes

Inflow discharges in the reservoir were obtained through a mass balance with outflow discharges and storage volumes. The annual maxima series (AMS) of inflow discharges were obtained for the period 1978–2020. In addition, AMS of 15-min inflow discharge was extracted in the period 1998–2021, obtaining 23 pairs of flow peaks associated with the two time resolutions. A linear regression is fitted to these values to obtain 15 min- hydrograph peaks from daily data in the first part of the time series. A GEV distribution is fitted to the AMS of inflow discharge for the stochastic procedure (Section 5.2.4) to analyse the hydrological dam safety of the current scenario. In addition, the reservoir water level frequency curve has also been obtained to assess the probability associated with a given pool

level in the reservoir for the current scenario. Moreover, the reservoir water level frequency curve is also used for the calibration of the reservoir operation model (Section 5.2.3). Finally, the HBV model is calibrated with rainfall and temperature data at the gauging site EM25 (Table 5.2) over a period of 13 years from January 2008 to May 2021. Moreover, the model is validated in the last year of data, from June 2021 to July 2022. Climate change data consists of rainfall and temperature projections in the period 2006-2100 supplied by 12 climate models, considering two emission scenarios (RCP 4.5 and RCP 8.5) (Table 3.1 in Chapter 3).

5.4 Results

This section presents the results of the methodology applied to the Eugui Dam case study. The results of the statistical analysis with observed data are shown in Section 5.4.1, while the statistical analysis of some climate variables provided by projections or by the HBV model output is in Section 5.4.3; the reservoir water levels and peak inflow discharges obtained in the future are presented in Section 5.4.2; the findings on the changes in maxima reservoir water levels are in Section .4, while changes in maxima outflow discharges are in Section 5.4.5. Finally, the results that consider the overtopping probability are in Section 5.4.6.

5.4.1 Statistical analysis of observed data

A GEV distribution function is fitted to the AMS of 42 years of peak inflow discharges in the period 1979-2020 (Figure 5.4a). In addition, the empirical distribution of reservoir water levels in the current scenario is obtained with 15-minute observations in the period 1998-2021 (Figure 5.4b). The two frequency curves are used in the stochastic procedure to assess the maximum reservoir water level frequency curve in flood events in the current scenario.

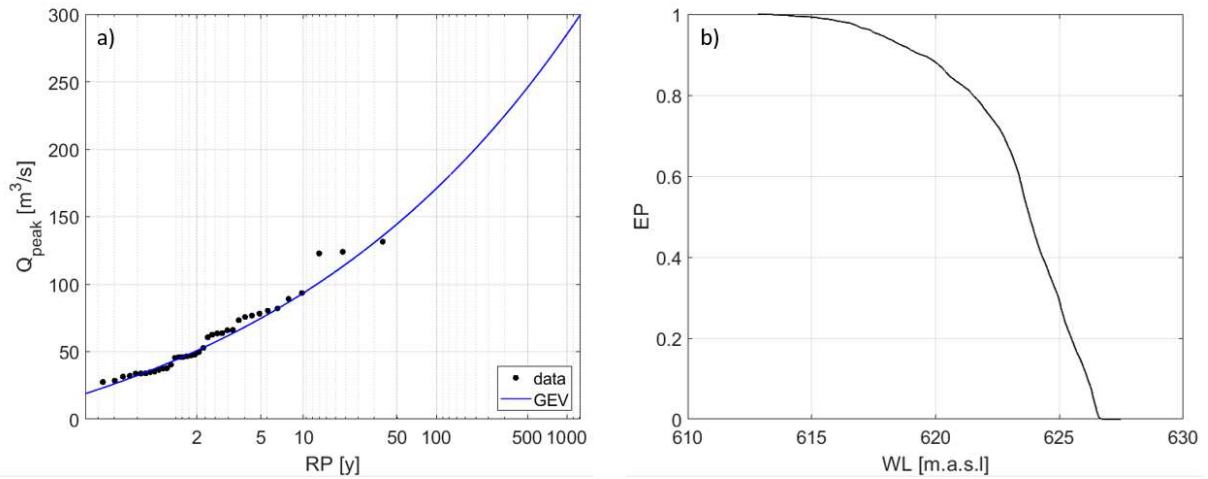


Figure 5.4. Frequency curves in the current scenario: a) peak inflow discharges in the reservoir, b) reservoir water levels.

The maxima inflow peaks discharge observed at the reservoir is $131.3 m^3/s$. The inflow peaks associated with Return Periods of 100, 500 and 1000 years are $170.9 m^3/s$, $245.8 m^3/s$ and $285.1 m^3/s$, respectively.

The reservoir water levels oscillate between 615 and 626 m a.s.l. However, a reservoir water level of 620 m a.s.l. has an exceedance probability of around 90 %. In addition, the EP of the water level at the spillway crest elevation (625 m a.s.l.) is 29%. The maximum reservoir water level ever recorded in the period 1998-2021 is 627.5 m a.s.l. Therefore, the EP of the water level associated with the

upper limb of the gates (628 m a.s.l.) is zero in the empirical frequency distribution in the period with observations. Indeed, the reservoir water level at the beginning of a given flood event cannot be above the maximum reservoir level in normal conditions. The maximum reservoir level is given by the upper limb of the spillway gates minus the expected wave height.

5.4.2 Reservoir water levels and peak inflows in the future

The HBV model is calibrated in the draining catchment to the Eugui dam with 13 years of observations (2008-2021). Figure 5.5 shows the results in the period 2019-2022. A set of 20 000 random combinations of the 11 HBV model parameters is considered using Monte-Carlo simulations.

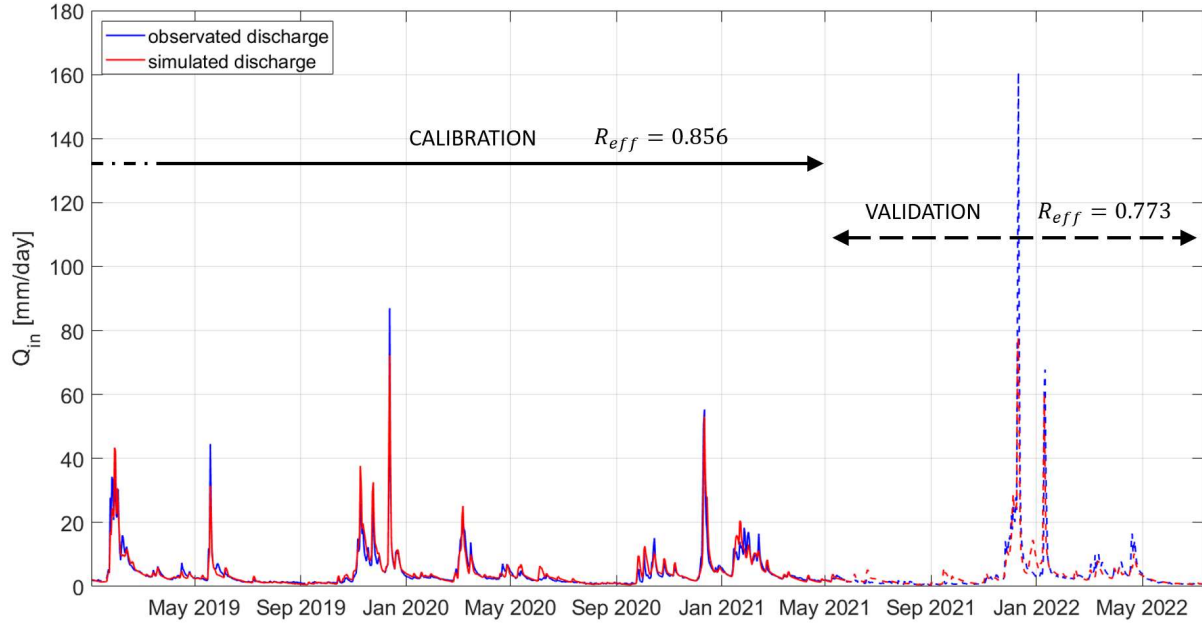


Figure 5.5. Results of the calibration (solid line) and validation (dashed lines) of the HBV model in the period 2019-2022. The blue line represents the observed daily discharges by the HBV model, while the red line shows the observations.

The efficiency of model quantified by the R_{eff} statistic in the calibration period is 0.856 reaching the calibration target, as the R_{eff} value is greater than 0.85. The performance of the model in the validation period remains quite good as the objective function is in this case 0.773, highlighting the goodness of the calibration process.

The time series of daily inflow discharges to the Eugui reservoir simulated by the HBV model in the current scenario (2008-2021) are used as input data of the reservoir operation model described in Section 5.2.3 to simulate daily reservoir water levels in the last 13 years. Monthly environmental flows (EF_m) used in the reservoir operation model are presented in Table 5.3.

Table 5.3. Monthly environmental flows used in the reservoir operation model.

Month	Jan	Feb	Mar	Apr	May	Jun	Jul	Aug	Sep	Oct	Nov	Dec
EF_m [m ³ /s]	2.51	2.72	2.46	1.87	1.43	1.44	1.02	0.92	0.93	1.20	1.87	2.18

The reservoir operation model is also calibrated using Monte Carlo simulations to reduce the bias between daily simulated and observed reservoir water levels. Varying values of the 36 parameters α_m , β_m , γ_m of the reservoir operation model have been considered (Section 5.2.3), analysing the Root Mean Squared Error (RMSE) and the Nash-Sutcliffe model Efficiency (NSE) between observed and simulated daily water levels. Figure 5.6 shows that the simulated frequency curve of WL is close to the frequency curve fitted to observations.

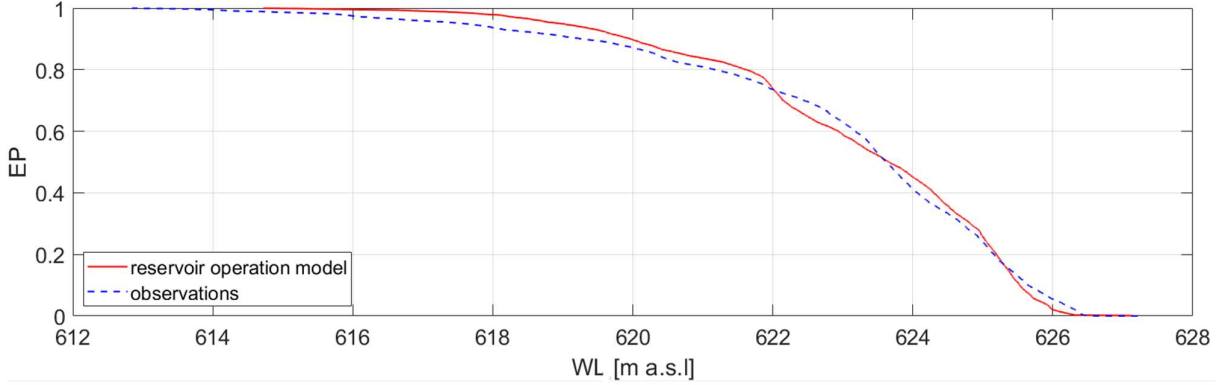


Figure 5.6. Calibration results of the reservoir operation model. The dashed blue line represents the empirical frequency curve of reservoir water levels extrapolated from the observations. The red line represents the reservoir water levels simulated by the reservoir operation model.

The climate projections of rainfall and temperature are used to assess the future initial reservoir water level for each climate model, RCP and future period. Climate projections are used as input data of the calibrated HBV model, obtaining time series of daily inflow discharges in the reservoir (Q_{in}) (Figure 5.7a). The calibrated reservoir operation model uses Q_{in} as input data to simulate the time series of daily reservoir water levels (Figure 5.7b). The first row of Figure 5.7 shows the simulated time series of future Q_{in} obtained with the HBV model for the MPI-CCL climate model, RCP 4.5 in the future (2006-2100). The second row of Figure 5.7 shows the time series of reservoir water levels simulated by the reservoir operation model for the same climate model and scenario.

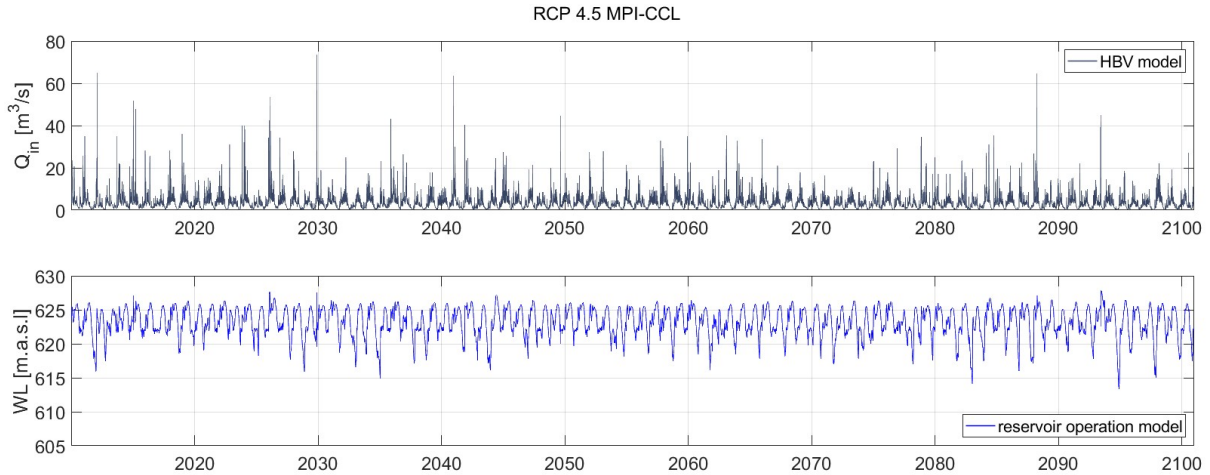


Figure 5.7. Results for the MPI-CCL climate model and RCP 4.5 in the period 2006-2100. a) Inflow discharge time series in the reservoir simulated by the HBV model. b) Reservoir water levels obtained by the reservoir operation model.

Time series of daily reservoir water levels are generated for each scenario in the period 2006 to 2100. However, the first four years are skipped for the HBV model stabilisations. The remaining part of the time series is divided into three time windows (2011-2040, 2041-2070, 2071-2100). These three

periods correspond to the time windows used in [Lompi et al. \(2021\)](#). Initial reservoir water level frequency curves are obtained from the outputs of HBV and reservoir operation models (Figure 5.8). Figure 5.8 shows the impact of climate change on initial reservoir water levels expected at the beginning of flood events for the ICH-CCL climate model. The impact of climate change on initial reservoir water levels at the beginning of flood events for all the other climate models is in Appendix B (from Figure B1 to Figure B11).

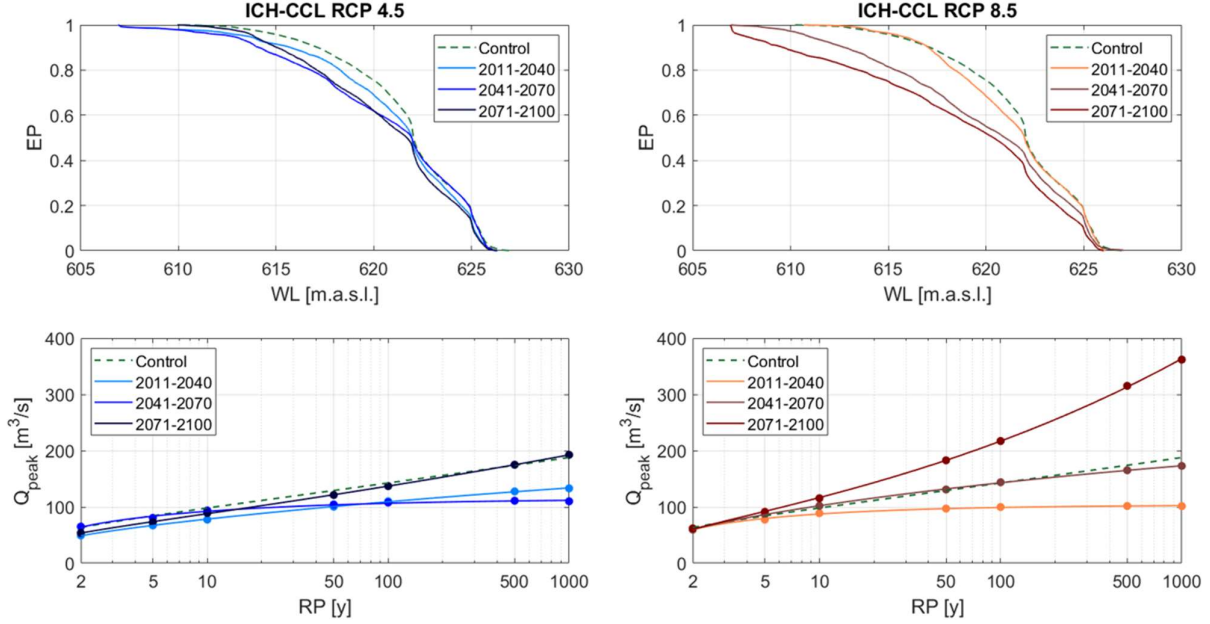


Figure 5.8. Initial reservoir water level and inflow peak discharge frequency curves for the ICH-CCL climate model in the three time windows. The left column shows the results for RCP 4.5. The right column offers the results for RCP 8.5. Each time window is represented with a given colour. Control periods are represented with dashed lines and future periods with solid lines.

In the future, reservoir water levels are expected to decrease compared with water levels in the current scenario. Such a decrease is clear for the 12 climate models in both RCPs, but it is greater in the RCP 8.5 than in the RCP 4.5. In addition, flood peaks will increase in time for the RCP 8.5, expecting the greatest changes in the 2071-2100 time window. Therefore, the greatest flood events will encounter lower reservoir initial water levels.

5.4.3 Statistical analysis of climate variables: projections and HBV model output

A statistical analysis of some climate variables is conducted to analyse the drivers that lead to decreasing reservoir water levels in the future. Particularly, Figure 5.9 shows the Exceedance Probability (EP) of some climate variables in the future for the ICH-CCL climate model as an example, which is the climate model also shown in Figure 5.8. Each scenario is associated with a given colour: the dashed green line is the control period, the RCP 4.5 is in a blue scale for the different time windows, and the RCP 8.5 is in a brown scale. The figures with the statistical analysis of the climate variables for all the other climate models are in Appendix C (from Figure C1 to Figure C11).

The first column shows how daily potential evapotranspiration (PET), obtained with the Hargreaves equation from future daily temperature, will increase in the future with respect to the control period,

especially in the RCP 8.5. This relates to the increase of temperature expected in both the emission scenarios, but especially in the RCP 8.5, with more greenhouse gas emissions. The second column shows that the future daily precipitation (P) is expected to decrease in the future. Particularly, Figure 5.9 shows how the EP of the daily precipitation with less than 10 mm will decrease continuously over time, from the control period to the end of the century. The plot also shows how a decrease in wet days (i.e. days with P greater than 0 mm) is expected in the future in the Eugui river basin.

Particularly, the EP of 0 mm is 0.51 in the control period (a mean of 186 wet days), while it is 0.39 in the RCP 8.5 in the 2071-2100 time window (a mean of 142 wet days). The third column shows how the soil moisture condition SM (see section 3.3.2 for the description of the model) obtained with the HBV model will decrease in the future in both the emission scenarios, but especially in the RCP 8.5.

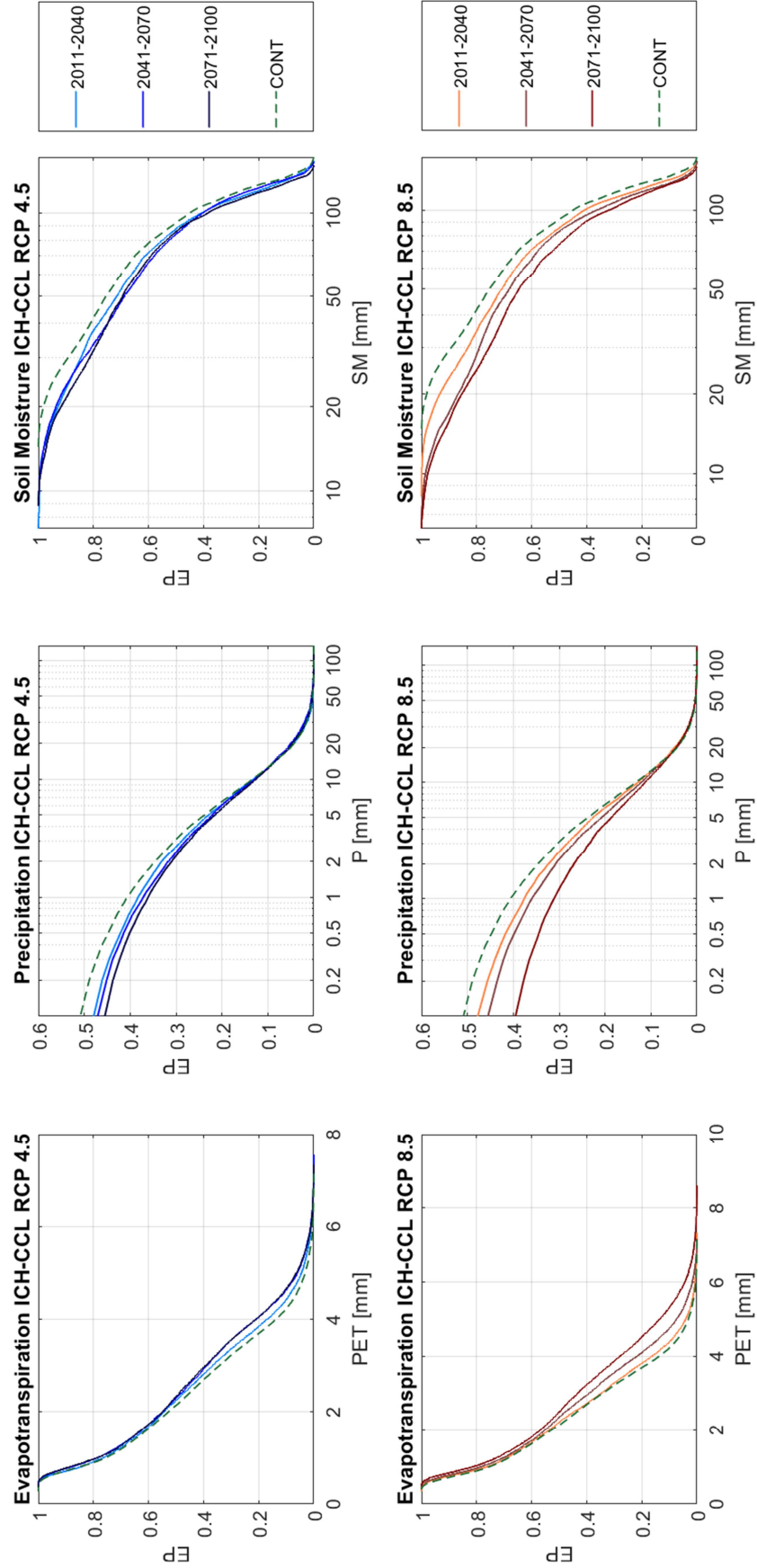


Figure 5.9. Exceedance Probability (EP) of some future climate variables under the ICH-CCCL climate projections: the first column shows the daily potential evapotranspiration PET obtained with the Hargreaves equation from future daily temperature, the second column shows the future daily precipitation P and the third column shows soil moisture condition SM obtained with the HBV model. Each scenario is associated to a given colour: dashed green line is the control period, the RCP 4.5 is in a blue scale for the different time windows, the RCP 8.5 is in a brown scale.

5.4.4 Changes in maximum reservoir water levels

Figure 5.10 shows the expected elevations of maxima reservoir water levels (WL_{max}) in flood events for the IPS-WRF climate model. The dam is represented in grey, showing the maxima water levels should not exceed the dam crest elevation at 630 m a.s.l. However, the overtopping threshold (dotted red line) is at the elevation of 628.71 m a.s.l. because the potential wave height induced by wind is also considered (see Section 5.2.6). If WL_{max} exceeds the overtopping threshold, it is assumed that water can exceed the dam crest, as for the IPS-WRF model in the 2041-2070 time window and RCP 8.5 (upper right part of Figure 5.10). Figure 5.10 also shows the expected delta changes in maxima reservoir water levels (ΔWL) extracted for seven return periods (2, 5, 10, 50, 100, 500 and 1000 years). ΔWL positive values will be over the horizontal green line, pointing to an increase in the maximum reservoir water levels in flood events in the future. ΔWL negative values will be under the horizontal green line, pointing to a decrease in the maximum reservoir water levels in flood events in the future.

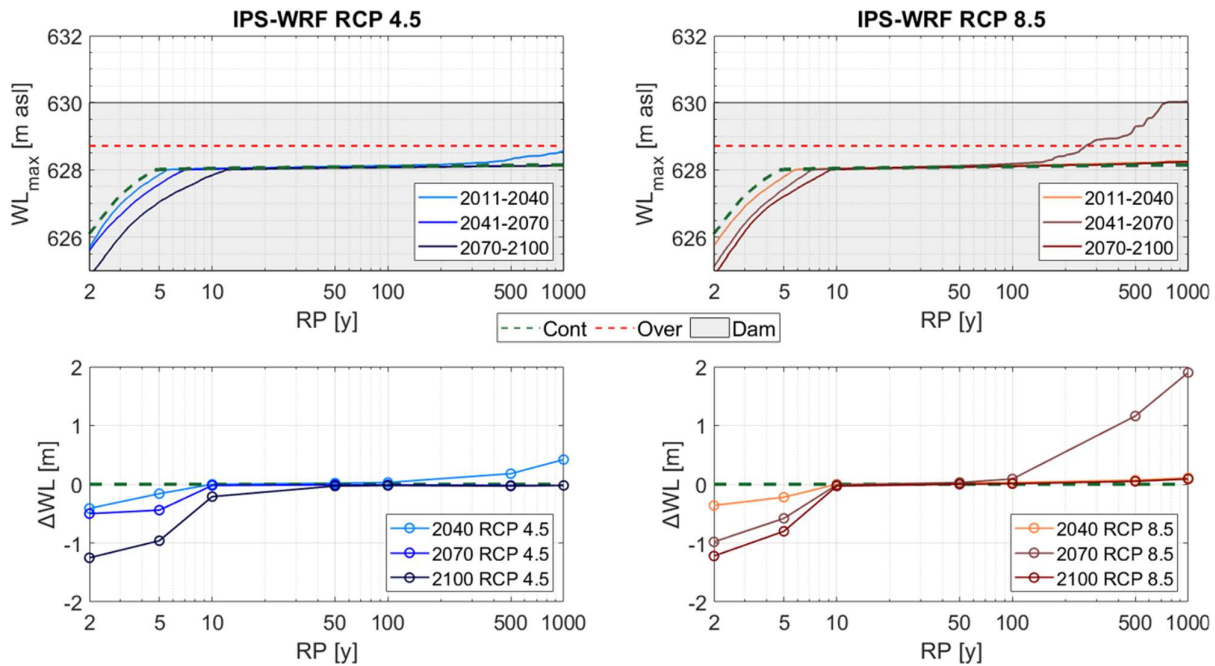


Figure 5.10. Comparison of maxima reservoir water level frequency curves in the three periods in the future with the control period for the IPS-WRF climate model. The first row shows maxima reservoir water level elevations and the second row shows the delta changes in maxima reservoir water levels extracted for seven return periods. The dashed green line represents the control period. The grey-filled box represents the dam with its crest elevation at 630 m a.s.l. The horizontal dashed red line represents the overtopping threshold. The first column offers the results for RCP 4.5 and the second column for RCP 8.5. Future periods are represented with solid lines in a blue scale for RCP 4.5 and in a brown scale for RCP 8.5.

Figure 5.10 shows how the operation of spillway gates can maintain the maximum reservoir water level at the elevation of their upper limb (628 m a.s.l.) for the events with a RP between five-10 and 100-500 years, despite inflow peak discharges associated with different return periods can differ. Indeed, the VEM tries to maintain this level as longer as possible. Nevertheless, maxima peak outflow discharges increase for the highest return periods to avoid exceeding the elevation of the upper limb of spillway gates. Only a slight increase in the maxima reservoir water level for the 500 and 1000-year RP is obtained for the RCP 4.5 in the 2011-2040 time window. Similarly, the greatest expected changes in maxima reservoir water levels in the RCP 4.5 for the 1000-year flood are found in the 2011-2040 time window for 10 out of 12 climate models. Figure 5.10 also shows how the greatest

expected changes of maxima water levels are in the 2041-2070 time window for the RCP 8.5, where the maximum reservoir water level can cause dam overtopping. Nevertheless, the IPS-WRF climate model is the only one with the greatest water levels expected in such a time window. Indeed, while five of the 12 climate models show that the greatest maxima water levels are expected at the end of the century in the RCP 8.5, no changes are expected in this emission scenario by six climate models.

The results of all the other climate models are in Appendix D (from Figure D1 to Figure D11) and are represented as red dots for the seven considered return periods. Figures in Appendix D show the results also considering the assessment of the uncertainty chain, which is described in the next chapter. The results regarding delta changes in maxima water levels obtained with the ensemble of the 12 climate models are presented with boxplots in Figure 5.11 for each scenario.

Looking at the delta changes obtained with the ensemble of all the climate models in Figure 5.11, it is evident that no changes are expected in the future maxima water levels for all the events with a RP within 10 and 500 years, in all the time windows and emission scenarios. This is because the spillway gates operation can maintain the maximum level at 628 m a.s.l. More variability is present in the results associated with the RP of 2 and 5 years because of the many different values under 628 m a.s.l., which is the maximum level where the spillway gates operations start. There is some variability also in the 1000 years maximum water level, in the 2011-2040 time window in the RCP 4.5 and especially in the 2071-2100 time window in the RCP 8.5. This is due to the different values above 628 m a.s.l., because the outflow discharge of the dam operations is not sufficient to maintain the level at 628 m a.s.l. The median values of the boxplots show an increase in the maximum water level only in the RCP 8.5 in the 2071-2100 time window with a relatively small increase of 7 cm.

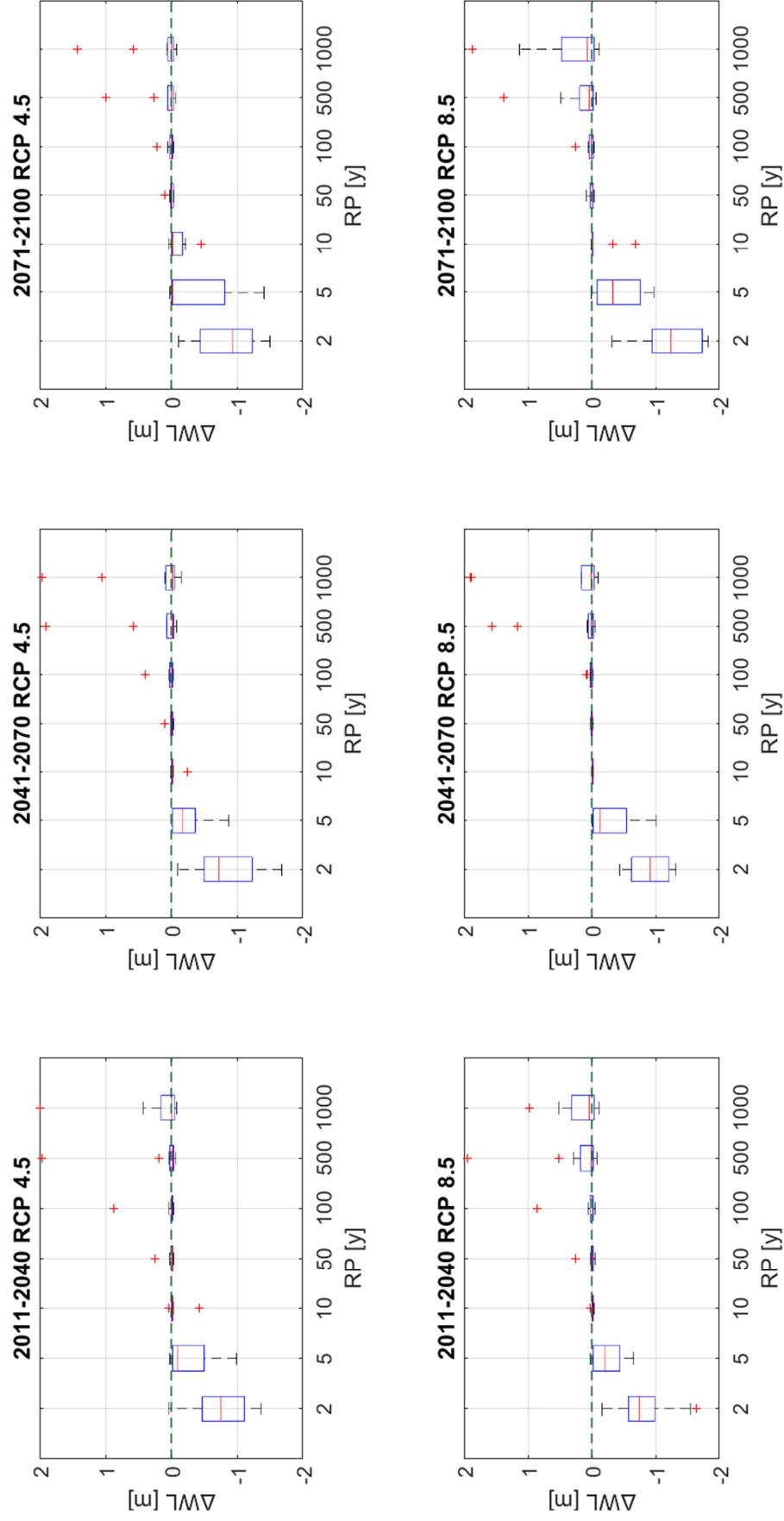


Figure 5.11: Boxplots of delta changes of maximum water level considering the ensemble of all the climate models in the three time windows and for the two emission scenarios (columns represent time windows (2011-2040, 2041-2070, 2071-2100); rows represent emission scenarios (RCP 4.5 and RCP 8.5)).

5.4.5 Changes in maximum outflow discharges

Figure 5.12 shows the expected maxima outflow discharges ($Q_{out,max}$) in flood events for the MPI-RCA climate model. The first row shows the maximum outflow discharge associated with each RP, while the second row shows the delta changes of maxima outflow discharges rQ . If rQ is greater than one, i.e. over the horizontal dashed green line, the maximum outflow discharge will increase in the future. If the rQ is lower than one, i.e. below the horizontal dashed green line, the maximum outflow discharge will decrease in the future. The results with expected maxima outflow discharges for all the other climate models are in Appendix E (from Figure E1 to Figure E11) and are represented as red dots for the seven considered return periods. Figures in Appendix E also show the results considering the assessment of the uncertainty chain, which is described in the next chapter.

Delta changes of maximum outflow discharge for the MPI-RCA climate model are greater than one just for return periods greater than 100 years in the 2011-2040 time window (left part of Figure 5.12). Again, the greatest expected change for the most extreme events seems to be related to the greenhouse gas emission peak, as also shown by the delta changes in maxima water levels. Indeed ΔQ are expected to be greater than one in the RCP 4.5 only in the 2011-2040 time window. On the contrary, the MPI-RCA climate model shows a similar increase in all the time windows in the RCP 8.5.

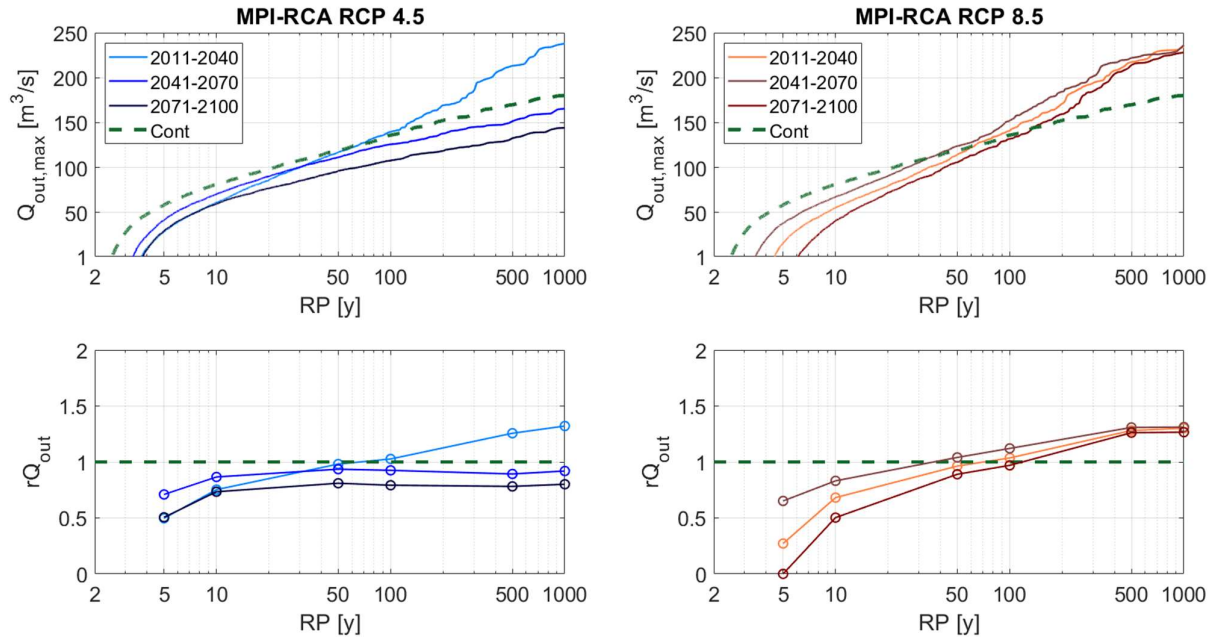


Figure 5.12. Comparison of future maximum outflow discharge frequency curves in the three windows with the control periods for the MPI-RCA climate model. The first row shows the maximum outflow discharges and the second row the delta changes in maximum outflow discharge extracted for seven return periods. The first column offers the results for the RCP 4.5 and the second column for the RCP 8.5. Future periods are represented with dashed lines for the RCP 4.5 and solid lines for RCP 8.5.

Moreover, Figure 5.12 shows how the maximum outflow peak discharge with a RP of 2 years is equal to zero for the MPI-RCA climate model. This result does not mean that there is no outflow discharge for two years but that the outflow from the spillway gates usually occurs with a return period between 2 and 5 years. It is interesting to see how only the 2071-2100 time window in the RCP 8.5 has a maximum outflow discharge with 5 years RP equal to zero, with a spillway gates operation return period between 5 and 10 years. At the same time, the maximum outflow discharge is greater in the 2071-2100 time window in the RCP 8.5 than in all the other scenarios. Therefore, looking at the MPI-

RCA climate model, it seems that in the future the spillway gates operations will be less frequent but with a greater outflow discharge for the most extreme events.

The results regarding delta changes in maxima outflow discharges obtained with the ensemble of the 12 climate models are presented with boxplots in Figure 5.13 for each scenario. Figure 5.13 highlights how the maxima outflow discharges associated with the most extreme events will increase in the future in the RCP 8.5: 13% and 16%, respectively for the 500 years and 1000 years maximum outflow discharge in the 2011-2040 time window; 29% of increase for both the 500 and 1000 years maximum outflow discharge in the 2071-2100 time window. On the contrary, maxima outflow discharges for all the other return periods and scenarios will decrease in the future, especially in the RCP 4.5.

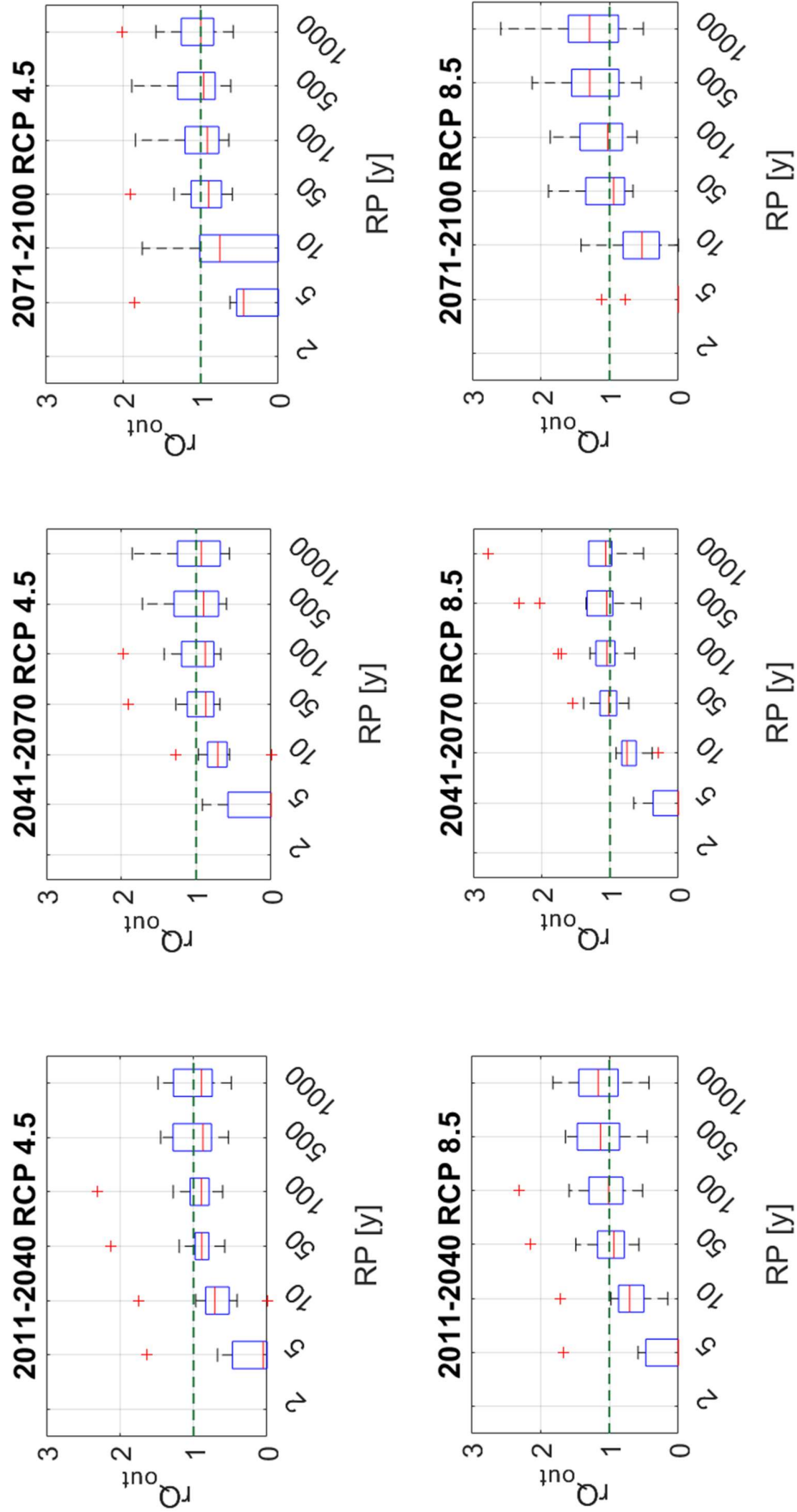


Figure 5.13: Boxplots of delta changes of maximum outflow discharge considering the ensemble of all the climate models in the three time windows and for the two emission scenarios; columns represent time windows (2011-2040, 2041-2070, 2071-2100); rows represent emission scenarios (RCP 4.5 and RCP 8.5).

5.4.6 Overtopping probability in the future

Delta changes shown in Figure 5.11 and Figure 5.13 just represent variations of maxima reservoir water levels and maxima outflow discharges with respect to the control periods, but they don't supply any information on the overtopping probability. The overtopping probability obtained with the ensemble of all the climate models is shown in Figure 5.14.

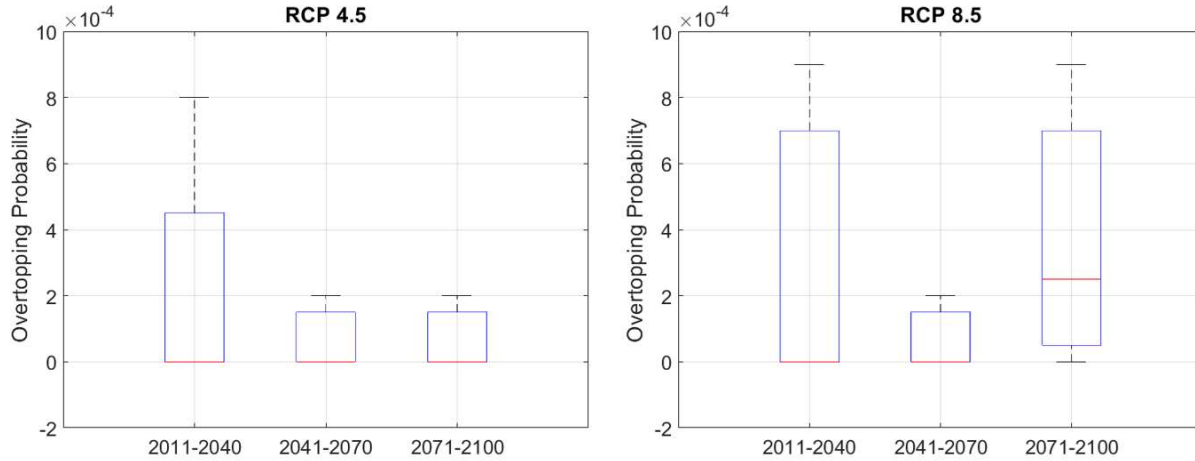


Figure 5.14. Boxplots of the overtopping probabilities considering the ensemble of the climate models in the three time window for the RCP 4.5 (a) and for the RCP 8.5 (b).

Only the RCP 8.5 have non-zero median values, with a median overtopping probability of 0.0025 (RP=4000 years) in the 2071-2100 time window. Moreover, the greatest upper quartiles of the boxplot in the two emission scenarios are when also the greenhouse gasses emission peak is present: in the 2011-2040 time window for the RCP 4.5, at the end of the century for the RCP 8.5.

The exceedance probabilities of dam overtopping (determined with reservoir water levels at the overtopping threshold considering waves induced by wind) are shown in Table 5.4 for each climate model. Zeros in the table are associated with an Overtopping Probability lower than 10^{-4} .

Table 5.4. Overtopping probability in each scenario for all the climate models. The null probability (zeros in the Table) corresponds to a probability lower than 10^{-4} .

climate model	RCP 4.5			RCP 8.5		
	2011-2040	2041-2070	2071-2100	2011-2040	2041-2070	2071-2100
ICH-CCL	0	0	0	0	0	0.0009
MPI-CCL	0.0128	0.0081	0.0045	0.013	0.0001	0.0055
MOH-RAC	0	0	0	0	0	0
CNR-CCL	0	0.002	0.0011	0.0009	0.0002	0.0005
ICH-RAC	0	0.0001	0	0	0	0.0001
MOH-CCL	0	0	0.0001	0.0018	0	0.0017
IPS-WRF	0.0008	0	0	0.0004	0.0038	0.0003
IPS-RCA	0.0001	0.0001	0	0.0005	0.0043	0
MOH-RCA	0	0	0	0	0	0
ICH-RCA	0	0.0002	0	0	0	0.0002
CNR-RCA	0.0007	0	0.0002	0	0	0.0002
MPI-RCA	0.0002	0	0	0	0	0.0005

5.5 Discussion

The decreasing pattern in initial reservoir water levels at the beginning of flood events (Figure 5.8) relates to the increase in potential evapotranspiration and the decrease in daily precipitation expected in the future (Figure 5.9). Indeed, increasing mean temperature in the Eugui Dam catchment will increase evapotranspiration rates both in the reservoir, decreasing water storage volumes, and in the catchment, decreasing soil moisture content and runoff volumes. Second, decreasing mean annual precipitation in the catchment will also reduce runoff volumes, reducing reservoir water storage volumes and levels. A warmer climate will also decrease the number of wet days in the Eugui river basin. All these changes will cause a decrease in the reservoir water levels in the future. The reduction of water volumes in a warmer climate is found in other studies. Indeed, a warmer climate will reduce reservoir storage volumes because of the decrease in catchment runoff and the increase of evapotranspiration rates also in [Konapala et al., 2020](#). These results also agree with [Fluixa-Sanmartin et al. \(2019b\)](#) that found lower water levels in the future with respect to the control period in another dam in western Spain. In addition, the decreasing trend in reservoir storage volumes in the future at the Eugui dam agrees with the reduction of water availability in some Mediterranean reservoirs ([Bukac et al., 2017](#)) and catchments ([Iglesias et al., 2006](#)). Moreover, global annual mean reservoir evaporation rates are expected to increase by 16% by 2100 ([Woolway et al., 2020](#)). Furthermore, mean annual streamflow is projected to decrease in Southern Europe catchments ([Blöschl et al., 2019](#)). In this study, such decreasing reservoir water levels seem to relate more to the decrease in daily precipitation rather than the increase in evapotranspiration. Indeed, the number of wet days will decrease in the future in all the climate projections (Appendix C). The greatest expected changes in daily precipitation are found in the CCL regional climate model.

Figure 5.10 shows how the spillway gates can maintain the maximum water level at 628 m asl for the most extreme events, despite the inflow discharges associated with the different return periods are expected to change. Nevertheless, the maximum outflow discharge must increase for the highest return periods to maintain the water level at 628 m asl, as shown in Figure 5.12 for the MPI-RCA climate model. In [Lompi et al. \(2021\)](#), the greatest expected changes in flood quantiles were found in the 2011-2040 time window in the RCP 4.5, when the peak of emission occurs. In this study, 10 of the 12 climate models also show greatest delta changes of maxima water levels in such a scenario, pointing to a relationship between the future hydraulic dam safety and the greenhouse gas emission peak. Nevertheless, this signal disappears when the delta changes in maxima reservoir water levels in this scenario are considered with the ensemble of all the climate models (Figure 5.11). Nonetheless, despite the median values of the overtopping probability will not increase in the RCP 4.5, the upper quartile of the boxplot is greater in the 2011-2040 time window (Figure 5.14). Figure 5.10 shows that the greatest expected changes in maxima reservoir water levels are expected in the 2041-2070 time window. Nevertheless, this result represents just an anomaly and an outlier both in the ensemble of the delta changes (Figure 5.11). Also in this case, if the ensemble of all the climate models is considered, the greatest expected changes in the maximum reservoir water level are expected to be when the peak of emission is present, i.e. the end of the century in the RCP 8.5.

Despite the increase in the maximum reservoir water level being quite negligible, the expected changes in maximum outflow discharge due to climate change can have a key role for the hydraulic risk of the downstream population. Indeed, maxima outflow discharges associated with the most extreme events will increase in the future in the RCP 8.5.

Table 5.4 shows how several climate models lead to an overtopping probability greater than 10^{-4} . Also, in this case overtopping is more likely to occur in the RCP 8.5 in the 2071-2100 time window, where nine climate models show a probability greater than zero. This is evident by looking at the median values of the boxplot that ensemble the overtopping probabilities in Figure 5.14. Only the

RCP 8.5 have non-zero median values, with a median overtopping probability of 0.0025 (RP=4000 years) in the 2071-2100 time window. Despite it is another case study, the results do not agree with [Fluixa-Sanmartin et al. \(2019\)](#) that found no clear signal for this scenario, while a higher probability of damages was found in the RCP 4.5.

5.6 Conclusions

A methodology to assess the impact of climate change on hydrological dam safety has been proposed. The methodology considers climate change impacts on reservoir water level and inflow hydrograph frequency. The results of this work show how climate change will impact hydrological dam safety, especially the hydraulic risk of the downstream population. Indeed, the greatest expected changes in maxima water levels will be in the higher greenhouse gas emissions scenario at the end of the century. At the same time, the results show how cutting the emissions around 2040, as in the RCP 4.5, could guarantee a greater hydrological dam safety. Moreover, lower outflow discharges are expected in this RCP 4.5, highlighting how fewer greenhouse gas emissions could ensure a lower hydraulic risk for the downstream population. These results cannot be representative for other dams, but the methodology proposed could fulfil the requirements of recent regulations that recommend the climate projection to be included in the hydrological dam risk assessment.

Chapter 6

Uncertainty chain assessment for the future hydrological dam safety

6.1 Introduction

Where the propagation of uncertainty is a concern, [Katz \(1999\)](#) recommends ‘disintegrating’ uncertainty analysis and separately assessing each of the elements within an integrated framework. In this study, the uncertainty chain is evaluated by analysing each source of errors separately. Then the errors are combined to see how they interact and propagate in the methodology.

According to [Morales-Torres et al. 2016](#), climate-related uncertainties have the greatest impact on risk analysis models for dam management. Indeed, high return periods are usually involved in dam risk analysis, but the time series length of observed data is not adequate for their characterization. For this reason, there are several studies that proposed to incorporate climate uncertainty in dam management both in future ([Fluixá-Sanmartín et al., 2021](#)) and current scenario ([Tarouilly et al., 2021](#)). Moreover, epistemic uncertainty affects hydrological dam safety analysis, as the models involved in the analysis have not a complete knowledge of the system. Hence, Monte-Carlo simulations can be used to reduce the uncertainty associated to the estimation of peak flows and initial water surface levels in overtopping risk assessment ([Goodarzy et al., 2014](#)).

There are three main sources of uncertainty in the methodology proposed to evaluate future hydrological dam safety (Chapter 5). These sources of uncertainty compose the uncertainty chain shown in Figure 6.1. Uncertainty affects the estimation of the inflow hydrographs in the reservoir and the probability of reservoir water levels in current and future scenarios. The two sources of uncertainty that characterise the estimation of the future flood quantiles in the reservoir are the rainfall delta changes estimation with a given return period (red in Figure 6.1) and the errors of the RIBS model in assessing peak discharges in the reservoir (blue in Figure 6.1). On the other side, the uncertainty in the initial water level estimation is due to the HBV model error (green in Figure 6.1).

This chapter is divided as follows: methodology (Section 6.2), which explains how uncertainty is assessed; results (Section 6.3) and discussion and conclusions (Section 6.4). In this chapter, the case study section is not present as it is the same already shown in Chapter 5, i.e. the Eugui Dam.

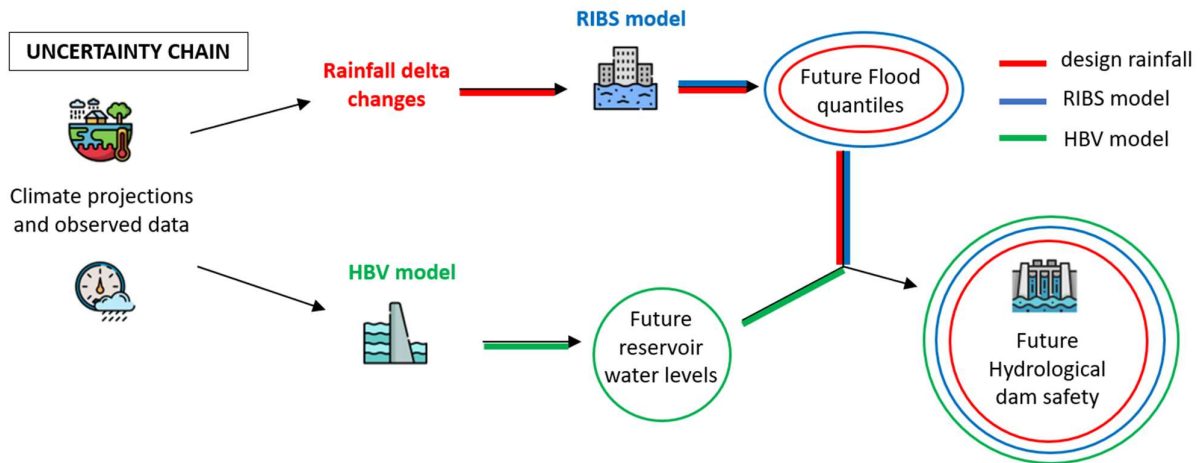


Figure 6.1: Uncertainty chain in the evaluation of hydrological dam safety. Three sources of errors are assessed: design rainfall uncertainty is red, the uncertainty of the hydrological models is blue for RIBS and green for HBV.

6.2 Methodology

The methodology to assess the three sources of uncertainty is described in this section. Particularly, the uncertainty on rainfall delta changes is in section 6.2.1, the uncertainty due to the RIBS model errors is in section 6.2.2 and the uncertainty associated with the HBV model is in section 6.2.3. All the sources of uncertainty are combined in the Uncertainty chain (Section 6.2.4) to obtain new corrected results (Section 6.2.5).

6.2.1 Uncertainty on rainfall delta changes

The uncertainty related to the estimation of design rainfalls with a short rainfall data time series is assessed by generating 10,000 sets of N_{obs} annual maxima, where N_{obs} is the number of years considered in the estimation of the design rainfall in each time window. The 10,000 sets of annual maxima are generated using a uniform distribution to generate the probabilities and a GEV to fit those probabilities to obtain design rainfalls. Each value determines a delta change of rainfall by comparing the precipitation in each time window and the control period. Therefore, 10,000 values of delta changes of rainfall are generated for each scenario (climate model, RCP and time window). Ten thousand mean values of precipitation in the Eugui Dam catchment are calculated by analysing together the spatial distribution of the delta changes and the spatial distribution of the rain gauges used to determine the design rainfall in the current scenario, replicating the methodology of [Lompi et al. 2021](#) (Figure 4.1 in Chapter 4). Figure 6.2 shows the boxplots of the mean precipitation in each scenario and return periods for the MPI-RCA climate model, displaying the uncertainty that affects the estimation of rainfall delta changes.

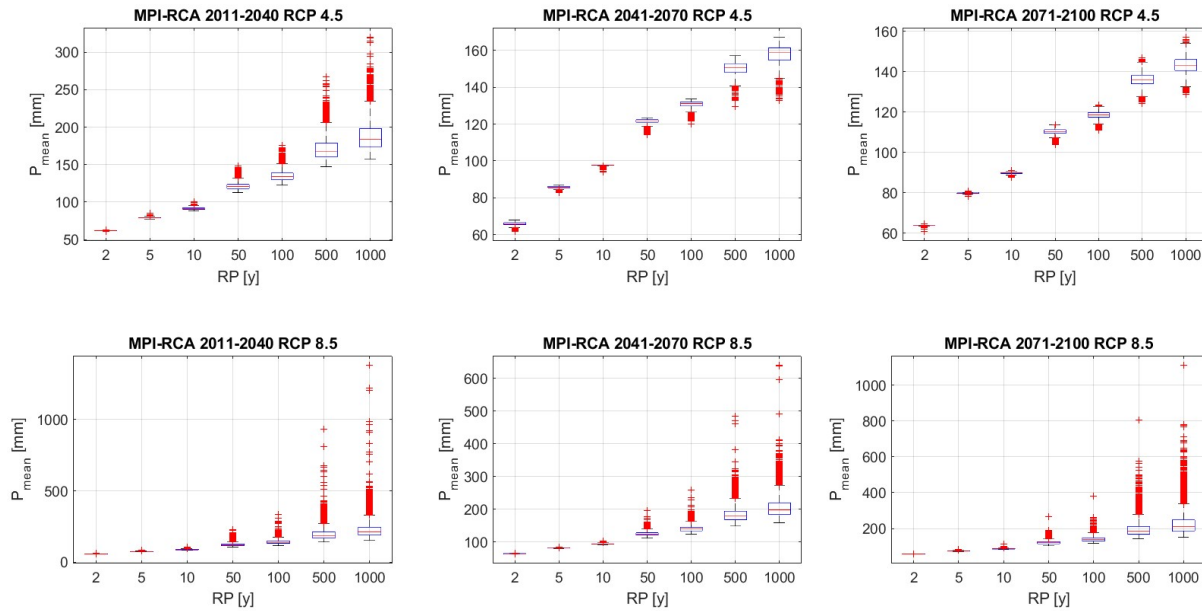


Figure 6.2: Uncertainty in the estimation of the delta changes of rainfall for the MPI-RCA climate model in all the scenarios for the seven return periods: columns represent time windows (2011-2040, 2041-2070, 2071-2100), rows represent emission scenarios (RCP 4.5 and RCP 8.5).

6.2.2 Uncertainty due to the RIBS model errors

After the determination of the mean precipitation in the river basin, a neural network is trained to reproduce the performance of the RIBS model. In [Lompi et al. \(2021\)](#), 504 simulations have been done with RIBS combining seven return periods, 12 climate models, two RCPs and three time windows. The artificial intelligence is trained with these 504 couples of mean precipitation P_{mean} and hydrograph peak Q_{max} . A neural network is needed to reduce the computational cost of the distributed hydrological model. Indeed, 5,040,000 simulations must be considered with 10,000 simulations for each scenario, which are impossible to do with the RIBS model computational costs.

The RIBS model uncertainty in the estimation of the peak discharges is considered with a parameter K_{RIBS} . K_{RIBS} represents the ratio between the observed, $Q_{\text{peak,obs}}$, and the modelled, $Q_{\text{peak,RIBS}}$, peak discharges. The observed peaks refer to the real event considered in the calibration of the model. (Figure 4.3 and Table 4.3 in Chapter 4).

$$K_{\text{RIBS}} = \frac{Q_{\text{peak,obs}}}{Q_{\text{peak,RIBS}}} \quad (6.2)$$

K_{RIBS} is used to multiply the modelled peak discharge to obtain an estimation closer to the observations. Figure 6.3 shows on the left the comparison between modelled and observed peak discharges in the Eugui Dam for the seven events used in the calibration and validation of the model; on the right the boxplot of K_{RIBS} , calculate using Eq. 6.2.

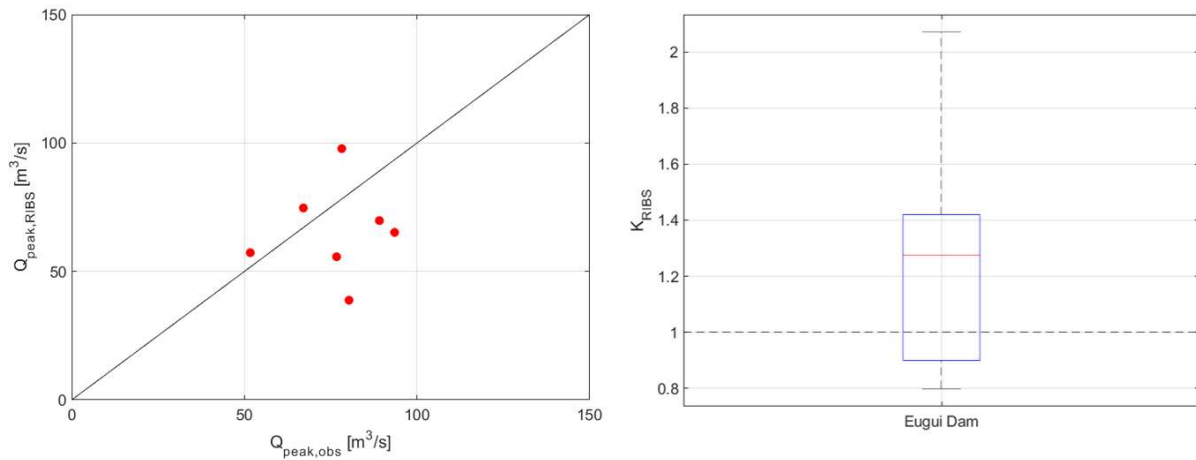


Figure 6.3. Evaluation of RIBS model uncertainty using K_{RIBS} : a) comparison between the modelled and observed peak discharges at the Eugui dam for the seven events used in the calibration and validation of the RIBS model; b) boxplot of K_{RIBS} .

A normal probability distribution is fitted on the K_{RIBS} values, to generate random K_{RIBS} values for each peak flow, aiming to consider the uncertainty of the RIBS model. Therefore, 10,000 random RIBS errors are generated, one for each Q_{max} estimated with the neural network. The normal distribution has been chosen comparing several fitting models (Normal, Log-normal, Logistic, Log-Logistic, GEV) with the cumulative frequency of the observed errors.

6.2.3 Uncertainty associated with the HBV model

The water level frequency curve uncertainty depends on the HBV model errors. HBV model is corrected as the RIBS model, i.e. calculating a K_{HBV} as the ratio between the daily modelled and observed discharge obtained after the calibration of HBV.

$$K_{HBV} = \frac{Q_{in,D,obs}}{Q_{in,D,HBV}} \quad (6.3)$$

The red dots in Figure 6.4 represent K_{HBV} obtained comparing the daily observed and modelled time series. K_{HBV} varies as a function of the simulated daily discharge $Q_{in,D,HBV}$ and the values can be read on the left axis.

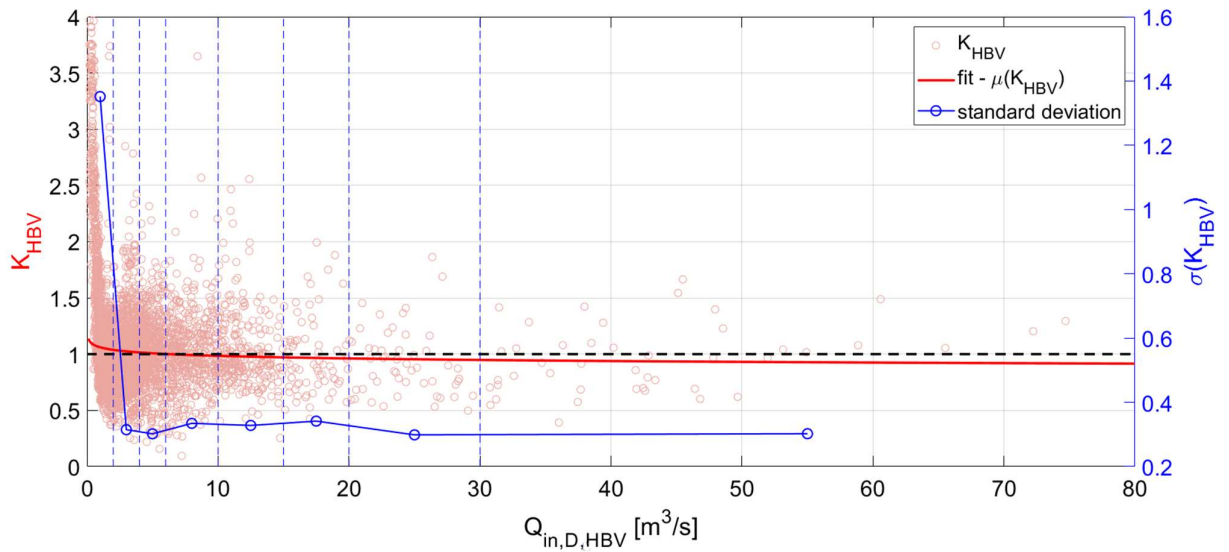


Figure 6.4. HBV model error dependency with the simulated daily discharge: the purple circles represent the HBV model errors evaluated after its calibration on each day of the time series in the current scenario (2008-2021); the red line is used to fit the observed errors. The standard deviation of K_{HBV} is evaluated within different bins (vertical dotted blue lines) and can be read in the right axis.

The error of the HBV model has greater values when the simulated daily discharge goes to zero. Indeed, even if the mean absolute error in these cases is very small, the ratio between a small number and another one very close to zero can be high, as shown in Figure 6.4. Therefore, a curve fits the K_{HBV} values to find the mean K_{HBV} for each different simulated discharge value $Q_{in,D,HBV}$ (red line in Figure 6.4). Moreover, the variance of K_{HBV} also changes with respect to $Q_{in,D,HBV}$, as can be seen in the right axis of Figure 6.4. In each day of simulation, a K_{HBV} is generated by a normal distribution to correct the $Q_{in,D,HBV}$ as in Eq 6.4.

$$K_{HBV} \sim N(\mu(K_{HBV}), \overline{\sigma^2(K_{HBV})}) \quad (6.4)$$

The mean of the normal distribution is evaluated with the fitting curve of Figure 6.4, whereas the variance of K_{HBV} is obtained with a mean standard deviation. The mean standard deviation is obtained after calculating its value in different bins, which are shown in Figure 6.4 with vertical dotted blue lines. The generated K_{HBV} multiply in each day $Q_{in,D,HBV}$, obtaining a corrected value $Q_{in,i}$, which is used in the reservoir model (Eq 5.4). The complete time series of inflow discharge is corrected 50 times with daily random K_{HBV} values, as 10,000 simulations with the reservoir operation model for

each scenario are unaffordable due to their computational cost. A sensitivity analysis concluded that 50 simulations were enough, as the difference between the mean water level frequency curve obtained with 50 and 10,000 simulations was negligible. The reservoir water level frequency curve considered for estimating initial reservoir water levels is obtained as the mean value of the 50 water reservoir level frequency curves, as it is shown for example for the control period of the MOH-RCA climate model in Figure 6.5. All the inflow hydrographs are associated to the mean water level frequency curve in the stochastic procedure (Section 5.2.4).

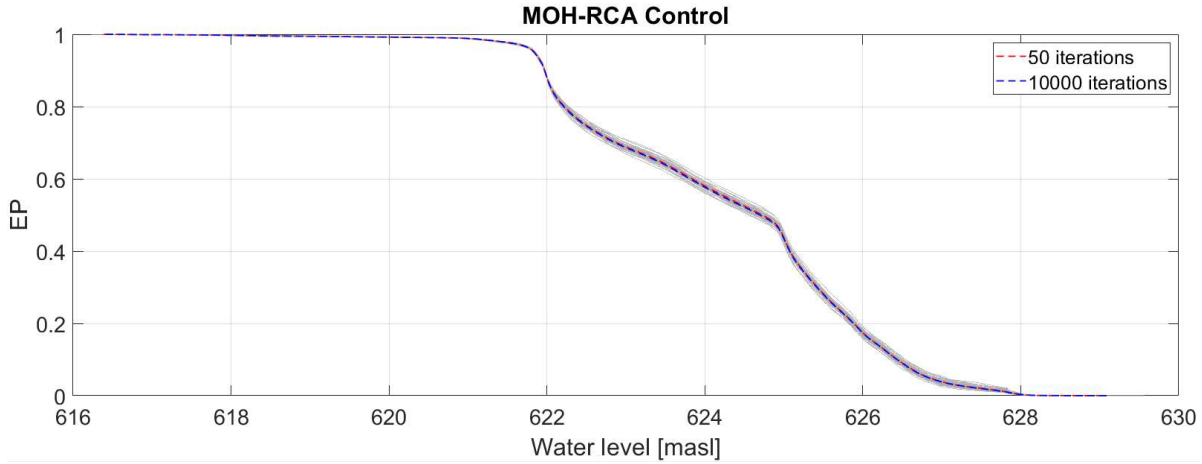


Figure 6.5. Uncertainty assessment of reservoir water level frequency using the mean water level frequency curve. The mean water level frequency curve of the MOH-RCA control period is shown as an example. The results of the sensitivity analysis show how the mean reservoir water level obtained with 50 iterations (dashed red line) is close to the one obtained with the 10,000 iterations (dashed blue line).

6.2.4 Uncertainty chain

Seven percentiles are extracted by the 10,000 values of peak discharge after the correction of the RIBS uncertainty: 5%, 10%, 32%, 50%, 68%, 90%, 95%. A GEV distribution is fitted to the peak flow quantiles obtained for each percentile (Figure 6.7). Therefore, the GEVs are obtained for each of the 12 climate models, each time window (2011-2040, 2041-2070, 2071-2100), emission scenario (RCP 4.5, RCP 8.5) and percentiles (5%, 10%, 32%, 50%, 68%, 90% and 95%) also to consider the uncertainty of the methodology.

For each GEV, 10,000 random NEPs values or RPs are generated as described in Section 5.2.4. All the generated inflow hydrographs are associated with the corrected initial water level frequency (previous section). Since each scenario has 10,000 values, the minimum overtopping probability that can be detected is 10^{-4} . If overtopping does not occur in a given scenario with the 10,000 generated RPs, the probability of overtopping is equal to zero in that scenario. Indeed, the number of synthetic events considered depends on the combination of 12 climate models, seven scenarios (two emission scenarios in three time windows plus the control period) and seven percentiles corresponding to seven GEVs. Combining all these scenarios, 5,880,000 flood routing processes are required with the VEM in the reservoir. This computational cost clarifies why it is impossible to deeply involve higher Return Periods, such as those analysed in [Fluixa-Santmartin et al. \(2019\)](#), even if those scenarios are even more uncertain.

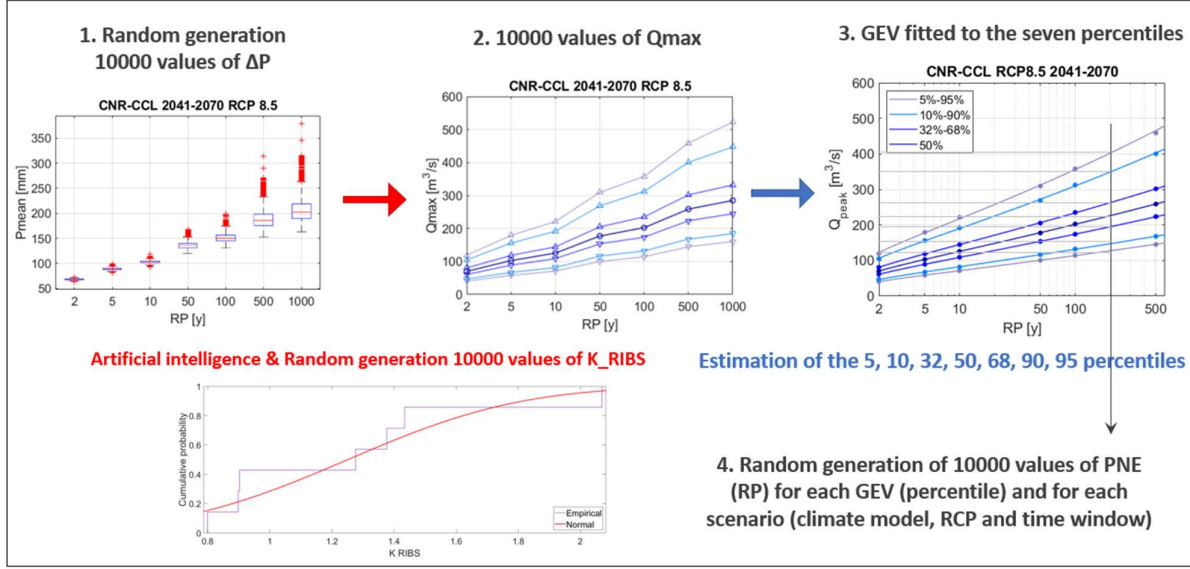


Figure 6.7. Stochastic procedure to incorporate uncertainty in the estimation of the inflow hydrographs.

6.2.5 Delta changes with uncertainty

The delta changes of maximum water level, ΔWL , and maximum outflow discharge, ΔQ , are expressed in this case just with the median values after the incorporation of the uncertainty, i.e. the 50th percentile:

$$\Delta WL(RP_i, 50^{th}) = WL_{max,fut}(RP_i, 50^{th}) - WL_{max,cur}(RP_i, 50^{th}) \quad (6.5)$$

where $WL_{fut}(RP_i, 50^{th})$ is the maximum reservoir water level expected in the future associated with a given return period RP_i for the 50th percentile after the uncertainty incorporation, and $WL_{cur}(RP_i)$ is the maximum reservoir water level in the current scenario for return period RP_i and 50th percentile. The delta changes of maximum outflow discharge, ΔQ , are expressed as:

$$rQ_{out}(RP_i, 50^{th}) = \frac{Q_{out,max,fut}(RP_i, 50^{th})}{Q_{out,max,cur}(RP_i, 50^{th})} \quad (6.6)$$

where $Q_{out,max,fut}(RP_i, 50^{th})$ is the maximum outflow discharge expected in the future associated with a given return period RP_i for the 50th percentile after the uncertainty incorporation, and $Q_{out,max,cur}(RP_i, 50^{th})$ is the maximum outflow discharge for the same return period and percentile of the current scenario.

6.3 Results

This section has a structure similar to the result section of the previous chapter, even if the results are obtained after the incorporation of uncertainty. First, results on changes in maxima reservoir water levels are considered (Section 6.3.1); second, results on changes in maxima outflow discharges are shown (Section 6.3.2); finally, the results of overtopping probability are presented (Section 6.3.3).

6.3.1 Changes in maxima reservoir water levels after the incorporation of uncertainty

Figure 6.7 shows the results of the IPS-WRF climate model, also shown in the previous Chapter in Figure 5.9, after the consideration of the uncertainty chain. The figure represents the maximum reservoir water level frequency curve for the seven considered percentiles. Moreover, the results obtained without accounting for the uncertainty in the previous Chapter (Figure 5.9) are also shown here in each subplot with red dots. The first row shows the results for the three time window in the RCP 4.5, while the second one shows the results of the RCP 8.5.

Figure 6.7 highlights the importance of considering uncertainty in the methodology. In some cases, the uncertainty assessment supplies a confidence interval to the results obtained without uncertainty. In these cases, the red dots overlap the curve for the 50th percentile, such as in the 2041-2070 time window for the RCP 8.5. In other cases, the results without considering the uncertainty (red dots) are below the median values obtained considering uncertainty, usually underestimating the maxima reservoir water levels. For example, the results obtained without the uncertainty assessment do not point to an increase in the hydrological dam risk for the time window 2071-2100 in the RCP 8.5. However, an increase of almost one meter is expected when the uncertainty is considered in the same scenario.

Nevertheless, a complete overview of the results can be obtained by looking at the ensemble of all the climate models. After the uncertainty chain assessment, delta changes are evaluated with the difference between the median reservoir maxima water levels (50th percentile) in the future and the median value of the control period (Section 6.2.5). Delta changes of maxima reservoir water levels for each RP and scenario are obtained with the ensemble of the 12 climate models and shown with boxplots in Figure 6.8. The expected maxima reservoir water levels in the future can be obtained by applying the delta changes (Figure 6.8b) to the maximum reservoir water level frequency curve in the current scenario (Figure 6.8a). Figure 6.8a shows that no overtopping risk is expected for events with a RP below 1000 years in the current scenario. Delta changes point to no expected changes in maxima reservoir water levels for RPs between five and 500 years in the three time windows and two emission scenarios with high confidence. This is because the spillway gate operation can maintain the maximum water level at 628 m a.s.l. for the magnitude of such events. Nevertheless, despite dam operations can maintain the maximum water level at 628 m a.s.l., outflow discharges will increase to maintain such a level in those RPs, as shown with the boxplots of delta changes of maximum outflow discharge in the next section. A higher variability is found in the results associated with the RP of two, 500 and 1000 years. In the first case, the variability is generated by many cases in which maxima reservoir water levels are below 628 m a.s.l., which is the water level when the spillway gates begin to operate. For extreme events with return periods of 500 and 1000 years, the variability is driven by water levels above 628 m a.s.l., as dam operations are not able to maintain such a water level because the spillway has not enough capacity to release the required outflow discharges for avoiding increasing water levels.

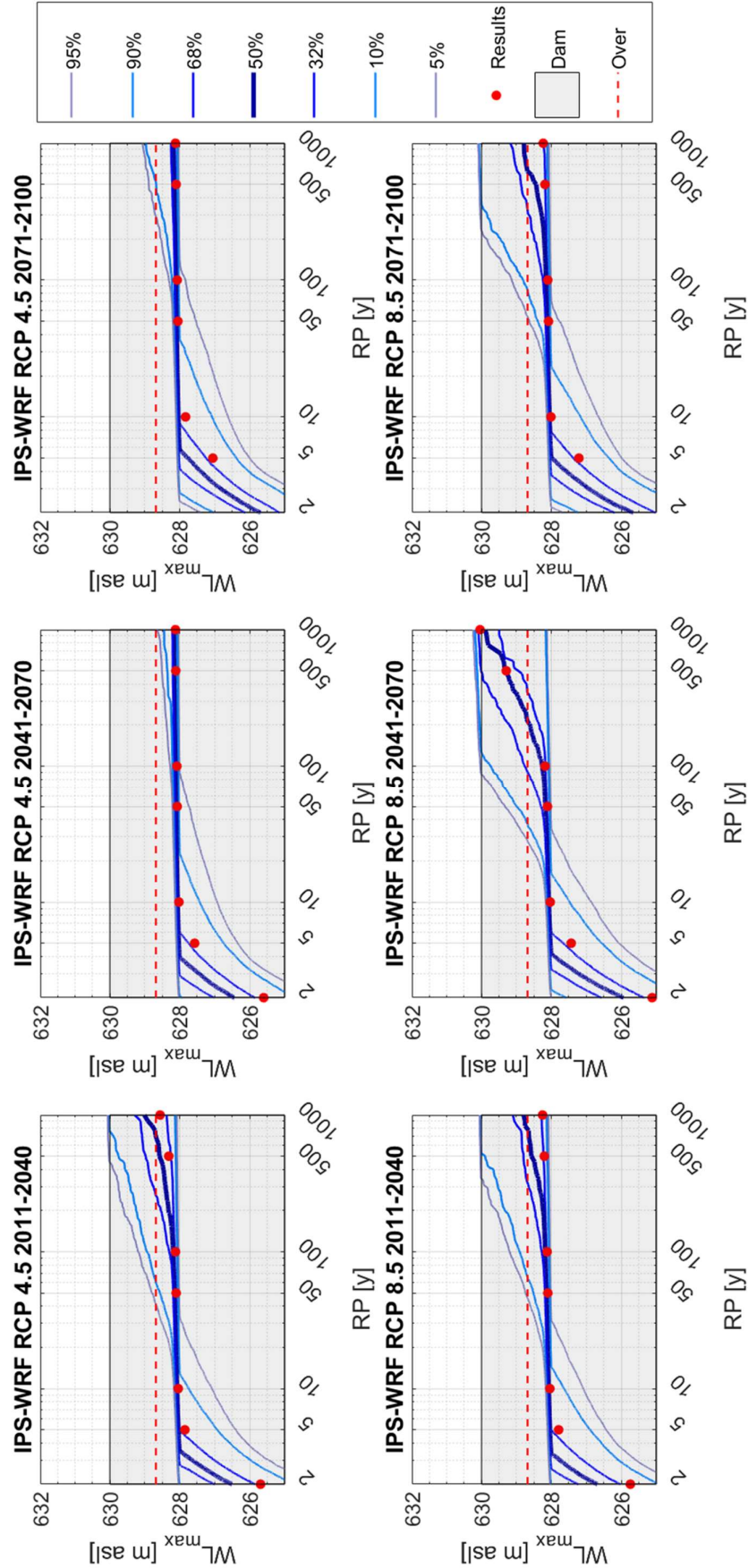


Figure 6.7. Expected maxima reservoir water levels in the future for the IPS-WRF climate model considering uncertainty. The first row includes the results for RCP 4.5 and the second row includes the results for RCP 8.5. Columns present results by time windows in the future. The thickest blue line represents the median values. Thinner light blue lines represent the rest of percentiles. Red points represent the results without considering uncertainty for the seven return periods. The grey filled box represents the dam with its crest elevation at 630 m a.s.l. The horizontal dashed red line represents the overtopping threshold.

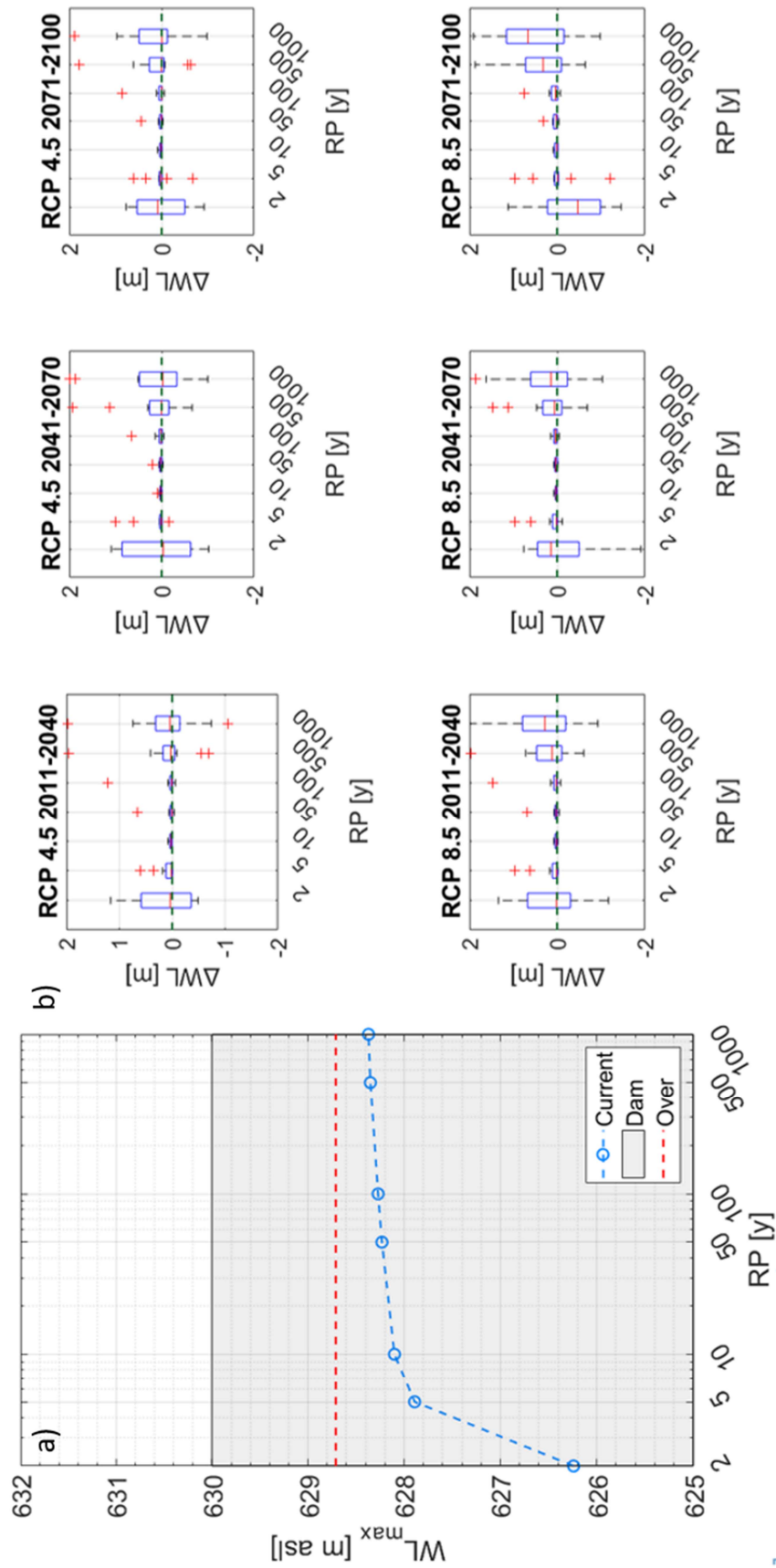


Figure 6.8. a) Maximum reservoir water level frequency curve in the current scenario; b) delta changes in maxima reservoir water levels for the ensemble of 12 climate models considering uncertainty.

6.3.2 Changes in maxima outflow discharges after the incorporation of uncertainty

Figure 6.9 shows the results of the maximum outflow discharge frequency curve also accounting for uncertainty for the MPI-RCA climate model in all the time windows and RCPs. The maximum outflow discharge frequency curve is shown in the subplots for the seven considered percentiles. Moreover, the results obtained without accounting for uncertainty already shown in the previous Chapter (Figure 5.11) are also presented here in each subplot with red dots. As in Figure 6.7, the first row shows the results for the three time window in the RCP 4.5, while the second one shows the results of the RCP 8.5.

The importance of considering uncertainty in the methodology emerges also analysing Figure 6.9, as the results without its consideration underestimate the maxima outflow discharges. Indeed, the red dots are usually closer to the 32th percentile rather than the median value.

The right part of Figure 6.10 shows the boxplots of delta changes of maxima outflow discharges obtained with the ensemble of the climate models and the median values after the uncertainty chain assessment. In this case, the delta changes rQ_{out} must be considered as values that must multiply the maximum outflow discharge of the current scenario shown in the left part of Figure 6.10.

Figure 6.10 shows how the delta changes of maxima outflow discharges increase for all the return periods and time windows in RCP 8.5, except for the 5-year flood at the end of the century. Another important result is represented by the delta changes of maxima outflow discharge in the RCP 4.5. Indeed, they are on average close to one, pointing to non-change in the hydrological dam safety in this scenario. On the contrary, delta changes of maxima outflow discharges without the consideration of uncertainty are always lower than zero in this scenario (Figure 5.12). Therefore, if uncertainty is considered, delta changes of maximum outflow discharge are greater in all the scenarios and time windows.

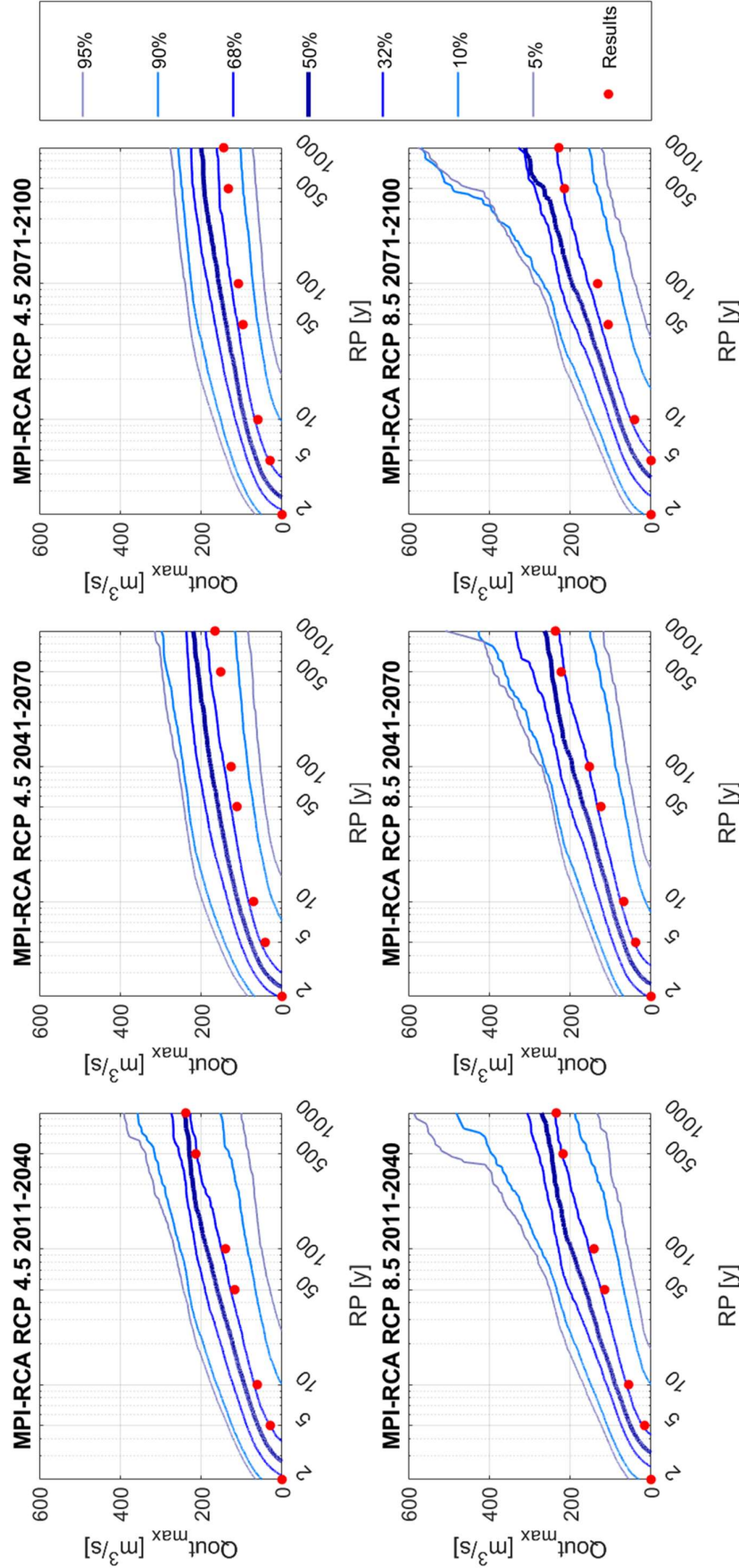


Figure 6.9. Expected maxima outflow discharge in the future for the MPI-RCA climate model considering uncertainty. The first row includes the results for RCP 4.5 and the second row includes the results for RCP 8.5. Columns present results by time windows in the future. The thickest blue line represents the median values. Thinner light blue lines represent the rest of percentiles. Red points represent the results without considering uncertainty for the seven return periods

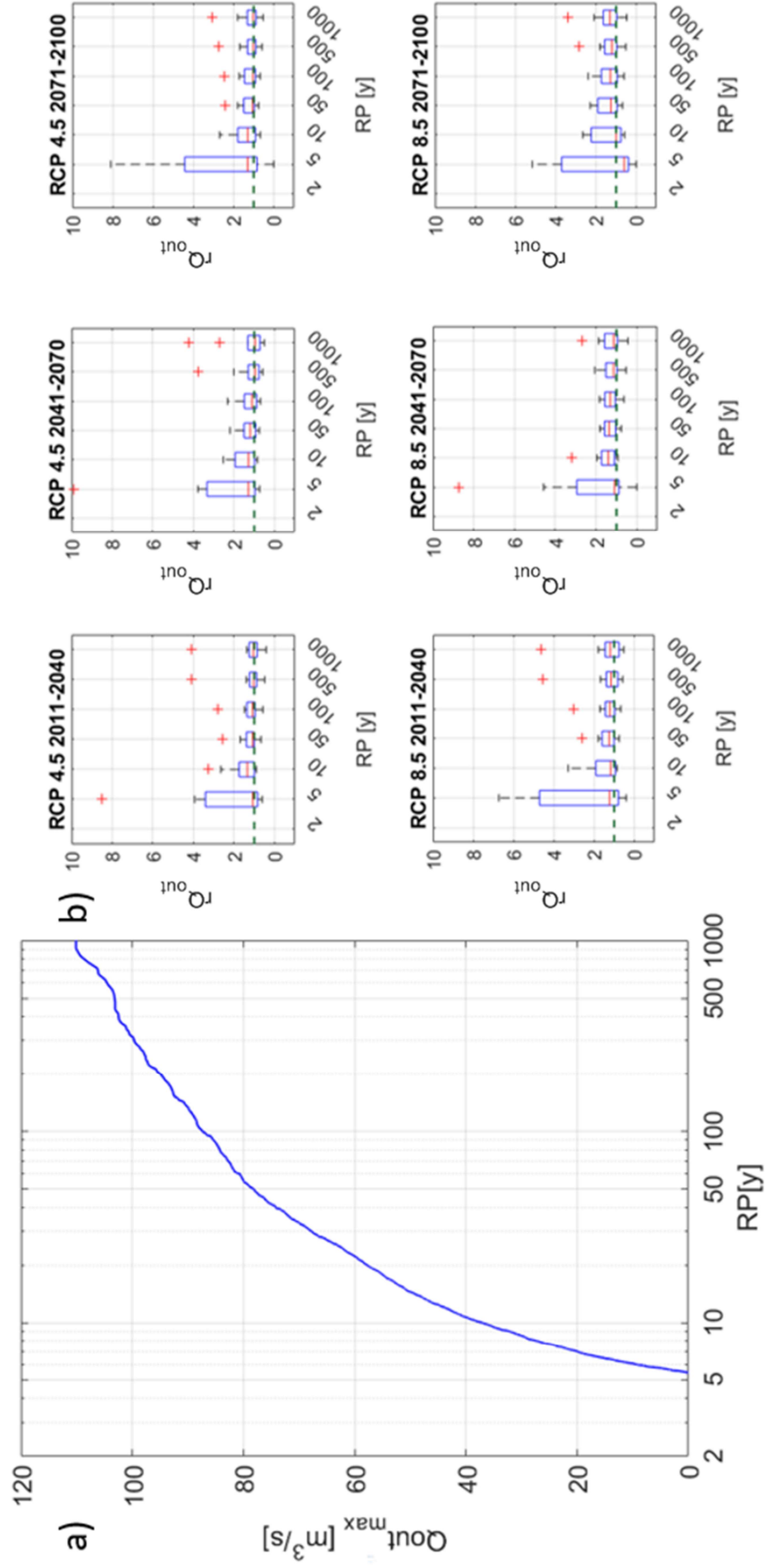


Figure 6.10. a) Maximum outflow discharge frequency curve in the current scenario; b) delta changes in maxima outflow discharges for the ensemble of 12 climate models considering uncertainty.

6.3.3 Overtopping probability after the incorporation of uncertainty

The information on the Overtopping Probability is shown in Table 6.1, where the probabilities for all the climate models, scenarios and time windows are associated with the 50th percentiles after the uncertainty incorporation. All the null probabilities in Table 6.1 correspond to a probability lower than 10^{-4} .

Table 6.1. Overtopping probability associated with the 50th percentile after the incorporation of uncertainty for all the climate models in the different scenarios. The null probability (zeros in the Table) corresponds to a probability lower than 10^{-4} .

climate model	RCP 4.5			RCP 8.5		
	2011-2040	2041-2070	2071-2100	2011-2040	2041-2070	2071-2100
ICH-CCL	0	0	0	0	0	0.0023
MPI-CCL	0.0208	0.0105	0.0157	0.0214	0.0016	0.0121
MOH-RAC	0	0	0	0	0	0
CNR-CCL	0	0.0037	0.0021	0.0018	0.0006	0.0026
ICH-RAC	0	0.0009	0.0016	0.0001	0	0.0005
MOH-CCL	0	0	0.0002	0.0033	0	0.0028
IPS-WRF	0.0012	0	0	0.0012	0.0042	0.0014
IPS-RCA	0.0007	0.0003	0	0.0011	0.004	0.0004
MOH-RCA	0	0	0	0	0	0
ICH-RCA	0	0.0003	0.0001	0.0003	0.0004	0.0023
CNR-RCA	0.0009	0	0.0007	0	0.0002	0
MPI-RCA	0.0002	0	0	0.0006	0.0006	0.0018

The Overtopping Probabilities of each climate model are ensembled together and shown with boxplots in Figure 6.11, on the left for the RCP 4.5 and the right for the RCP 8.5. The median values of the boxplot are greater than zeros in all three time windows in the RCP 8.5, highlighting an increase in the overtopping probability with respect to the current period. Moreover, the results show how accounting uncertainty also overtopping probability changes. Indeed, when uncertainty is not considered, the exceedance probability of dam overtopping is greater than zero only at the end of the century (Figure 5.13 in the previous chapter).

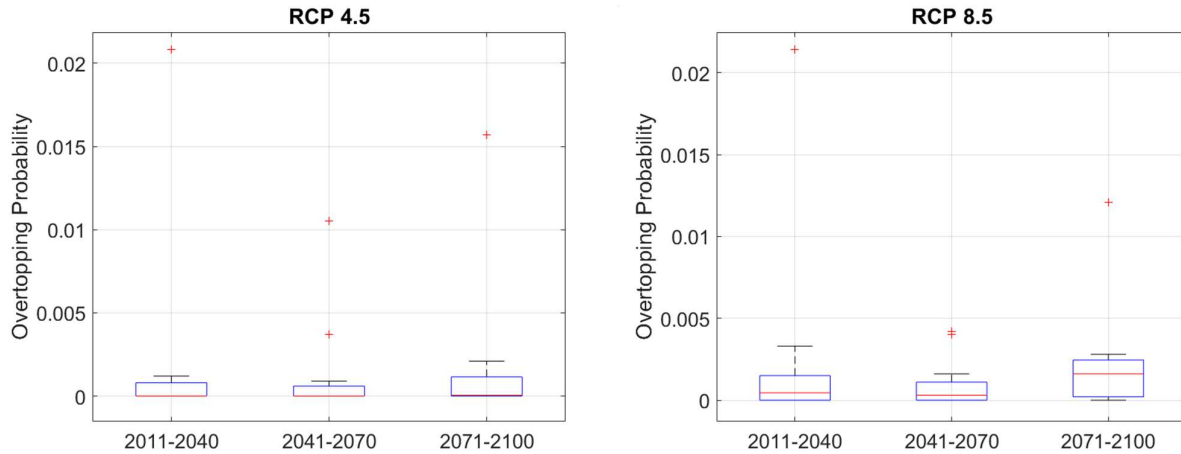


Figure 6.11. Overtopping Probability with the ensemble of all the climate models accounting uncertainty for the two Representative Concentration Pathways and the three time windows.

Table 6.2 shows the difference between the overtopping probability associated with the 50th percentile after the incorporation of uncertainty (Table 6.1) and the overtopping probability evaluated without uncertainty (Table 5.3) for all the climate models and scenarios. A positive value of this difference means that the overtopping probability is underestimated in a given scenario if uncertainty is not considered.

Table 6.2. Difference between the overtopping probability associated with the 50th percentile after the incorporation of uncertainty and the overtopping probability evaluated without uncertainty for all the climate models and scenarios.

climate model	RCP 4.5			RCP 8.5		
	2011-2040	2041-2070	2071-2100	2011-2040	2041-2070	2071-2100
ICH-CCL	0	0	0	0	0	0.0014
MPI-CCL	0.008	0.0024	0.0112	0.0084	0.0015	0.0066
MOH-RAC	0	0	0	0	0	0
CNR-CCL	0	0.0017	0.001	0.0009	0.0004	0.0021
ICH-RAC	0	0.0008	0.0016	0.0001	0	0.0004
MOH-CCL	0	0	0.0001	0.0015	0	0.0011
IPS-WRF	0.0004	0	0	0.0008	0.0004	0.0011
IPS-RCA	0.0006	0.0002	0	0.0006	-0.0003	0.0004
MOH-RCA	0	0	0	0	0	0
ICH-RCA	0	0.0001	0.0001	0.0003	0.0004	0.0021
CNR-RCA	0.0002	0	0.0005	0	0.0002	-0.0002
MPI-RCA	0	0	0	0.0006	0.0006	0.0013

6.4 Discussion

The accounting of uncertainty has a key role in hydrological dam safety assessment, as the results without its consideration are underestimated. Indeed, greater expected changes in maxima reservoir water levels, maxima outflow discharges and exceedance probability of dam overtopping are found after considering uncertainty. This could mainly be related to the RIBS model uncertainty due to its underestimation of the peaks at the Eugui Dam. Indeed, the correction with K_{RIBS} more likely tends to increase the results without the uncertainty. At the same time, the estimation of the delta changes in rainfall quantiles could have a crucial role in the underestimation of the highest return periods since the uncertainty associated with the extreme design rainfalls is very high, as shown for the MPI-RCA in Figure 6.2. On the contrary, the uncertainty of reservoir water levels seems to affect less the results, as K_{HBV} tend to be closer one, showing the good calibration of the HBV model. The model more likely underestimates low-flow and this could be related with the runoff generation from the groundwater boxes SUZ and SLZ of the model (see section 3.3.2). Nevertheless, the errors on low flow are negligible for the definition of the reservoir water levels, as they are connected with low reservoir volume variations. Moreover, the uncertainty chain assessment anyway considers this kind of errors.

Figure 6.7 and Figure 6.9 show how the red dots are more likely to be under the median values after the incorporation of the uncertainty, i.e. how an underestimation of the maxima reservoir water levels and maxima outflow discharges is detected if uncertainty is not included in the results. Moreover, Figure 6.10 shows how the maxima outflow discharges will increase almost 50% for the RPs between 10 and 100 years in the time window 2041-2070 in the RCP 8.5 and 30% for the RPs between 50 and 1000 years in the time window 2071-2100 in the same RCP. Therefore, the hydraulic risk of the downstream population is expected to increase in the future, especially in the RCP 8.5. Even if the variability of the delta changes associated with the most extreme event is evident for both the emission scenarios, the median values of the boxplots show an increase in the maxima water levels only in the RCP 8.5, especially in the 2071-2100 time window with an increase of 0.67 m for the 1000 year flood (this increase causes overtopping if summed to the maximum water level of the current scenario).

Table 6.1 show how many climate models have overtopping with a probability greater than 10^{-4} . Also, in this case overtopping is more likely to occur in the RCP 8.5 in the 2071-2100 time window, where 9 climate models show a probability greater than zero. This is evident by looking at the median values of the boxplot that ensemble the overtopping probabilities in Figure 6.11. Only the RCP 8.5 have non-zero median values, especially in the time window 2071-2100 when the overtopping probability is 0.0016 (RP=625 years). The overtopping probability in the same scenario has a RP of 4000 years if uncertainty is not considered. Table 6.2 shows again how the uncertainty evaluation tends to increase the probability of overtopping if compared with the results obtained without the uncertainty chain assessment. Indeed, just two scenarios have a slight decrease of the overtopping probability after the consideration of uncertainty.

6.5 Conclusions

All the sources of uncertainty in the methodology were assessed and incorporated to obtain sounder results that can increase the reliability of the conclusions. The proposed stochastic procedure can incorporate the main sources of uncertainty in the future dam risk analysis, and it could be done by some other decision-makers also using different hydrological models. This study shows that accounting for all the sources of uncertainty in a hydrological dam safety analysis is crucial. As a matter of fact, the hydrological dam safety assessment without the incorporation of uncertainty tends to underestimate the delta changes of maxima water levels and maxima outflow discharges.

Moreover, overtopping probabilities obtained with the ensemble of climate models are greater after the consideration of uncertainty. In other studies, uncertainty could have less importance if the hydrological models have a lower residual error after the calibration process or if the delta changes of precipitation have a lower variance for each return period. Nonetheless, uncertainty should always be accounted for when possible, to provide more reliable results.

Chapter 7

Improving flash floods risk assessment at the regional scale with the adaptation of the design floods

7.1 Introduction

This Chapter aims to define a simple methodology to identify river basins with design discharges that underestimate the flash flood risk (Lompi et al., 2022). This methodology was developed within an agreement with the District River Basin Authority of Northern Apennine, which managed the flood risk in the study area. Indeed, the area is really prone to convective storms due to its topographical characteristics: steep concave-shaped orography that reaches high elevations within a few kilometres from the coast (Miglietta & Davolio, 2022). Moreover, several flash floods with a limited area extent (even less than 100 km²) have occurred in the last few years in this area, causing damages and fatalities (Faccini et al. 2021).

The underestimation of flash flood risk can be relevant where design rainfall depths are affected by a greater uncertainty due to short time series length or in the ungauged river basins. Furthermore, an adaptation of the short-duration design floods is also needed to face the intensification of hourly precipitation, which can be expected in a warmer climate (Section 2.5). The methodologies proposed in the previous chapters, based on climate projections and uncertainty assessment, require huge computational costs if many river basins must be analysed. Moreover, flash floods usually occur in small and ungauged river basin, where the lack of measurement prevents any possible uncertainty assessment. Furthermore, climate projections of short-duration rainfall are not available everywhere. Therefore, this chapter proposes a simple methodology based on observed data and historical events only, which can be used at the regional scale. The methodology is purposefully for the decision makers that must assess flood risks in the river basin authorities and aims to improve flash flood risk analysis by adapting the design discharges commonly used in the small river basins.

Synthetic hyetographs are used to evaluate the short duration design floods performance. Particularly, the hyetographs extrapolated by observed events are used in a hydrological model to make a comparison with the design floods and, if needed, to adapt them (Section 3.1). Indeed, the comparison produces an index for the adaptation of the design event peak discharge. The hyetographs are extrapolated from observed events using the Areal Reduction Factors (ARF) and the Stochastic Storm Transposition (SST). ARF are used to scale the intensity of an event over different river basin sizes, while SST to move the scaled hyetographs to other locations.

Indeed, ARF is defined as the factor that gives the areal rainfall for a specified duration and return period if applied to point rainfall for the same duration and return period (NERC, 1975; De Michele et al., 2001). The ARF can be obtained in two different ways: a fixed-area approach, which focuses on the rain gauge sites within a “geographically fixed-area” like a watershed, and a storm-centred approach, in which the area considered is not fixed but varies depending on specific rainfall events (Kim et al., 2019). Many empirical and analytical methods have been developed for estimating ARFs (Pavlovic et al., 2016; Bacchi & Ranzi, 1996; Barbero et al., 2014). Sivapalan and Blöschl (1998) note that storm-centred ARFs are usually smaller than geographically fixed ARFs, probably due to convective events of a limited area. The storm-centred approach is used in this study. Therefore, the hyetograph recorded by the rain gauge with the maximum rainfall depth within an event (point rainfall) is scaled with the ARFs on different river basin sizes (areal rainfall).

Instead, SST is described in Wright et al. (2020) as the process that involves resampling and transposing (i.e., geographically moving in the zonal and meridional directions) storm events to generate hypothetical events from a collection of real events. The synthetic hyetographs obtained by the past events can only be tested on the river basins with a similar rainfall statistical distribution of the place where the events occurred. In this way, they are tested over catchments that can statistically have similar events, avoiding unrealistic comparisons with the design hydrographs. Fofoula-Georgiou (1989) defined the Storm Transposition Area (STA) as the area within which all the occurred storms can be transposed anywhere with the same occurrence probability but with an

adjustment to their depth. Indeed, in homogeneous regions storms are expected to have similarities in their internal structure despite their different durations and total rainfall depths (Koutsoyiannis & Foufoula-Georgiou, 1993).

Franchini et al. (1996) made a similar attempt by coupling the SST with rainfall-runoff modelling to estimate the exceedance probabilities of design floods. A similar attempt was carried out by Nnadi et al. (1999), where a comparison between design storms and occurred events was made to understand if a set of different hydrological models overestimated or underestimated the risk of short-duration storms. The proposed methodology is applied in Northern Tuscany (central Italy) to identify where the design discharges used in the region underestimate the flash flood risk. A recent review article shows how several studies on trend analysis of observed precipitation highlighted no evidence of changes in the precipitation intensity or extreme events frequency in this area (Caporali et al., 2021). Nevertheless, the signal of climate change on sub-daily rainfall may have been not detected yet for the shortness of the time series. The study aims to understand if the design events are precautionary also in depicting the flash flood risk and how, if needed, they could be adjusted. Indeed, the comparison between short-duration events and design floods is summarised by introducing a Flash Flood Design Adaptation index (FFDA), which represents a factor that can be used to correct the design event peak.

7.2 Methodology

The methodology is purposefully applied at the regional scale to improve the flash flood hazard assessment on a set of small river basins. The methodology, already described with a flow chart in Figure 3.2 (Chapter 3), is composed of five steps: selection of the most extreme short-duration events based on rainfall data (Section 7.2.1); spatial distribution of the selected events (Section 7.2.2) to calculate the ARFs (Section 7.2.3), hydrological modelling (Section 7.2.4) and comparison of the selected events with the design hydrographs in a set of small river basins (Section 7.2.5).

7.2.1 Selection of the most intense Short-Duration Events (SDEs)

The most intense events occurred over a large region are selected using rainfall data rather than discharge data because some isolated heavy rainfall may not cause extreme runoff to impact discharge measurement (Svensson and Jones, 2010). Furthermore, since flash flood events are usually consequential to extreme rainfall within a few hours, the selection is made to identify Short-Duration Events (SDEs) only. When flood events are selected from discharge time series, just a POT on some hydrometers data is necessary. On the contrary, when the events are selected using rainfall timeseries, some characteristic of the rainfall events must be considered in the selection (rainfall, intensity, duration). If SDEs are selected based on their duration, some of them may accidentally not be considered. Indeed, some of them can have a longer duration, even if all the rainfall occur in a very short duration. Moreover, all the events that have a huge intensity in a long duration are not considered in this study. For this reason, a SDE is defined in this study as an event with at least 80% of the total rainfall within 3 hours. Hence, a dataset with at least a 15-minute time step is required to analyse if an event fulfils the definition of SDE. The analysis is focused on rainfall data, regardless of whether the rainfalls generate a flash flood. Indeed, some SDEs can occur over large river basins without flood damages despite a great rainfall intensity or runoff. The SDEs have been selected by analysing maxima rainfall in the duration of three hours. Using a Peak Over Threshold (POT) on rainfall height to select the events can represent a problem if there is a huge variability in the intensity of the rainfall events in the analysed region. Indeed, the SDEs are found only in the rainiest part of the study area without normalisation of the maxima rainfall. For this reason, the events are selected looking at the

highest values of rainfall depths standardised with the design rainfall depth for a given return period, in this case 200 years (Eq. 7.1) as

$$h_n = h_{ev}/h_{200} \quad (7.1)$$

where h_n is the normalised rainfall depth, h_{ev} is the measured precipitation and h_{200} is the design rainfall depth at the rain gauge location. The normalisation must be done considering the same duration. Hence, h_{ev} is a SDE rainfall recorded by a rain gauge in a given duration, and h_{200} is the design rainfall depth in the same location and duration. The frequency of a given event can be estimated by selecting the event with the normalised rainfall depth. Indeed, h_n contextualises the SDE with where it occurs and compares its depth with the values commonly in the design phase in the same area. All the events found with the normalised rainfall depth that do not fulfil the SDE definition are not considered. Sometimes more than one rain gauge site recorded the same SDE and entered it in the classification more than once. In these cases, only the hyetograph of the rain gauge with the maximum value is taken for the scaling procedure. Hence, the obtained hyetographs associated with a given SDE have the same shape, but their intensity changes with the river basin area of the catchment on which the real event is modelled. Since the selected events must be applied only to sites with similar design rainfall depths, a set of SDEs must be found for each Storm Transposition Area (STA) to avoid meaningless comparison between occurred and design hydrograph. Moreover, the number of selected events for each STA is estimated with a Peak Over Threshold (POT) on the normalised rainfall depth h_n . The threshold is set equal to 0.9 to identify the most extreme SDEs occurred in the area.

7.2.2 Rainfall spatial distribution of the selected events assessment

After the identification of the most intense SDEs, the selected hyetographs have been scaled using a spatial analysis. All the rain gauges with a rainfall depth greater than 1 mm around the one with the maximum rainfall are considered for each event in the analysis. Spatial rainfall distributions are estimated with the Inverse Distance Weighting method (IDW) (Eq. 7.2 and 7.3) as

$$h(x) = \left\{ \frac{\sum_{i=1}^N w_i(x) h_i}{\sum_{i=1}^N w_i(x)}, d(x, x_i) \neq 0 \right. \quad h_i, d(x, x_i) = 0 \quad (7.2)$$

where

$$w_i(x) = \frac{1}{d(x, x_i)^p} \quad (7.3)$$

In the previous equations h is the total rainfall depth in a given location x , h_i is the total rainfall depth recorded at the gauging site x_i , w_i is the weight for the rainfall recorded at the gauging site i , N is the number of rain gauges that record the SDE, $d(x, x_i)$ is the Euclidean distance between a given point x and the rain gauging site i , and p is a power parameter that is set equal to two. Indeed, with a high parameter, the IDW tends to be a Thiessen Polygons spatial interpolation and rainfall doesn't decrease moving away from the rain gauges. Nevertheless, extreme SDEs can often be convective storms with a localised storm centre. Therefore, the selected parameter produces rainfall peaks localized around the rain gauges with rainfall intensity that sharply decrease moving away from them.

For the same reason, the number of rain gauges considered for each event can be very small. Hence this methodology better works if the spatial information density of the rain gauge network in the study

area is high, with indicatively at least a rain gauge every 100 km². Indeed, the spatial distribution of some localised SDE cannot be described with a lower information density. The Kriging method has not been used to interpolate observations because of the small number of semivariance values for the construction of the semivariogram. Sometimes, SDEs can cover a larger scale, though they often show a reduced area where the highest rainfall intensities are concentrated. Rainfall spatial distributions are gridded to simplify the procedure, as explained in the next section.

7.2.3 Areal Reduction Factors computing

ARFs are computed for each SDE with the spatial distribution obtained in the previous section to scale the rainfall event over different catchment areas. The punctual intensity recorded in the rain gauge with the maximum value is scaled with the ARF and distributed on a given area. A specific river basin is not considered, such as in the fixed-area approach. Indeed, the fixed area approach simply consists of evaluating the ARF in a “geographically” fixed area. On the contrary, in this study, the ARF of each SDE is evaluated on moving squared locations (as in Figure 7.1 and Figure 7.2) to identity the storm centre (the square with more precipitation for a given dimension). The ARF are calculated for different extensions centred on the storm. Therefore, ARF indicates how much the average rainfall depths change on different storm-centred surfaces, becoming smaller as the area increases. Indeed, there is a higher probability of finding greater precipitation values nearby the rain gauge with the maximum rainfall. At the same time, decreasing rainfall intensities are found with increasing distances to the storm centre.

Since the cells of the rainfall spatial distribution have the same area, there is a biunique correspondence between the river basin area in which ARF is evaluated and the number of cells that must be considered. For instance, with a rainfall raster resolution of 100 m and a river basin of 20 km², the ARF is calculated by finding the 2000 neighbouring cells with the greater values in the raster and calculating the average rainfall depth on those cells. Indeed, the identification of the storm centre within the raster is made by looking for the maximum average rainfall depth for a given area. As such, the storm centre of a SDE can change for different considered areas. In this study, the ARF is evaluated in groups of neighbouring cells with a squared shape. Hence, the rainfall depth is averaged over a box of $L \times L$ size centred around a given location (i, j) , as in [Venugopal et al. \(1999\)](#), where L is the number of cells in the box side. A fixed shape is useful to guarantee a unique ARF associated with a specific event and a generic extension. Therefore, the hyetograph of a given event is scaled with the same ARF for all the river basins with the same area.

The rainfall raster can be considered a square matrix, whereas the square aggregation of neighbouring cells are submatrices. Therefore, all the possible combinations of cell groups with a given dimension can be evaluated. If the entire raster is a square matrix $A(K \cdot K)$, the number of possible submatrices within the raster with L cells on their side is equal to n^2 , where n is:

$$n = K - L + 1 \quad (7.4)$$

Figure 7.1 shows an example of a square raster with 25 cells ($K = 5$), considering two hypothetical catchment areas. With L equal to three, there are nine possible submatrices with an area of nine cells. With L equal to four, there are four submatrices with an area of 16 cells.

The average rainfall depth is calculated for each submatrix, obtaining the ARF by using Eq. 7.5:

$$ARF = H_a / H_{max} \quad (7.5)$$

where H_a is the greatest average rainfall depth within the set of all n^2 possible sub-matrices with a given dimension L , and H_{max} is the maximum value recorded by the rain gauge. The rainfall depth H_{max} is different from h_{ev} in Eq. 7.1 because it represents the total precipitation of the event, not the maximum value recorded in the given duration (three hours).

To find the maximum average rainfall depth H_a within the entire raster $A(K \cdot K)$, a matrix $B(n \cdot n)$ is composed of the average values for each submatrix.

$$B(i, j) = \frac{\sum_i^{L+i-1} \sum_j^{L+j-1} A(i, j)}{L^2} \quad (7.6)$$

where $B(i, j)$ represents the average of all the elements belonging to the submatrix $S(i, j)$ with its (1,1)-element in the i -th row and j -th column of the matrix A , and L is the number of cells in the submatrix side.

<div><div>$K = 5$</div><div>$L = 3$</div><div>$A = 9$</div><div>$n^2 = 9$</div></div>											
121	137	140	128	107	121	137	140	128	107	121	137
143	166	170	152	127	143	166	170	152	127	143	166
152	177	182	161	137	152	177	182	161	137	152	177
146	163	166	152	135	146	163	166	152	135	146	163
133	141	142	136	128	133	141	142	136	128	133	141
121	137	140	128	107	121	137	140	128	107	121	137
143	166	170	152	127	143	166	170	152	127	143	166
152	177	182	161	137	152	177	182	161	137	152	177
146	163	166	152	135	146	163	166	152	135	146	163
133	141	142	136	128	133	141	142	136	128	133	141
121	137	140	128	107	121	137	140	128	107	121	137
143	166	170	152	127	143	166	170	152	127	143	166
152	177	182	161	137	152	177	182	161	137	152	177
146	163	166	152	135	146	163	166	152	135	146	163
133	141	142	136	128	133	141	142	136	128	133	141
121	137	140	128	107	121	137	140	128	107	121	137
143	166	170	152	127	143	166	170	152	127	143	166
152	177	182	161	137	152	177	182	161	137	152	177
146	163	166	152	135	146	163	166	152	135	146	163
133	141	142	136	128	133	141	142	136	128	133	141
121	137	140	128	107	121	137	140	128	107	121	137
143	166	170	152	127	143	166	170	152	127	143	166
152	177	182	161	137	152	177	182	161	137	152	177
146	163	166	152	135	146	163	166	152	135	146	163
133	141	142	136	128	133	141	142	136	128	133	141
121	137	140	128	107	121	137	140	128	107	121	137
143	166	170	152	127	143	166	170	152	127	143	166
152	177	182	161	137	152	177	182	161	137	152	177
146	163	166	152	135	146	163	166	152	135	146	163
133	141	142	136	128	133	141	142	136	128	133	141

<div><div>$K = 5$</div><div>$L = 4$</div><div>$A = 16$</div><div>$n^2 = 4$</div></div>											
121	137	140	128	107	121	137	140	128	107	121	137
143	166	170	152	127	143	166	170	152	127	143	166
152	177	182	161	137	152	177	182	161	137	152	177
146	163	166	152	135	146	163	166	152	135	146	163
133	141	142	136	128	133	141	142	136	128	133	141
121	137	140	128	107	121	137	140	128	107	121	137
143	166	170	152	127	143	166	170	152	127	143	166
152	177	182	161	137	152	177	182	161	137	152	177
146	163	166	152	135	146	163	166	152	135	146	163
133	141	142	136	128	133	141	142	136	128	133	141
121	137	140	128	107	121	137	140	128	107	121	137
143	166	170	152	127	143	166	170	152	127	143	166
152	177	182	161	137	152	177	182	161	137	152	177
146	163	166	152	135	146	163	166	152	135	146	163
133	141	142	136	128	133	141	142	136	128	133	141
121	137	140	128	107	121	137	140	128	107	121	137
143	166	170	152	127	143	166	170	152	127	143	166
152	177	182	161	137	152	177	182	161	137	152	177
146	163	166	152	135	146	163	166	152	135	146	163
133	141	142	136	128	133	141	142	136	128	133	141
121	137	140	128	107	121	137	140	128	107	121	137
143	166	170	152	127	143	166	170	152	127	143	166
152	177	182	161	137	152	177	182	161	137	152	177
146	163	166	152	135	146	163	166	152	135	146	163
133	141	142	136	128	133	141	142	136	128	133	141
121	137	140	128	107	121	137	140	128	107	121	137
143	166	170	152	127	143	166	170	152	127	143	166
152	177	182	161	137	152	177	182	161	137	152	177
146	163	166	152	135	146	163	166	152	135	146	163
133	141	142	136	128	133	141	142	136	128	133	141
121	137	140	128	107	121	137	140	128	107	121	137
143	166	170	152	127	143	166	170	152	127	143	166
152	177	182	161	137	152	177	182	161	137	152	177
146	163	166	152	135	146	163	166	152	135	146	163
133	141	142	136	128	133	141	142	136	128	133	141
121	137	140	128	107	121	137	140	128	107	121	137
143	166	170	152	127	143	166	170	152	127	143	166
152	177	182	161	137	152	177	182	161	137	152	177
146	163	166	152	135	146	163	166	152	135	146	163
133	141	142	136	128	133	141	142	136	128	133	141
121	137	140	128	107	121	137	140	128	107	121	137
143	166	170	152	127	143	166	170	152	127	143	166
152	177	182	161	137	152	177	182	161	137	152	177
146	163	166	152	135	146	163	166	152	135	146	163
133	141	142	136	128	133	141	142	136	128	133	141
121	137	140	128	107	121	137	140	128	107	121	137
143	166	170	152	127	143	166	170	152	127	143	166
152	177	182	161	137	152	177	182	161	137	152	177
146	163	166	152	135	146	163	166	152	135	146	163
133	141	142	136	128	133	141	142	136	128	133	141
121	137	140	128	107	121	137	140	128	107	121	137
143	166	170	152	127	143	166	170	152	127	143	166
152	177	182	161	137	152	177	182	161	137	152	177
146	163	166	152	135	146	163	166	152	135	146	163
133	141	142	136	128	133	141	142	136	128	133	141
121	137	140	128	107	121	137	140	128	107	121	137
143	166	170	152	127	143	166	170	152	127	143	166
152	177	182	161	137	152	177	182	161	137	152	177
146	163	166	152	135	146	163	166	152	135	146	163
133	141	142	136	128	133	141	142	136	128	133	141
121	137	140	128	107	121	137	140	128	107	121	137
143	166	170	152	127	143	166	170	152	127	143	166
152	177	182	161	137	152	177	182	161	137	152	177
146	163	166	152	135	146	163	166	152	135	146	163
133	141	142	136	128	133	141	142	136	128	133	141
121	137	140	128	107	121	137	140	128	107	121	137
143	166	170	152	127	143	166	170	152	127	143	166
152	177	182	161	137	152	177	182	161	137	152	177
146	163	166	152	135	146	163	166	152	135	146	163
133	141	142	136	128	133	141	142	136	128	133	141
121	137	140	128	107	121	137	140	128	107	121	137
143	166	170	152	127	143	166	170	152	127	143	166
152	177	182	161	137	152	177	182	161	137	152	177
146	163	166	152	135	146	163	166	152	135	146	163
133	141	142	136	128	133	141	142	136	128	133	141
121	137	140	128	107	121	137	140	128	107	121	137
143	166	170	152	127	143	166	170	152	127	143	166
152	177	182	161	137	152	177	182	161	137	152	177
146	163	166	152	135	146	163	166	152	135	146	163
133	141	142	136	128	133	141	142	136	128	133	141
121	137	140	128	107	121	137	140	128	107	121	137
143	166	170	152	127	143	166	170	152	127	143	166
152	177	182	161	137	152	177	182	161	137	152	177
146	163	166	152	135	146	163	166	152	135	146	163
133	141	142	136	128	133	141	142	136	128	133	141
121	137	140	128	107	121	137	140	128	107	121	137
143	166	170	152	127	143	166	170	152	127	143	166
152	177	182	161	137	152	177	182	161	137	152	177
146	163	166	152	135	146	163	166	152	135	146	163
133	141	142	136	128	133	141	142				

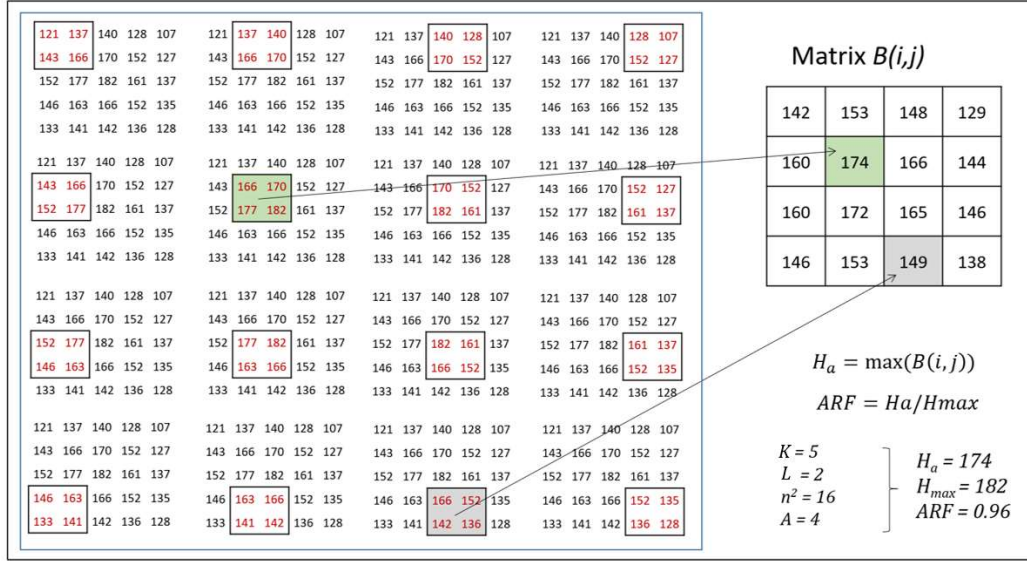


Figure 7.2. Evaluation of the maximum average rainfall depth H_a to calculate the Areal Reduction Factor for river basins with an area of 4 cells.

Each SDE is represented with the hyetograph recorded at the rain gauge station with the maximum within the event and a set of ARF values associated with the river basin areas in which it must be tested.

7.2.4 Hydrological Modelling

A hydrological model is used to compare the hydrographs of the SDEs and the design events. The SDE hyetographs can be the input of the river basins with similar rainfall statistics of where the SDE occurred. Therefore, a SDE is moved within its Storm Transposition Area only. In the proposed methodology, the SDEs are the input of the river basins with a design rainfall greater than the one at the location of the occurred event. Indeed, the assumption is that “an event occurred in a certain location is likely to occur also where the design rainfall depths are greater”.

A semi-distributed hydrological model is used, as the hyetographs obtained with the ARFs already consider the spatial distribution of the precipitation, giving a measure of the average precipitation over the entire river basin area. For this reason, the hyetographs scaled with the ARF must be the input of each sub-basin if the catchment area is further divided in the model. In addition, a semi-distributed hydrological model is used to consider a higher number of catchments to test the methodology, reducing the computational time.

Even if a fully distributed hydrological model can better describe the hydrological processes of runoff generation in a storm, its use shows a drawback, consisting of the relative position between the rainfall raster and the river basin. When a real event is modelled where it occurred, the position of the rainfall raster is obtained just with an interpolation of the rain gauges in their location. On the contrary, when a meteorological event is tested over a different location, the subjective choice of the distance between the centre of the event and the river basin barycentre is introduced. Therefore, more combinations for the same rainfall raster are possible using a distributed model, with cells that lie in or outside the river basin, depending on its reciprocal position with the storm centre. Lastly, this procedure is designed to be easily applied by decision-makers who need to assess and manage flood risks. For all these reasons, the software used in this study is HEC-HMS (USACE, 2013). HEC-HMS is a well-known and widely used semi-distributed hydrological model, but other semi-distributed hydrological models can be used to replicate this methodology.

7.2.5 Comparison of the design and short-duration events

The comparison between design event and SDEs discharges is made by looking at the peaks of the hydrographs. To summarise the results of this comparison, an index called Flash Flood Design Adaptation (FFDA) index is introduced as:

$$\text{FFDA} = \frac{\sum_1^{ne} q_{SDE}/ne}{q_{200}} \quad (7.8)$$

The FFDA index represents the ratio between the mean of the peak discharges q_{SDE} of the selected SDEs, and the peak of the design discharge, in this study the 200-year flood. If FFDA is greater than 1 in a river basin, the design discharge of that river basin underestimates the flash flood risk.

7.3 Application of the SDE hyetographs on Northern Tuscany

7.3.1 Dataset and Short-Duration Events – SDEs identification

The dataset of this work has been provided by the District River Basin Authority of Northern Apennine (“Autorità di Bacino Distrettuale dell’Appennino Settentrionale” in Italian), and it covers the period 2002-2017. The study considers 191 rain gauges of the Tuscany Region (central Italy). The rain gauge network covers an area of 16000 km² (Figure 7.3).

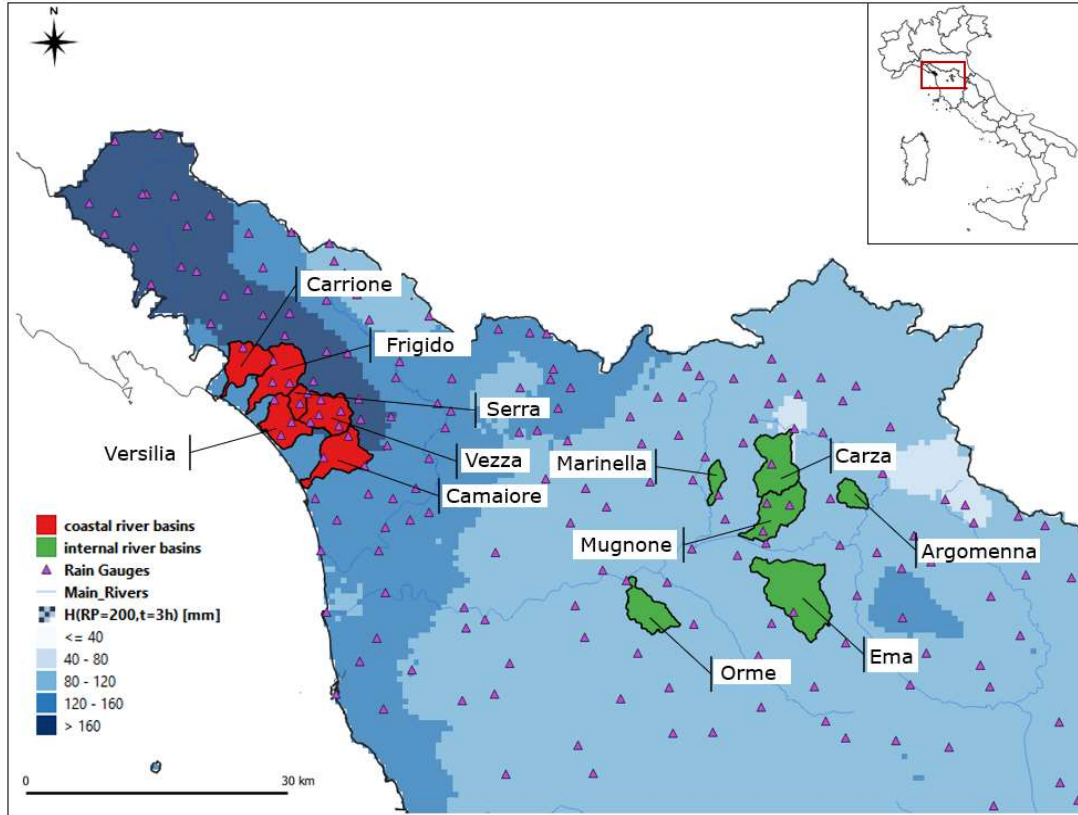


Figure 7.3. Rain gauge network and spatial distribution of the design rainfall depths H for a return period of 200 years and a duration of three hours in the study area. The catchments selected in this study are shown: the coastal river basins are red; the internal river basin are green.

The time resolution of the rainfall data is 15 minutes. Extreme rainfall depths are greater along the coast of Tuscany. This is evident looking at the design rainfalls with a given return period and duration, as is shown with the 200 years flood in the duration of 3 hours (Figure 7.3). The 200-year flood event is commonly used in the hydrological design in the region. The rainfall depths are obtained with the Intensity-Duration-Frequency curves developed by [Caporali et al. 2018](#). Indeed, these are the design rainfalls used by professionals and decision-makers in the Tuscany Region. The most intense SDEs recorded near the coast would produce floods greater than the design one if tested on river basins in the inner parts of Tuscany. Consequently, the analysis is divided in this study into two different datasets, i.e. Storm Transposition Areas (STAs): the real events that occurred near the sea are tested on the coastal river basins where the design rainfall depths are comparable with the coastal SDEs. The real events in the inner part of the region have been tested on the internal river basins.

After rainfall data analysis, the most intense SDEs are selected for the two groups with a Peak Over Threshold on the normalised rainfall depth (see Section 7.2.1). The Internal Short-Duration events are named ISDE and presented in Table 7.1; the Coastal Short-Duration events are named CSDE and shown in Table 7.2. The tables contain the name of the rain gauge that has the maximum within the event, the date of the day the event began, maxima rainfall for a duration of three hours, h_{ev} , in descending order of normalised depths, h_n . The normalisation is done with the design rainfall with a Return Period (RP) of 200 years, h_{200} .

Table 7.1. Short-Duration Events – SDEs for the inner part of the Region.

COD	Rain Gauge	Date	h_{ev} [mm]	h_{200} [mm]	h_n
ISDE1	Cavallina	09/20/2014	112.6	83.4	1.35
ISDE2	Certaldo	09/18/2010	108.8	92.5	1.18
ISDE3	Poggibonsi	06/05/2011	96.2	96.8	0.99
ISDE4	Radda in Chianti	08/31/2012	100.2	104.4	0.96
ISDE5	Vinci	10/05/2010	90.8	98.2	0.92

Table 7.2. Short-Duration Events – SDEs for the coastal part of the Region.

COD	Rain Gauge	Date	h_{ev} [mm]	h_{200} [mm]	h_n
CSDE1	Valle Beneditta	09/09/2017	235.0	137.7	1.71
CSDE2	Bocca d'Arno	10/26/2004	143.0	119.9	1.19
CSDE3	Pisa (Facoltà di Agraria)	08/24/2015	143.8	131.0	1.10
CSDE4	Gombitelli	07/21/2014	150.0	150.4	1.00

The average design rainfall with a RP of 200 years is 95 mm for the rain gauges in the inner part of the region (Table 7.1) and 135 mm for the coastal ones (Table 7.2). An event with 150 mm in three hours represents almost a 200-year event in the coastal area and has a RP greater than 500 years in the inner part of the region. The two river basin groups are summarised in Table 7.3 and Table 7.4 and shown in Figure 7.3. Six river basins have been chosen with different catchment areas for each group. This way, FFDA can be compared with the river basin area and the time of concentrations (t_c), highlighting differences between flash floods and design events. Moreover, the river basins with the greatest design rainfall within the two areas for given catchment areas are selected, as can be clearly seen by the coastal river basin in Figure 7.3.

Table 7.3. Set of the river basins in the inner parts of Tuscany.

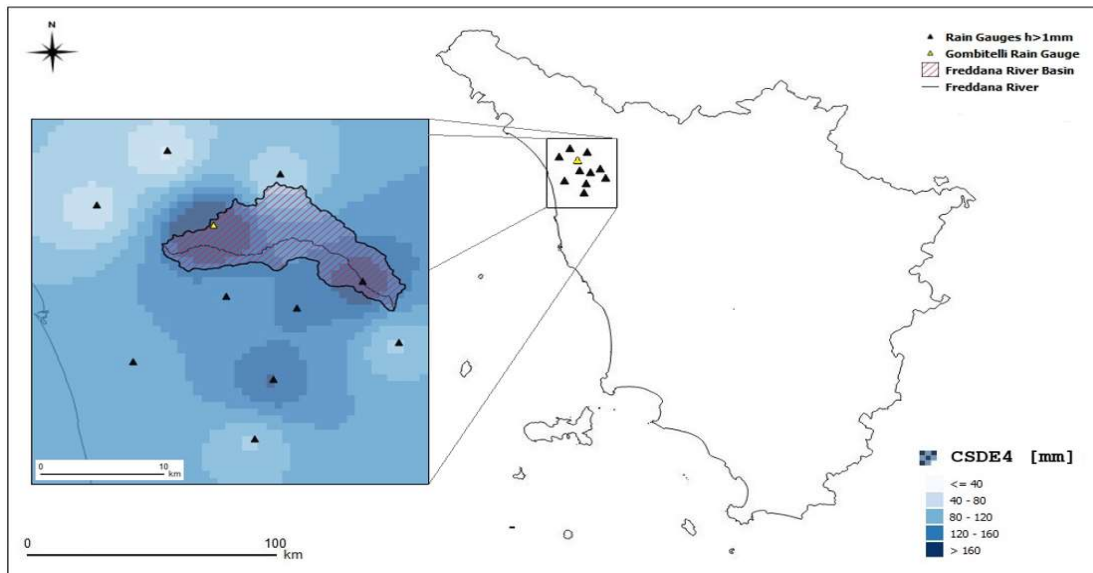
Name	A [km ²]	t_c [h]	Nearest rain gauge	h_{200} [mm]
Marinella	14.7	1.9	Calenzano	90.0
Argomenna	20.3	1.6	S. Brigida all'Opaco	97.1
Orme	47.5	3.1	Empoli	96.0
Mugnone	60.8	2.8	Caldine	94.2
Carza	66.7	2.9	Vaglia	78.4
Ema	112.3	4.0	Strada in Chianti	98.4

Table 7.4. Set of the river basins near the Tyrrhenian Sea.

Name	A [km ²]	t_c [h]	Nearest rain gauge	h_{200} [mm]
Serra	16.0	.5	Cerreto	162.6
Carrione	49.2	2.7	Torano	162.0
Vezza	52.0	3.1	Terrinca	189.7
Camaione	58.8	3.1	Camaione	147.8
Frigido	62.7	3.5	Canevara	171.6
Versilia	115.1	4.8	Strettoia	159.4

In this way the SDE are tested on the small river basins that have the safest design discharge in the area. The nearest rain gauge of each river basin is included in the tables, showing the significant difference in the design rainfall depths between the two STAs (also in this case h_{200} refers to the duration of 3 hours). The average 200-year design rainfall in the duration of 3 hours (h_{200}) is 92.4 mm for the internal river basins and 165.5 mm for the coastal ones.

Figure 7.4 shows as an example the spatial distribution and the rain gauges involved in the CSDE4, which occurred on 21 July 2014 (Table 7.2).

**Figure 7.4.** Rain Gauges and rainfall raster of CSDE4 (coastal short-duration event).

Eleven rain gauges recorded a total rainfall greater than 1 mm during the event. The rainfall spatial distribution is obtained with the IDW method. The maximum rainfall depth in 3 hours recorded by the Gombitelli rain gauge was 150 mm. The Freddana river basin had a flash flood during this event.

7.3.2 Hydrological models: comparison between design and SDE hyetographs

A semi-distributed hydrological model is used (Section 7.2.4). The simulations are made at an event temporal scale rather than using a continuous hydrological model, as it is meant to be applied during the design phase. Each SDE hyetograph has the shape of the hyetograph recorded at the rain gauge

with the maximum rainfall depth and can be scaled with all the ARFs for the different river basin extensions. Figure 7.5 shows the ISDE1 hyetograph (Table 7.1) recorded by the Cavallina rain gauge and the ARFs associated with the event as an example. The example also shows the same event modelled on the Carza river basin (internal river basin in Table 7.2). Since the entire river basin area is 67 Km², the hyetograph recorded by the rain gauge with the maximum depth (Figure 7.5 left) is scaled with an ARF of 0.73 and applied to each subbasin. Therefore, rainfall depths recorded in the rain gauge are reduced by 27%, considering the spatial distribution of the event over the given area.

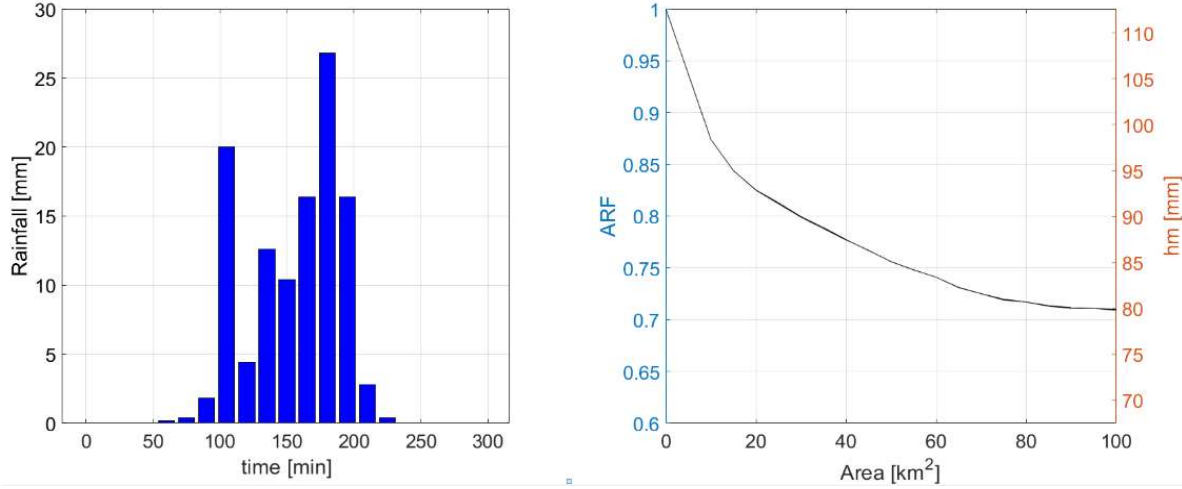


Figure 7.5. ISDE1 (internal short-duration event) hyetograph and Areal Reduction Factors associated with the event.

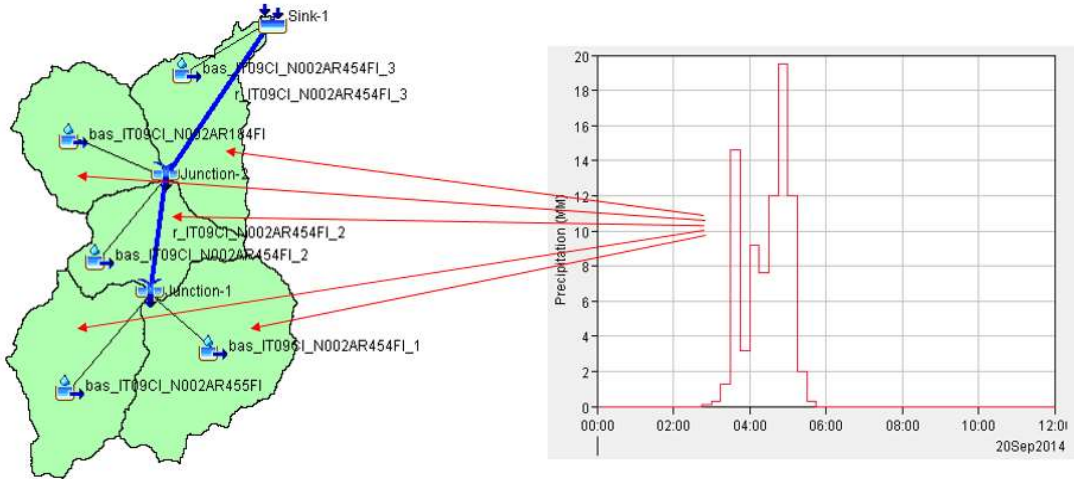


Figure 7.6. Carza river basin model: ISDE1 (internal short-duration event) hyetograph is scaled on the entire river basin area and is the input of all the subbasins.

The design hydrographs are based on the rainfall depths obtained with the Intensity-Duration-Frequency curves developed by [Caporali et al. 2018](#). Indeed, as already said, these are the design rainfalls used by professionals and decision-makers in the Tuscany Region. Particularly, the design rainfalls are obtained for each river basin by Eq. 7.9.

$$h_{RP,t_c} = a_{RP} * t_c^{n_{RP}} \quad (7.9)$$

where t_c is the time of concentration of a generic river basin, h_{RP,t_c} is the design rainfall depth for the return period RP and the duration t_c , and a_{RP} and n_{RP} are the intercept and the slope of the Intensity-Duration-Frequency linear curve in the Gumbel probability plot for a given return period,

respectively. The temporal distribution of the design storm is assigned with a triangular shape because it is the peak hyetograph commonly used in the region: the peak timing corresponds to $0.4 t_c$, and the magnitude of the peak has an intensity equal to double the constant intensity hyetograph. The loss method used in the hydrological model is the SCS Curve Number since the professionals commonly used it in the study area. Therefore, the runoff R is estimated as:

$$R = \frac{(P - 0.2 S)^2}{(P + 0.8 S)} \quad (7.10)$$

where P is the rainfall, and S is the potential maximum retention after runoff begins, which depends on the Curve number (CN) value as in the Eq.11.

$$S = 254 \left(\frac{100}{CN} - 1 \right) \quad (7.11)$$

The CN is obtained by combining the soil type information with the land use obtained with the Corine Land Curve (CLC 2013). The Antecedent soil Moisture Condition (AMC) is assumed to be the same in the comparison between the design events and the SDEs. The AMC is assumed to be the mean condition, considered with the CNII. The transform method is the SCS Unit Hydrograph, in which the lag time is estimated as 60% of each subbasin time of concentrations. The model is used without a calibration for two reasons: almost all the considered river basins are ungauged, and no streamflow data are available; the model estimates only the difference between the SDEs and the design event peaks with the same initial soil moisture conditions.

7.4 Results

The ARFs associated with the nine events considered in the study are shown in Figure 7.7. The internal events are on the left, while the coastal events are on the right. The distribution of the ARFs with respect to the river basin size A is shown just until a river basin extension of 100 km^2 since this study focuses on small river basins and concentrated storms on the spatial scale. The results of the hydrological modelling are shown for the river basins in the internal STA (Figure 7.8) and coastal STA (Figure 7.9) of Northern Tuscany. The peak discharge of the 200-year design storm of each river basin (red line) is compared with the peaks of the hydrographs generated by the SDEs (blue points) and with the mean of all the peaks obtained with the SDEs (blue dotted line).

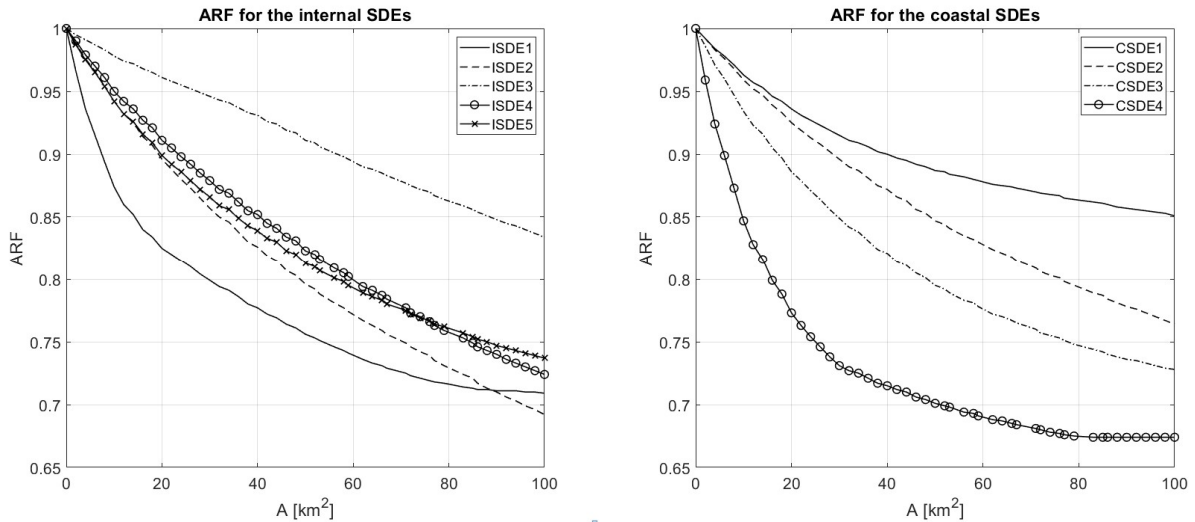


Figure 7.7. Areal Reduction Factors associated with the internal Short-Duration Events (left) and the coastal Short-Duration Events (right).

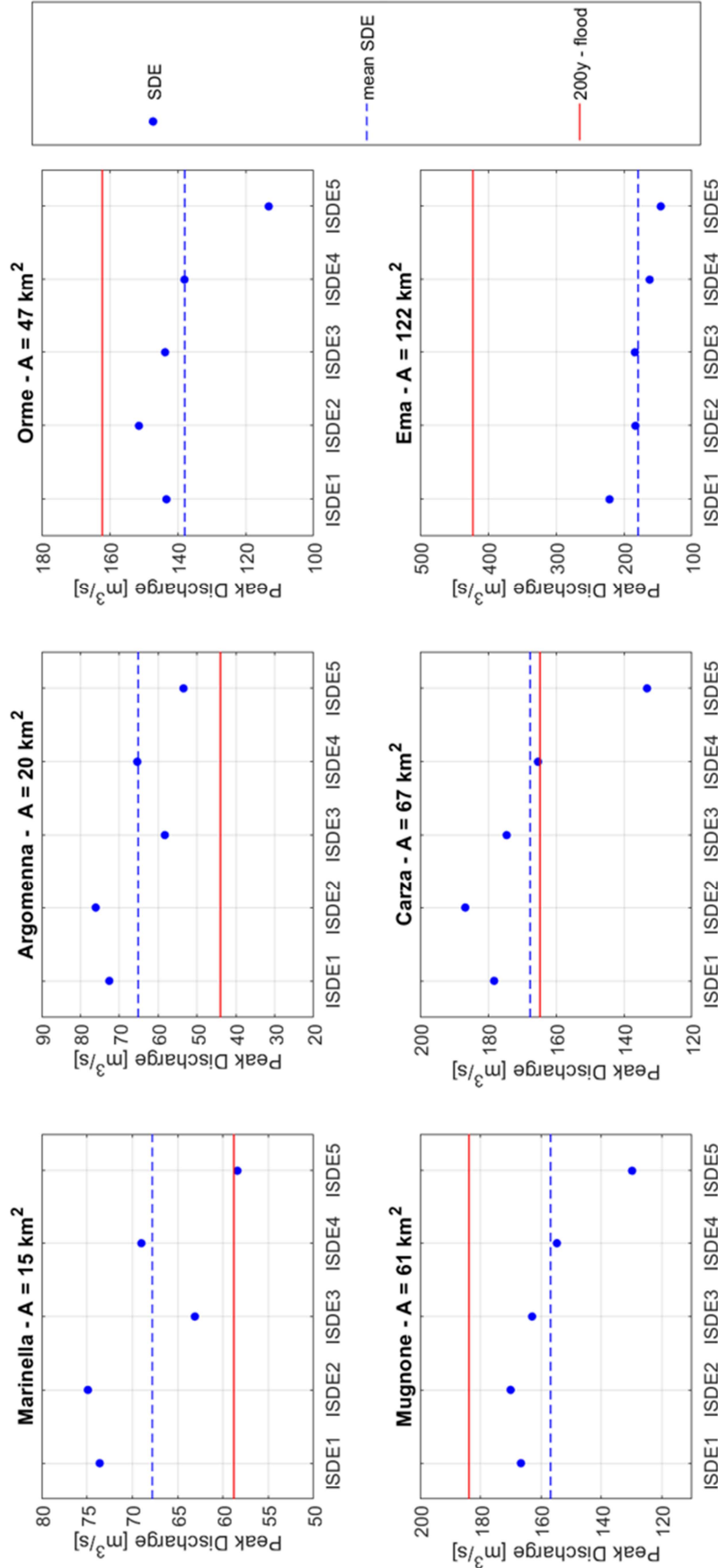


Figure 7.8. Results of all Short-Duration Events occurred inland (Table 7.1) in the set of internal river basins. The red line shows the 200-year design storm flood peak, the blue points represent the peaks of the Short-Duration Events, the dotted blue line the mean of the SDEs peaks.

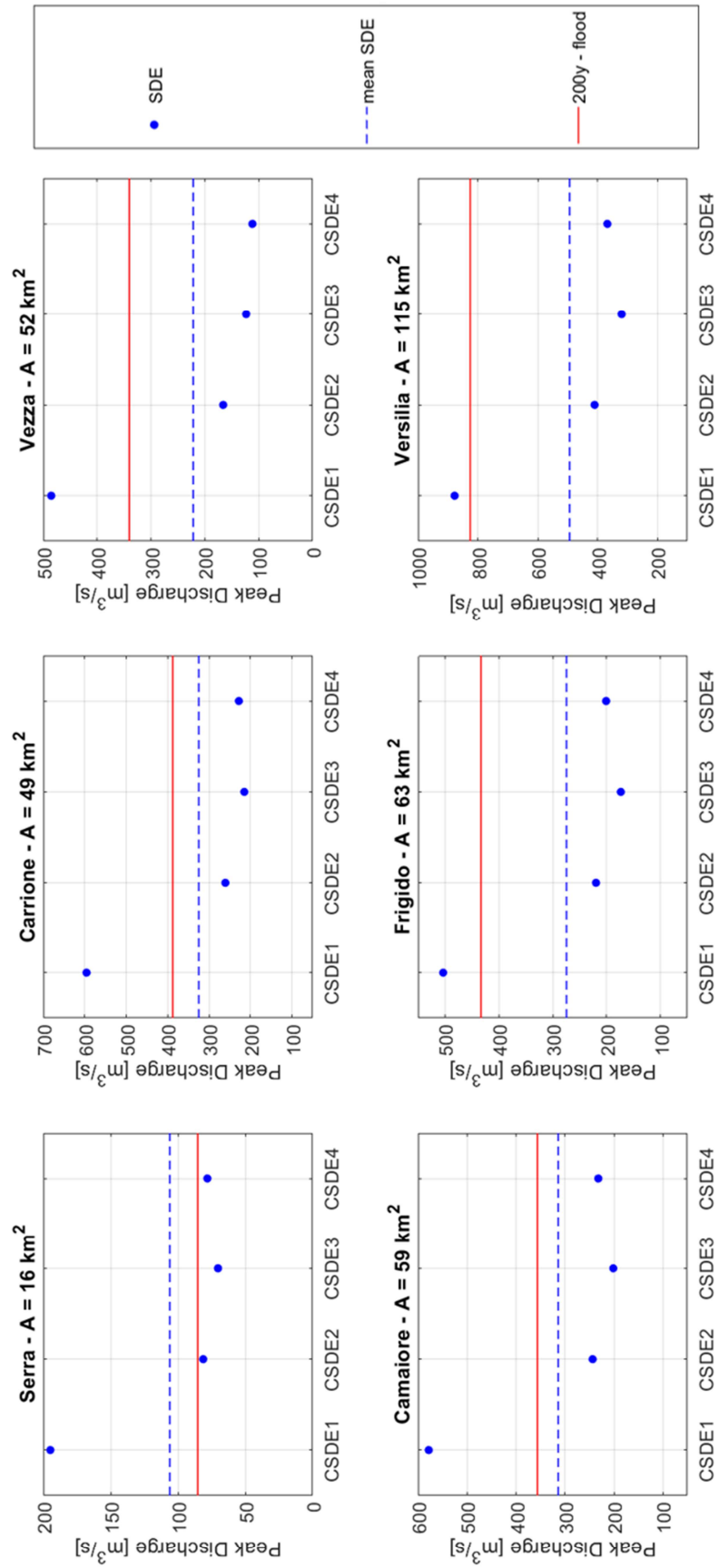


Figure 7.9. Results of all Short-Duration Events occurred near the coast (Table 7.2) in the set of coastal river basins. The red line shows the 200-year design storm flood peak, the blue points represent the peaks of the Short-Duration Events, the dotted blue line the mean of the SDEs peaks.

The Flash Flood Design Adaptation index (Section 7.2.5), FFDA, has been evaluated for each river basin, and it is shown with respect to the river basin area for the two STAs in Figure 7.10: the green dots represent the index for the internal river basins, the red dots for the coastal river basins.

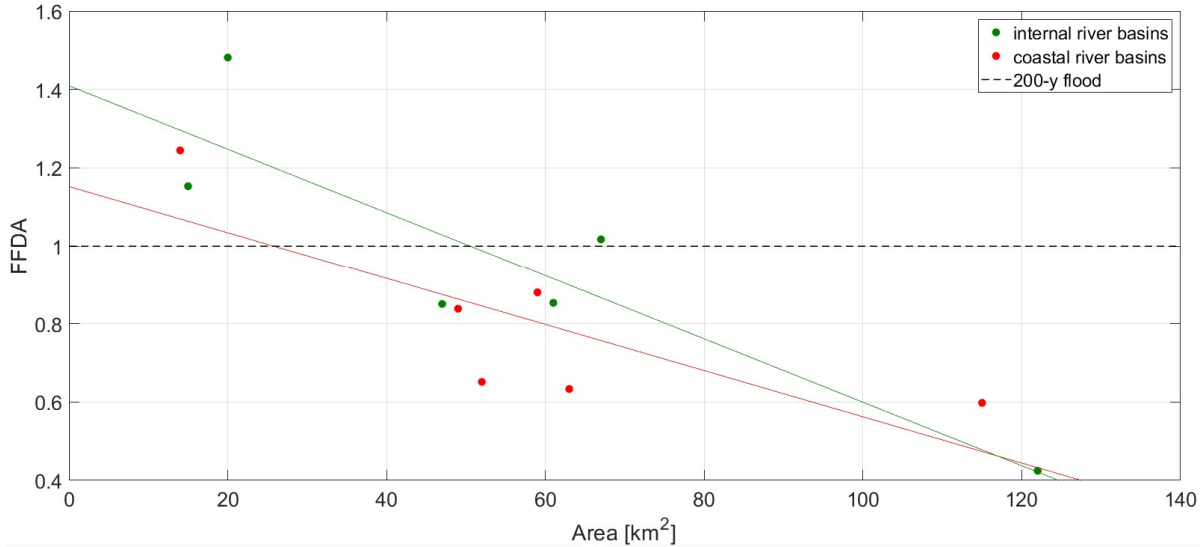


Figure 7.10. Flash Flood Design Adaptation index (FFDA) with respect to the river basin area for the internal and coastal river basins.

7.5 Discussion

Using past SDEs as synthetic hyetographs in hydrological modelling can be a strategy to better understand the flash flood hazard of small river basins. ARFs guarantee that past events can also be modelled in other locations. The proposed procedure ensures that each SDE is spatially analysed, and a single ARF is obtained for each river basin size. Each SDE has its spatial distribution, and the ARFs associated with each event show a different behaviour as the river basin area increases, as shown in Figure 7.7. Some ARFs scale almost linearly with the river basin area, which could be due to the weighting parameter used in the IDW. Nevertheless, almost all the short-duration events lose 30% of their intensity in just 100 km². This result agrees with other studies showing that short-duration events have more sharply decreasing ARFs with increasing areas than long-duration events, probably due to the convective origin of these storms (NERC, 1975; Ramos et al., 2005).

In Northern Tuscany, design discharges relate to flash flood events with different patterns depending on the zone and the river basin size. Considering the inner part of the region, the design discharges of the internal river basins are generally smaller than the magnitude of the hydrographs produced by the ISDEs for river basins smaller than 30 km² (upper part of Figure 7.8). The hydraulic risk assessment according to the 200-year design event is non-precautionary against the flash flood hazards in such river basins. On the contrary, when greater river basins are considered, the design flood seems to be precautionary also against the short-duration events, except for the Carza river basin, which shows a FFDA slightly higher than one. Even when the coastal area is considered, design events underestimate the flash flood risk in the river basins with an area generally less than 30 km². Indeed, the Serra River basin shows a FFDA greater than one (Figure 7.9). Nevertheless, the design storms obtained according to the regional frequency analysis of the Tuscany Region (Caporali et al., 2018) seem to be more adequate also against the flash flood risks in the coastal area. Indeed, there

are three river basins in the inner part of the region with a design discharge that underestimates the flash flood risk (Figure 7.10). On the contrary, only the smallest river basin has a FFDA greater than one along the coast. Several aspects can affect the relation between design and short-duration events peaks, such as the rain gauges time series length or the density of the gauging network. Therefore, the linear regression of FFDA with respect to the river basin area in Figure 7.10 is not derived to obtain a factor for other river basin areas. The red and green lines in Figure 7.10 emphasise how the coastal river basins generally appear safer against flash flood risk than the internal river basins for all the river basin extensions. According to some findings in the literature, convective storms are more frequent near the coast, and flash flood intensity decreases when moving inland (Gaume et al., 2009). Nevertheless, this study points out that a greater frequency and magnitude of extreme short-duration events along the coast can partially explain why the design rainfalls are also greater and precautionary against flash flood risk in that region. Indeed, just a single coastal short-duration event (CSDE1) exceeds the design hydrograph of all the river basins along the coast. Nevertheless, this event corresponds to the flash flood that occurred in Livorno during the night between the 9th and 10th of September 2017, which has been proved to have an extremely rare intensity if compared with the design event also in other studies (Ricciardelli et al., 2018; Arrighi and Castelli, 2020).

7.6 Conclusions

Evaluating if the design discharge commonly used for the flood risk assessment can underestimate the flood peak discharges of extreme short-duration events in small river basins is very important for decision making. This study proposes a methodology to characterise hyetographs of short-duration events that can be applied for the flash flood assessment at the river basin scale to identify river basins with design discharges that underestimate that risk. A simple methodology that considers the spatial distribution of past rainfall events has been proposed using the areal reduction factors. The short-duration event hyetographs are used as input data in a semi-distributed hydrological model for a set of small river basins in Northern Tuscany to analyse the impacts of the possible consequent flash floods. The results have underlined that the 200-year flood, commonly used in the flood risk assessment in the region, should be combined with the analysis of the response of a river basin to intense short-duration events to be more precautionary against flash flood risk. This is important for small river basins with an area generally less than 30 km².

The results cannot be extended to other regions, but the simplicity of the proposed method could bring some decision-makers to replicate the methodology in other case studies for a better evaluation of flash flood hazards at the river basin scale. The procedure is not meant to replace the classical modelling with design events, though it seeks to be a methodology that could be used alongside the classic hydraulic risk evaluation to improve the flash flood risk assessment. If the design flood exceeds the mean of the short-duration events peaks, the flash flood hazard is considered just using the classical approach with the design flood for that river basin. On the contrary, the decision makers could consider the additional risk due to flash flood events using the Flash Flood Design Adaptation index.

Chapter 8

Conclusions and Outlook

The partial conclusions reached in each part of the research work have already been presented in each previous chapter. The general conclusions, the original contributions and possible future developments of this work are highlighted in this Chapter.

8.1 Conclusions

This section is divided into two subsections. First, the conclusions regarding the impact of climate change on river floods and hydrological dam safety are presented (Section 8.1.1). Second, the conclusions about the methodology to improve flash flood hazards at the regional scale are included (Section 8.1.2).

8.1.1 Impact of climate change on river floods and hydrological dam safety

Climate change impact assessment studies need to consider different methodologies in terms of their different spatial scale. Indeed, large-scale studies are usually carried out to detect expected changes in river floods at the national or continental scales, though they cannot provide useful information for single points of interest, such as cities or hydraulic infrastructure. In addition, large-scale studies often have a spatial resolution too coarse to properly identify river floods in small- and medium-sized river basins, where most urban areas are located. Moreover, the results of large-scale studies usually have greater uncertainty. Therefore, the small-scale study should be preferred to manage and assess future hydraulic risk in urban areas, as uncertainty has a crucial role in flood risk assessment.

A fully distributed hydrological model (RIBS) has been used to assess the impact of climate change on the river flood hazard, using the city of Pamplona (Spain) as a case study. A fully distributed hydrological model can properly describe the spatial distribution of rainfall, increasing the model performance. The model has been calibrated with historical floods that occurred in recent years in the city. Expected changes in flood quantiles have been evaluated by comparing future and current scenarios. The future scenarios are generated considering three time windows (2011-2040, 2041-2070, 2071-2100), two emission scenarios (RCP 4.5 and RCP 8.5), and seven return periods (2, 5, 10, 50, 100, 500, 1000 years). The magnitude of frequent floods associated with low return periods tends to decrease in a warmer climate, while the less frequent floods tend to increase their magnitude, especially in the RCP 8.5.

The main conclusion of this work can be summarised as follows:

- A decrease in design peak discharges for return periods smaller than 10 years and an increase for the 500- and 1000-year floods for both RCPs in the three-time windows are found.
- The emission scenario RCP 8.5 usually provides the greatest increases in flood quantiles.
- Change magnitudes for the most extreme events are related to the greenhouse gas emission predictions in each RCP, as the greatest expected changes are found in 2040 for the RCP 4.5 and in 2100 for the RCP 8.5.
- Changes in flood quantiles are driven more by GCMs rather than RCMs.

Expected changes in flood quantiles are also used to evaluate the future hydrological dam safety of the Eugui Dam, which is upstream of the city of Pamplona. The study evaluates the risk for both the Eugui Dam, analysing the expected changes in the maximum reservoir water level frequency reached in flood events, and the downstream population in Pamplona, evaluating the expected changes in maximum reservoir outflow discharge frequency in flood events. A stochastic procedure has been proposed to consider how different inflow hydrograph magnitudes interact with different initial reservoir water levels at the beginning of flood events. The impact of climate change on inflow hydrographs is evaluated with the same fully distributed hydrological model used in the Pamplona

case study. The impact of climate change on initial reservoir water levels is conducted with a continuous hydrological model (HBV) and a reservoir operation model. Moreover, all the sources of uncertainty in the methodology are evaluated. The results show how cutting gas emissions will enhance hydrological dam safety, as a lower increase in maximum reservoir water levels is expected in the RCP 4.5 than in the RCP 8.5, especially for the most extreme events. Uncertainty has a key role in the findings. Therefore, methodologies that neglect uncertainties could underestimate the results.

The main conclusions obtained analysing the impact of climate change on hydrological dam safety are:

- Impacts of climate change on both inflow hydrographs and expected reservoir water levels at the beginning of flood events are assessed, considering uncertainties in the simulation chain.
- A stochastic procedure to assess the impact of climate change on hydrological dam safety is proposed, evaluating the expected changes in maxima reservoir water levels in the future.
- Maxima reservoir water levels are expected to increase for the most extreme events in the RCP 8.5, especially at the end of the century, while no significant changes are expected in the RCP 4.5.
- Maxima outflow discharges increase in both the emission scenarios, especially in the RCP 8.5 for all the return periods.
- Overtopping probability will increase at the Eugui Dam in the RCP 8.5 at the end of the century.
- Results without considering uncertainties tend to underestimate risks in hydrology dam safety.

The results obtained in the Arga river generally show how policies that aim to reduce greenhouse gas emissions could lead to a reduction in flood risks in the future. It could also reduce costs related to flood damages generated by extreme events and guarantee a greater hydrological dam safety. Nevertheless, maximum reservoir outflow discharges will increase in the RCP 4.5 to maintain the maximum reservoir water level. Therefore, new strategies to manage reservoir water levels could be required in the future to maintain lower initial water levels at the beginning of flood events. These new strategies could be represented by dam operations that reduce the water storage capacity in the reservoir, reducing the flood risk in the downstream population.

8.1.2 Improve flash flood risk assessment at the regional scale

Flood risk assessment of small river basins requires different methodologies because floods usually occur suddenly at this spatial scale, as catchment response times are comparable with short durations of extreme events. Flash flood hazard assessment in small river basins changes the domain of the analysis, moving from daily data and data-rich hydrology to hourly/sub-hourly data with shorter time series. Moreover, there are few climate projections with sub-daily durations. Models cannot be often calibrated, and uncertainty cannot be evaluated as flash flood usually occurs in ungauged river basins. For this reason, a simple procedure for flash flood risk assessment at the regional scale has been proposed to determine where design floods of short durations can underestimate flash flood risk. The procedure is based on the Stochastic Storm Transposition approach to increase the number of synthetic events modelled in the design phase of a river basin. Moreover, each event is spatially analysed and scaled with the areal reduction factors to evaluate the maximum mean intensity of each event over different river basin extensions. The main conclusions of this study are the following:

- A simple methodology to improve flash flood assessment is proposed using synthetic hyetographs obtained with areal reduction factors and Stochastic Storm Transposition of observed storms.
- The Flash Flood Design Adaptation index (FFDA) is introduced to adjust the design floods of small river basins.
- The results show how peak discharges of short-duration events in northern Tuscany are usually greater than the design floods of the small river basins for an area generally less than 30 km².

8.2 Original Contributions

The original contributions provided by the present research are described in this subsection:

- **Obtaining delta changes in flood quantiles by considering the spatial distribution of future design rainfalls in climate change with a fully distributed hydrological model**

The input data used to describe future design rainfalls are obtained by combining delta changes of precipitation in climate change with the observed precipitation in the control period. Impact assessment studies that involve climate projections are usually conducted with lumped or semi-distributed hydrological models. Therefore, delta changes are generally assigned to the nearest rain gauge. Nevertheless, the spatial distribution of future rainfalls is usually simplified, considering that the grid of the delta changes is different from the rain gauge network distribution. In this study, the spatial distribution of future design rainfalls is deeply described by combining the grid of the delta changes with the rainfall field of the design rainfalls in the current scenario obtained from observations. A good description of the spatial rainfall distribution has a key role in flood hazard assessment to obtain a good performance in the calibration of historical events and the assessment of future scenarios. As delta changes are provided by 12 climate models, three time windows, two RCP scenarios and seven return periods, 504 rainfall events are considered in the analysis. Moreover, each event has a hyetograph with 24 time steps. Therefore, 12,096 rainfall spatial distributions have been used as input in the RIBS model.

- **Assessing the contribution of both GCMs and RCMs in the expected changes in flood quantiles**

Downscaling of GCMs with RCMs is frequent to conduct impact assessment studies. Several studies use projections with combinations of GCMs and RCMs. Nonetheless, the contribution of GCMs or RCMs to the expected changes in flood quantiles is not deeply investigated. In this study, the expected changes in flood quantiles are analysed by grouping the results by GCMs and RCMs to extract the contribution of each type of climate model considered in the ensemble on the results. The results highlight that GCMs may have a greater impact on the results compared with RCMs. Therefore, studies that analyse the impact of climate change with an ensemble with a higher number of GCMs should be preferred, as they have a stronger influence on the results. Furthermore, for a given number of ensemble members with the same computational cost, the use of more GCMs rather than RCMs will reduce estimate uncertainties.

- **Development of a complete stochastic procedure for hydrological dam safety assessment in climate change**

This study provides a procedure to evaluate hydrological dam safety under climate projections. The procedure is based on random generations of inflow hydrographs and initial reservoir water levels at the beginning of flood events. Indeed, the assessment of climate change on both inflow peak discharges and initial reservoir water level frequency is assessed. The impact of climate change on

inflow hydrographs is assessed with the fully distributed RIBS model, while the expected changes in initial reservoir water level frequency are evaluated by combining the continuous HBV model with a reservoir operation model. Nevertheless, the procedure is based on the determination of the probability associated with given peak flow discharges and initial reservoir water levels at the beginning of the flood events that could be assessed with other hydrological models. Nonetheless, an event-based and fully distributed hydrological model is recommended to properly simulate the catchment response in extreme floods, as they are suitable to describe flood processes at the single event scale in more detail. In addition, the initial reservoir water level frequency is evaluated considering the long-term inflow discharge time series within the reservoir, which must be estimated with a continuous hydrological model. The procedure can be integrated with the uncertainty chain assessment to evaluate all the sources of errors that could affect the hydrological estimates.

- **Development of a reservoir operation model to estimate changes in the reservoir water levels expected at the beginning of flood events in climate change**

A model that can describe reservoir operation rules determining daily releases is necessary to assess the reservoir water level frequency in a given scenario in the future. A reservoir operation model has been developed in this work. Similar simulation tools could be HEC-ResSim (Klipsch and Hurst, 2007) or MODSIM. However, they are more useful for managing a reservoir network on a given river or system rather than modelling a single dam. The reservoir operation model developed in this work calculates daily releases considering monthly environmental flows, water supply for the downstream population, inflow discharges and the release curves that regulate outflow discharges as a function of reservoir water levels. The inputs of the reservoir operation model are two daily time series: inflow discharge in the reservoir (in this work provided by the HBV model) and evaporation from the reservoir, representing input and output volumes, respectively. Moreover, inflow discharges are also used to understand if the reservoir operation model must release an outflow discharge that needs to account for the flood routing process in flood events. Other data used as input of the reservoir operation model are the monthly environmental flow and the water supply for the downstream population. The reservoir operation model evaluates the daily maximum discharge that the daily reservoir water level can supply. Indeed, the outflow discharge must be in each day not greater than the daily maximum outflow discharge, which is evaluated with the release curves that relate discharges in closed pipes (or from spillways) to the reservoir water level in each day. The reservoir operation model evaluates the reservoir water level of the day after by using a mass balance. The output of the model are daily time series of reservoir water volumes and levels and the reservoir water level frequency of the whole-time window.

- **Assessing the uncertainty chain in the methodology for hydrological dam safety analysis in climate change**

This work highlights how uncertainty has a key role in the determination of hydrological dam safety. Indeed, without its consideration the methodology underestimates maxima outflow discharges, maxima water levels and overtopping probability. First, the procedure evaluates the uncertainty of rainfall delta changes since design rainfalls are estimated with short time series. Then, residual errors of the hydrological models after the calibration are accounted for to evaluate the uncertainty in the inflow peak discharge estimates and the initial reservoir water frequency. The stochastic procedure to evaluate uncertainty could be replied to in other studies using different hydrological models. The assessment is based on the correction of the inflow peaks, generating random peak discharge errors, and the adjustment of the initial water level frequency, correcting daily inflow discharges in the reservoir supplied by the HBV model. In this study, the uncertainty of initial water level frequency at the beginning of a flood event is evaluated by considering a mean reservoir water level frequency in the stochastic procedure. The mean water reservoir level frequency is obtained with 50 simulations for each scenario, according to a sensitivity analysis which has evaluated that the mean stabilises after

this number of iterations. The uncertainty of the inflow peak discharges is evaluated considering different percentiles.

- **Flash Flood Design Adaptation index**

There are several methodologies to consider flash flood risk assessment in literature. The most famous one is the Flash Flood Guidance, based on a rainfall threshold to supply a forewarning in real time. Nevertheless, such a method is more suitable in river basins where the response times are at least three hours. Although it is possible to forecast rainfall and establish a given alert threshold previously, the uncertainty behind all the procedure (forecasting, rainfall-runoff model, initial soil moisture condition) prevents the possibility of a system with high reliability, especially in ungauged river basins. Therefore, this study proposed a methodology to pre-assess flash flood risk. The approach is based on the correction of the design rainfalls of short durations with a Flash Flood Design Adaptation index (FFDA). The FFDA is assessed by comparing the peak discharges of short-duration events that occurred in the past with the design events used in a given river basin. The short-duration events generate synthetic events with the Stochastic Storm Transposition and the Areal Reduction Factors. The index could be easily applied by decision makers that need to manage several small and ungauged river basins in a given area to correct in some cases their design floods in favour of safety.

8.3 Future developments

Future studies to continue the present line of research could be related to:

- **Assessing expecting changes in direct flood damages in climate change downstream of dams**

This study provides results regarding the impact of climate change on outflow discharges by the dam. However, no information is supplied regarding possible direct damages to infrastructure and urban areas located downstream of the dam caused by the expected changes in flood events. A first future development of this study could be completing the hydraulic risk analysis assessment by also considering the direct flood damages in infrastructure subject to the increased hazard. In this way, projection of discharges in the city that account for both the impact of climate change on the natural contribution of the river basin and on the outflow discharges by dam can be considered. Such outputs can be used to assess expected changes in the direct flood damages in urban areas.

- **Considering seasonality patterns to estimate the expected seasonal initial reservoir water levels in climate change in the stochastic procedure**

The stochastic procedure proposed in this study considers the impact of climate change on hydrological dam safety using reservoir water level frequency and inflow discharges on annual basis, but the seasonality of both inflow peaks and water levels in the reservoir is not considered. However, initial reservoir water levels can be related to seasons. Indeed, reservoir water levels are usually higher in late spring than in early autumn at the end of the dry season, as the reservoir storage volume is used for water supplies. Hence, the characterization of seasonality in the assessment of climate change impacts on hydrological dam safety could be an improvement of the stochastic procedure. In the current version of the stochastic procedure, an annual reservoir water level frequency curve is obtained for each scenario (climate model, time window and RCP scenario). The introduction of 12 monthly reservoir water level frequency curves would improve the methodology.

- **Generation of pairs of inflow hydrographs and initial reservoir water levels considering the relationship between them**

In the analysis conducted on an annual basis, no correlation between the frequencies of inflow peak discharges and initial water level at the beginning of flood events was detected. Therefore, the two vectors of probability used in the stochastic procedure are generated independently. A further integration of the stochastic procedure could be the use of copulas in the generation of inflow hydrographs considering seasonality, as in the monthly data some correlation between inflow peaks and initial water level at the beginning of flood events is expected.

- **Generation of random hydrograph shapes for assessing hydrological dam safety in climate change**

In this study, a unique shape is assigned to each synthetic event, multiplying the peak provided by the GEV by a unit hydrograph. The hydrograph shape is obtained as the mean of all the unit hydrographs provided by the RIBS model. The importance of hydrograph shapes in hydrological dam safety analysis is relevant, as different shapes can represent different hydrograph volumes with a given peak discharge. A further step in the stochastic procedure could be represented by a random generation of hydrograph shapes, that could scale the random inflow peaks.

- **Generalization of the reservoir operation model code in a free tool**

An important step for the replicability of this procedure is the availability of a reservoir operation model. So far, the model has been developed in Matlab and it is focused on the Eugui Dam case studies. Indeed, several rows of the code contain data and characteristics of the reservoir upstream of Pamplona. The code could be generalized to provide an open tool that could be used to assess reservoir water levels time series or frequency, using as input inflow discharges and geometric data of the dam that is intended to be model.

- **Improve the uncertainty chain assessment for assessing hydrological dam safety in climate change and evaluate the weight of each source of uncertainty**

The procedure used to assess uncertainty combines all the source of errors together. Therefore, no information about the weight of each source of uncertainty within the uncertainty chain is given. Indeed, the final evaluation of uncertainty it is not just the linear sum of all the single sources of uncertainty, as some of them can be compensated. Indeed, uncertainty in rainfall delta change estimates could have an “opposite direction” to the uncertainty in the estimation of the peak discharges for a given synthetic event. For instance, for some of the 10,000 synthetic events delta changes of precipitation could be lower than the median value (i.e. the value used without the consideration of uncertainty) and they could be corrected with a K_{RIBS} value greater than one (i.e. with a peak that is greater than the one used without the consideration of the model uncertainty). Therefore, the stochastic procedure could be repeated several times considering only one source of uncertainty (such as rainfall, peak discharges, or initial water levels), to evaluate how each source of uncertainty weights in the methodology. Moreover, the assessment of HBV model uncertainty could be improved. Indeed, the biases between the model and the observations are evaluated for entire time series rather than single events. Therefore, bias have a temporal dependence that could be better describe by a time series model.

- **Use of a stochastic weather generator to generate short-durations event**

In the definition of the Flash Flood Design Adaptation index, the used of the Stochastic Storm Transposition approach guarantees a given number of short-duration events in each small ungauged river basin. Therefore, the synthetic hyetographs are obtained transposing past observed rainfall events after the scaling procedure with the areal reduction factors. Another approach to improve the definition of the index could be represented by the use of a stochastic weather generator. Indeed, a rainfall generator can both apply a temporal disaggregation of daily time series and generate random short-duration events. Nevertheless, the use of a stochastic generator can introduce additional sources

of uncertainty in the generation of the synthetic events, given the impossibility of a perfect calibration of the model. However, it could lead to a higher complexity in the analysis, that is instead meant to be easily used by the decision makers that work in the river basin authorities to assess flood risk.

Reference

- Alfieri, L. et al. (2015) ‘Global warming increases the frequency of river floods in Europe’, *Hydrology and Earth System Sciences*, 19(5), pp. 2247–2260. doi: 10.5194/hess-19-2247-2015.
- Alfieri, L. et al. (2017) ‘Global projections of river flood risk in a warmer world’, *Earth’s Future*, 5, pp. 171–182. doi:10.1002/2016EF000485
- Ali, K. et al. (2017) ‘Advances and Challenges in Flash Flood Risk Assessment: A Review’, *Journal of Geography & Natural Disasters*, 07(02). doi:10.4172/2167-0587.1000195
- Arnell, N. W. and Lloyd-Hughes B. (2014) ‘The global-scale impacts of climate change on water resources and flooding under new climate and socio-economic scenarios’, *Climate Change*, 122, pp. 127–140 doi:10.1007/s10584-013-0948-4
- Arrighi C. and Castelli F. (2020) ‘The 2017 Flash Flood of Livorno (Italy): Lessons Learnt from an Exceptional Hydrologic Event’, In: Fernandes F., Malheiro A., Chaminé H. (eds) *Advances in Natural Hazards and Hydrological Risks: Meeting the Challenge. Advances in Science, Technology & Innovation (IEREK Interdisciplinary Series for Sustainable Development)*. Springer, Cham. doi:10.1007/978-3-030-34397-2_23
- Babur, M. et al. (2016) ‘Assessment of Climate Change Impact on Reservoir Inflows Using Multi Climate-Models under RCPs - The Case of Mangla Dam in Pakistan’, *Water (Switzerland)*, 8(9), p. 389. doi: 10.3390/w8090389.
- Bacchi, B. and Ranzi, R. (1996) ‘On the derivation of the areal reduction factor of storms’, *Atmospheric Research*, 42(1–4), pp. 123–135. doi:10.1016/0169-8095(95)00058-5
- Bahls, V. and Holman, K. (2014) ‘Climate Change in Hydrologic Hazard Analyses: Friant Dam Pilot Study - Part I: Hydrometeorological Model Inputs’, Tech. rep., U.S. Department of the Interior, Bureau of Reclamation.
- Barbero, G. et al. (2014) ‘Evaluation of the areal reduction factor in an urban area through rainfall records of limited length: A case study’, *Journal of Hydrologic Engineering*, 19(11), pp. 1–10. doi:10.1061/(ASCE)HE.1943-5584.0001022
- Berg, P. et al. (2013) ‘Strong increase in convective precipitation in response to higher temperatures’, *Nature Geoscience*, 6(3), pp. 181–185. doi:10.1038/ngeo1731
- Bergström, S. (1976) ‘Development and application of a conceptual runoff model for Scandinavian catchments’, SMHI Norrköping, Report RH07.
- Bergström, S. (1992) ‘The HBV-Model — Its Structure and Applications’. SMHI Reports RH No. 4, Norrköping.
- Beven, K.J. (2006) ‘A manifesto for the equifinality thesis’, *Journal of Hydrology*, 320, pp. 18–36.
- Blöschl, G. et al. (2019) ‘Changing climate both increases and decreases European river floods’, *Nature*, 573(7772), pp. 108–111. doi: 10.1038/s41586-019-1495-6.
- Bowles, D. et al. (2013) ‘Guide to risk assessment for reservoir safety management’, Guide, Tech. Rep. SC090001/R1, Environment Agency, Horison House, Deanery Road, Bristol, BS1 9AH.
- Bucak, T. et al. (2017) ‘Future water availability in the largest freshwater Mediterranean lake is at great risk as evidenced from simulations with the SWAT model’, *Science of the Total Environment*, 582, pp. 413–425. doi: 10.1016/j.scitotenv.2016.12.149.
- Cabral, M.C. et al. (1992) ‘A kinematic model of infiltration and runoff generation in layered and sloped soils’, *Advances in Water Resources*, 15, pp. 311–324. doi:10.1016/0309-1708(92)90017-V.

-
- Cao, C. et al. (2016) 'Flash flood hazard susceptibility mapping using frequency ratio and statistical index methods in coalmine subsidence areas', *Sustainability (Switzerland)*, 8(9), doi:10.3390/su8090948.
 - Caporali, E. et al. (2018) 'Regional frequency analysis and geosadditive modeling for design storm estimates in the Arno river basin (Italy)', *Environmental and Ecological Statistics*, 25(1), pp. 31–52. doi:10.1007/s10651-018-0399-1
 - Caporali, E. et al. (2021) 'A review of studies on observed precipitation trends in Italy', *International Journal of Climatology*, 41(S1), E1–E25. doi:10.1002/joc.6741.
 - Castellarin, A. et al. (2012) 'Review of applied-statistical methods for flood-frequency analysis in Europe'. NERC/Centre for Ecology & Hydrology, 122pp. (ESSEM COST Action ES0901)
 - Chen, X. and Hossain, F. (2019) 'Understanding Future Safety of Dams in a Changing Climate', *Bulletin of the American Meteorological Society*, 100(8), pp. 1395–1404. doi: 10.1175/BAMS-D-17-0150.1.
 - Chernet, H. H. et al. (2014) 'Safety of Hydropower Dams in a Changing Climate', *Journal of Hydrologic Engineering*, 19, pp. 569–582. doi:10.1061/(ASCE)HE.1943- 5584.0000836, 2014
 - Dankers, R. and Feyen, L. (2008) 'Climate change impact on flood hazard in Europe: An assessment based on high-resolution climate simulations', *Journal of Geophysical Research Atmospheres*, 113(19), pp. 1–17. doi: 10.1029/2007JD009719.
 - Dankers, R. and Feyen, L. (2009) 'Flood hazard in Europe in an ensemble of regional climate scenarios', *Journal of Geophysical Research: Atmospheres*, 114, pp. 47–62. doi:10.1029/2008JD011523.
 - Dawod, G. M. et al. (2011) 'GIS-Based Spatial Mapping of Flash Flood Hazard in Makkah City, Saudi Arabia'. *Journal of Geographic Information System*, 03(03), pp. 225–231. doi:10.4236/jgis.2011.33019.
 - De Michele, C., Kottegoda, N. T., & Rosso, R. (2001). The derivation of areal reduction factor of storm rainfall from its scaling properties. *Water Resources*, 37(12), 3247–3252
 - de Moel, H. et al. (2015) 'Flood risk assessments at different spatial scales', *Mitigation and Adaptation Strategies for Global Change*, 20(6), pp. 865-890, doi:10.1007/s11027-015-9654-z
 - Dee, D.P. et al. (2011) 'The ERA-Interim reanalysis: Configuration and performance of the data assimilation system', *Quarterly Journal of the Royal Meteorological Society*, 137(656), pp. 553-597, doi: 10.1002/qj.828
 - Déqué, M. (2007) 'Frequency of precipitation and temperature extremes over France in an anthropogenic scenario: Model results and statistical correction according to observed values', *Global and Planetary Change*, 57, pp. 16-26, doi: 10.1016/j.gloplacha.2006.11.030
 - Devi, G.K. et al. (2015) 'A review on hydrological models', *Aquatic Procedia*, 4, pp. 1001-1007. doi:10.1016/j.aqpro.2015.02.126.
 - Donat, M. G. et al. (2016) 'More extreme precipitation in the world's dry and wet regions', *Nature Climate Change*, 6(5), pp. 508–513. doi: 10.1038/nclimate2941.
 - Doocy, S. et al. (2013) 'The Human Impact of Floods: a Historical Review of Events 1980-2009 and Systematic Literature Review', *PLoS Curr. D*, 16(1). doi:10.1371/currents.dis.f4deb457904936b07c09daa98ee8171a.
 - Dougherty, E. and Rasmussen, K. L. (2021) 'Variations in Flash Flood-Producing Storm Characteristics Associated with Changes in Vertical Velocity in a Future Climate in the Mississippi River Basin', *Journal of Hydrometeorology*, pp. 671–687. doi:10.1175/JHM-D-20-0254.1.
-

-
- Ducharne, A. et al. (2010) 'Climate change impacts on water resources and hydrological extremes in northern France'. In: Carrera, J. (Ed.), Proceedings of the XVIII International Conference on Computation Methods in Water Resources, 21–24 June, 2010, Barcelona.
 - Engen-Skaugen, T. (2007) 'Refinement of dynamically downscaled precipitation and temperature scenarios', *Climate Change*, 84, 365–382. doi: 10.1007/s10584-007-9251-6
 - ES: Directive 2007/60/EC of the European Parliament and of the Council of 23 October 2007 on the assessment and management of flood risks, European Parliament, Council, 2007
 - Esposito, G. et al. (2018) 'Analysis of increasing flash flood frequency in the densely urbanized coastline of the campi flegrei volcanic area, Italy', *Frontiers in Earth Science*, 6(June), pp. 1–17. doi:10.3389/feart.2018.00063
 - Faccini, F. et al. (2015) 'The 4th October 2010 flash flood event in Genoa Sestri Ponente (Liguria, Italy)', *Disaster Advances*, 8, pp.1–14. doi:10.13140/RG.2.1.1604.9124.
 - Faccini, F. et al. (2018) 'Role of rainfall intensity and urban sprawl in the 2014 flash flood in Genoa City, Bisagno catchment (Liguria, Italy)', *Applied Geography*, 98, pp. 224–241. doi:10.1016/j.apgeog.2018.07.022
 - Faccini, F. et al. (2021) 'Flash Flood Events along the West Mediterranean Coasts: Inundations of Urbanized Areas Conditioned by Anthropic Impacts', *Land*, 10, 620. doi:10.3390/land10060620
 - Fluixá-sanmartín, J. et al. (2018) 'Review article: Climate change impacts on dam safety', *Natural Hazards and Earth System Science*, 18, pp. 2471–2488. doi:10.5194/nhess-18-2471-2018.
 - Fluixá-sanmartín, J. et al. (2019a) 'Empirical Tool for the Assessment of Annual Overtopping Probabilities of Dams', *Journal of Water Resources Planning and Management*, 145(1), pp. 1–12. doi: 10.1061/(ASCE)WR.1943-5452.0001017.
 - Fluixá-sanmartín, J. et al. (2019b) 'Quantification of climate change impact on dam failure risk under hydrological scenarios: a case study from a Spanish dam', *Natural Hazards and Earth System Science*, 19, pp. 2117–2139.
 - Fluixá-sanmartín, J. et al. (2021) 'Accounting for Climate Change Uncertainty in Long-Term Dam Risk Management', *Journal of Water Resources Planning and Management*, 147(4) 4. doi: 10.1061/(ASCE)WR.1943-5452.0001355
 - Foufoula-Georgiou, E. (1989) 'A probabilistic storm transposition approach for estimating exceedance probabilities of extreme precipitation depths', *Water Resources Research*, 25, pp. 799–815 doi:10.1029/WR025I005P00799
 - Franchini, M. et al. (1996) 'Stochastic storm transposition coupled with rainfall runoff modeling for estimation of exceedance probabilities of design floods', *Journal of Hydrology*. 175(1–4), pp.511–532. M
 - Garijo, C. and Mediero, L. (2018) 'Influence of climate change on flood magnitude and seasonality in the Arga River catchment in Spain', *Acta Geophysica*, 66, pp. 769–790. doi:10.1007/s11600-018-0143-0.
 - Garijo, C. and Mediero, L. (2019) 'Assessment of changes in annual maximum precipitations in the Iberian Peninsula under climate change', *Water (Switzerland)*, 11(11). doi: 10.3390/w11112375.
 - Garrote, L. and Bras, R. L. (1995a) 'A distributed model for real time forecasting using digital elevation models', *Journal of Hydrology*. 167(1–4), pp. 279–306. doi: 10.1016/0022-1694(94)02592-Y.
 - Garrote, L. and Bras, R. L. (1995b) 'An integrated software environment for real-time use of a distributed hydrologic model', *Journal of Hydrology*, 167(1–4), pp. 307–326. doi: 10.1016/0022-1694(94)02593-Z.
 - Gaume, E. et al. (2009) 'A compilation of data on European flash floods'. *Journal of Hydrology*, 367(1–2), pp. 70–78. doi:10.1016/j.jhydrol.2008.12.028
-

-
- Girón, F. (1988) 'The Evacuation of Floods during the operation of reservoirs', Commission Internationale des Grands Barrages, San Francisco, Q.63-R.85, pp. 1261-1283.
 - Goodarzi, E. et al. (2014) 'Risk and uncertainty analysis for dam overtopping – Case study: The Doroudzan Dam, Iran', *Journal of Hydro-environment Research*, 8(1), pp.50-61. doi: 10.1016/j.jher.2013.02.001
 - Graham, L.P. et al. (2007) 'Assessing climate change impacts on hydrology from an ensemble of regional climate models, model scales and linking methods - a case study on the Lule River basin', *Climate Change*, 81, pp 293-307. doi: 10.1007/s10584-006-9215-2.
 - Gupta, H.V. et al. (1998) 'Toward improved calibration of hydrologic models: Multiple and noncommensurable measures of information', *Water Resources Research*, 34, pp.751–763, doi:10.1029/97WR03495
 - Hall, J. et al (2014) 'Understanding flood regime changes in Europe: A state-of-the-art assessment'. *Hydrology and Earth System Sciences*, 18, pp.2735–2772, doi:10.5194/hess-18-2735-2014.
 - Hargreaves, G. H. (1981) 'Responding to tropical climates' *The 1980-81 Food and Climate Review*, The Food and Climate Forum, Aspen Institute for Humanistic Studies, Boulder, Colorado, 29–32.
 - Hargreaves, G. H. and Samani, Z. A. (1985) 'Reference crop evapotranspiration from temperature', *Applied Engineering in Agriculture*, 1, pp. 96–99. doi:10.13031/2013.26773
 - Hirabayashi, Y. et al. (2013) 'Global flood risk under climate change', *Nature Climate Change*, 3(9), pp. 816–821. doi:10.1038/nclimate1911.
 - Hlavčová, K. et al. (2007) 'A simple model for estimation of climate change induced extreme daily precipitation changes for flash flood modelling', In: Heinonen, M. (Ed.), *The 3rd International Conference on Climate and Water*, Finnish Environment Institute SYKE, Helsinki, pp. 188–193.
 - Hochrainer, S. et al. (2010) 'The European Union Solidarity Fund. Its legitimacy, viability and efficiency', *Mitigation and Adaptation Strategies for Global Change*, 15(7), pp.797–810. doi: 10.1007/s11027-009-9209-2
 - Hosking, J.R.M and Wallis, J.R. (1997) 'Regional Frequency Analysis: An Approach Based on L-moments', Cambridge University Press, UK. doi:10.1017/cbo9780511529443
 - Iglesias, A. et al. (2007) 'Challenges to Manage the Risk of Water Scarcity and Climate Change in the Mediterranean', *Water Resources Management*, 21, pp. 775–788. doi: 10.1007/s11269-006-9111-6.
 - IPCC (2012) 'Glossary of terms, in: Managing the Risks of Extreme Events and Disasters to Advance Climate Change Adaptation, edited by: Field, C., Barros, V., Stocker, T., Qin, D., Dokken, D., Ebi, K., Mastrandrea, M., Mach, K., Plattner, G.-K., Allen, S., Tignor, M., and Midgley, P., A Special Report of Working Groups I and II of the Intergovernmental Panel on Climate Change (IPCC), Cambridge University Press, Cambridge, UK, New York, NY, USA, pp. 555–564.
 - IPCC (2014) 'Impacts, Adaptation, and Vulnerability, Part A: Global and Sectoral Aspects, Contribution of Working Group II to the Fifth Assessment Report of the Intergovernmental Panel on Climate Change, Cambridge Univ. Press, Cambridge, UK, New York, NY, USA, 20.
 - Jacob, D. et al. (2020) 'Regional climate downscaling over Europe: perspectives from the EURO-CORDEX community', *Regional Environmental Change* 20(51) doi: 10.1007/s10113-020-01606-9
 - Jandora, J. et al. (2008) 'The failure of embankment dams due to overtopping'. Brno, Czechia: VUTUM
-

-
- Jiménez-Álvarez, A. et al. (2013) 'Bases metodológicas del mapa de caudales máximos de las cuencas intercomunitarias', Centro de Estudios y Experimentación de Obras Públicas, Madrid, Spain, 96 pp. (In Spanish).
 - Jonkman, S. and Kelman, I. (2005) 'An analysis of the causes and circumstances of flood disaster deaths'. *Disasters*, 29(1), pp. 75-97. doi: 10.1111/j.0361-3666.2005.00275.x.
 - Katz, R. W. (1999) 'Techniques for Estimating Uncertainty in Climate Change Studies', in Carter, T. R., Hulme, M., and Viner, D. (eds.), *Representing Uncertainty in Climate Change Scenarios and Impact Studies*, ECLAT-2 Workshop Report Number 1, Climatic Research Unit, Norwich, U.K. (in press).
 - Kendon, E. J. et al. (2018) 'When will we detect changes in short-duration precipitation extremes?', *Journal of Climate*, 31, pp. 2945–2964. doi:10.1175/JCLI-D-17-0435.1
 - Kim, J. et al. (2013) 'Impacts of changes in climate and land use / land cover under IPCC RCP scenarios on streamflow in the Hoeya River Basin, Korea', *Science of the Total Environment*, 452–453, pp. 181–195. doi: 10.1016/j.scitotenv.2013.02.005.
 - Kim, J. et al. (2019) 'The role of rainfall spatial variability in estimating areal reduction factors', *Journal of Hydrology*, 568(October 2018), pp. 416–426. doi:10.1016/j.jhydrol.2018.11.014.
 - Klipsch, J.D. and Hurst, M.B. (2007) 'HEC-ResSim reservoir system simulation user's manual version 3.0'. Davis, CA: US Army Corps of Engineers, 512
 - Konapala, G. et al. (2020) 'Climate change will affect global water availability through compounding changes in seasonal precipitation and evaporation', *Nature Communications*, 11(3044). doi: 10.1038/s41467-020-16757-w.
 - Kourgialas, N. N. and Karatzas, G. P. (2011) 'Gestion des inondations et méthode de modélisation sous SIG pour évaluer les zones d'aléa inondation-une étude de cas', *Hydrological Sciences Journal*, 56(2), pp. 212–225. doi:10.1080/02626667.2011.555836
 - Koutsoyiannis, D. and Foufoula-Georgiou, E. (1993) 'A scaling model of a storm hyetograph' *Water Resources Research*, 29(7), pp. 2345–2361. doi:10.1029/93WR00395
 - Kriaučiūnienė, J. et al. (2008) 'Climate change impact on hydrological processes in Lithuanian Nemunas river basin'. *Baltica* 21 (1–2), pp. 51–61.
 - Krysanova, V. et al. (2018) 'How the performance of hydrological models relates to credibility of projections under climate change', *Hydrological Sciences Journal*, 63(5), pp. 696–720. doi: 10.1080/02626667.2018.1446214
 - Kundzewicz, Z. W. et al. (2017) 'Differences in flood hazard projections in Europe—their causes and consequences for decision making', *Hydrological Sciences Journal*, 62(1), pp. 1–14. doi: 10.1080/02626667.2016.1241398.
 - Lawrence, D. and Haddeland, I. (2011) 'Uncertainty in hydrological modelling of climate change impacts in four Norwegian catchments', *Hydrology Research*, 42(6), pp. 457–471. doi:10.2166/nh.2011.010
 - Lee, B. and You, G. J. (2013) 'An assessment of long-term overtopping risk and optimal termination time of dam under climate change', *Journal of Environmental Management*, 121, pp. 57–71. doi: 10.1016/j.jenvman.2013.02.025.
 - Lenderink, G. and Van Meijgaard, E. (2008) 'Increase in hourly precipitation extremes beyond expectations from temperature changes', *Nature Geoscience*, 1(8), pp. 511–514. <https://doi.org/10.1038/ngeo262>
 - Li, C. et al. (2019) 'Larger Increases in More Extreme Local Precipitation Events as Climate Warms', *Geophysical Research Letters*, 46(12), pp. 6885–6891. doi: 10.1029/2019GL082908.
 - Llasat, M. C. et al. (2016) 'Trends in flash flood events versus convective precipitation in the Mediterranean region: The case of Catalonia', *Journal of Hydrology*, 541(October), pp. 24–37. doi:10.1016/j.jhydrol.2016.05.040
-

-
- Lompi, M. et al. (2021) 'Future Flood Hazard Assessment for the City of Pamplona (Spain) Using an Ensemble of Climate Change Projections', *Water (Switzerland)*, 13(792).
 - Lompi, M. et al. (2022) 'Improving flash flood risk assessment using a simple approach for extreme rainfall scaling and storms transposition', *Journal of Flood Risk Management*, pp. 1–14. doi:10.1111/jfr3.12796
 - Luo, X. et al. (2011) 'Comparison of interpolation methods for spatial precipitation under diverse orographic effects', *Proc. - 2011 19th Int. Conf. Geoinformatics*, *Geoinformatics 2011*, doi:10.1109/GeoInformatics.2011.5980666.
 - Luu, L.N. et al. (2018) 'Attribution of extreme rainfall events in the South of France using EURO-CORDEX simulations'. *Geophysical Research Letters*. doi:10.1029/2018gl077807
 - Madsen, H. et al (2013). 'A review of applied methods in Europe for flood-frequency analysis in a changing environment', *Tech. rep.*, the report has been prepared by Working Group 4 (Flood frequency estimation methods and environmental change). Freely available online – Official URL link provides full text <<http://nora.nerc.ac.uk/501751/>>.
 - Madsen, H. et al. (2014) 'Review of trend analysis and climate change projections of extreme precipitation and floods in Europe', *Journal of Hydrology*, 519, pp. 3634–3650. doi:10.1016/j.jhydrol.2014.11.003.
 - Mahmoud, S.H. and Gan, T.Y. (2018) 'Urbanization and climate change implications in flood risk management: developing an efficient decision support system for flood susceptibility mapping' *Science of Total Environment*, 636, pp. 152–167. doi:10.1016/j.scitotenv.2018.04.282.
 - Marahatta, S. et al. (2021) 'Application of SWAT in Hydrological Simulation of Complex Mountainous River Basin (Part II: Climate Change impact Assessment)', *Water (Switzerland)*, 13(1548). doi: 10.3390/w13111548.
 - Marchi, L. et al. (2010) 'Characterisation of selected extreme flash floods in Europe and implications for flood risk management', *Journal of Hydrology*, 394(1–2), pp.118–133. doi:10.1016/j.jhydrol.2010.07.017
 - Matott, L. S. et al. (2009) 'Evaluating uncertainty in integrated environmental models: A review of concepts and tools', *Water Resources Research*, 45(W06421). doi: 10.1029/2008WR007301.
 - Mediero, L. et al. (2011) 'Probabilistic calibration of a distributed hydrological model for flood forecasting', *Hydrological Sciences Journal*, 56(7), pp. 1129–1149. doi:10.1080/02626667.2011.610322.
 - Mediero, L. et al. (2014) 'Detection and attribution of trends in magnitude, frequency and timing of floods in Spain', *Journal of Hydrology*, 517, pp. 1072–1088. doi:10.1016/j.jhydrol.2014.06.040.
 - Meinshausen, M. et al. (2011) 'The RCP greenhouse gas concentrations and their extensions from 1765 to 2300', *Climatic Change*, 109(1), pp. 213–241. doi:10.1007/s10584-011-0156-z.
 - Michailidi, E. M. and Bacchi, B. (2017) 'Dealing with uncertainty in the probability of overtopping of a flood mitigation dam', *Hydrology and Earth System Sciences*, 21, pp. 2497–2507. doi: 10.5194/hess-21-2497-2017.
 - Michele, C. et al. (2001) 'The derivation of areal reduction factor of storm rainfall from its scaling properties', *Water Resources*, 37(12), pp. 3247–3252. doi:10.1029/2001wr000346
 - Miglietta, M.M. and Davolio, S. (2022) 'Dynamical forcings in heavy precipitation events over Italy: lessons from the HyMeX SOP1 campaign', *Hydrology and Earth System Sciences*, 26, pp.627–646. doi:10.5194/hess-26-627-2022
 - Miller, J.D. and Hutchins, M. (2017) 'The impacts of urbanisation and climate change on urban flooding and urban water quality: A review of the evidence concerning the United

-
- Kingdom', *Journal of Hydrology Regional Studies*, 12, pp. 345–362. doi:10.1016/j.ejrh.2017.06.006.
- Milly, P.C.D. et al. (2008) 'Stationarity Is Dead – Whither Water management?' *Science*, 319, pp. 573–574. doi: 10.1126/science.1151915
 - Myhre, G. et al. (2019) 'Frequency of extreme precipitation increases extensively with event rareness under global warming', *Scientific Reports*, 9(16063), pp. 1–10. doi: 10.1038/s41598-019-52277-4.
 - Mogil, H. M. et al. (1978) 'NWS's Flash Flood Warning and Disaster Preparedness Programs', *Bulletin of the American Meteorological Society*, 59(6), pp. 690–699. doi:10.1175/1520-0477(1978)059<0690:nffwad>2.0.co;2
 - Monteith, J. L. (1965) 'Evaporation and environment', *Symposia of the Society for Experimental Biology*, 19, pp. 205–224.
 - Morales-Torres, A. et al. (2016) 'The suitability of risk reduction indicators to inform dam safety management', *Structure and Infrastructure Engineering*, 12(11), pp. 1465–1476. doi: 10.1080/15732479.2015.1136830
 - Najibi, N. and Devineni, N. (2018) 'Recent trends in the frequency and duration of global floods', *Earth System Dynamics*, 9, pp. 757–783. doi: 10.5194/esd-9-757-2018.
 - Nash, J. E. and Sutcliffe, J.V. (1970) 'River flow forecasting through conceptual models part I — A discussion of principles', *Journal of Hydrology*, 10(3), pp. 282–290. doi:10.1016/0022-1694(70)90255-6
 - Natural Environment Research Council (NERC) (1975). *Flood Studies Report*. Vol. 1, London.
 - Nilawar, A. P. and Waikar, M. L. (2019) 'Impacts of climate change on stream flow and sediment concentration under RCP 4.5 and 8.5: A case study in Purna river basin, India', *Science of the Total Environment*, 650, pp. 2685–2696. doi: 10.1016/j.scitotenv.2018.09.334.
 - Nnadi, F. N. et al. (1999) 'Comparison of design storm concepts using continuous simulation with short duration storms', *Journal of the American Water Resources Association*, 35(1), pp. 61–72. doi:10.1111/j.1752-1688.1999.tb05452.x
 - Novembre, N. et al. (2015) 'Climate Change in Hydrologic Hazard Analyses: Friant Dam Pilot Study – Part II: Using the SEFM with Climate-Adjusted Hydrometeorological Inputs', *Technical Memorandum 8250-2015-010*, U.S. Department of the Interior, Bureau of Reclamation.
 - Oubennaceur, K. et al. (2021) 'Flood Risk Assessment under Climate Change: The Petite Nation River Watershed', *Climate*, 9(8), 125. doi: 10.3390/cli9080125.
 - Osuch, M. et al. (2012) 'Adaptation strategy of Poland to climate change'. IOS (in Polish).
 - Pastor, A. V. et al. (2014) 'Accounting for environmental flow requirements in global water assessment', *Hydrology and Earth System Sciences*, 18, pp. 5041–5059. doi: 10.5194/hess-18-5041-2014.
 - Pavlovic, S. et al. (2016) 'Intercomparison of selected fixed-area areal reduction factor methods', *Journal of Hydrology*, 537, pp. 419–430. doi:10.1016/j.jhydrol.2016.03.027
 - Pechlivanidis, I.G. et al. (2017) 'Analysis of hydrological extremes at different hydro-climatic regimes under present and future conditions', *Climate Change*, 141, pp. 467–481, doi:10.1007/s10584-016-1723-0.
 - Pham, H.V. et al. (2019) 'Coupling scenarios of climate and land-use change with assessments of potential ecosystem services at the river basin scale', *Ecosyst Service*, 40, 101045, doi:10.1016/j.ecoser.2019.101045.
 - Prein, A.F. et al. (2017) 'The future intensification of hourly precipitation extremes', *Nature Climate Change*, 7, pp. 48–52. doi:10.1038/nclimate3168.
-

-
- Prudhomme, C. and Davies, H. (2009) 'Assessing uncertainties in climate change impact analyses on the river flow regimes in the UK. Part 2: future climate', *Climatic Change*, 93, pp. 197–222. doi: 10.1007/s10584-008-9461-6.
 - Quintero, F. et al. (2018) 'Assessment of changes in flood frequency due to the effects of climate change: Implications for engineering design', *Hydrology*, 5(19). doi: 10.3390/hydrology5010019.
 - Ramos M.H. et al. (2005) 'Visualization of storm severity', *Journal of Hydrology*, 315(1–4), pp.295–307. doi:10.1016/j.jhydrol.2005.04.007.
 - Refsgaard, J. C. et al. (2007) 'Uncertainty in the environmental modelling process - A framework and guidance', *Environmental Modelling and Software*, 22, pp. 1543–1556. doi: 10.1016/j.envsoft.2007.02.004.
 - Riahi, K. et al. (2011) 'RCP 8.5 — A scenario of comparatively high greenhouse gas emissions', *Climatic Change*, 109, pp. 33–57. doi: 10.1007/s10584-011-0149-y.
 - Ricciardelli, E. et al. (2018) 'Analysis of Livorno heavy rainfall event: Examples of satellite-based observation techniques in support of numerical weather prediction', *Remote Sensing*, 10(10). doi:10.3390/rs10101549
 - Rojas, R. et al. (2012) 'Assessment of future flood hazard in Europe using a large ensemble of bi-as-corrected regional climate simulations'. *Journal of Geophysical Research Atmospheres*, 117, doi:10.1029/2012JD017461.
 - Roudier, P. et al. (2016) 'Projections of future floods and hydrological droughts in Europe under a +2°C global warming', *Climatic Change*, 135(2), pp. 341–355. doi: 10.1007/s10584-015-1570-4.
 - Saharia, M. et al. (2017) 'Mapping Flash Flood Severity in the United States', *Journal of Hydrometeorology*, 18(2), pp. 397–411. doi:10.1175/jhm-d-16-0082.1.
 - Segond, M. L. et al. (2007) 'The significance of spatial rainfall representation for flood runoff estimation: a numerical evaluation based on the Lee catchment, UK'. *Journal of Hydrology*, 347, pp. 116–131. doi:10.1016/j.jhydrol.2007.09.040.
 - Seibert, J. and Vis, M. J. P. (2012) 'Teaching hydrological modeling with a user-friendly catchment-runoff-model software package', *Hydrology and Earth System Sciences*, 16, pp. 3315–3325. doi: 10.5194/hess-16-3315-2012.
 - Sharma, A. et al. (2018) 'If Precipitation Extremes Are Increasing, Why Aren't Floods?' *Water Resource Research*, 54, pp. 8545–8551, doi:10.1029/2018WR023749.
 - Sivapalan, M. and Blöschl, G. (1998) 'Transformation of point rainfall to areal rainfall: intensity–duration–frequency curves', *Journal of Hydrology*, 204, (1–4), pp.150–167. doi:10.1016/S0022-1694(97)00117-0
 - Soriano, E. et al. (2020) 'Quantification of expected changes in peak flow quantiles in climate change by combining continuous hydrological modelling with the modified curve number method', *Water Resources Management*, 34(14), pp.1-17. doi:10.1007/s11269-020-02670-w.
 - Šraj, M. et al. (2016) 'The influence of non-stationarity in extreme hydrological events on flood frequency estimation'. *Journal of Hydrology and Hydromechanics*, 64(4), pp. 426-437, doi: 10.1515/johh-2016-0032
 - Stevenson, T. et al. (1981) 'The Stevenson formula for predicting wave height', *Technical note, Proceedings of the Institution of Civil Engineers*, 71(3), pp. 907-909. doi: 10.1680/iicep.1981.1826.
 - Sunyer, M.A. et al. (2012) 'A comparison of different regional climate models and statistical downscaling methods for extreme rainfall estimation under climate change', *Atmospheric Research*, 103, pp. 119-128 doi: 10.1016/j.atmosres.2011.06.011
 - Svensson, C. and Jones, D.A. (2010) 'Review of methods for deriving areal reduction factors', *Journal of Flood Risk Management*, 3(3), pp. 232–245. doi:10.1111/j.1753-318X.2010.01075.x.
-

-
- Tabari, H. (2020) 'Climate change impact on flood and extreme precipitation increases with water availability', *Scientific Report*, 10, pp. 1–10, doi:10.1038/s41598-020-70816-2.
 - Tarouilly, E. and Lettenmaier, D. (2021) 'Uncertainty in Probable Maximum Precipitation for Dam Safety', *EGU General Assembly Conference Abstracts*, doi: 10.5194/egusphere-egu21-2861
 - Tennant, D. L. (1976) 'Instream Flow Regimens for Fish, Wildlife, Recreation and Related Environmental Resources', *Fisheries Magazine*, 1(4), pp. 6–10. doi: 10.1577/1548-8446(1976)001<0006:IFRFFW>2.0.CO;2.
 - Tofiq, F.A. and Guven, A. (2014) 'Prediction of design flood discharge by statistical downscaling and General Circulation Models', *Journal of Hydrology*, 517, pp. 1145–1153, doi:10.1016/j.jhydrol.2014.06.028.
 - Thomson, A. M. et al. (2011) 'RCP 4.5: a pathway for stabilization of radiative forcing by 2100', *Climatic Change*, 109, pp. 77–94. doi: 10.1007/s10584-011-0151-4.
 - Turco, M. et al. (2013) 'Large biases and inconsistent climate change signals in ENSEMBLES regional projections', *Climate Change*, 120(4), pp.859–869. doi:10.1007/s10584-013-0844-y
 - USACE (2013) 'Hydrologic Modeling System HEC-HMS', User's Manual, version 4.0
 - USACE (2016) 'Guidance for Incorporating Climate Change Impacts to Inland Hydrology in Civil Works Studies, Designs, and Projects', United States Army Corps of Engineers, EBC 2016-25.
 - Van Der Keur, P. et al. (2010) 'Identifying Uncertainty Guidelines for Supporting Policy Making in Water Management Illustrated for Upper Guadiana and Rhine Basins Identifying Uncertainty Guidelines for Supporting Policy Making in Water Management Illustrated for Upper Guadiana and Rhine', *Water Resources Management*, 24(14), pp. 3901–3938. doi: 10.1007/s11269-010-9640-x.
 - Van Renssen, S. (2013) 'EU adaptation policy sputters and starts', *Nature Climate Change*, 3, pp. 614–615. doi:10.1038/nclimate1943.
 - Venugopal, V. et al. (1999) 'Evidence of dynamic scaling in space-time rainfall', *Journal of Geophysical Research Atmospheres*, 104(D24), pp. 31599–31610. doi:10.1029/1999JD900437
 - Winsemius, H. C. et al. (2015) 'Global drivers of future river flood risk', *Nature Climate Change*, 6, pp. 381–385. doi: 10.1038/nclimate2893.
 - Woolway, R. I. et al. (2020) 'Global lake responses to climate change', *Nature Reviews Earth & Environment*, 1, pp. 388–403. doi: 10.1038/s43017-020-0067-5.
 - Wright, D. B. et al. (2020) 'Six decades of rainfall and flood frequency analysis using stochastic storm transposition: Review, progress, and prospects', *Journal of Hydrology*, 585, 124816, doi:10.1016/j.jhydrol.2020.124816
 - Yu, L. et al. (2021) 'Multi-objective optimal operation of cascade hydropower plants considering ecological flow under different ecological conditions', *Journal of Hydrology*, 601(126599). doi: 10.1016/j.jhydrol.2021.126599.
 - Zhang, H. et al. (2013) 'Quantitative comparison of semi- and fully-distributed hydrologic models in simulating flood hydrographs on a mountain watershed in southwest China', *Journal of Hydrodynamics, Ser. B*, 25(6), pp.877-885, doi: 10.1016/S1001-6058(13)60436-9
 - Zhou, Q. et al. (2016) 'Impacts of future climate change on urban flood risks: benefits of climate mitigation and ad-aptations', *Hydrology and Earth System Sciences Discussions*, 1–31, doi:10.5194/hess-2016-369.
 - Zhang, Y. et al. (2016) 'Impacts of climate change on streamflows under RCP scenarios: A case study in Xin River Basin, China', *Atmospheric Research*. 178–179, pp. 521–534, doi:10.1016/j.atmosres.2016.04.018.
-

-
- Zhang, Y. et al. (2019) 'Assessment of future flash flood inundations in coastal regions under climate change scenarios - A case study of Hadahe River basin in northeastern China', *Science of the Total Environment*, 693, 133550. doi:10.1016/j.scitotenv.2019.07.356.
 - Zhang, Y. et al. (2021) 'Projection of changes in flash flood occurrence under climate change at tourist attractions', *Journal of Hydrology*, 595(126039).doi: 10.1016/j.jhydrol.2021.126039

Appendix A.

Future Design floods for the City of Pamplona with each climate model

Figures in this Appendix show the future design floods for the city of Pamplona, obtained with different climate model. The upper part of each figure represents the comparison between the current design flood (black dashed line) and the future design floods for the RCP 4.5 in a blue scale; the bottom part of each figure represents the comparison between the current design flood (black dashed line) and the future design floods for the RCP 8.5 in a brown scale. The columns correspond to the seven return periods considered in this thesis.

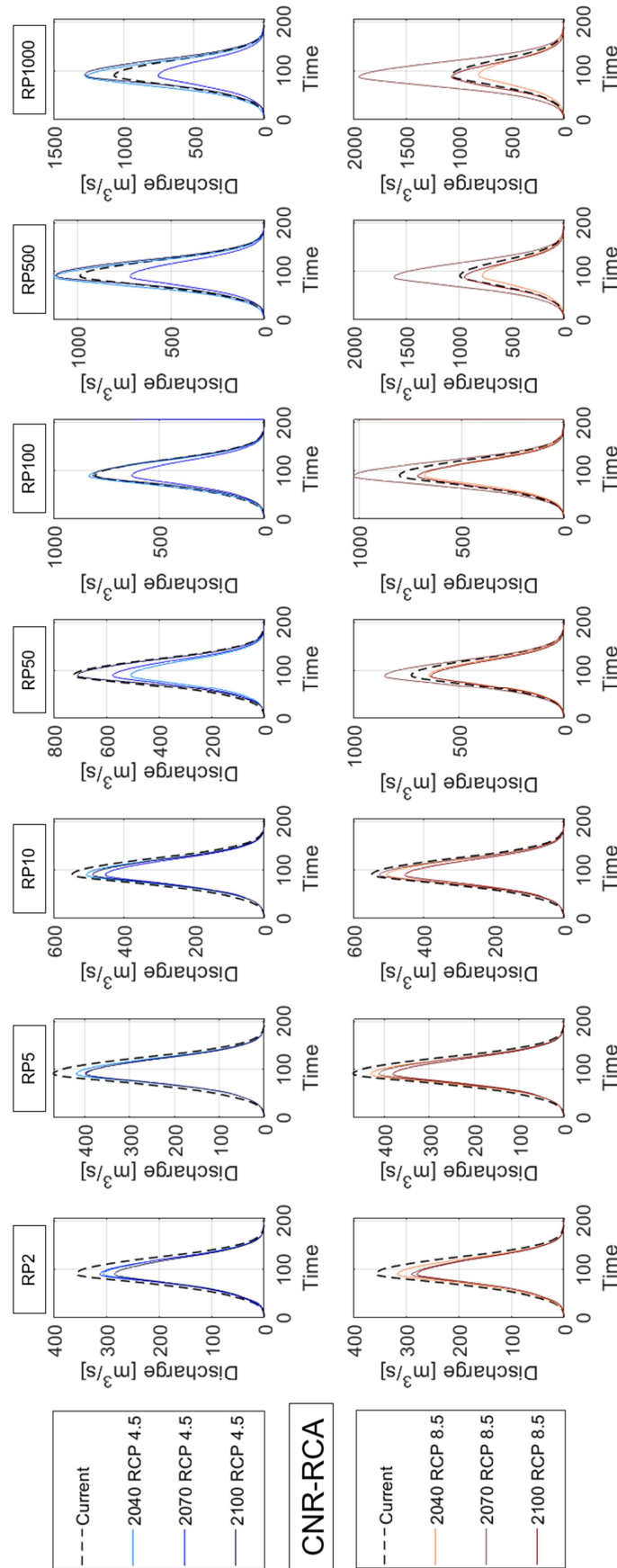


Figure A1. Hydrographs for the current (dashed black) and climate change (coloured) scenarios for the CNR-RCA climate model in the 3 periods and for the two Representative Concentration Pathways.

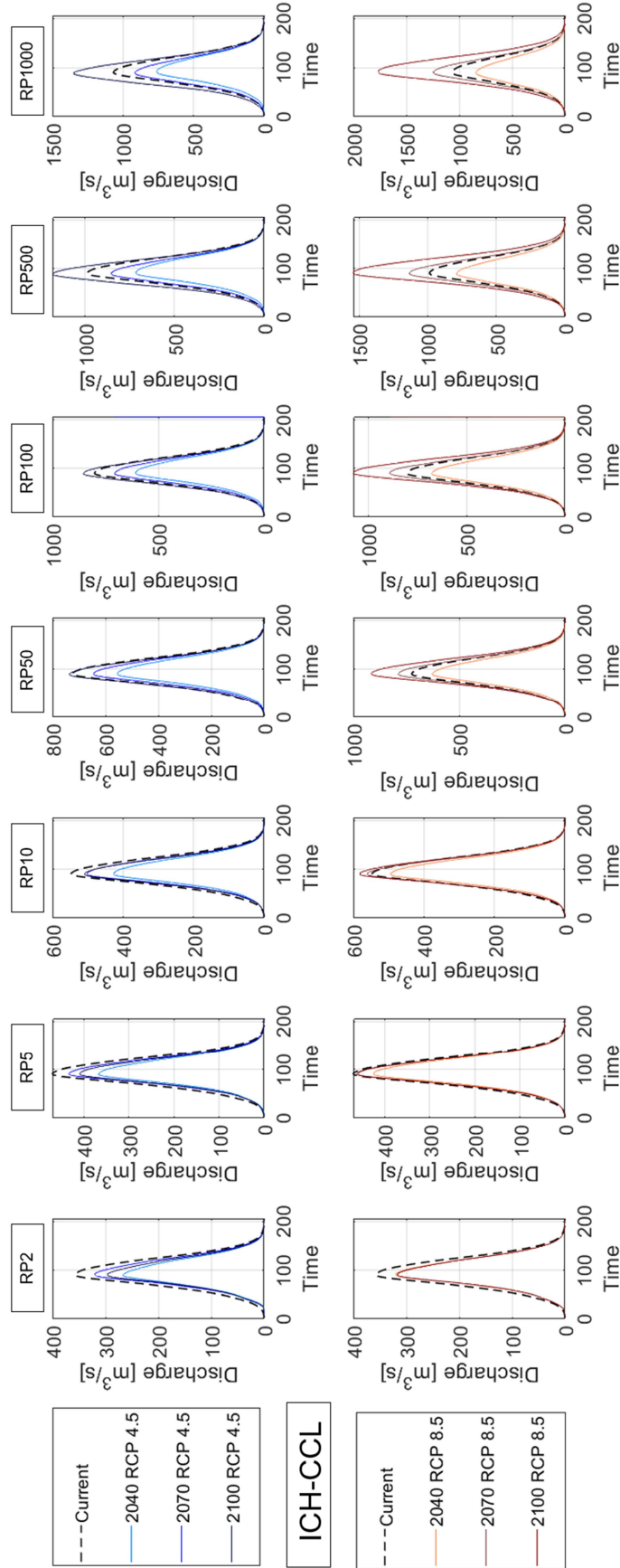


Figure A2. Hydrographs for the current (dashed black) and climate change (coloured) scenarios for the ICH-CCL climate model in the 3 periods and for the two Representative Concentration Pathways.

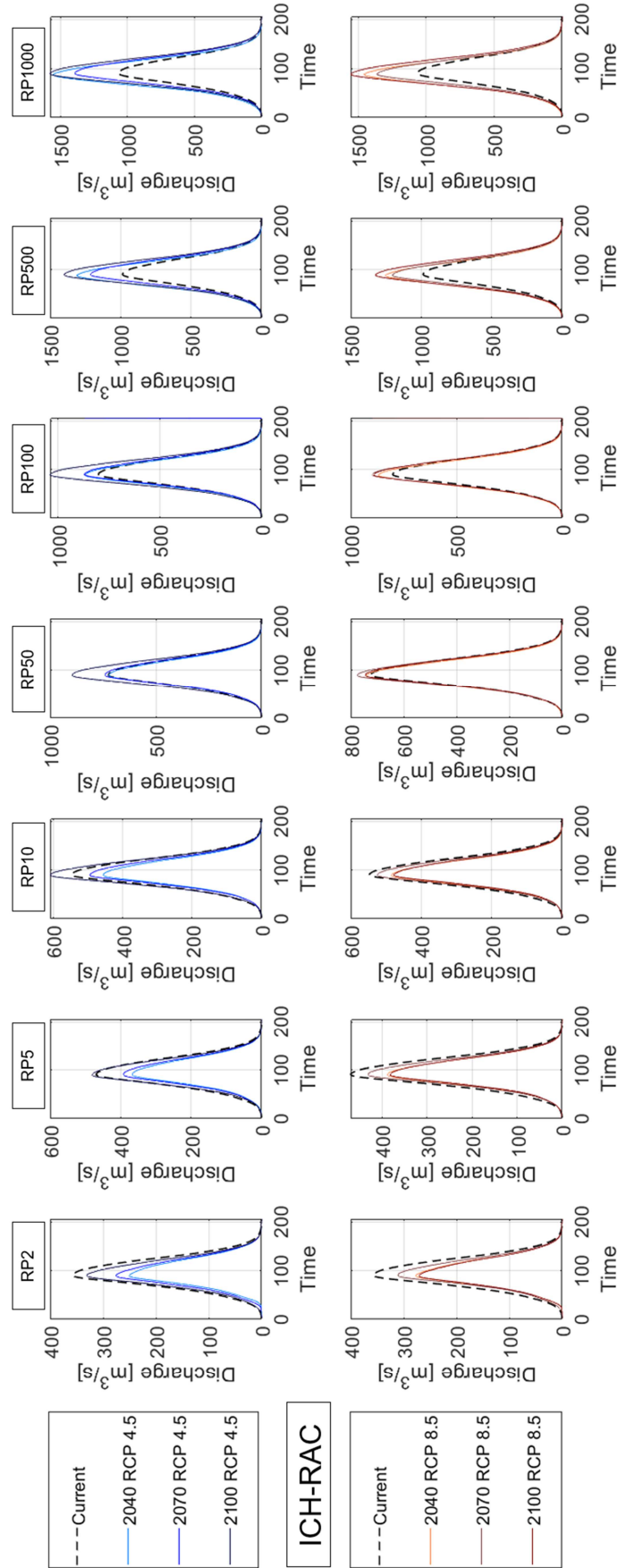


Figure A3. Hydrographs for the current (dashed black) and climate change (coloured) scenarios for the ICH-RAC climate model in the 3 periods and for the two Representative Concentration Pathways.

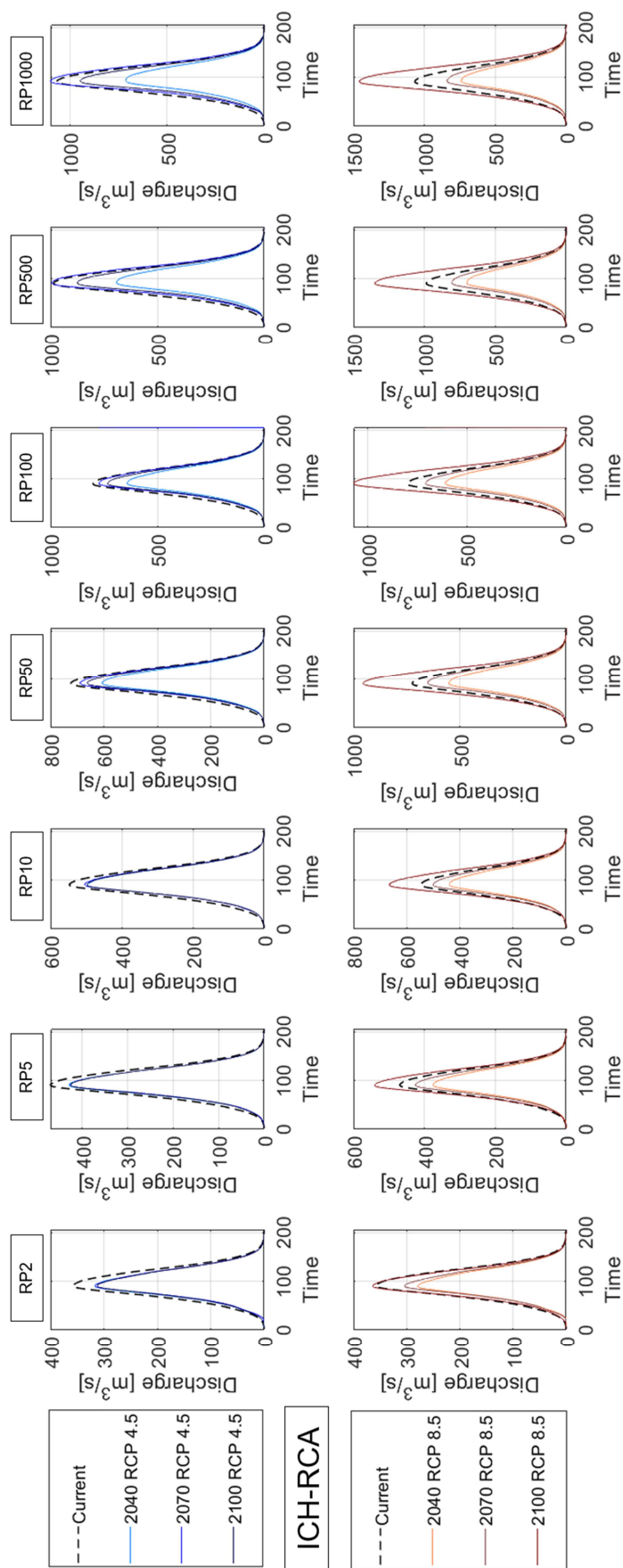


Figure A4. Hydrographs for the current (dashed black) and climate change (coloured) scenarios for the ICH-RCA climate model in the 3 periods and for the two Representative Concentration Pathways.

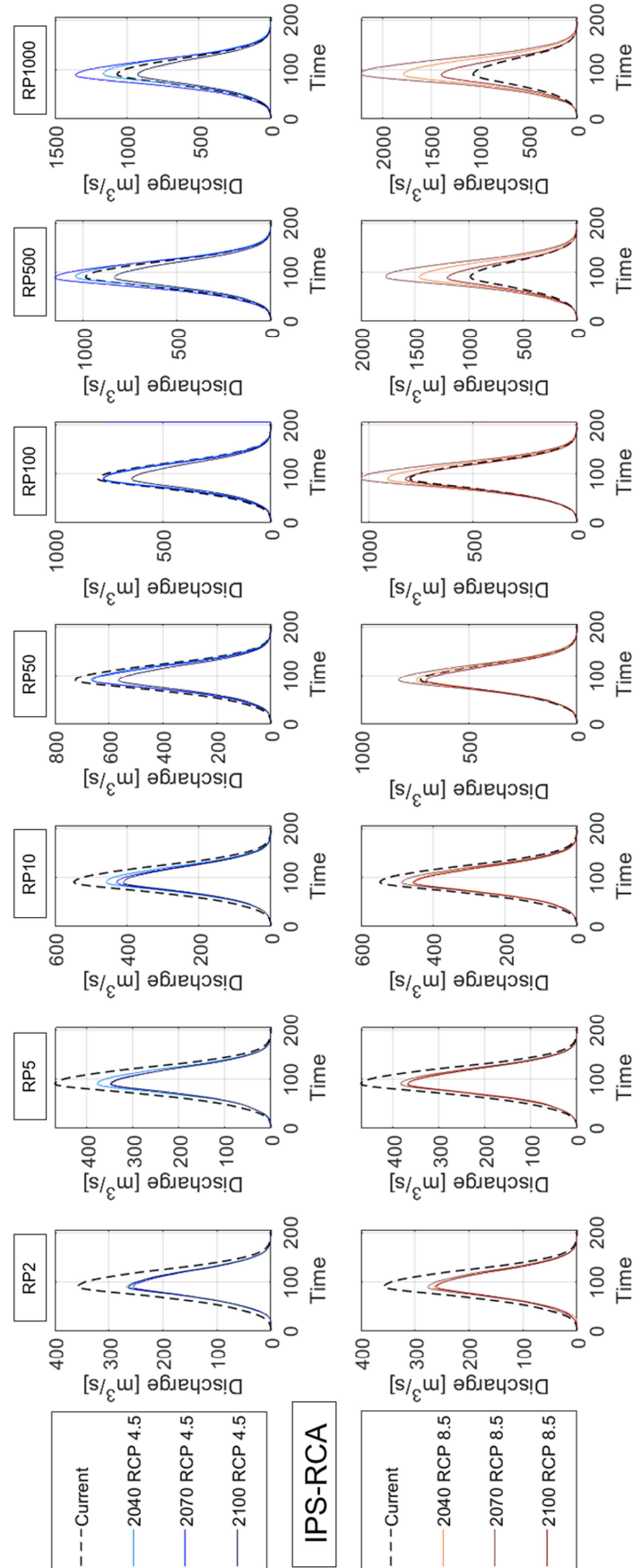


Figure A5. Hydrographs for the current (dashed black) and climate change (coloured) scenarios for the IPS-RCA climate model in the 3 periods and for the two Representative Concentration Pathways.

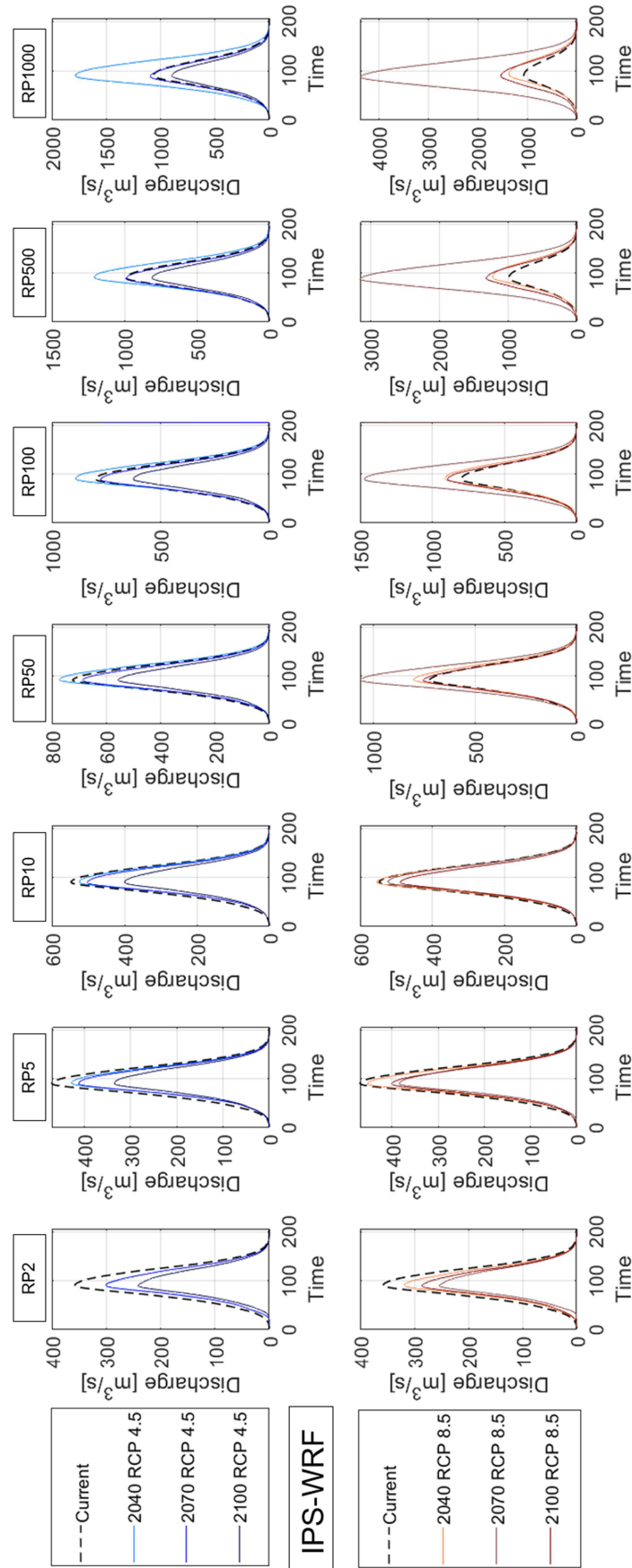


Figure A6. Hydrographs for the current (dashed black) and climate change (coloured) scenarios for the IPS-WRF climate model in the 3 periods and for the two Representative Concentration Pathways

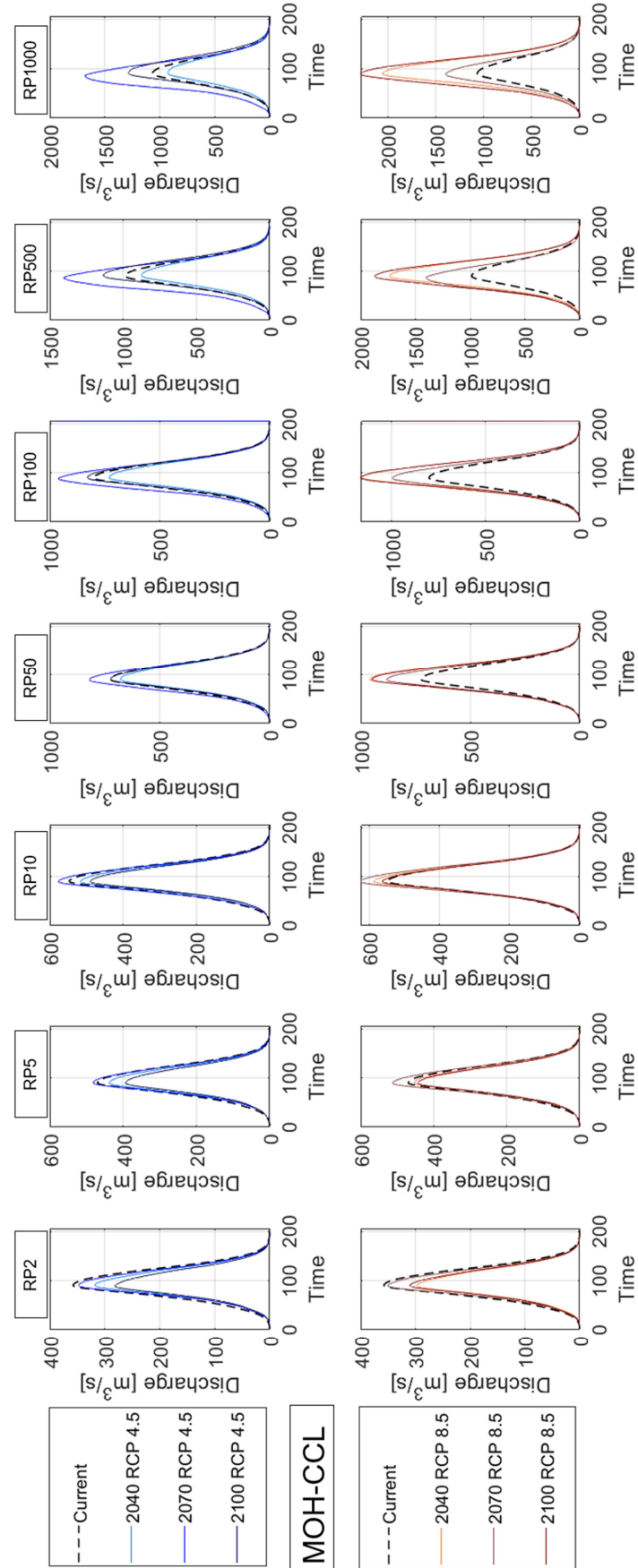


Figure A7. Hydrographs for the current (dashed black) and climate change (coloured) scenarios for the MOH-CCL climate model in the 3 periods and for the two Representative Concentration Pathways.

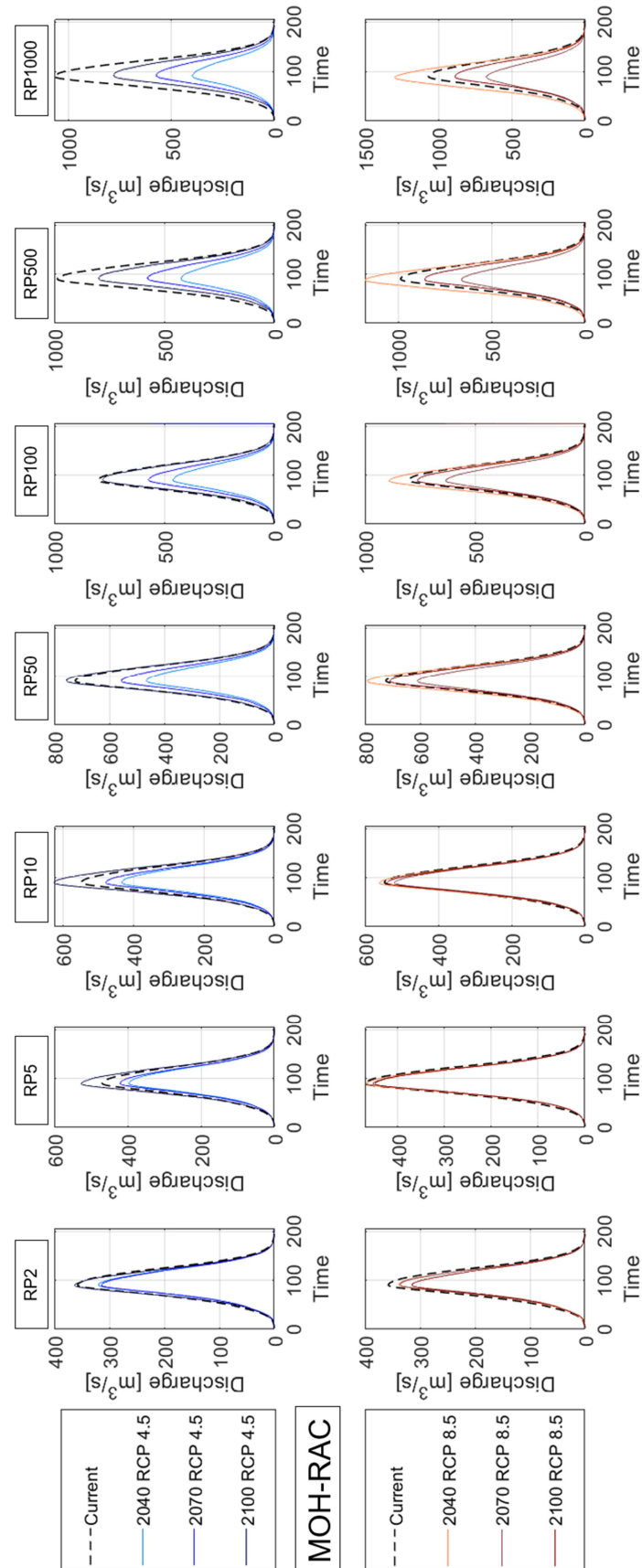


Figure A8. Hydrographs for the current (dashed black) and climate change (coloured) scenarios for the MOH-RAC climate model in the 3 periods and for the two Representative Concentration Pathways.

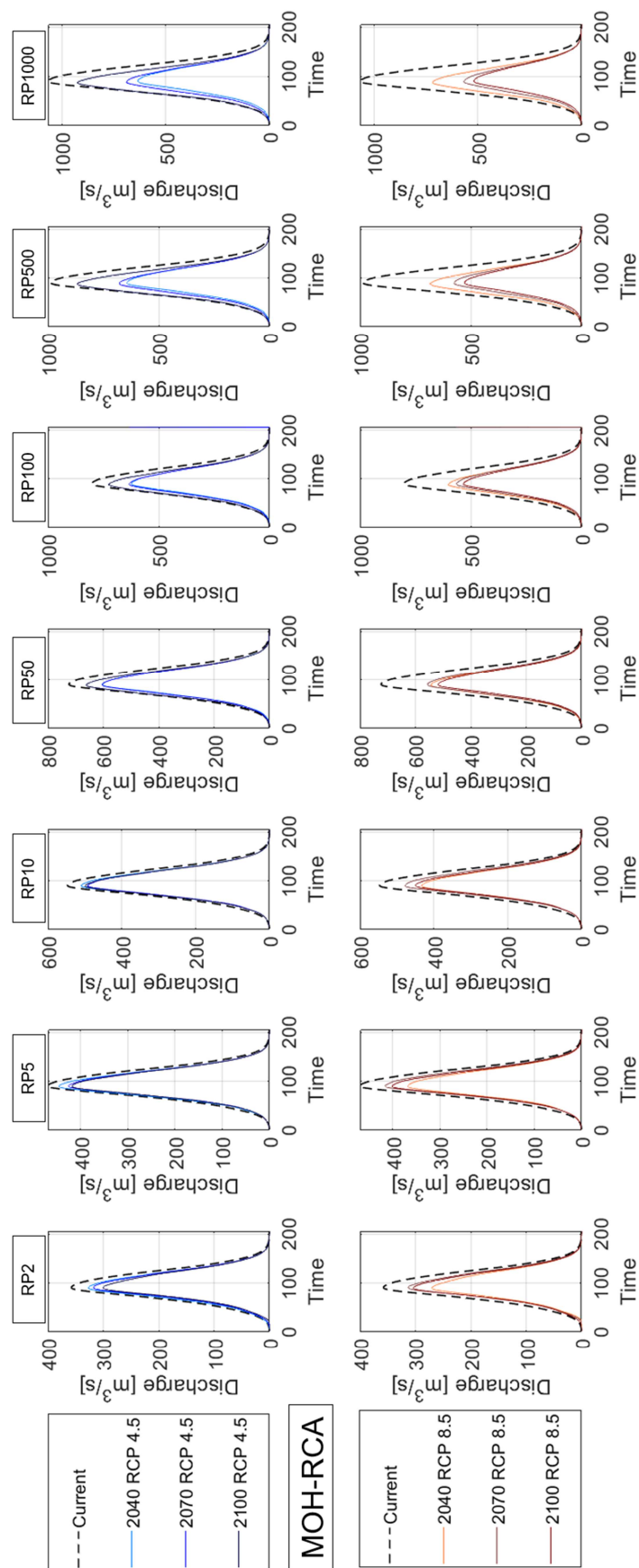


Figure A9. Hydrographs for the current (dashed black) and climate change (coloured) scenarios for the MOH-RCA climate model in the 3 periods and for the two Representative Concentration Pathways.

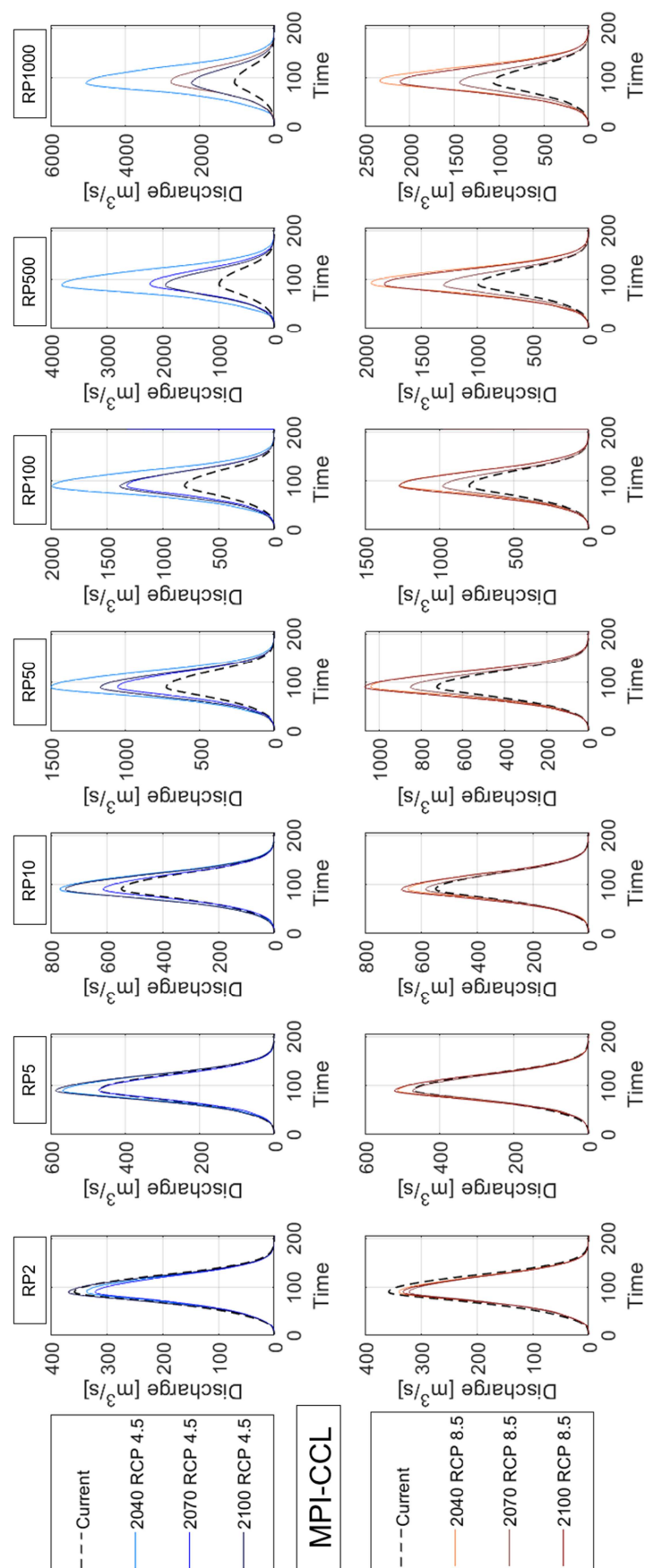


Figure A10. Hydrographs for the current (dashed black) and climate change (coloured) scenarios for the MPI-CCL climate model in the 3 periods and for the two Representative Concentration Pathways.

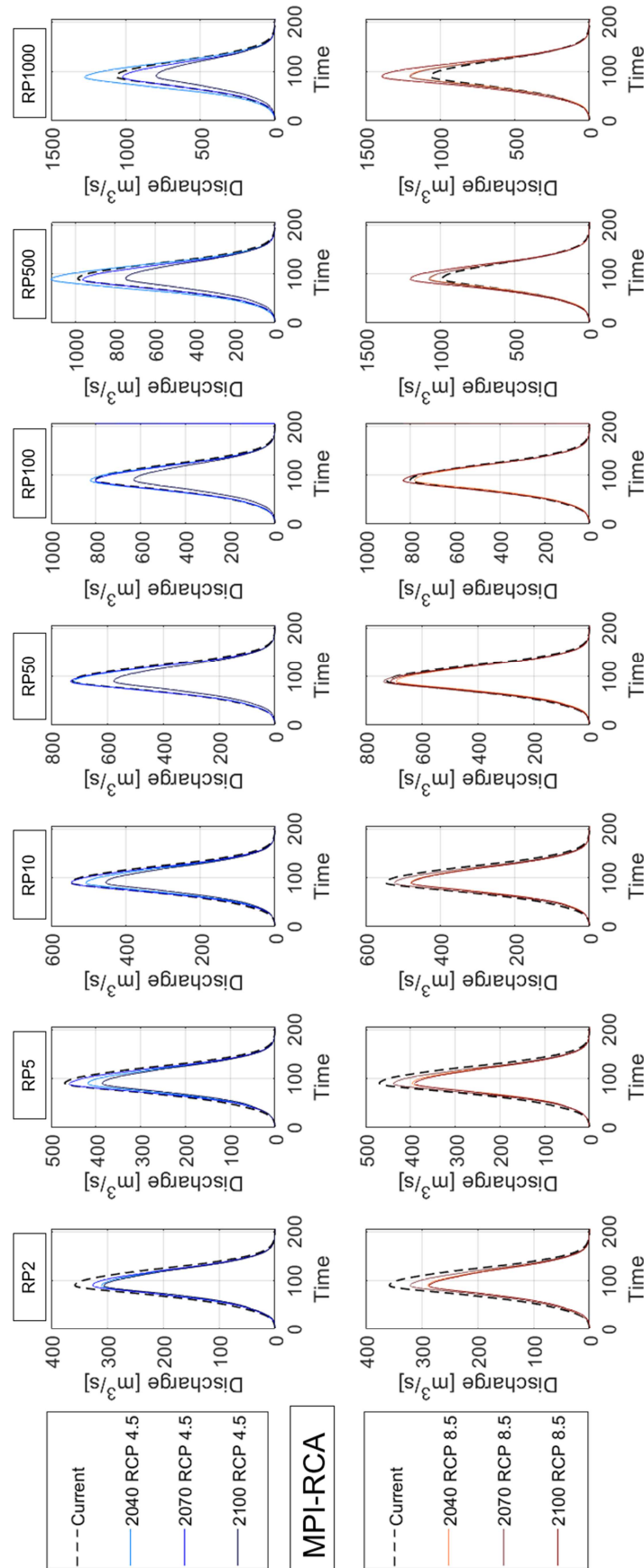


Figure A11. Hydrographs for the current (dashed black) and climate change (coloured) scenarios for the MPI-RCA climate model in the 3 periods and for the two Representative Concentration Pathways.

Appendix B.

Future inflow hydrographs and initial water levels of the Eugui dam for each climate model

Figures in this Appendix show the input of the stochastic procedure used to assess the impact of climate change on the hydrological dam safety of the Eugui Dam for each climate model. The inputs are the future water level frequency curve in each time window and RCP scenario and the inflow hydrograph associated with the seven return periods considered in the thesis for the three time windows. The upper part of the subplot shows the results of the HBV and reservoir operation model, the bottom part are the GEVs fitted on the RIBS output of Lompi et al. 2021.

In the upper part of the figures, the comparison between the water level frequency curves of the future and of the control period is shown for each climate model. In the bottom part of the figures, the future GEVs fitted to the maxima inflow peaks in the reservoir are compared with the GEV of the current scenario.

Each time window and emission scenarios is represented with a given colour. The RCP4.5 is described in a blue scale: cyan for 2011-2040 time window, blue for the 2041-2070, dark blue for the 2071-2100. In the same way, the RCP 8.5 is described in a brown scale where the darker colours are associate with time windows later in the future. In each subplot the control period is represented with a dotted green line.

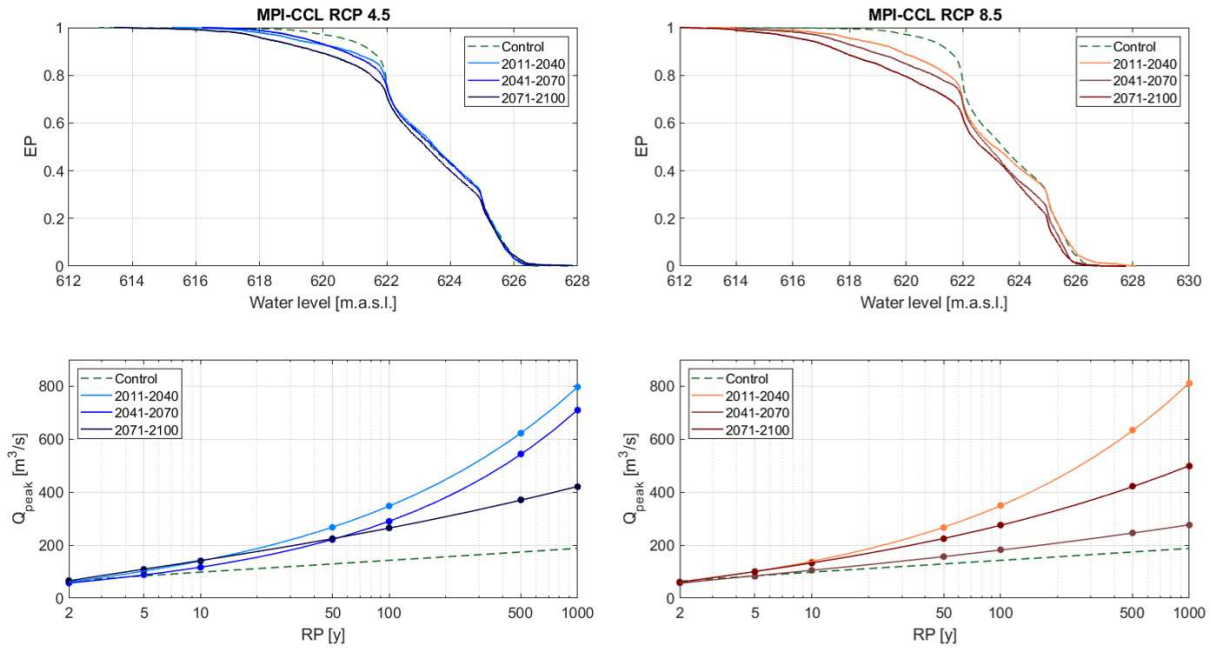


Figure B1: Initial reservoir water level and inflow peak discharge frequency curves for the MPI-CCL climate model in the three time windows. The left column shows the results for RCP 4.5. The right column offers the results for RCP 8.5. Each time window is represented with a given colour. Control periods are represented with dashed lines and future periods with solid lines.

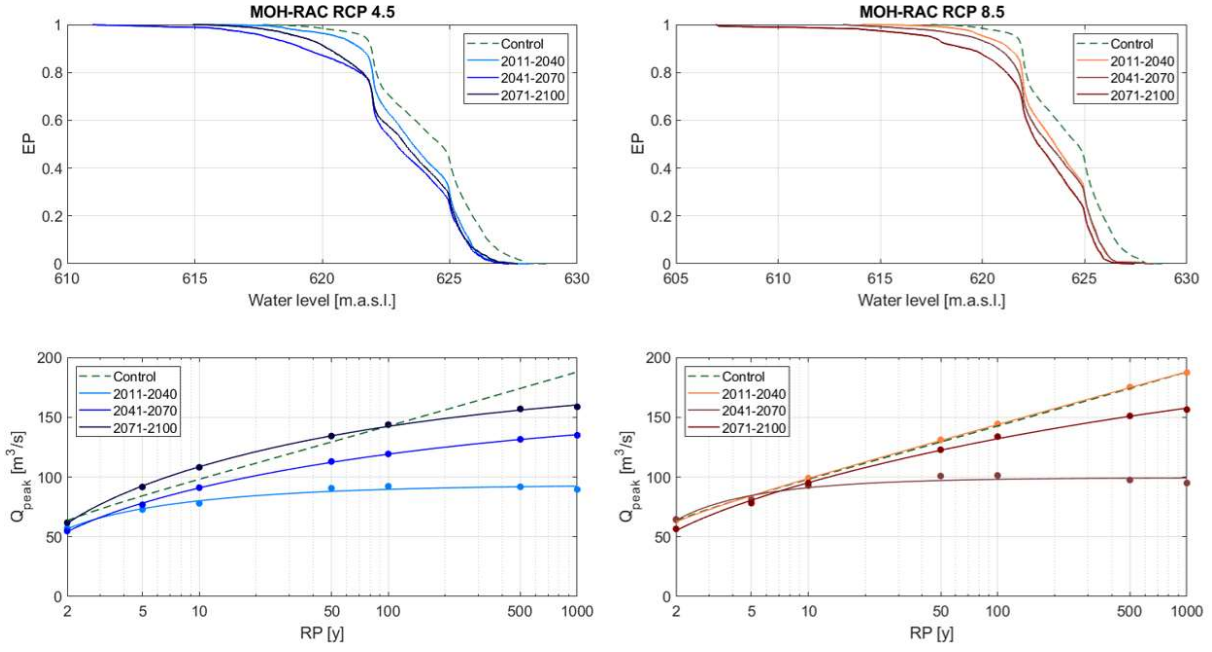


Figure B2: Initial reservoir water level and inflow peak discharge frequency curves for the MOH-RAC climate model in the three time windows. The left column shows the results for RCP 4.5. The right column offers the results for RCP 8.5. Each time window is represented with a given colour. Control periods are represented with dashed lines and future periods with solid lines.

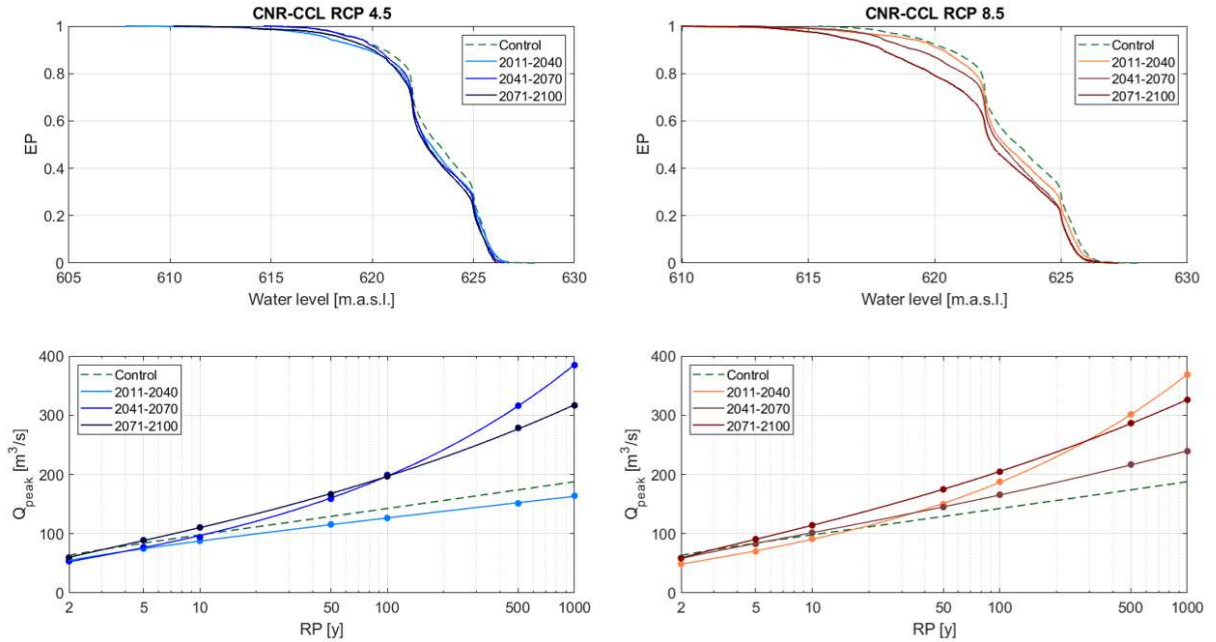


Figure B3: Initial reservoir water level and inflow peak discharge frequency curves for the CNR-CCL climate model in the three time windows. The left column shows the results for RCP 4.5. The right column offers the results for RCP 8.5. Each time window is represented with a given colour. Control periods are represented with dashed lines and future periods with solid lines.

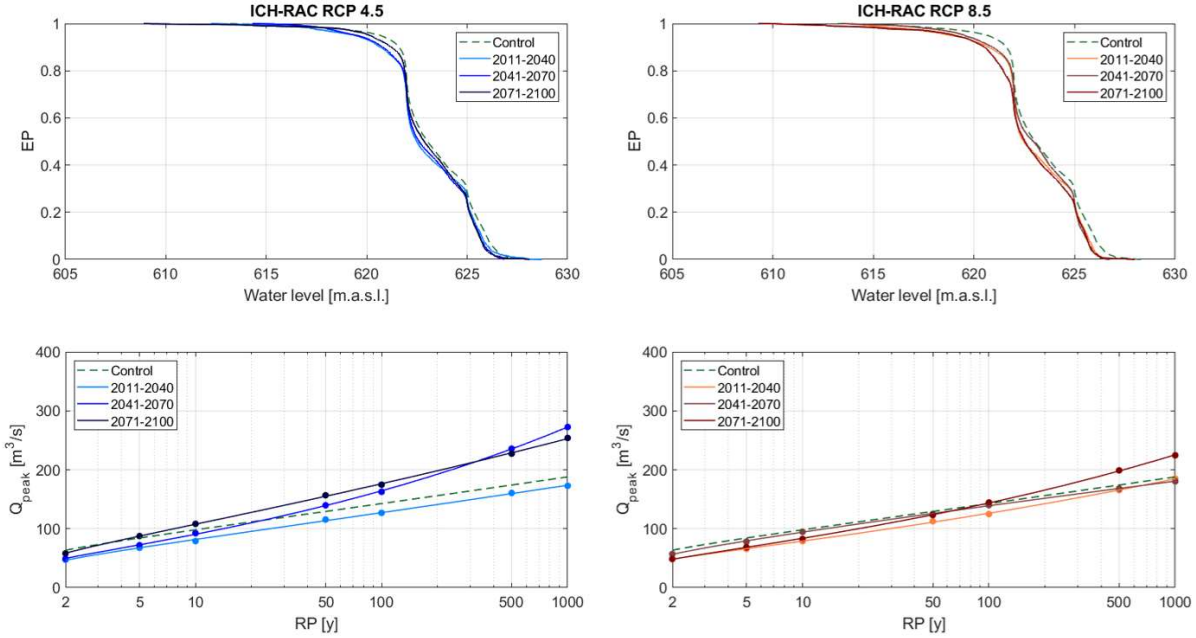


Figure B4: Initial reservoir water level and inflow peak discharge frequency curves for the ICH-RAC climate model in the three time windows. The left column shows the results for RCP 4.5. The right column offers the results for RCP 8.5. Each time window is represented with a given colour. Control periods are represented with dashed lines and future periods with solid lines.

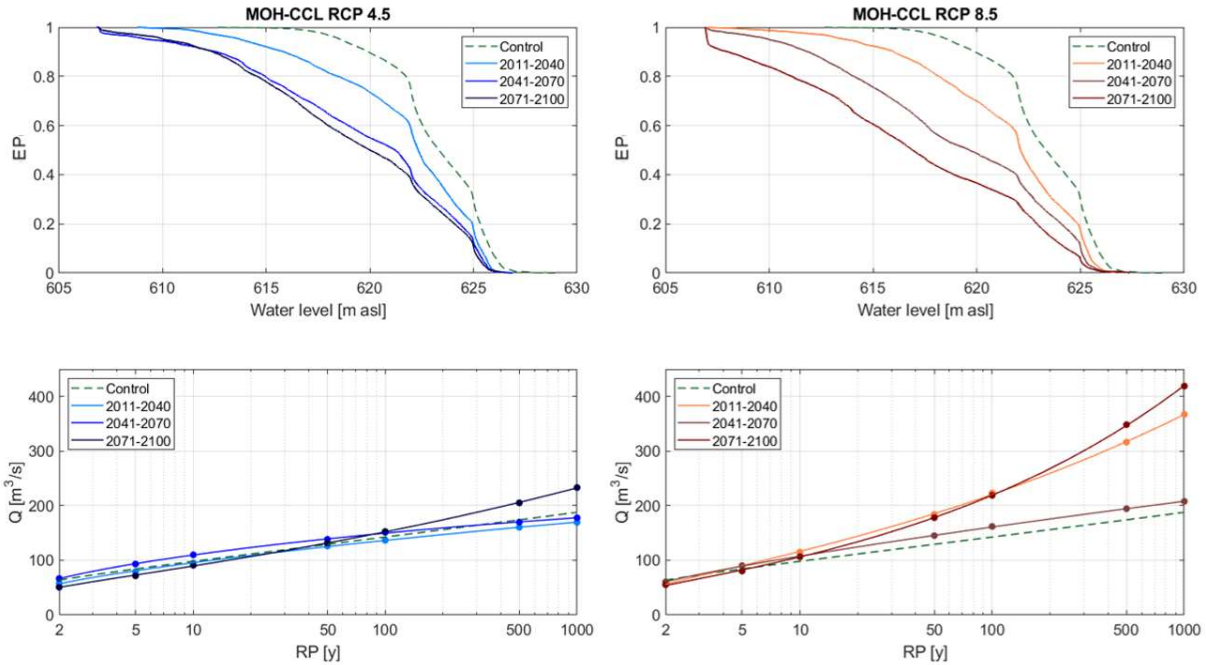


Figure B5: Initial reservoir water level and inflow peak discharge frequency curves for the MOH-CCL climate model in the three time windows. The left column shows the results for RCP 4.5. The right column offers the results for RCP 8.5. Each time window is represented with a given colour. Control periods are represented with dashed lines and future periods with solid lines.

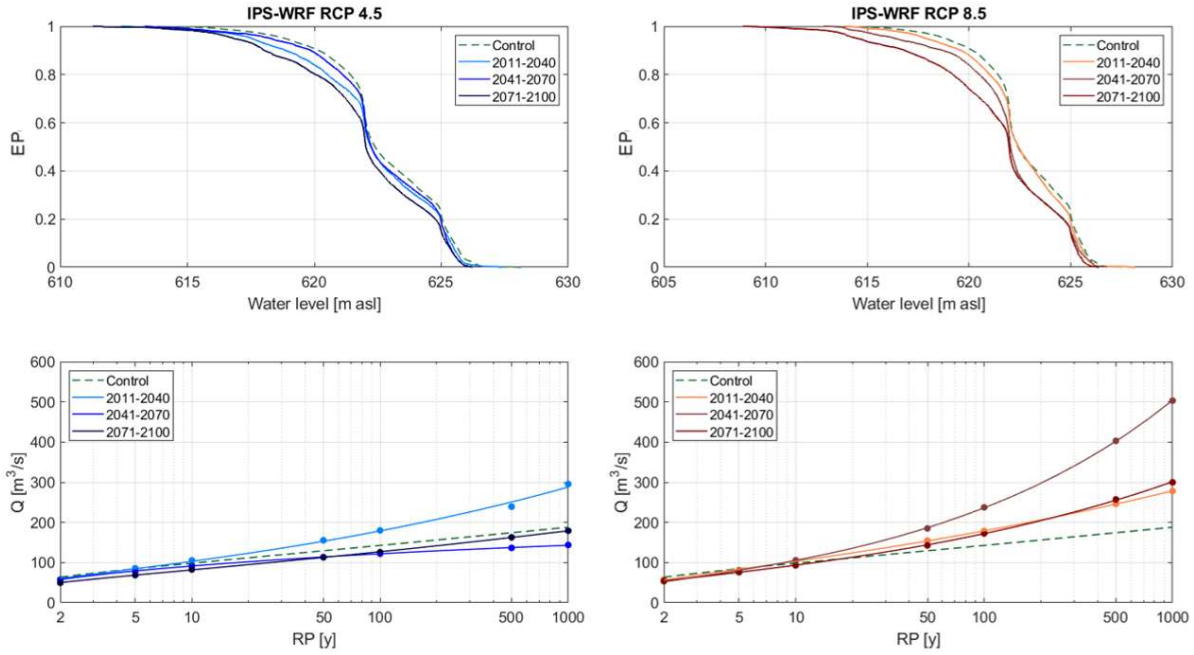


Figure B6: Initial reservoir water level and inflow peak discharge frequency curves for the IPS-WRF climate model in the three time windows. The left column shows the results for RCP 4.5. The right column offers the results for RCP 8.5. Each time window is represented with a given colour. Control periods are represented with dashed lines and future periods with solid lines.

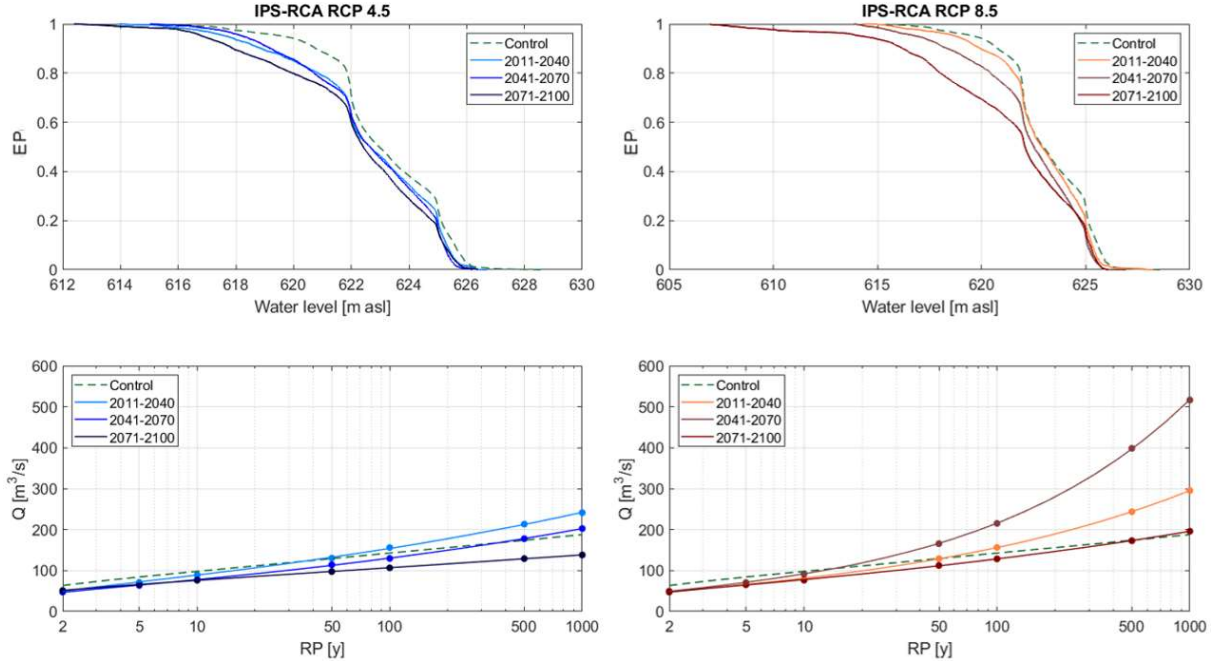


Figure B7: Initial reservoir water level and inflow peak discharge frequency curves for the IPS-RCA climate model in the three time windows. The left column shows the results for RCP 4.5. The right column offers the results for RCP 8.5. Each time window is represented with a given colour. Control periods are represented with dashed lines and future periods with solid lines.

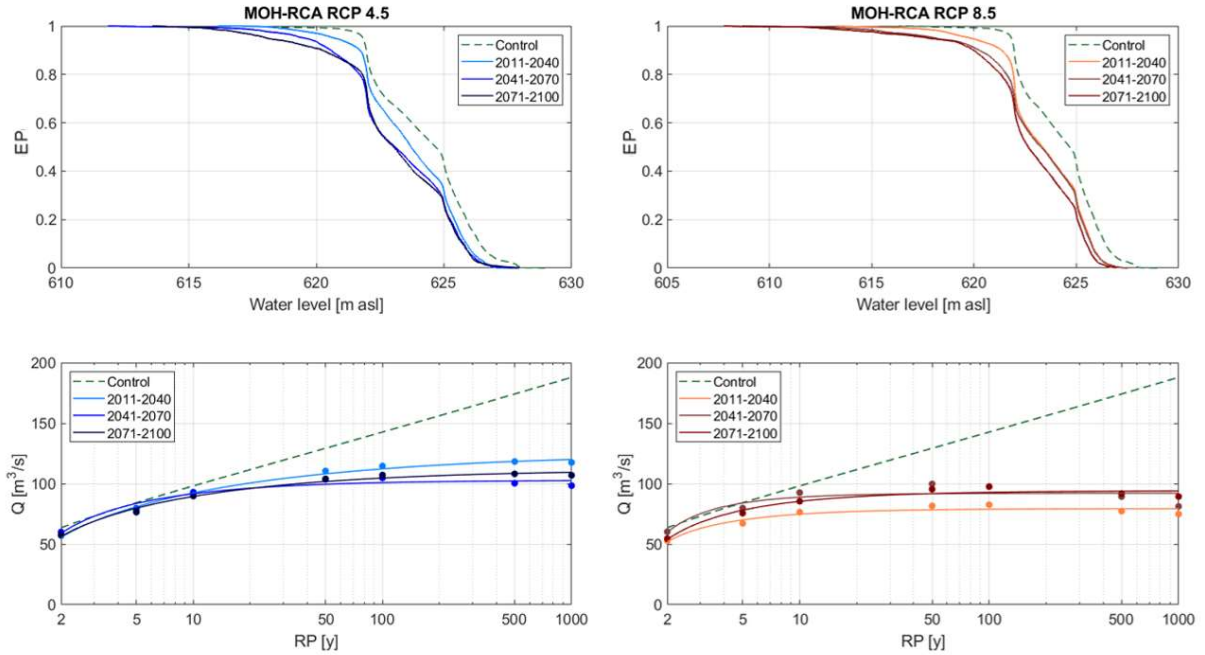


Figure B8: Initial reservoir water level and inflow peak discharge frequency curves for the MOH-RCA climate model in the three time windows. The left column shows the results for RCP 4.5. The right column offers the results for RCP 8.5. Each time window is represented with a given colour. Control periods are represented with dashed lines and future periods with solid lines.

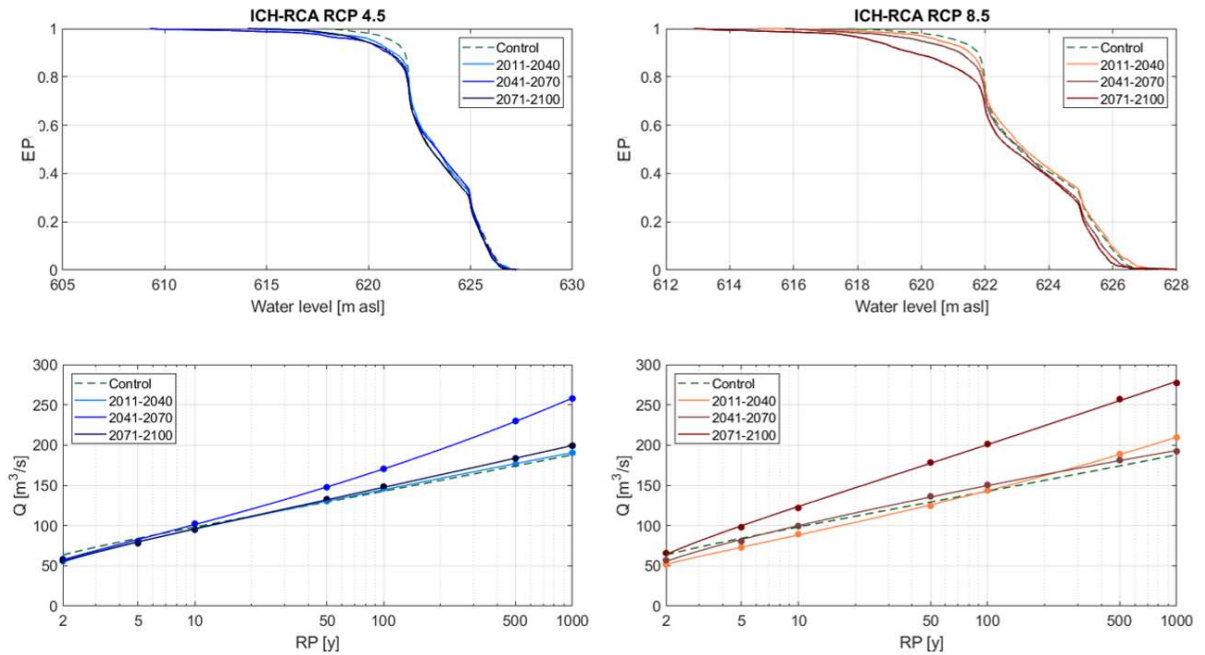


Figure B9: Initial reservoir water level and inflow peak discharge frequency curves for the ICH-RCA climate model in the three time windows. The left column shows the results for RCP 4.5. The right column offers the results for RCP 8.5. Each time window is represented with a given colour. Control periods are represented with dashed lines and future periods with solid lines.

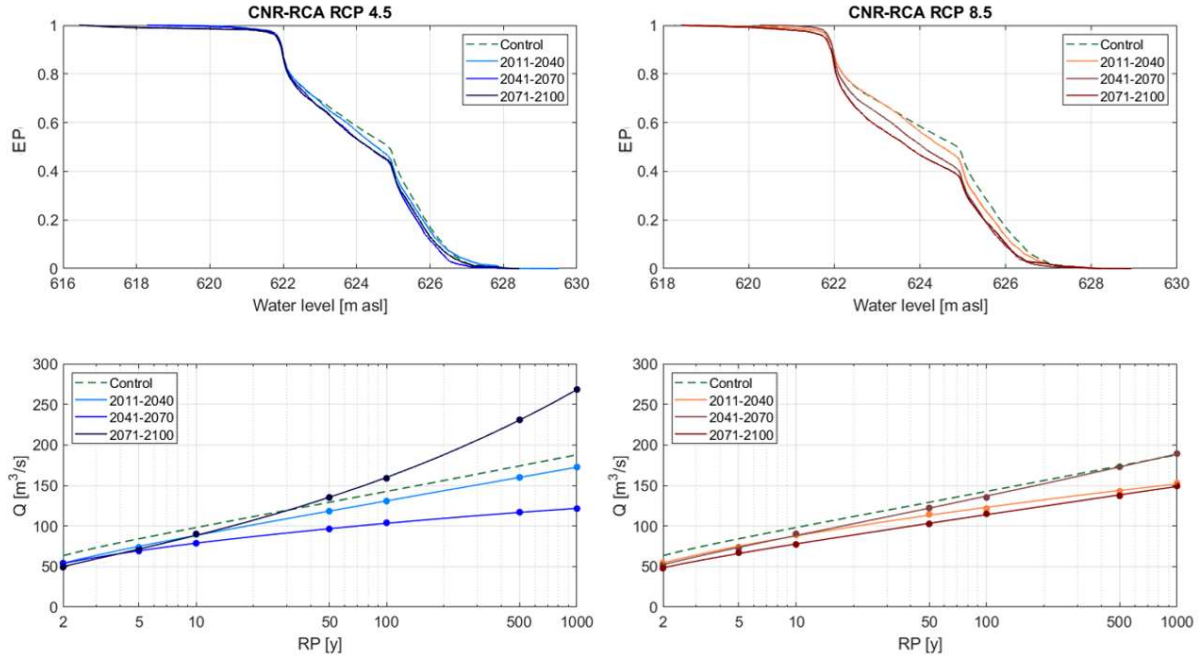


Figure B10: Initial reservoir water level and inflow peak discharge frequency curves for the CNR-RCA climate model in the three time windows. The left column shows the results for RCP 4.5. The right column offers the results for RCP 8.5. Each time window is represented with a given colour. Control periods are represented with dashed lines and future periods with solid lines.

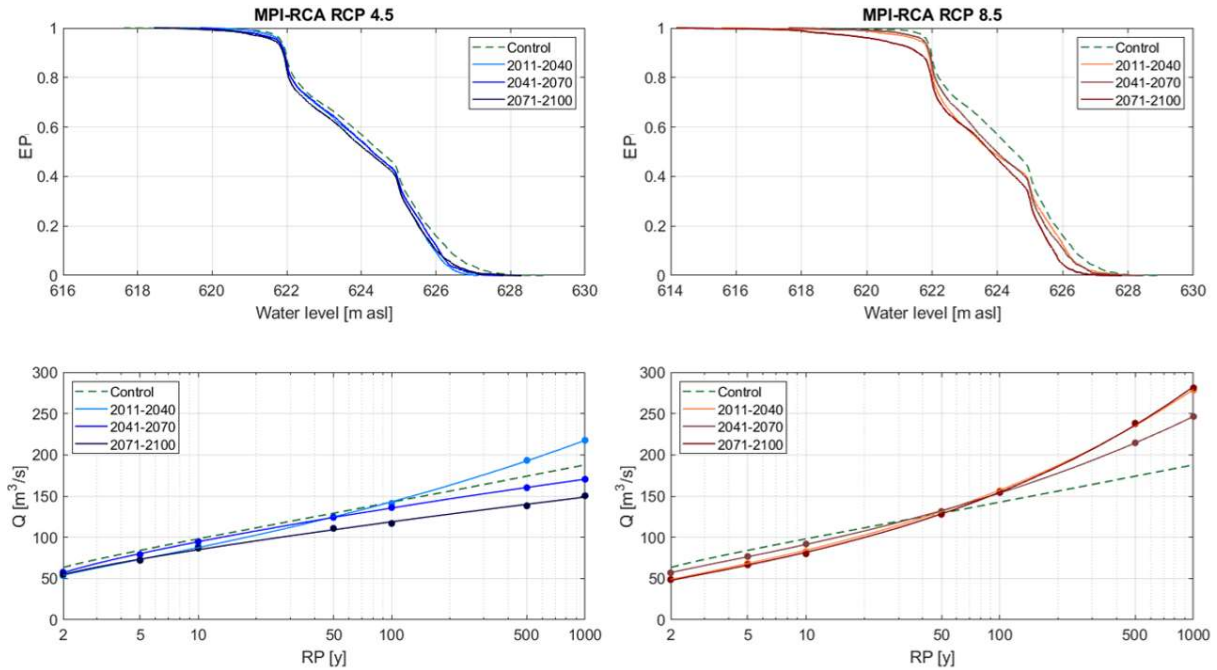


Figure B11: Initial reservoir water level and inflow peak discharge frequency curves for the MPI-RCA climate model in the three time windows. The left column shows the results for RCP 4.5. The right column offers the results for RCP 8.5. Each time window is represented with a given colour. Control periods are represented with dashed lines and future periods with solid lines.

Appendix C.

Future inflow hydrographs and initial water levels of the Eugui dam for each climate model

Figures in this Appendix show the Exceedance Probability (EP) of some future climate variables for the eleven climate projections that are not shown in Chapter 5.

The first column shows daily potential evapotranspiration PET, which have obtained with the Hargreaves equation from future daily temperature. The second column shows that the future daily precipitation P. The third column shows the soil moisture condition SM (see section 3.3.2 for the description of the model) obtained with the HBV model.

Each scenario is associated with a given colour: dashed green line is the control period, the RCP 4.5 is in a blue scale for the different time windows, the RCP 8.5 is in a brown scale.

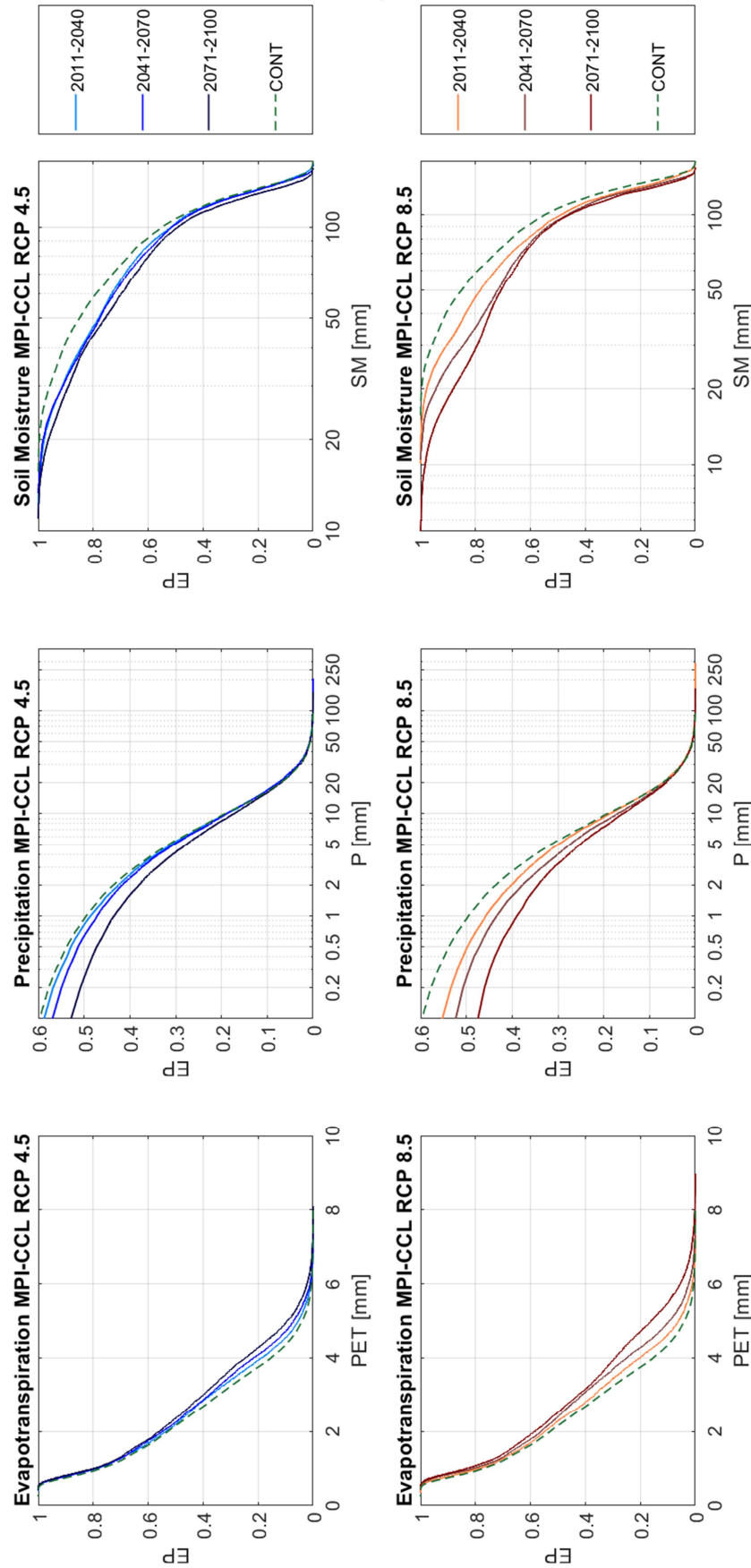


Figure C1. Exceedance Probability (EP) of some future climate variables under the MPI-CCL climate projections: the first column shows the daily potential evapotranspiration PET obtained with the Hargreaves equation from future daily temperature, the second column shows the future daily precipitation P and the third column shows soil moisture condition SM obtained with the HBV model. Each scenario is associated to a given colour: dashed green line is the control period, the RCP 4.5 is in a blue scale for the different time windows, the RCP 8.5 is in a brown scale.

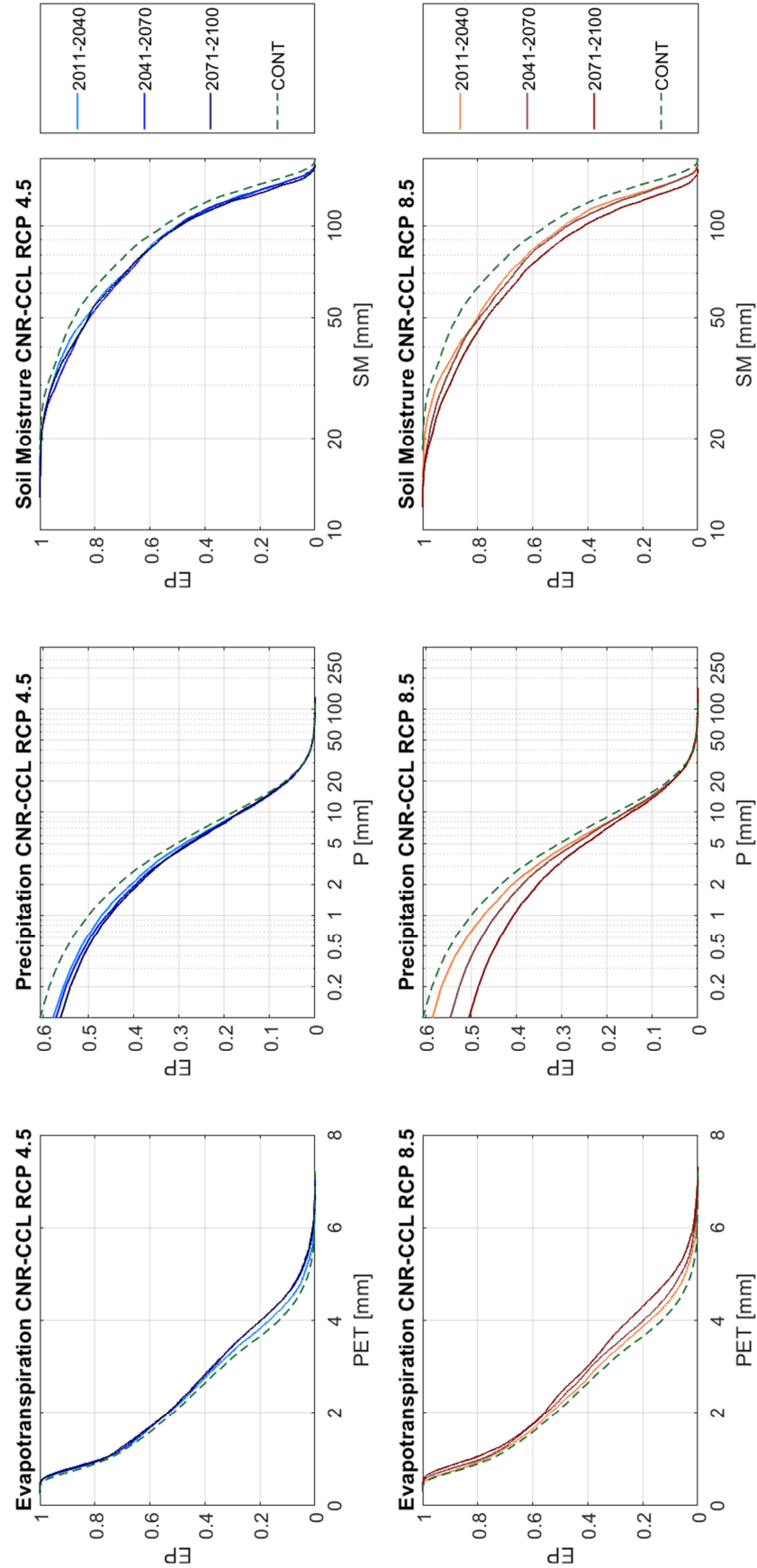


Figure C2. Exceedance Probability (EP) of some future climate variables under the CNR-CCCL climate projections: the first column shows the daily potential evapotranspiration PET obtained with the Hargreaves equation from future daily temperature, the second column shows the future daily precipitation P and the third column shows soil moisture condition SM obtained with the HBV model. Each scenario is associated to a given colour: dashed green line is the control period, the RCP 4.5 is in a blue scale for the different time windows, the RCP 8.5 is in a brown scale.

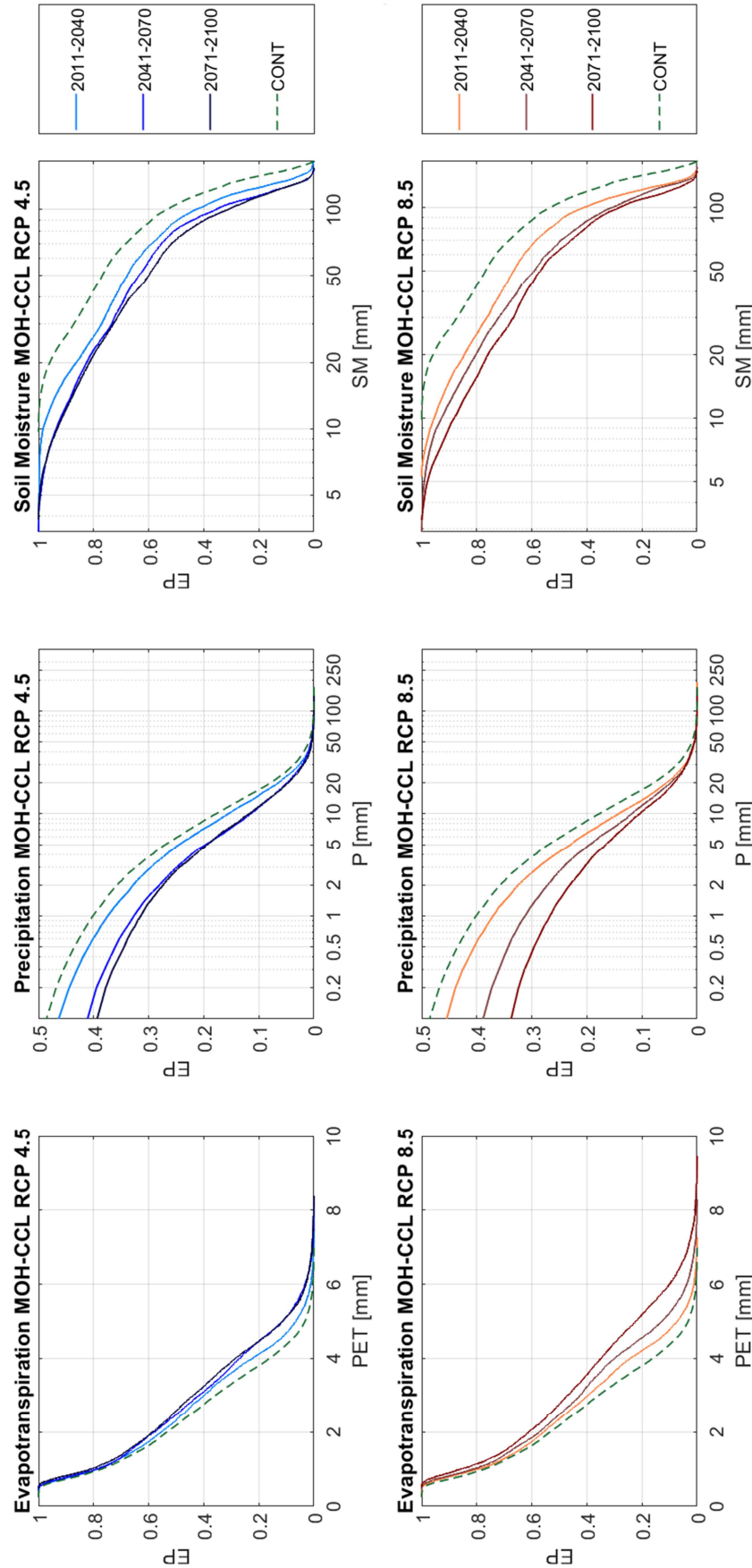


Figure C3. Exceedance Probability (EP) of some future climate variables under the MOH-CCL climate projections: the first column shows the daily potential evapotranspiration PET obtained with the Hargreaves equation from future daily temperature, the second column shows the future daily precipitation P and the third column shows soil moisture condition SM obtained with the HBV model. Each scenario is associated to a given colour: dashed green line is the control period, the RCP 4.5 is in a blue scale for the different time windows, the RCP 8.5 is in a brown scale.

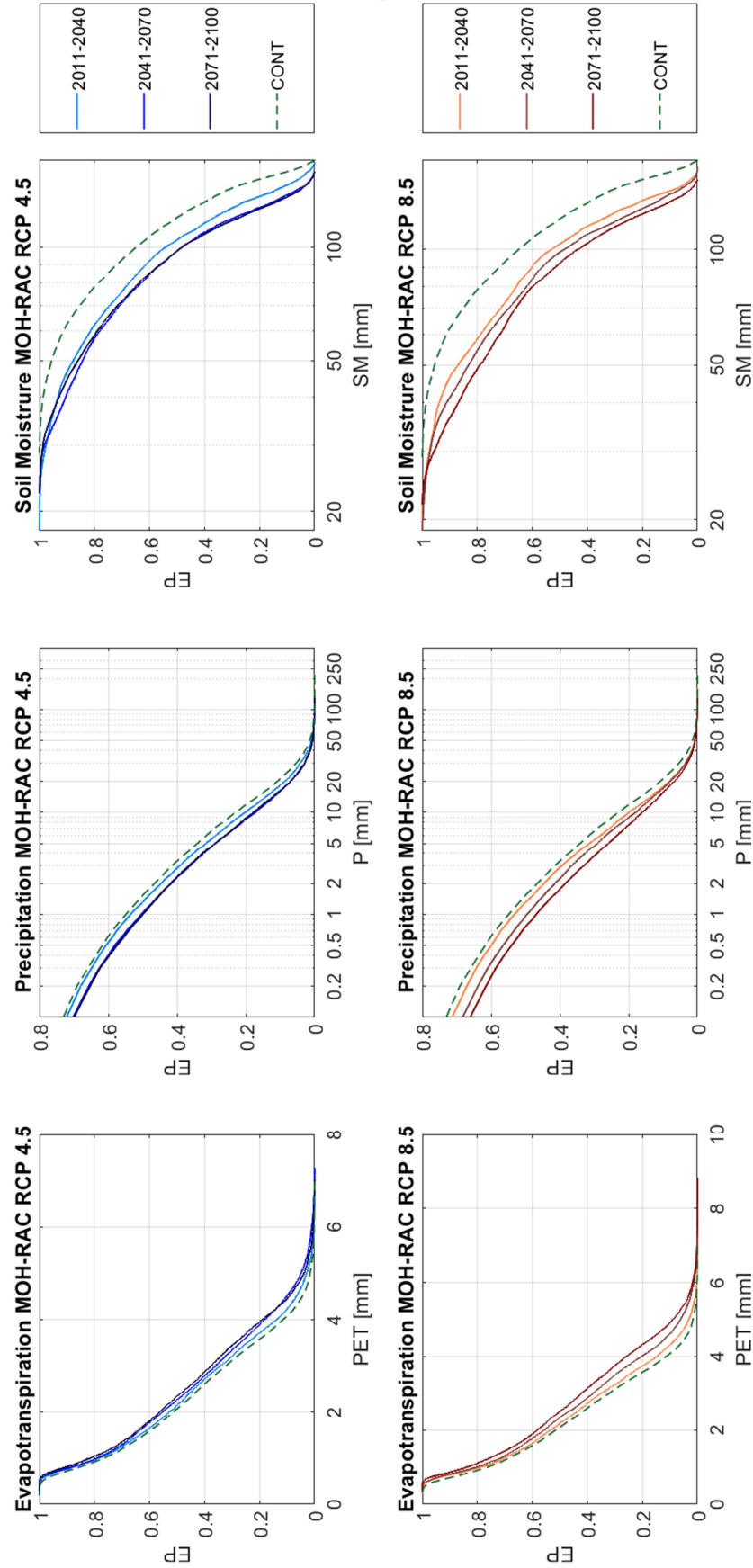


Figure C4. Exceedance Probability (EP) of some future climate variables under the MOH-RAC climate projections: the first column shows the daily potential evapotranspiration PET obtained with the Hargreaves equation from future daily temperature, the second column shows the future daily precipitation P and the third column shows soil moisture condition SM obtained with the HBV model. Each scenario is associated to a given colour: dashed green line is the control period, the RCP 4.5 is in a blue scale for the different time windows, the RCP 8.5 is in a brown scale.

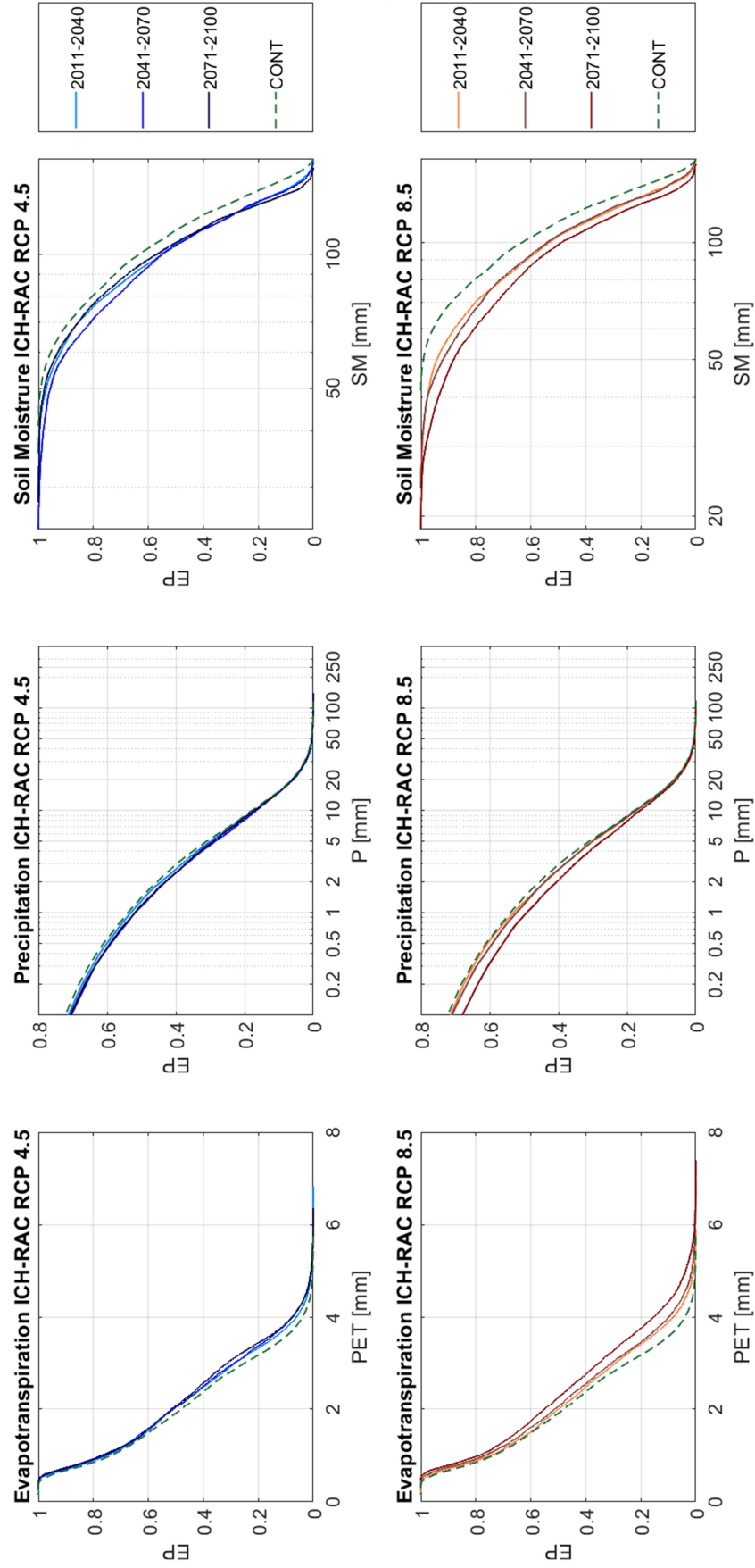


Figure C5. Exceedance Probability (EP) of some future climate variables under the ICH-RAC climate projections: the first column shows the daily potential evapotranspiration PET obtained with the Hargreaves equation from future daily temperature, the second column shows the future daily precipitation P and the third column shows soil moisture condition SM obtained with the HBV model. Each scenario is associated to a given colour: dashed green line is the control period, the RCP 4.5 is in a blue scale for the different time windows, the RCP 8.5 is in a brown scale.

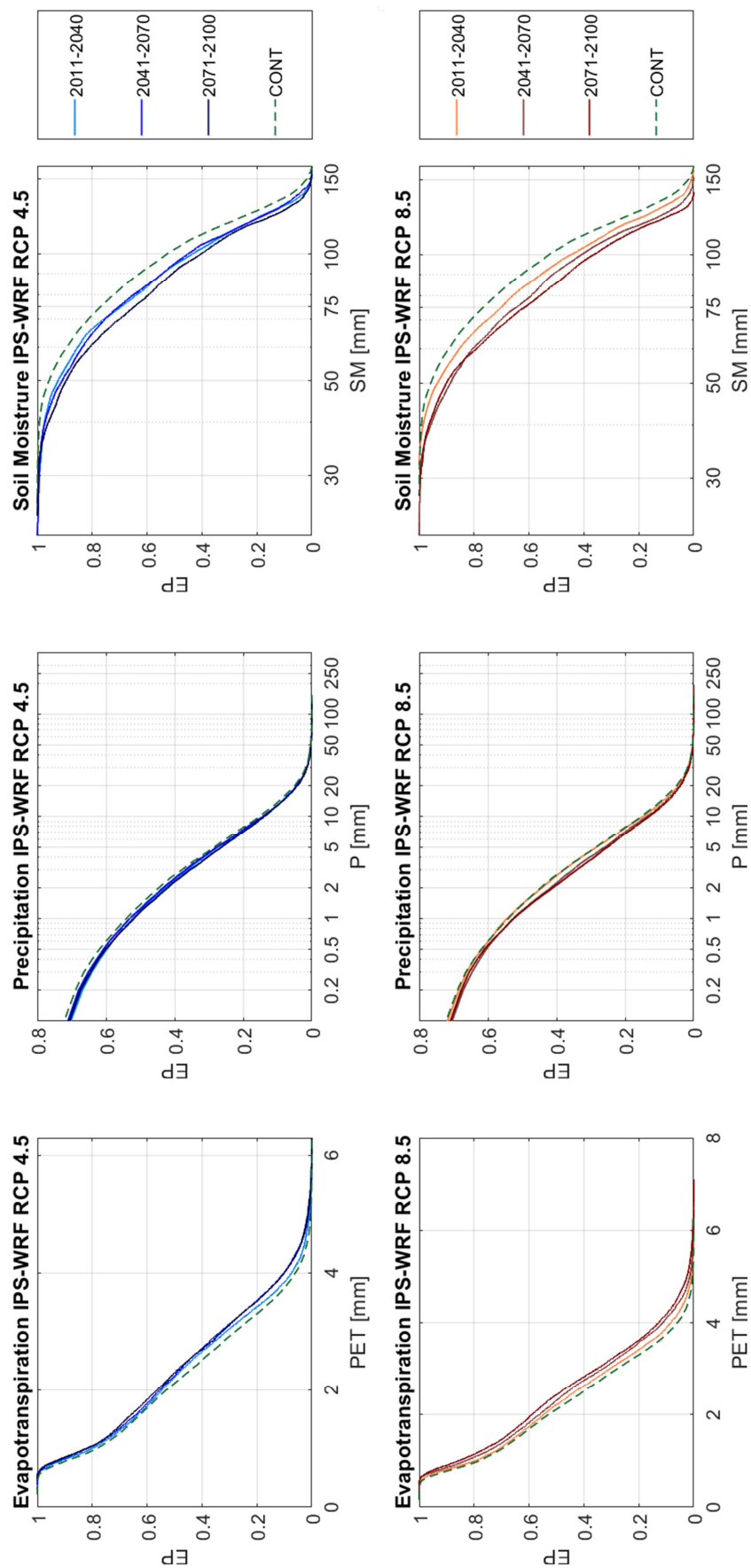


Figure C6. Exceedance Probability (EP) of some future climate variables under the IPS-WRF climate projections: the first column shows the daily potential evapotranspiration PET obtained with the Hargreaves equation from future daily temperature, the second column shows the future daily precipitation P and the third column shows soil moisture condition SM obtained with the HBV model. Each scenario is associated to a given colour: dashed green line is the control period, the RCP 4.5 is in a blue scale for the different time windows, the RCP 8.5 is in a brown scale.

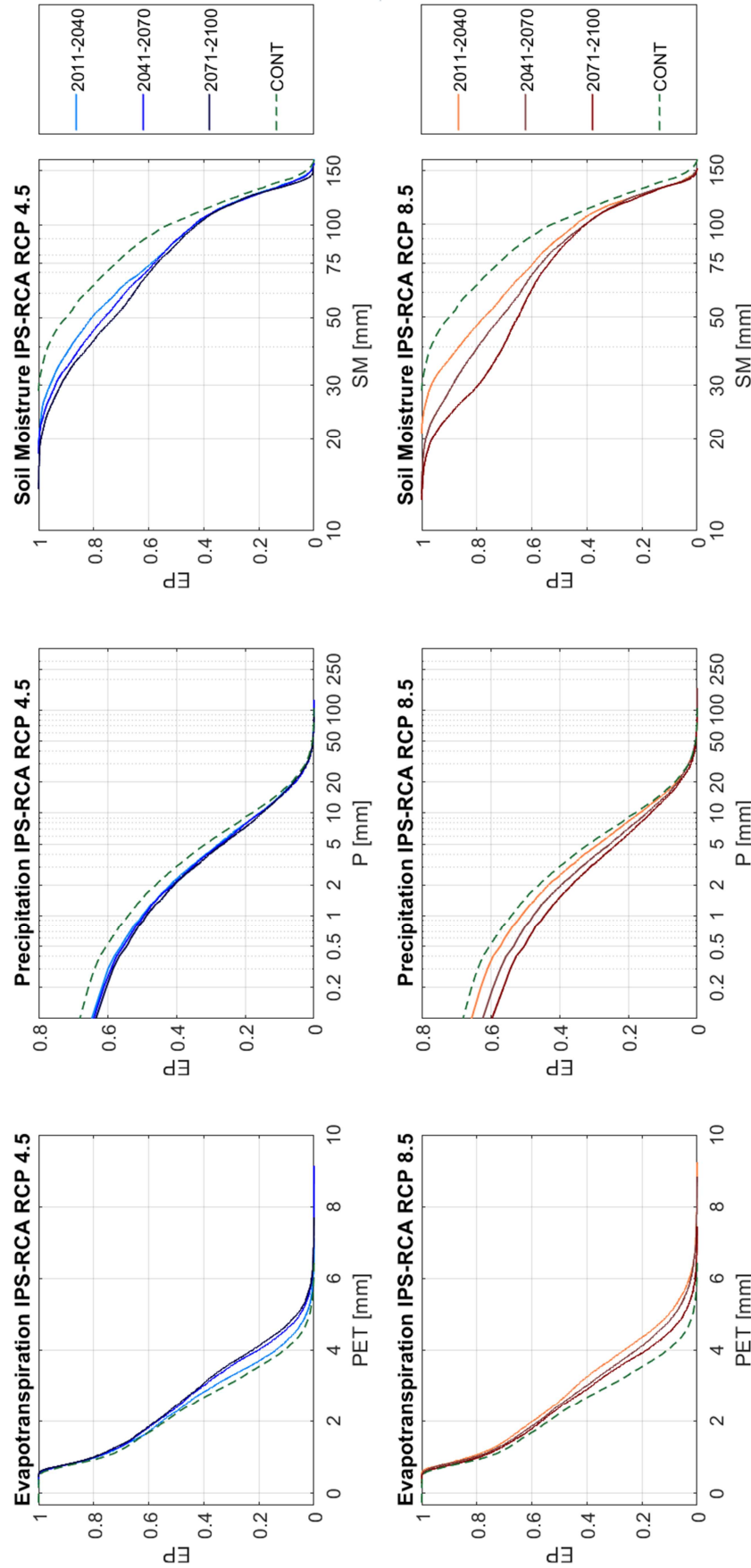


Figure C7. Exceedance Probability (EP) of some future climate variables under the IPS-RCA climate projections: the first column shows the daily potential evapotranspiration PET obtained with the Hargreaves equation from future daily temperature, the second column shows the future daily precipitation P and the third column shows soil moisture condition SM obtained with the HBV model. Each scenario is associated to a given colour: dashed green line is the control period, the RCP 4.5 is in a blue scale for the different time windows, the RCP 8.5 is in a brown scale.

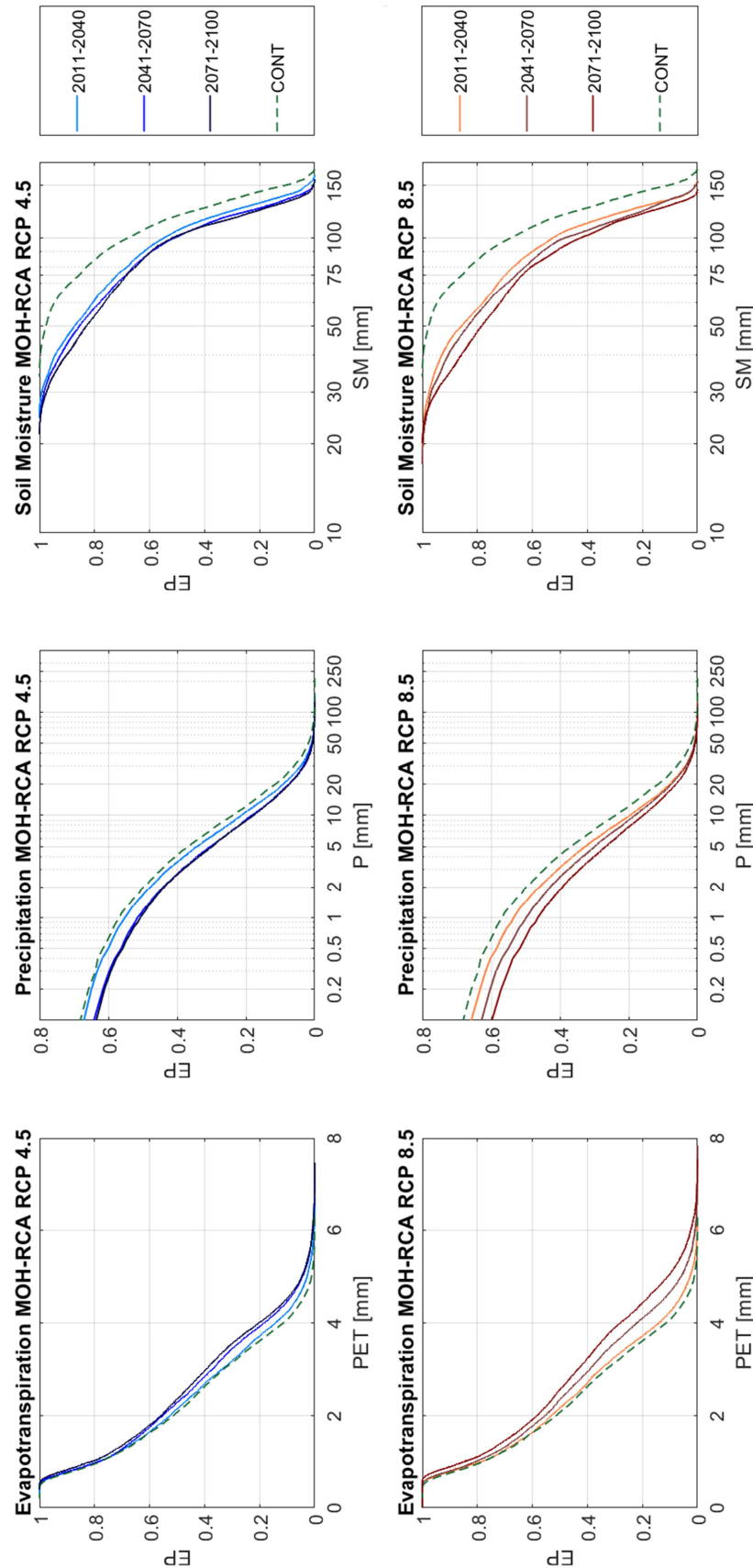


Figure C8. Exceedance Probability (EP) of some future climate variables under the MOH-RCA climate projections: the first column shows the daily potential evapotranspiration PET obtained with the Hargreaves equation from future daily temperature, the second column shows the future daily precipitation P and the third column shows soil moisture condition SM obtained with the HBV model. Each scenario is associated to a given colour: dashed green line is the control period, the RCP 4.5 is in a blue scale for the different time windows, the RCP 8.5 is in a brown scale.

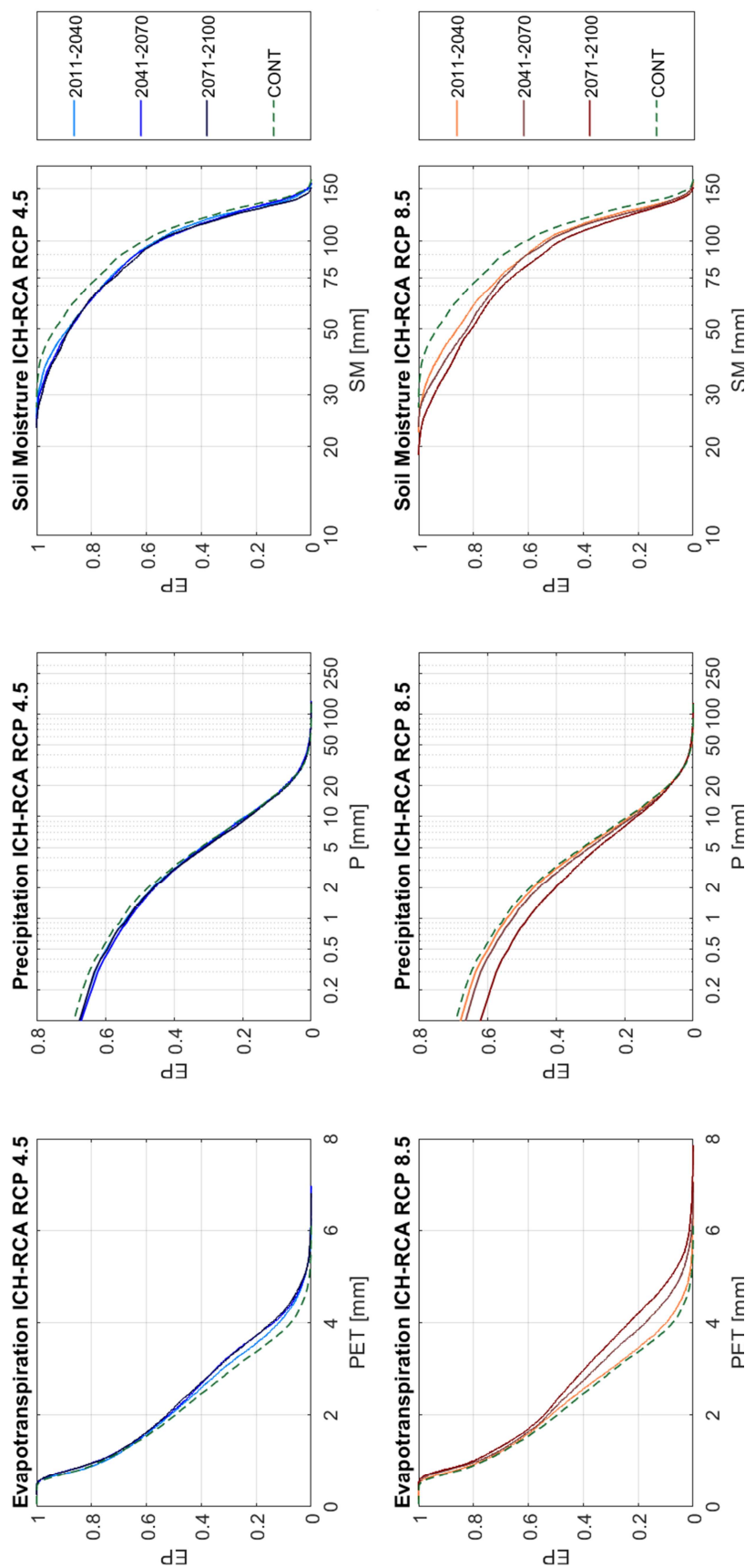


Figure C9. Exceedance Probability (EP) of some future climate variables under the ICH-RCA climate projections: the first column shows the daily potential evapotranspiration PET obtained with the Hargreaves equation from future daily temperature, the second column shows the future daily precipitation P and the third column shows soil moisture condition SM obtained with the HBV model. Each scenario is associated to a given colour: dashed green line is the control period, the RCP 4.5 is in a blue scale for the different time windows, the RCP 8.5 is in a brown scale.

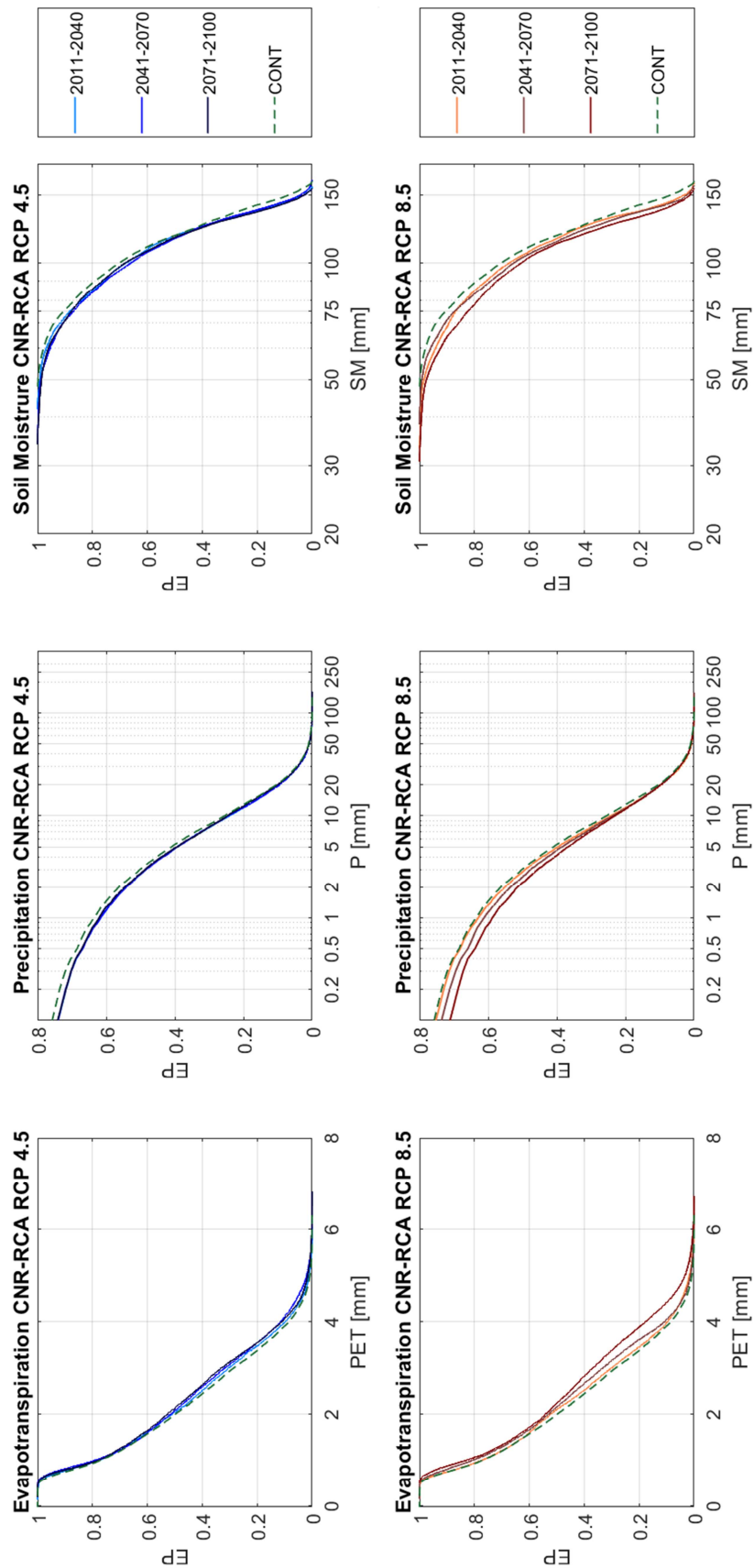


Figure C10. Exceedance Probability (EP) of some future climate variables under the CNR-RCA climate projections: the first column shows the daily potential evapotranspiration PET obtained with the Hargreaves equation from future daily temperature, the second column shows the future daily precipitation P and the third column shows soil moisture condition SM obtained with the HBV model. Each scenario is associated to a given colour: dashed green line is the control period, the RCP 4.5 is in a blue scale for the different time windows, the RCP 8.5 is in a brown scale.

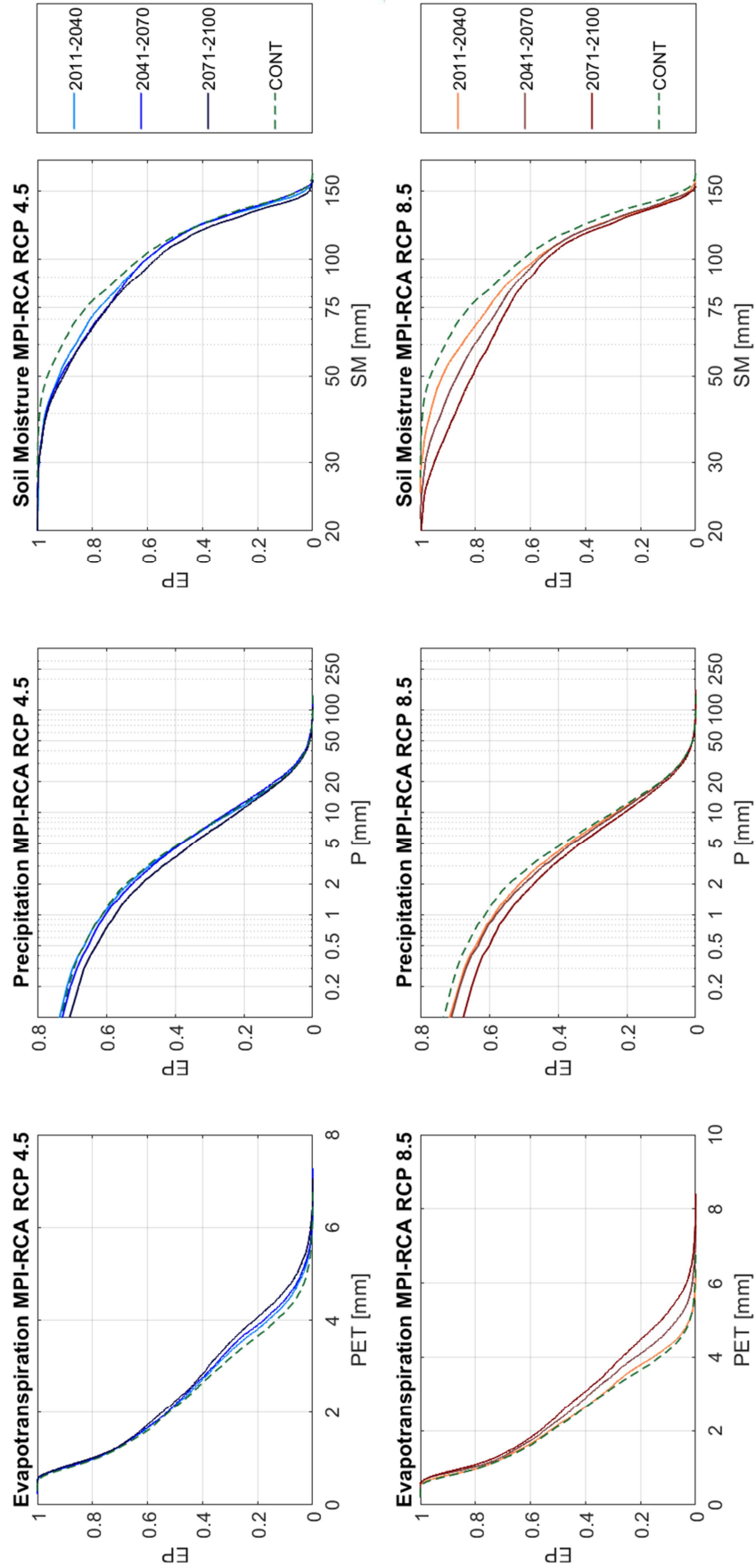


Figure C11. Exceedance Probability (EP) of some future climate variables under the MPI-RCA climate projections: the first column shows the daily potential evapotranspiration PET obtained with the Hargreaves equation from future daily temperature, the second column shows the future daily precipitation P and the third column shows soil moisture condition SM obtained with the HBV model. Each scenario is associated to a given colour: dashed green line is the control period, the RCP 4.5 is in a blue scale for the different time windows, the RCP 8.5 is in a brown scale.

Appendix D.

Future maximum water level for each climate model accounting uncertainty

Figures in this appendix show the results expressed as maximum water level frequency for each climate model, also considering the uncertainty chain. The upper part shows the results for the three time window in the RCP 4.5, while the bottom part shows the results of the RCP 8.5. In the subplot the maximum water level frequency curve is shown for the 7 considered percentiles (5%, 10%, 32%, 50%, 68%, 90% and 95%). Moreover, the results obtained without the accounting of the uncertainty are also presented in each subplot with red dots. The grey filled box of the subplots represent the dam, with its crest at the 630 m a.s.l. altitude, while the red dotted line shows the level in which the overtopping threshold, i.e. the maximum water level before overtopping occurs considering also the presence of waves induced by wind.

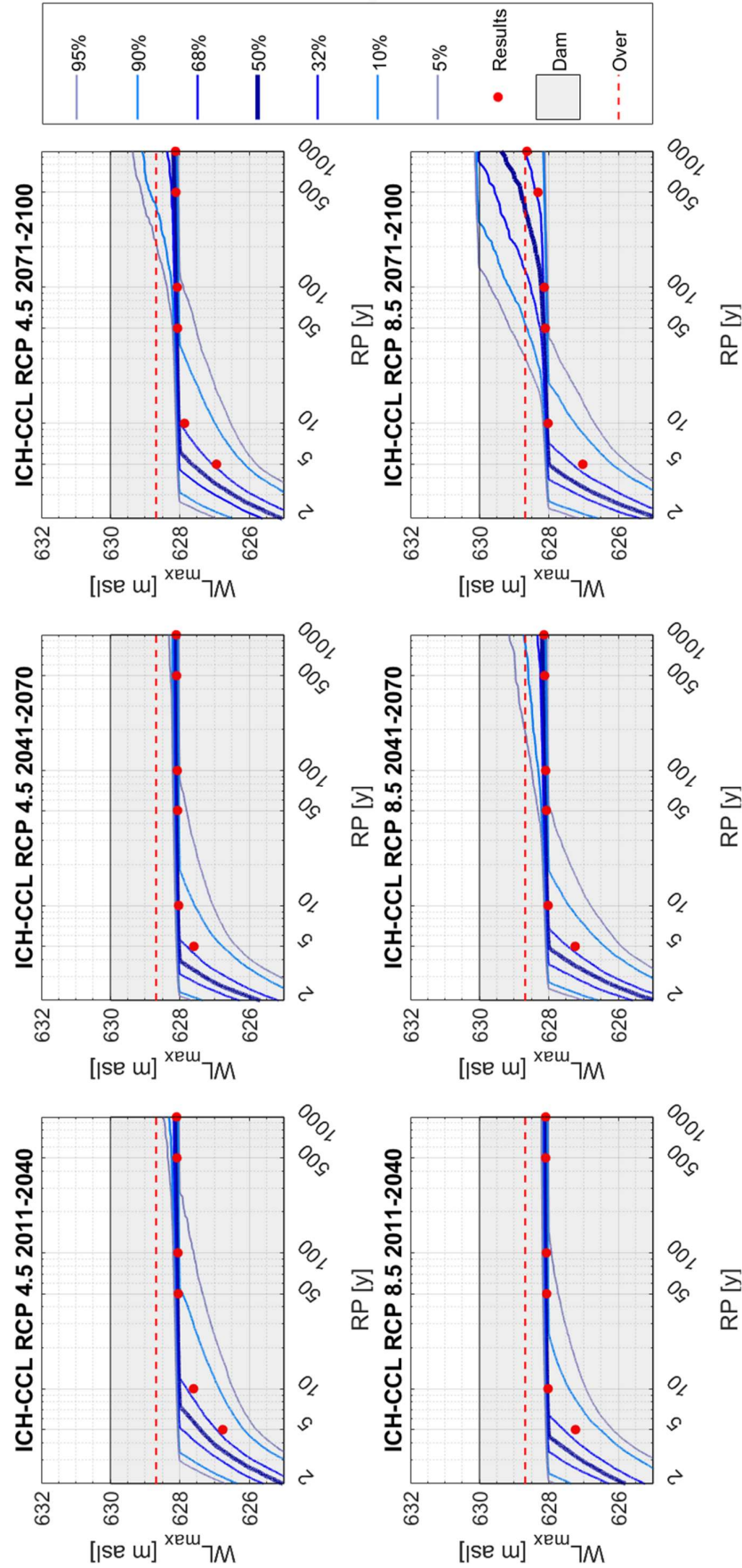


Figure D1: Expected maxima reservoir water levels in the future for the ICH-CCL climate model considering uncertainty. The first row includes the results for RCP 4.5 and the second row includes the results for RCP 8.5. Columns present results by time windows in the future. The thickest blue line represents the median values. Thinner light blue lines represent the rest of percentiles. Red points represent the results without considering uncertainty for the seven return periods. The grey filled box represents the dam with its crest elevation at 630 m a.s.l. The horizontal dashed red line represents the overtopping threshold.

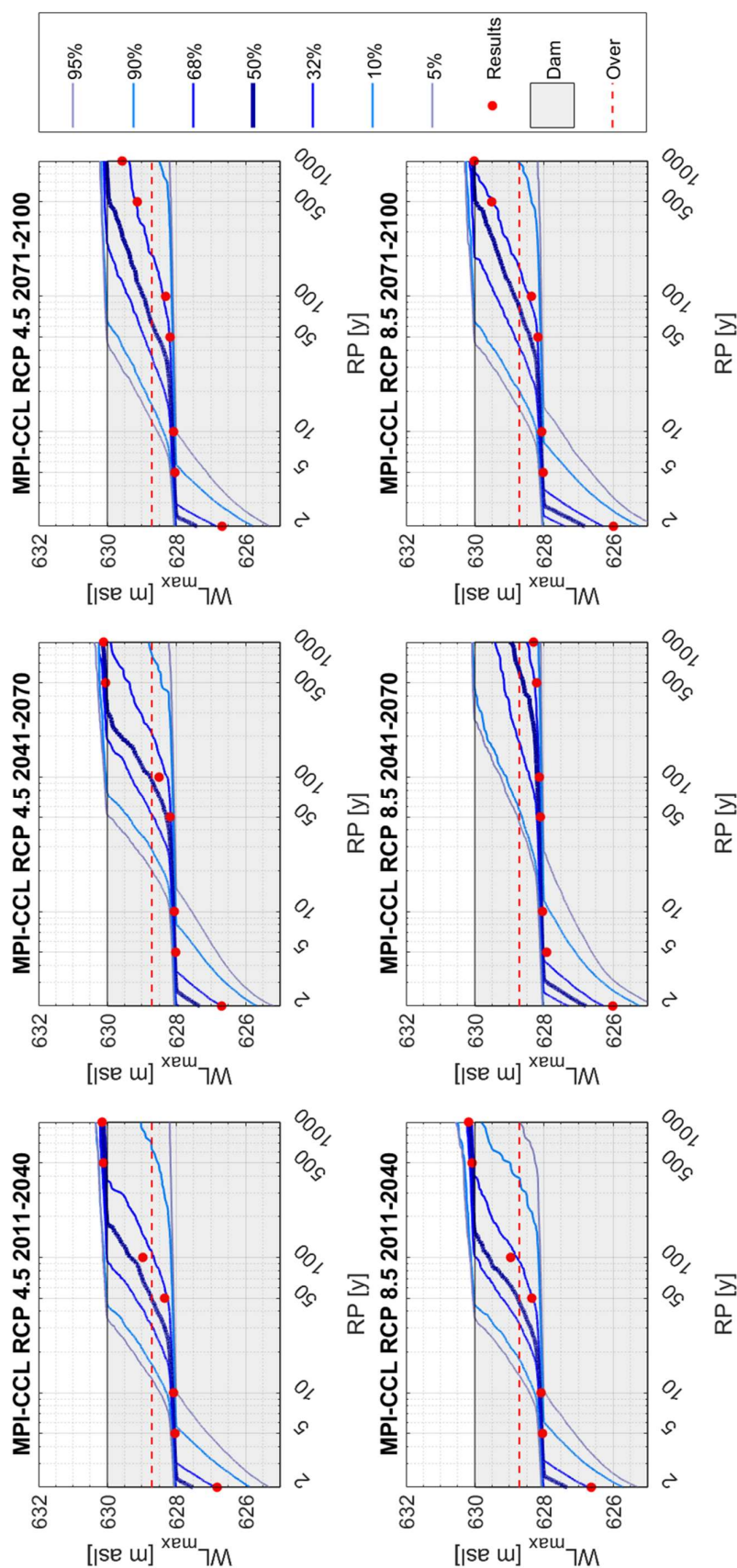


Figure D2: Expected maxima reservoir water levels in the future for the MPI-CCL climate model considering uncertainty. The first row includes the results for RCP 4.5 and the second row includes the results for RCP 8.5. Columns present results by time windows in the future. The thickest blue line represents the median values. Thinner light blue lines represent the rest of percentiles. Red points represent the results without considering uncertainty for the seven return periods. The grey filled box represents the dam with its crest elevation at 630 m a.s.l. The horizontal dashed red line represents the overtopping threshold.

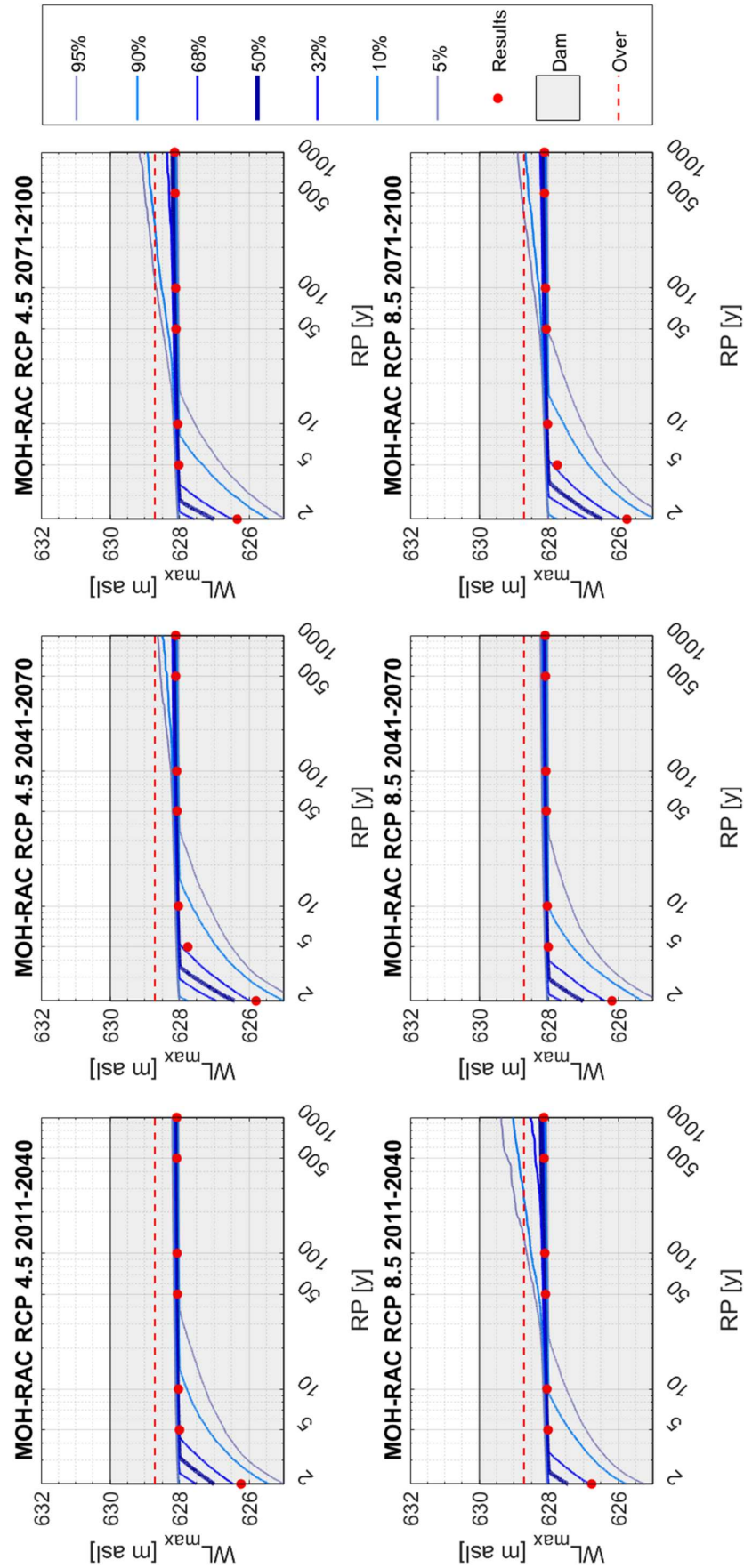


Figure D3: Expected maxima reservoir water levels in the future for the MOH-RAC climate model considering uncertainty. The first row includes the results for RCP 4.5 and the second row includes the results for RCP 8.5. Columns present results by time windows in the future. The thickest blue line represents the median values. Thinner light blue lines represent the rest of percentiles. Red points represent the results without considering uncertainty for the seven return periods. The grey filled box represents the dam with its crest elevation at 630 m a.s.l. The horizontal dashed red line represents the overtopping threshold.

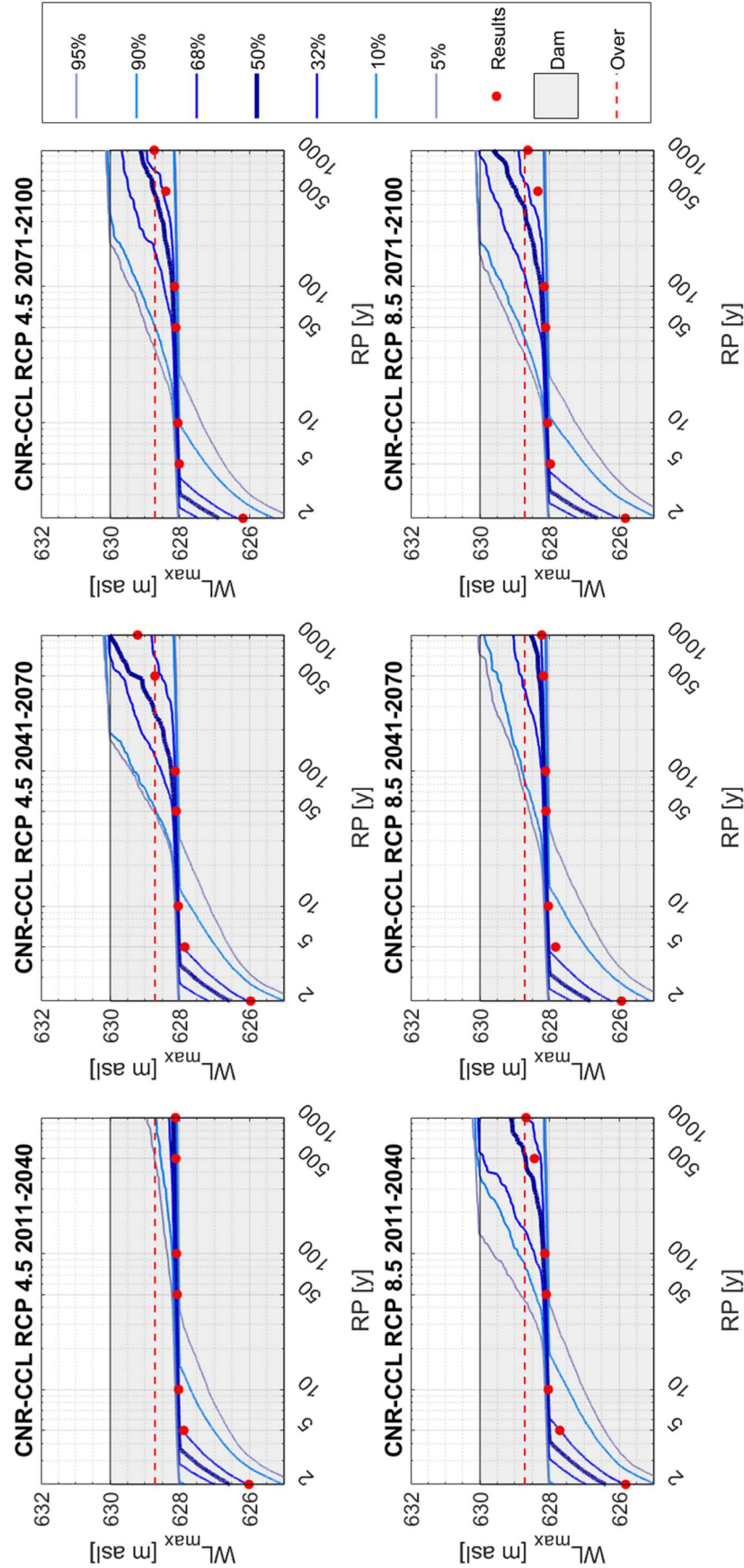


Figure D4: Expected maxima reservoir water levels in the future for the CNR-CCL climate model considering uncertainty. The first row includes the results for RCP 4.5 and the second row includes the results for RCP 8.5. Columns present results by time windows in the future. The thickest blue line represents the median values. Thinner light blue lines represent the rest of percentiles. Red points represent the results without considering uncertainty for the seven return periods. The grey filled box represents the dam with its crest elevation at 630 m a.s.l. The horizontal dashed red line represents the overtopping threshold.

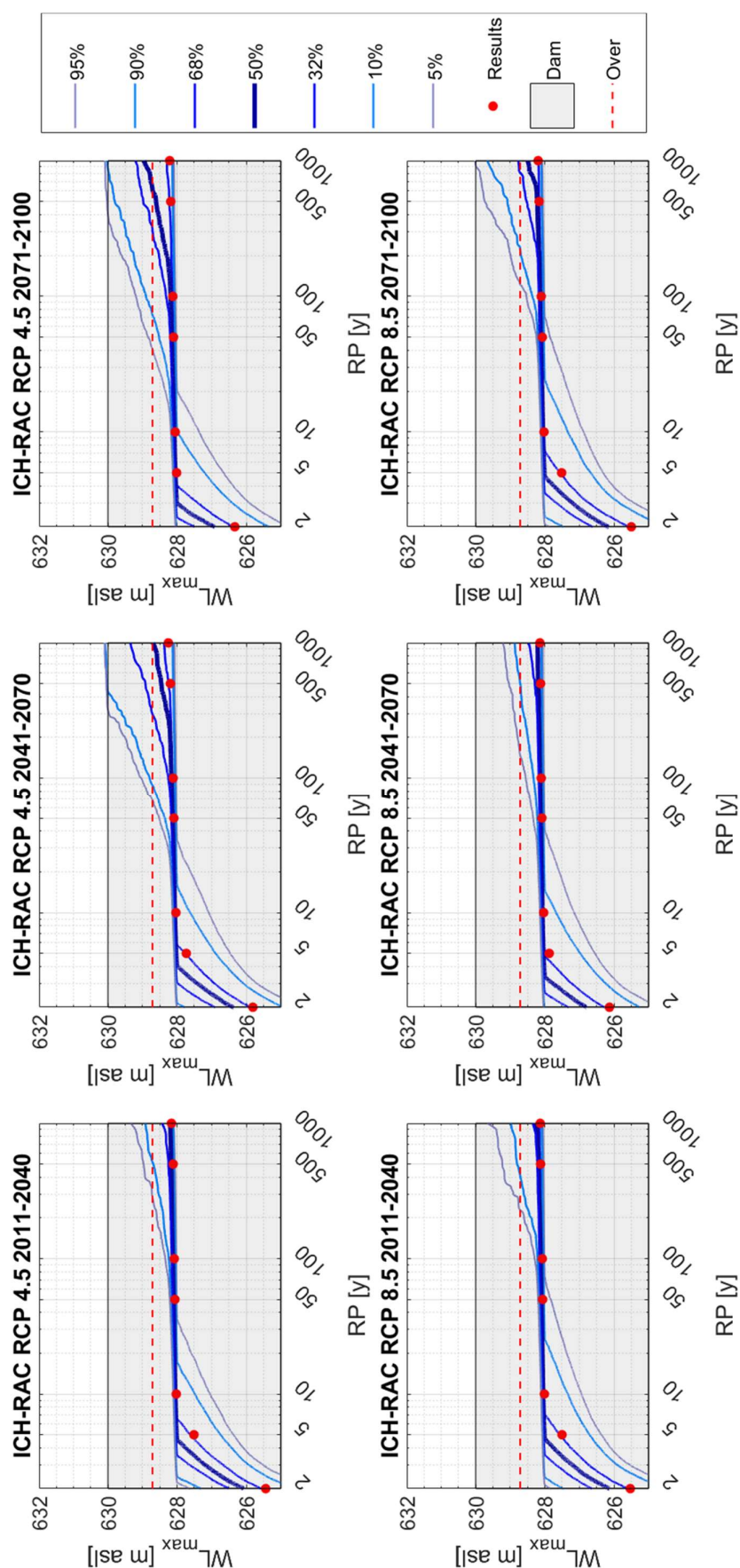


Figure D5 Expected maxima reservoir water levels in the future for the ICH-RAC climate model considering uncertainty. The first row includes the results for RCP 4.5 and the second row includes the results for RCP 8.5. Columns present results by time windows in the future. The thickest blue line represents the median values. Thinner light blue lines represent the rest of percentiles. Red points represent the results without considering uncertainty for the seven return periods. The grey filled box represents the dam with its crest elevation at 630 m a.s.l. The horizontal dashed red line represents the overtopping threshold.

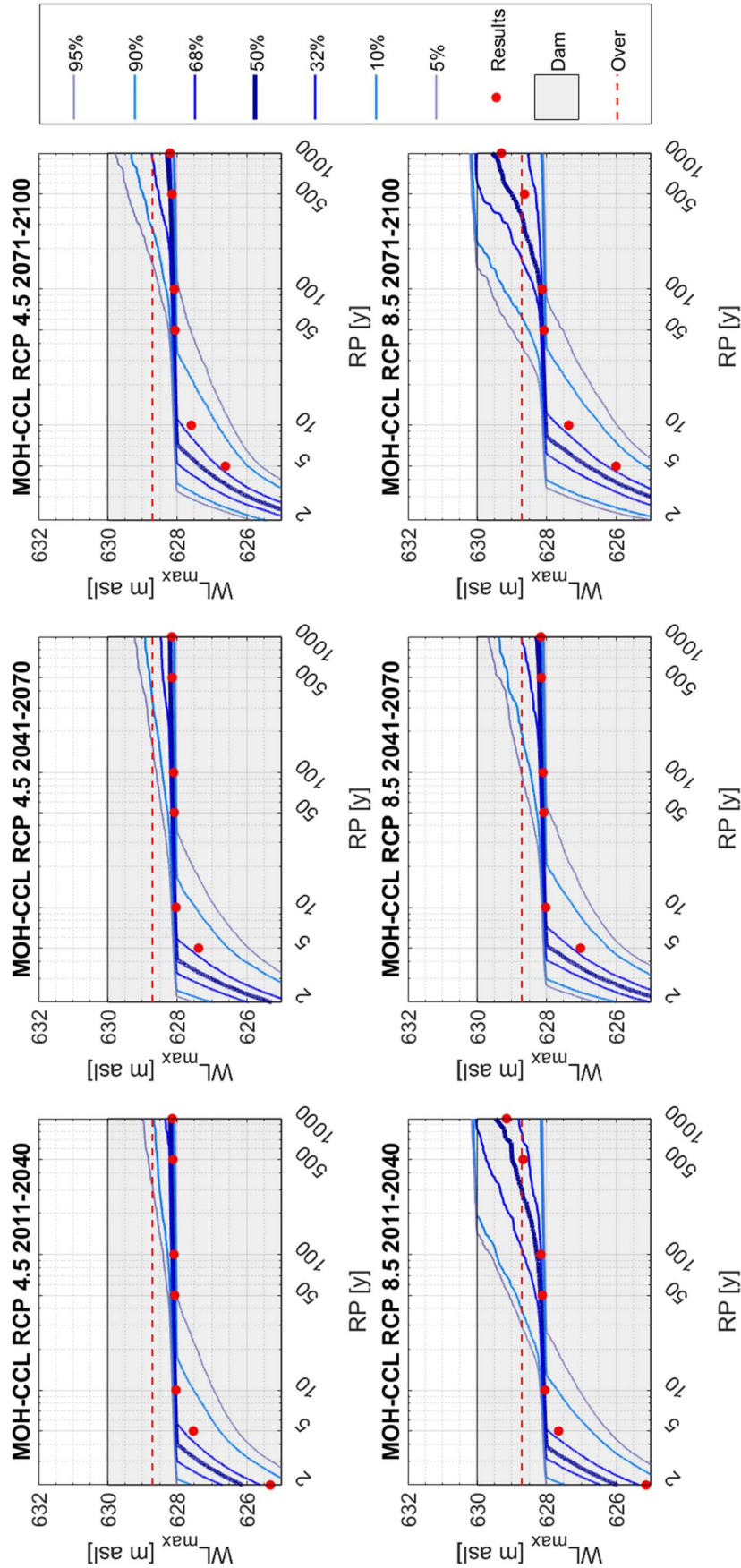


Figure D6: Expected maxima reservoir water levels in the future for the MOH-CCL climate model considering uncertainty. The first row includes the results for RCP 4.5 and the second row includes the results for RCP 8.5. Columns present results by time windows in the future. The thickest blue line represents the median values. Thinner light blue lines represent the rest of percentiles. Red points represent the results without considering uncertainty for the seven return periods. The grey filled box represents the dam with its crest elevation at 630 m a.s.l. The horizontal dashed red line represents the overtopping threshold.

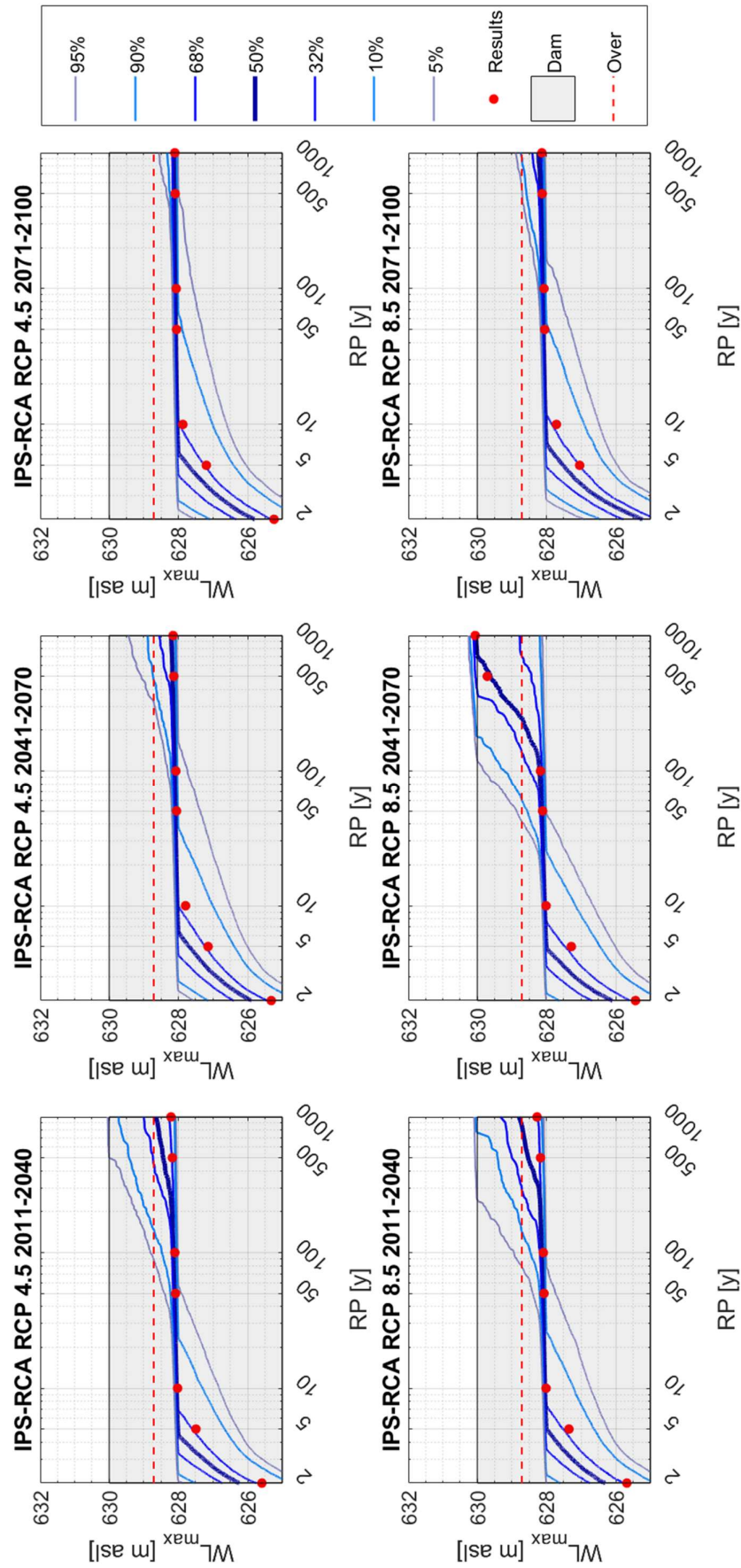


Figure D7: Expected maxima reservoir water levels in the future for the IPS-RCA climate model considering uncertainty. The first row includes the results for RCP 4.5 and the second row includes the results for RCP 8.5. Columns present results by time windows in the future. The thickest blue line represents the median values. Thinner light blue lines represent the rest of percentiles. Red points represent the results without considering uncertainty for the seven return periods. The grey filled box represents the dam with its crest elevation at 630 m a.s.l. The horizontal dashed red line represents the overtopping threshold.

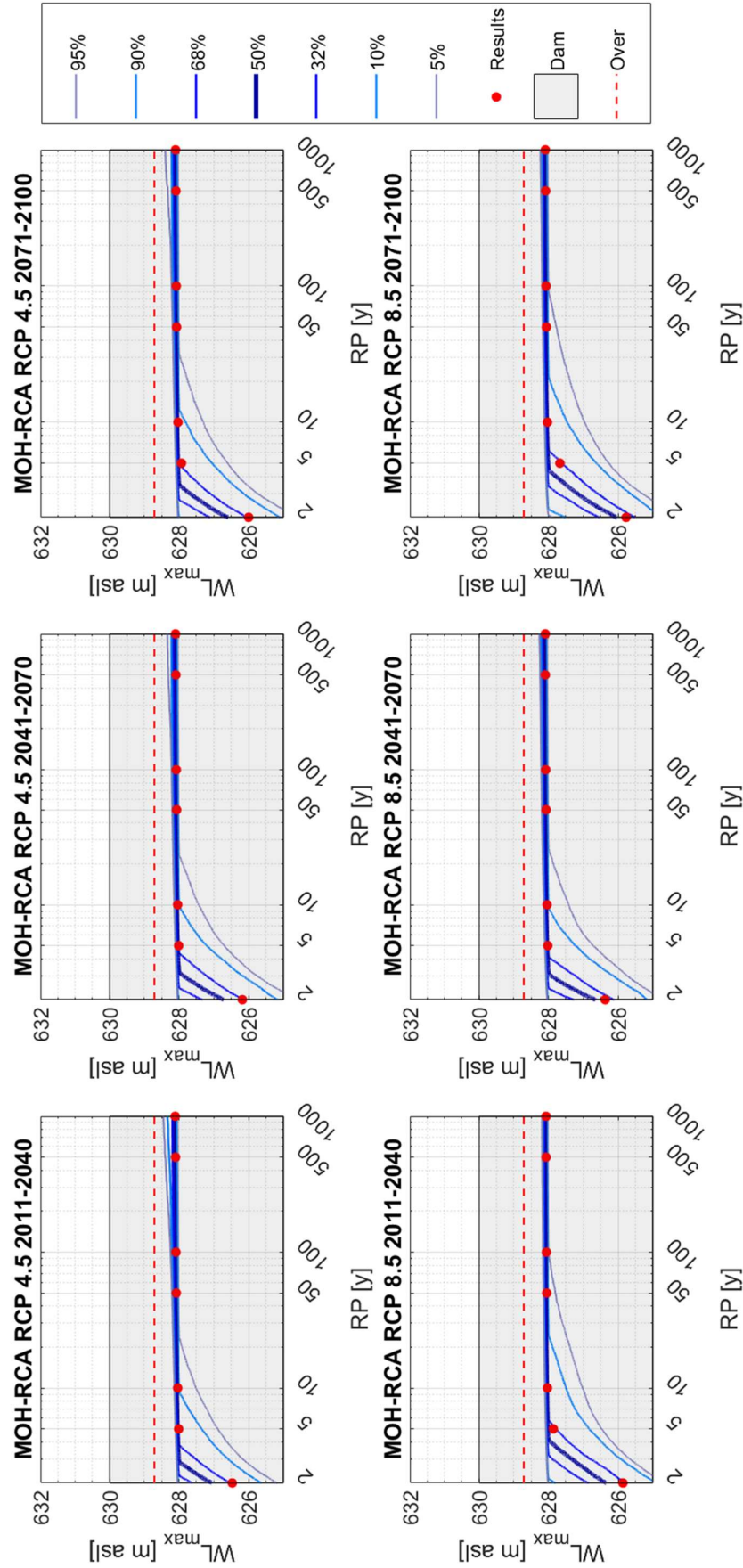


Figure D8 Expected maxima reservoir water levels in the future for the MOH-RCA climate model considering uncertainty. The first row includes the results for RCP 4.5 and the second row includes the results for RCP 8.5. Columns present results by time windows in the future. The thickest blue line represents the median values. Thinner light blue lines represent the rest of percentiles. Red points represent the results without considering uncertainty for the seven return periods. The grey filled box represents the dam with its crest elevation at 630 m a.s.l. The horizontal dashed red line represents the overtopping threshold.

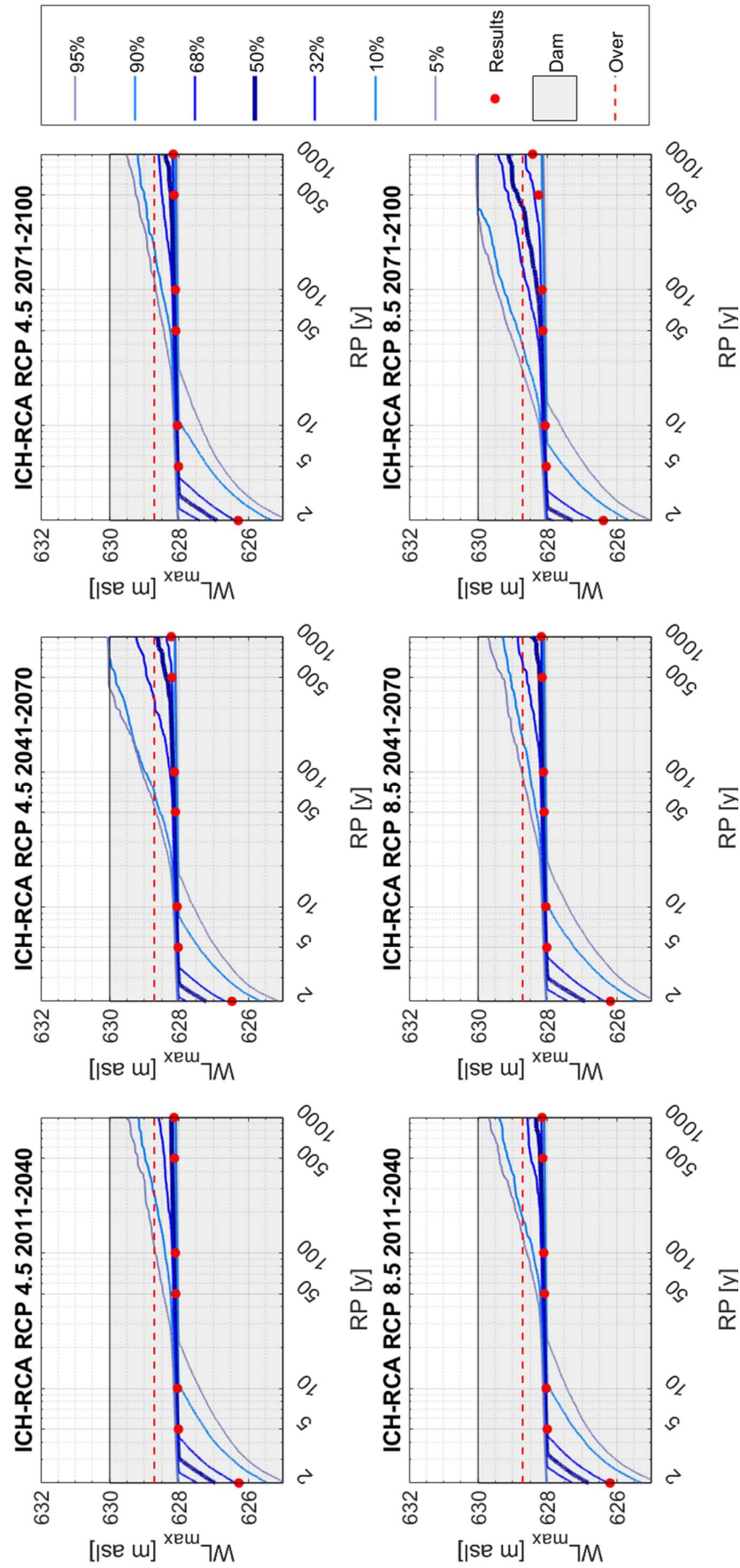


Figure D9: Expected maxima reservoir water levels in the future for the ICH-RCA climate model considering uncertainty. The first row includes the results for RCP 4.5 and the second row includes the results for RCP 8.5. Columns present results by time windows in the future. The thickest blue line represents the median values. Thinner light blue lines represent the rest of percentiles. Red points represent the results without considering uncertainty for the seven return periods. The grey filled box represents the dam with its crest elevation at 630 m a.s.l. The horizontal dashed red line represents the overtopping threshold.

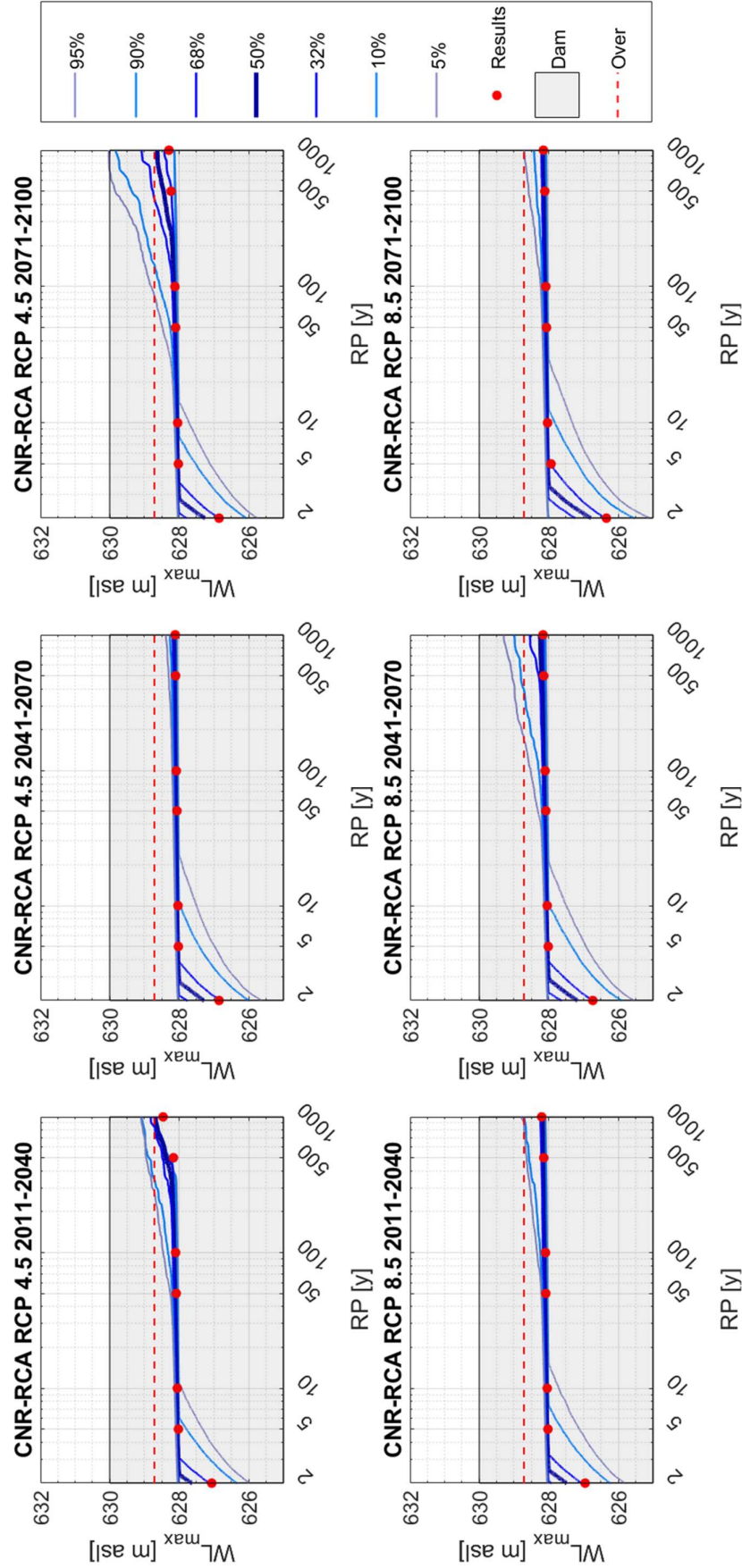


Figure D10: Expected maxima reservoir water levels in the future for the CNR-RCA climate model considering uncertainty. The first row includes the results for RCP 4.5 and the second row includes the results for RCP 8.5. Columns present results by time windows in the future. The thickest blue line represents the median values. Thinner light blue lines represent the rest of percentiles. Red points represent the results without considering uncertainty for the seven return periods. The grey filled box represents the dam with its crest elevation at 630 m a.s.l. The horizontal dashed red line represents the overtopping threshold.

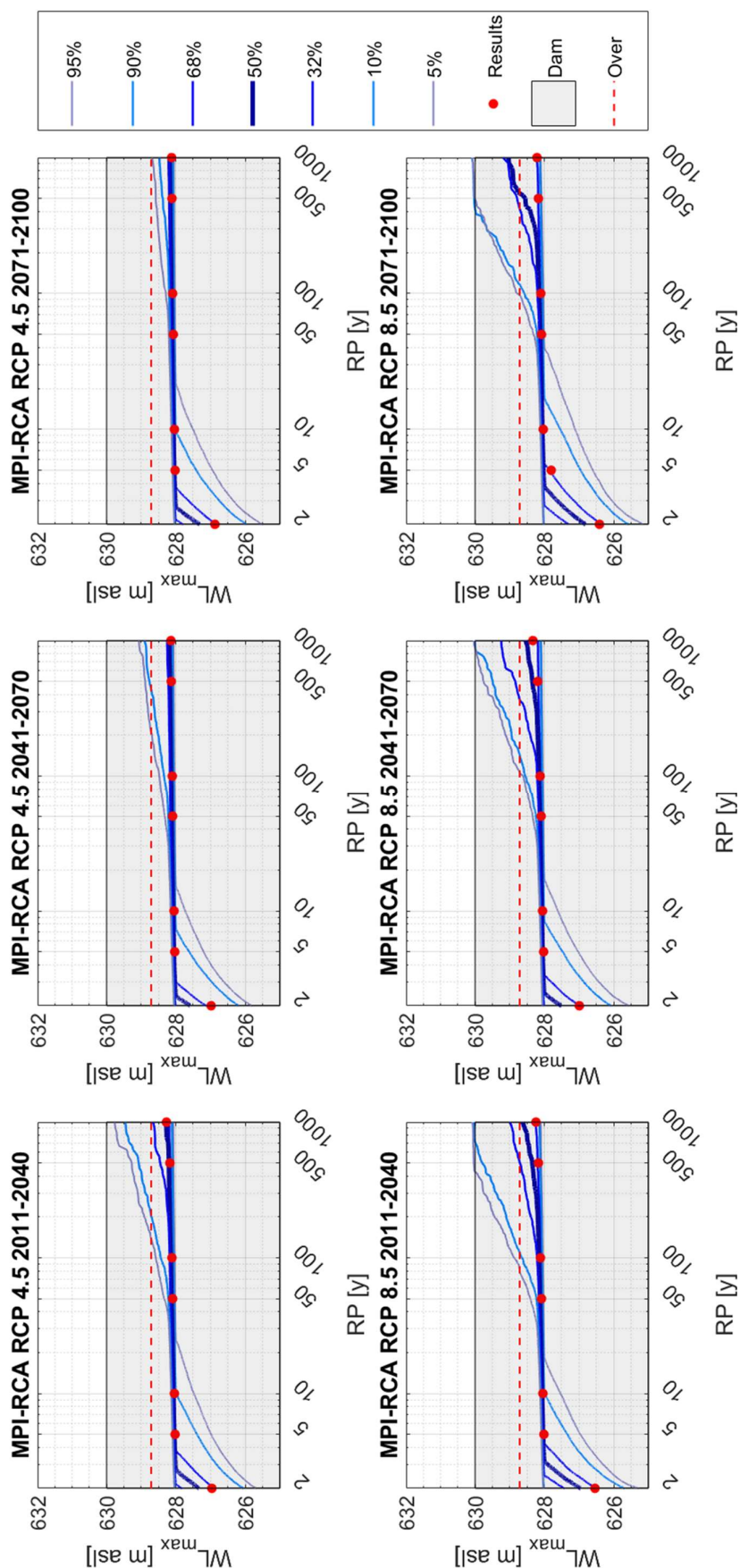


Figure D11: Expected maxima reservoir water levels in the future for the MPI-RCA climate model considering uncertainty. The first row includes the results for RCP 4.5 and the second row includes the results for RCP 8.5. Columns present results by time windows in the future. The thickest blue line represents the median values. Thinner light blue lines represent the rest of percentiles. Red points represent the results without considering uncertainty for the seven return periods. The grey filled box represents the dam with its crest elevation at 630 m a.s.l. The horizontal dashed red line represents the overtopping threshold.

Appendix E.

Future maximum outflow discharge for each climate model accounting uncertainty

Figures in this appendix show the results of the maximum outflow discharge frequency curve in all the time windows and RCP scenarios also accounting uncertainty for all the climate models. The upper part shows the results for the three time window in the RCP 4.5, while the bottom part shows the results of the RCP 8.5. In the subplot the maximum outflow discharge frequency curve is shown for the 7 considered percentiles (5%, 10%, 32%, 50%, 68%, 90% and 95%). Moreover, the results obtained without the accounting of the uncertainty are presented here in each subplot with red dots.

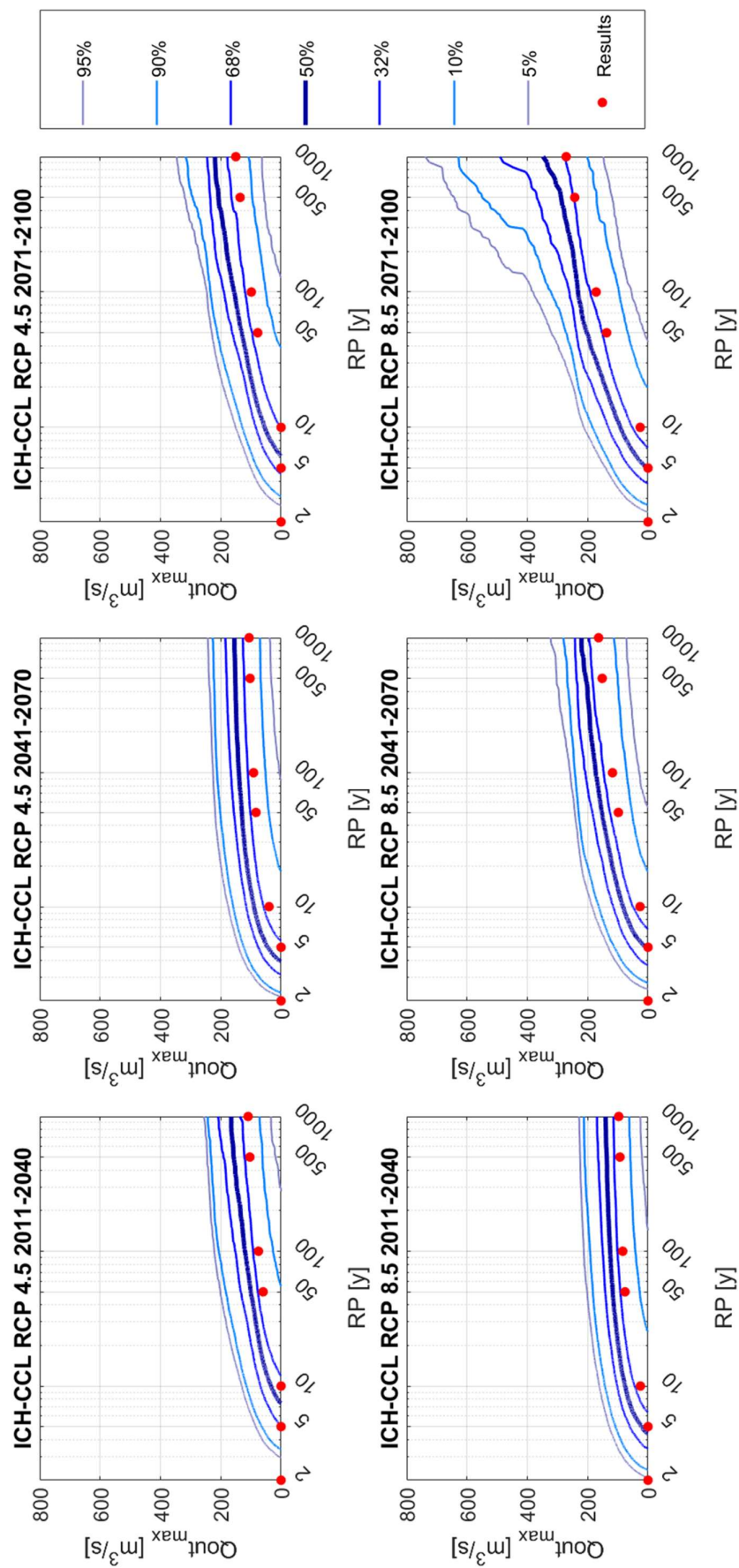


Figure E1: Expected maxima outflow discharge in the future for the ICH-CCL climate model considering uncertainty. The first row includes the results for RCP 4.5 and the second row includes the results for RCP 8.5. Columns present results by time windows in the future. The thickest blue line represents the median values. Thinner light blue lines represent the rest of percentiles. Red points represent the results without considering uncertainty for the seven return periods.

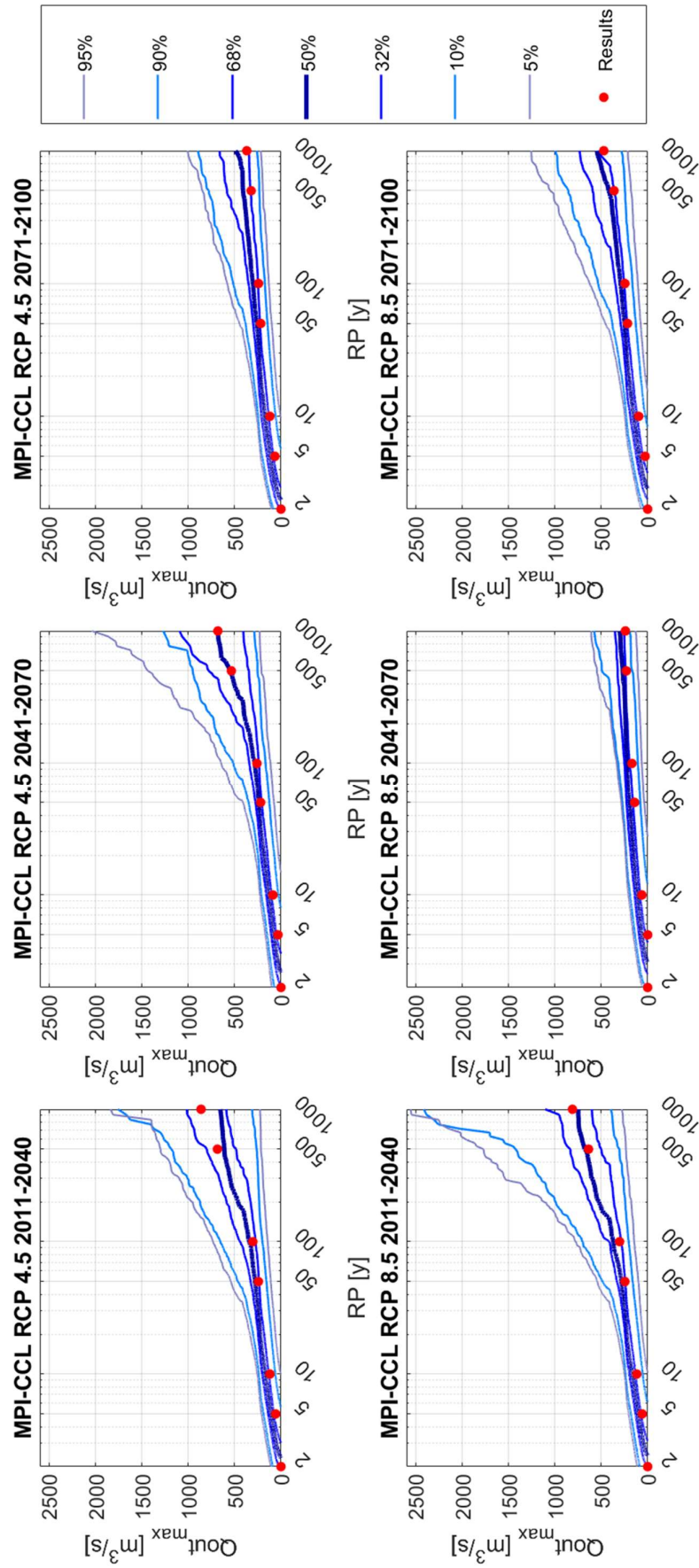


Figure E2 Expected maxima outflow discharge in the future for the MPI-CCL climate model considering uncertainty. The first row includes the results for RCP 4.5 and the second row includes the results for RCP 8.5. Columns present results by time windows in the future. The thickest blue line represents the median values. Thinner light blue lines represent the rest of percentiles. Red points represent the results without considering uncertainty for the seven return periods.

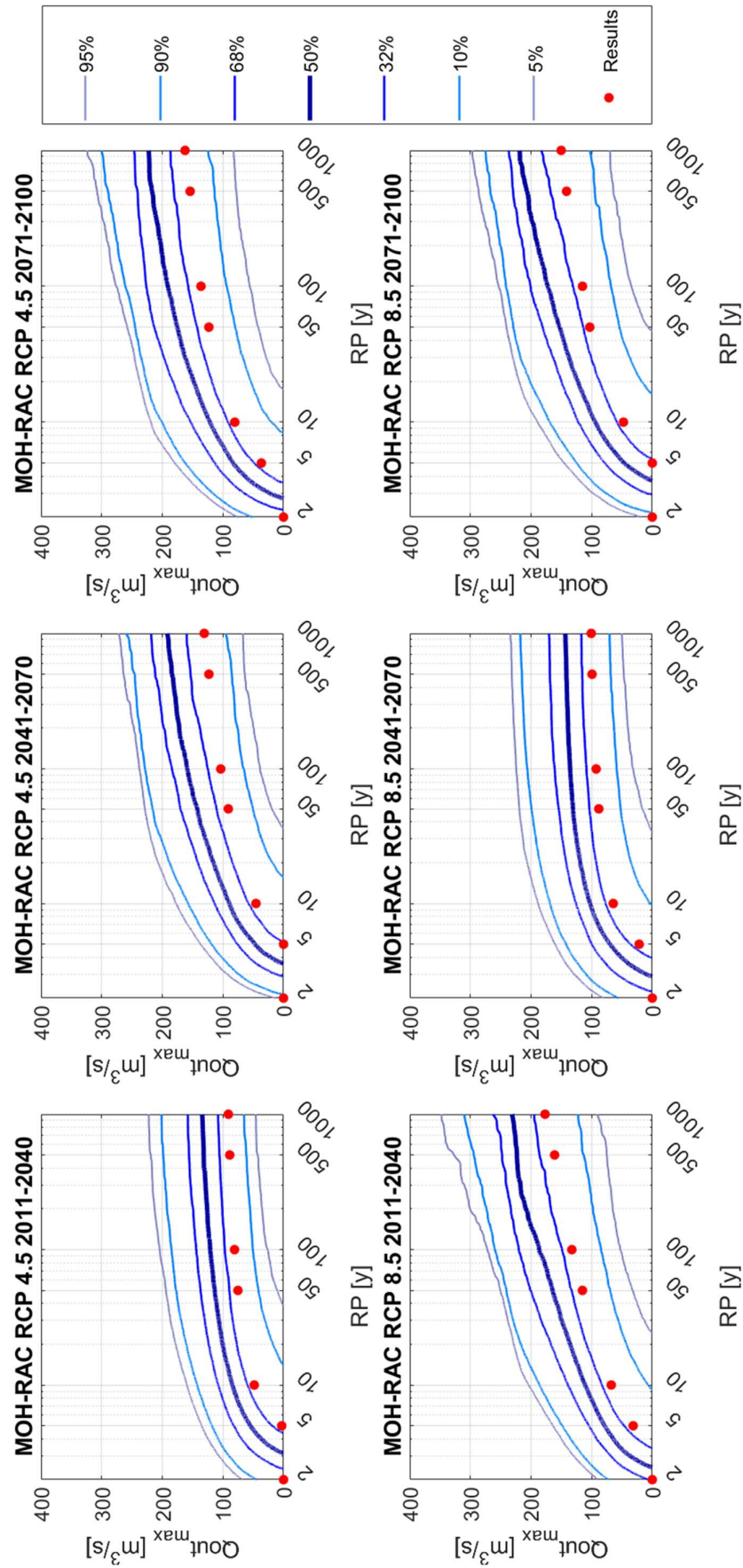


Figure E3: Expected maxima outflow discharge in the future for the MOH-RAC climate model considering uncertainty. The first row includes the results for RCP 4.5 and the second row includes the results for RCP 8.5. Columns present results by time windows in the future. The thickest blue line represents the median values. Thinner light blue lines represent the rest of percentiles. Red points represent the results without considering uncertainty for the seven return periods.

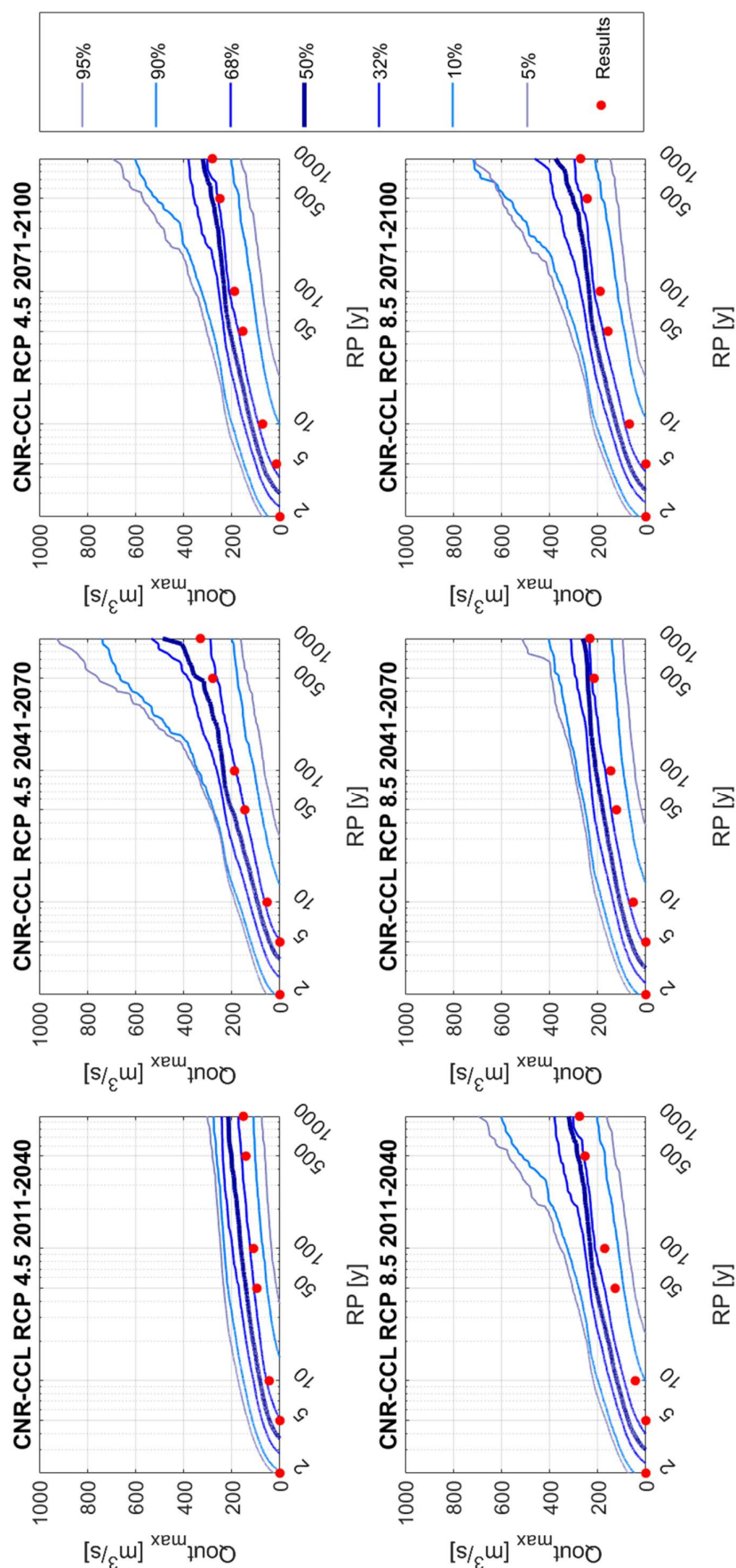


Figure E4: Expected maxima outflow discharge in the future for the CNR-CCCL climate model considering uncertainty. The first row includes the results for RCP 4.5 and the second row includes the results for RCP 8.5. Columns present results by time windows in the future. The thickest blue line represents the median values. Thinner light blue lines represent the rest of percentiles. Red points represent the results without considering uncertainty for the seven return periods.

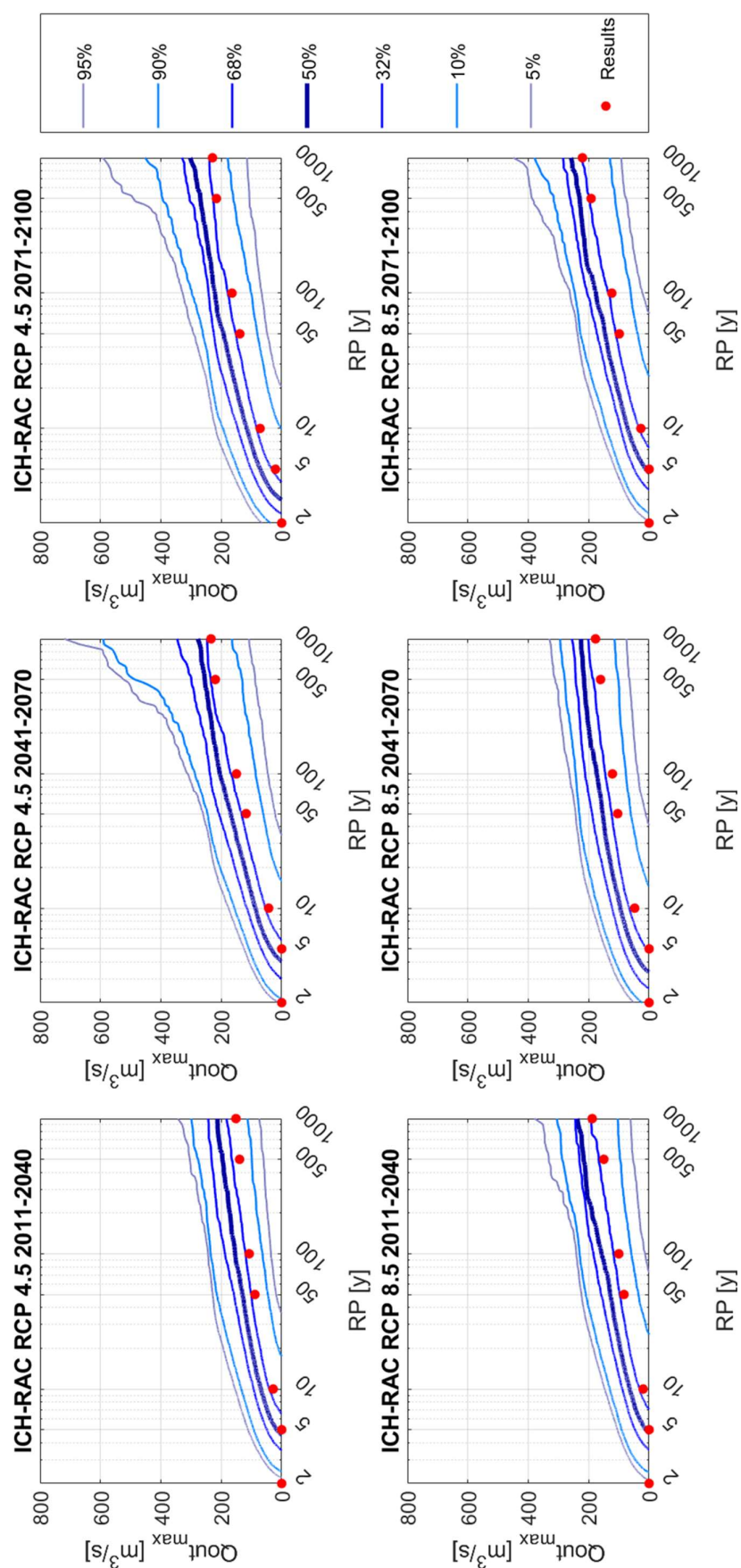


Figure E5: Expected maxima outflow discharge in the future for the ICH-RAC climate model considering uncertainty. The first row includes the results for RCP 4.5 and the second row includes the results for RCP 8.5. Columns present results by time windows in the future. The thickest blue line represents the median values. Thinner light blue lines represent the rest of percentiles. Red points represent the results without considering uncertainty for the seven return periods.

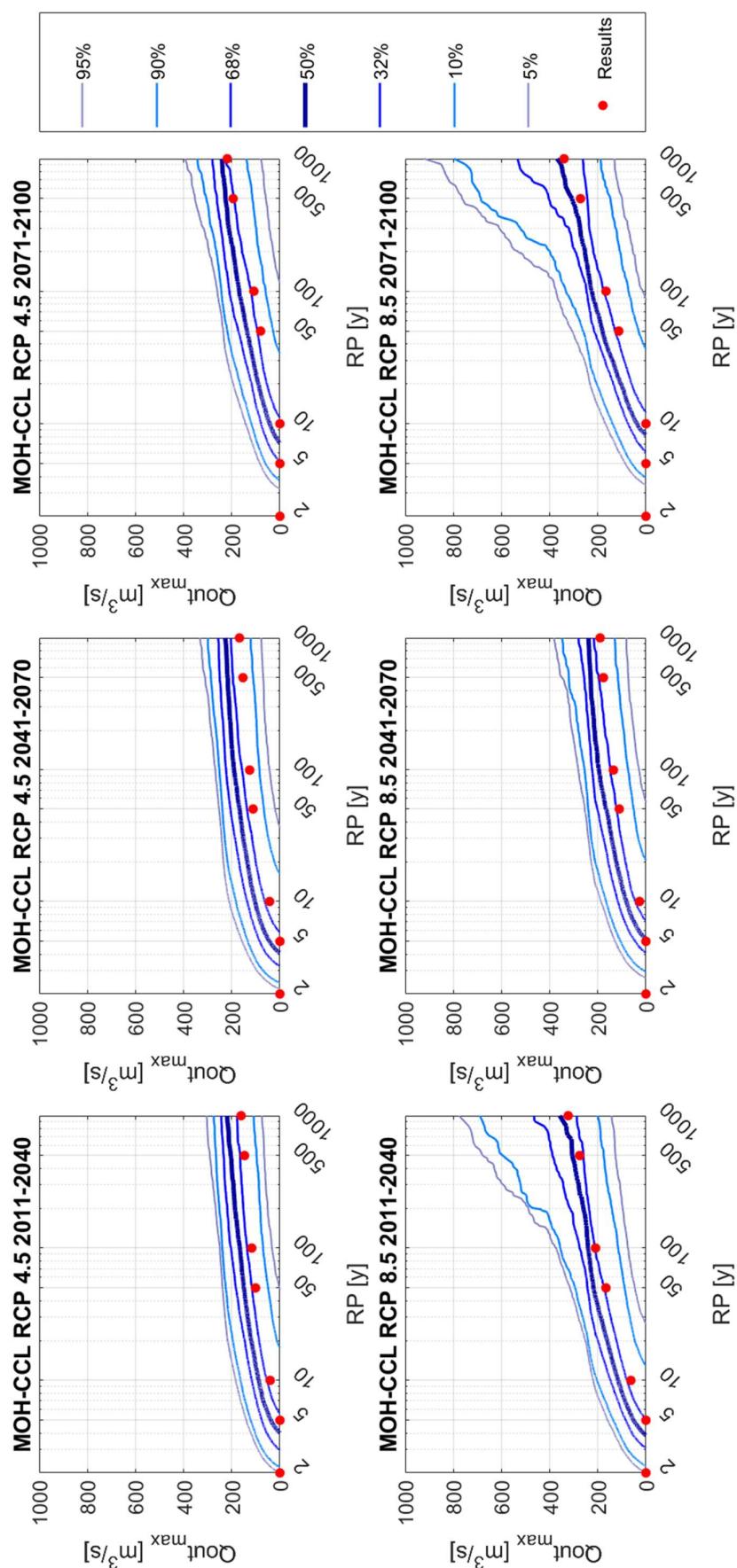


Figure E6: Expected maxima outflow discharge in the future for the MOH-CCL climate model considering uncertainty. The first row includes the results for RCP 4.5 and the second row includes the results for RCP 8.5. Columns present results by time windows in the future. The thickest blue line represents the median values. Thinner light blue lines represent the rest of percentiles. Red points represent the results without considering uncertainty for the seven return periods.

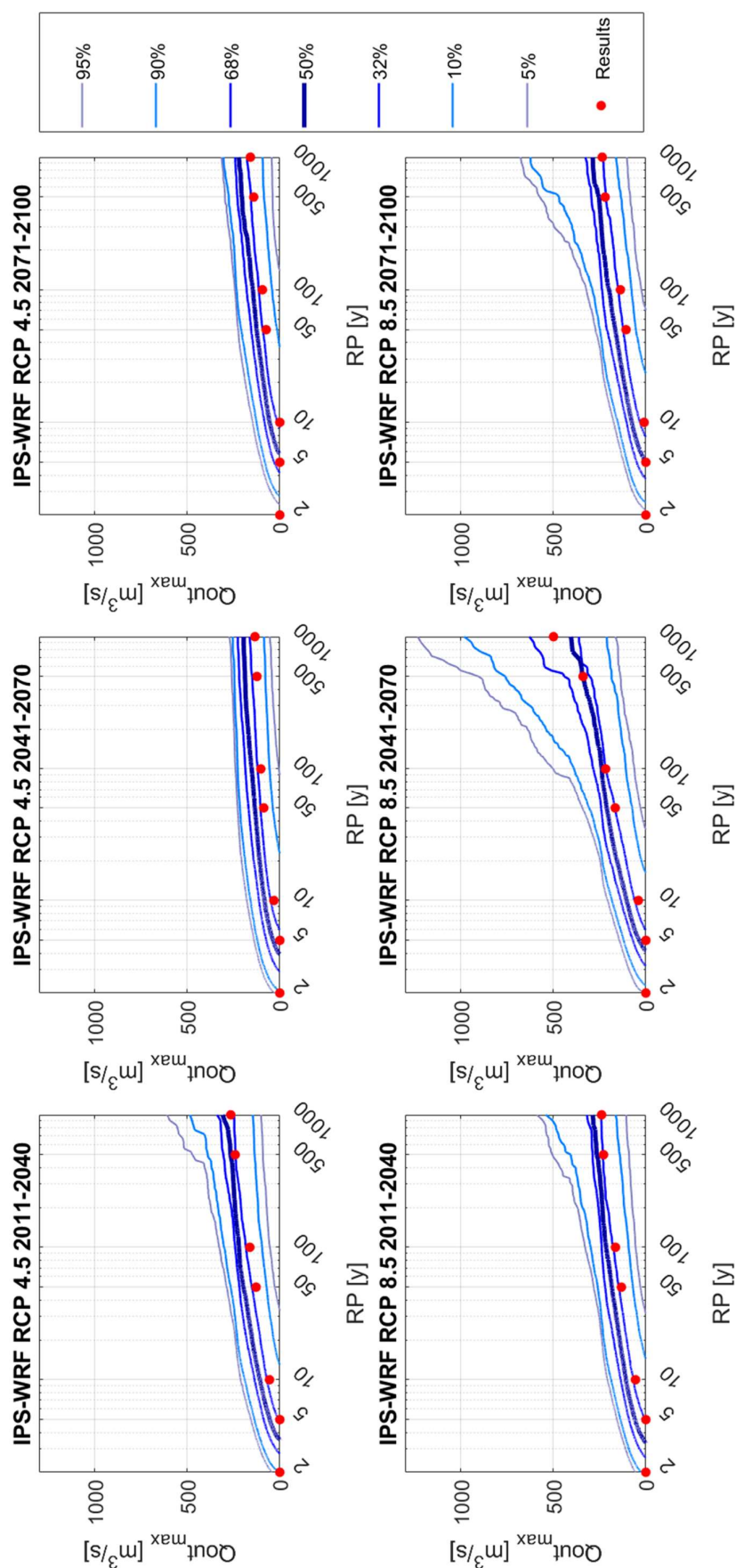


Figure E7: Expected maxima outflow discharge in the future for the IPS-WRF climate model considering uncertainty. The first row includes the results for RCP 4.5 and the second row includes the results for RCP 8.5. Columns present results by time windows in the future. The thickest blue line represents the median values. Thinner light blue lines represent the rest of percentiles. Red points represent the results without considering uncertainty for the seven return periods.

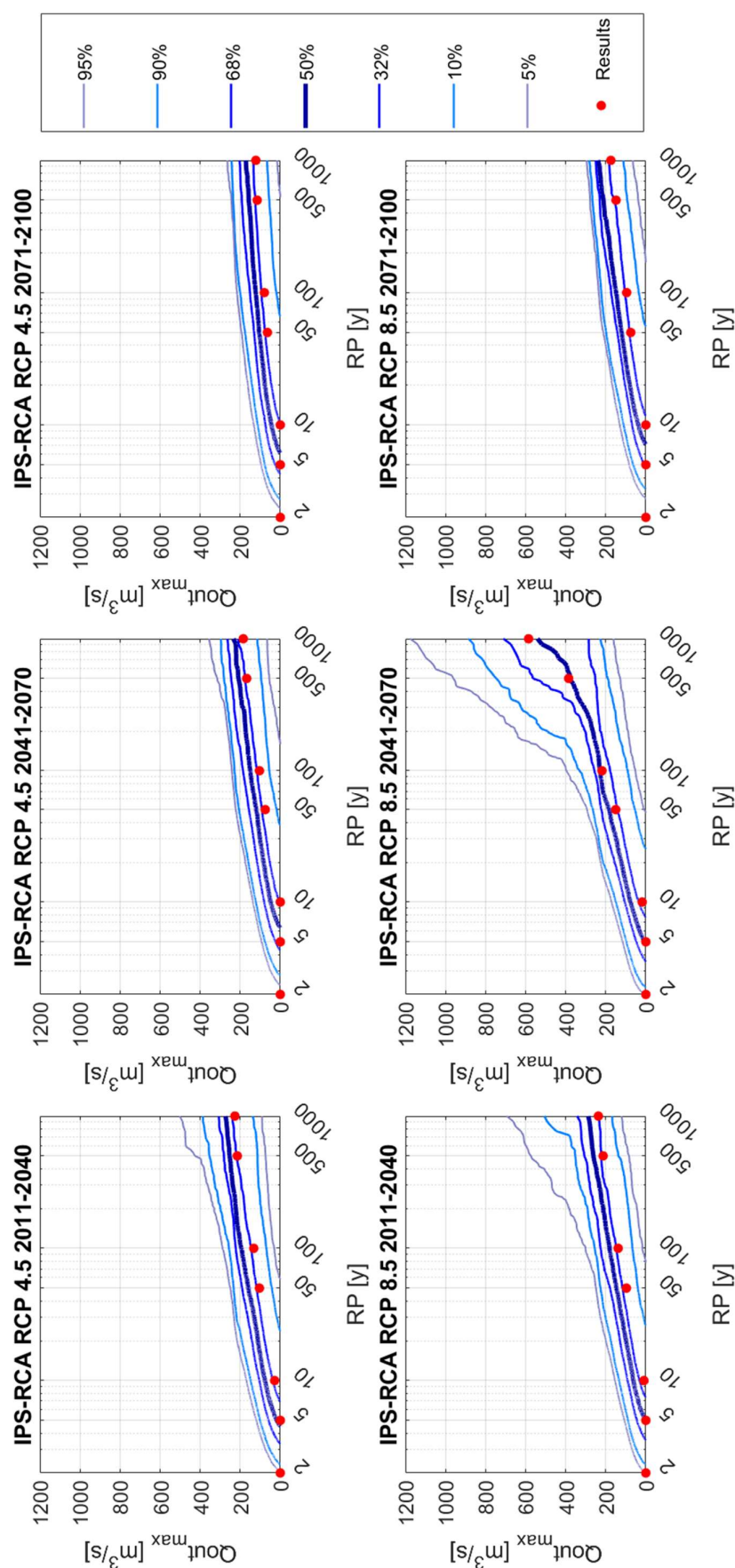


Figure E8: Expected maxima outflow discharge in the future for the IPS-RCA climate model considering uncertainty. The first row includes the results for RCP 4.5 and the second row includes the results for RCP 8.5. Columns present results by time windows in the future. The thickest blue line represents the median values. Thinner light blue lines represent the rest of percentiles. Red points represent the results without considering uncertainty for the seven return periods.

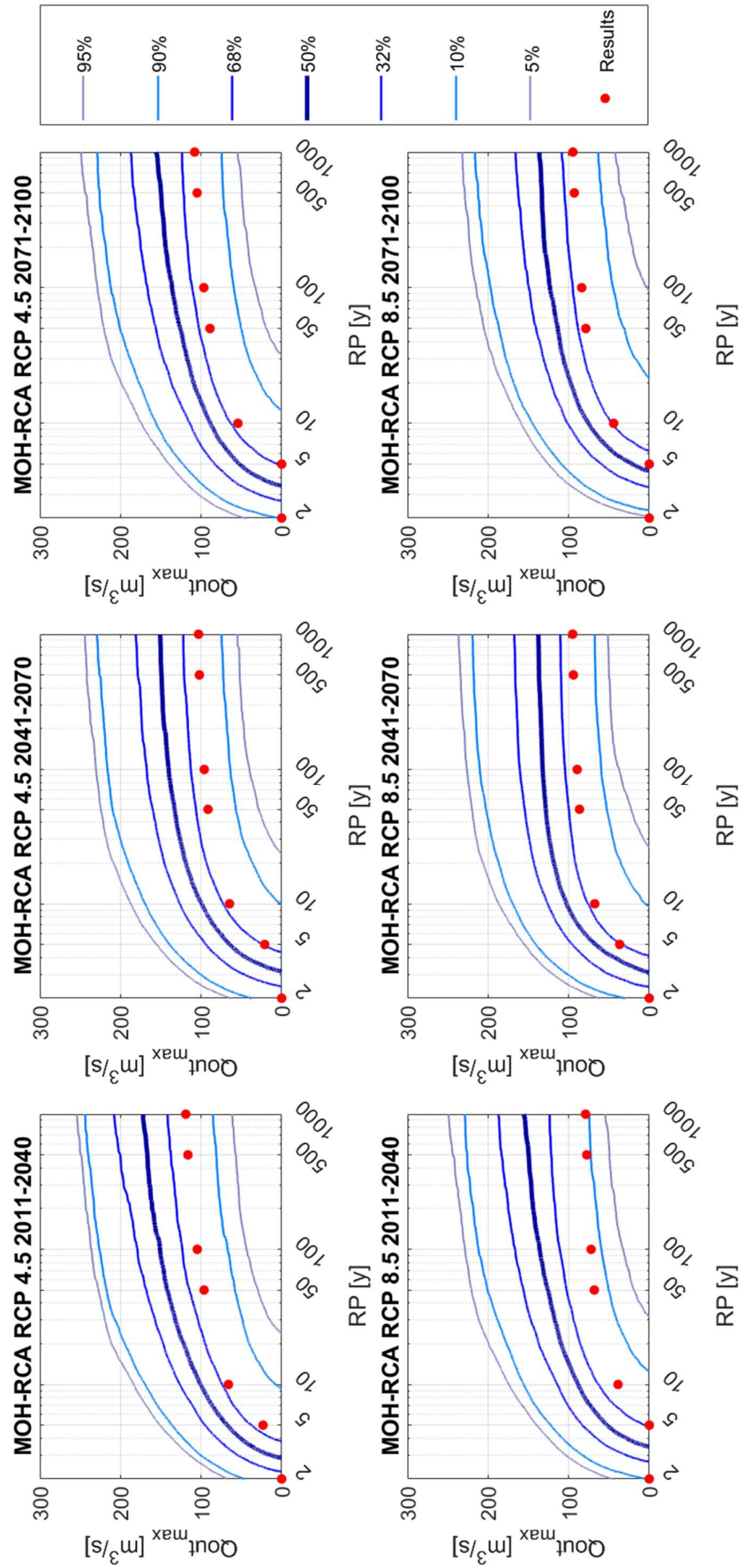


Figure E9: Expected maxima outflow discharge in the future for the MOH-RCA climate model considering uncertainty. The first row includes the results for RCP 4.5 and the second row includes the results for RCP 8.5. Columns present results by time windows in the future. The thickest blue line represents the median values. Thinner light blue lines represent the rest of percentiles. Red points represent the results without considering uncertainty for the seven return periods.

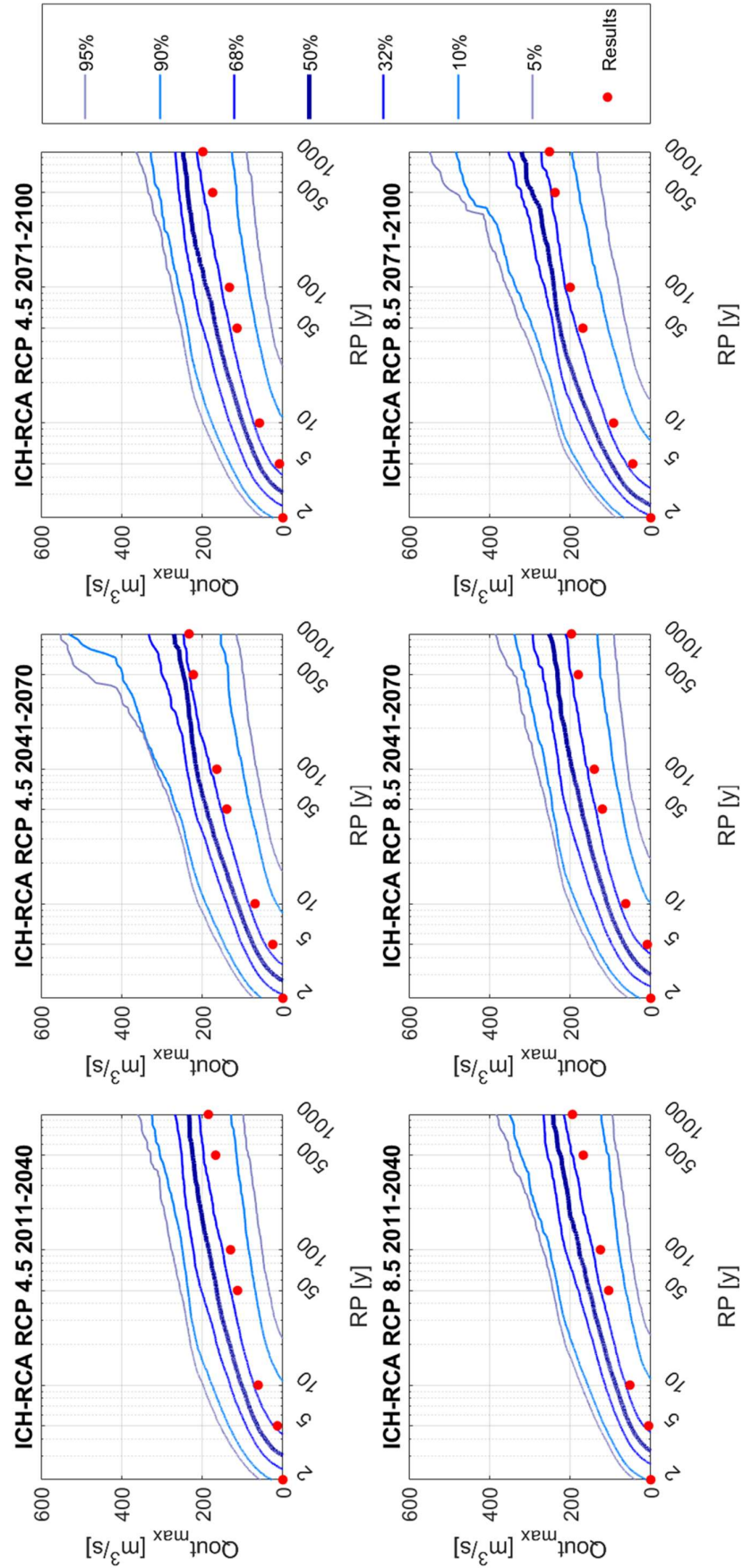


Figure E10: Expected maxima outflow discharge in the future for the ICH-RCA climate model considering uncertainty. The first row includes the results for RCP 4.5 and the second row includes the results for RCP 8.5. Columns present results by time windows in the future. The thickest blue line represents the median values. Thinner light blue lines represent the rest of percentiles. Red points represent the results without considering uncertainty for the seven return periods.

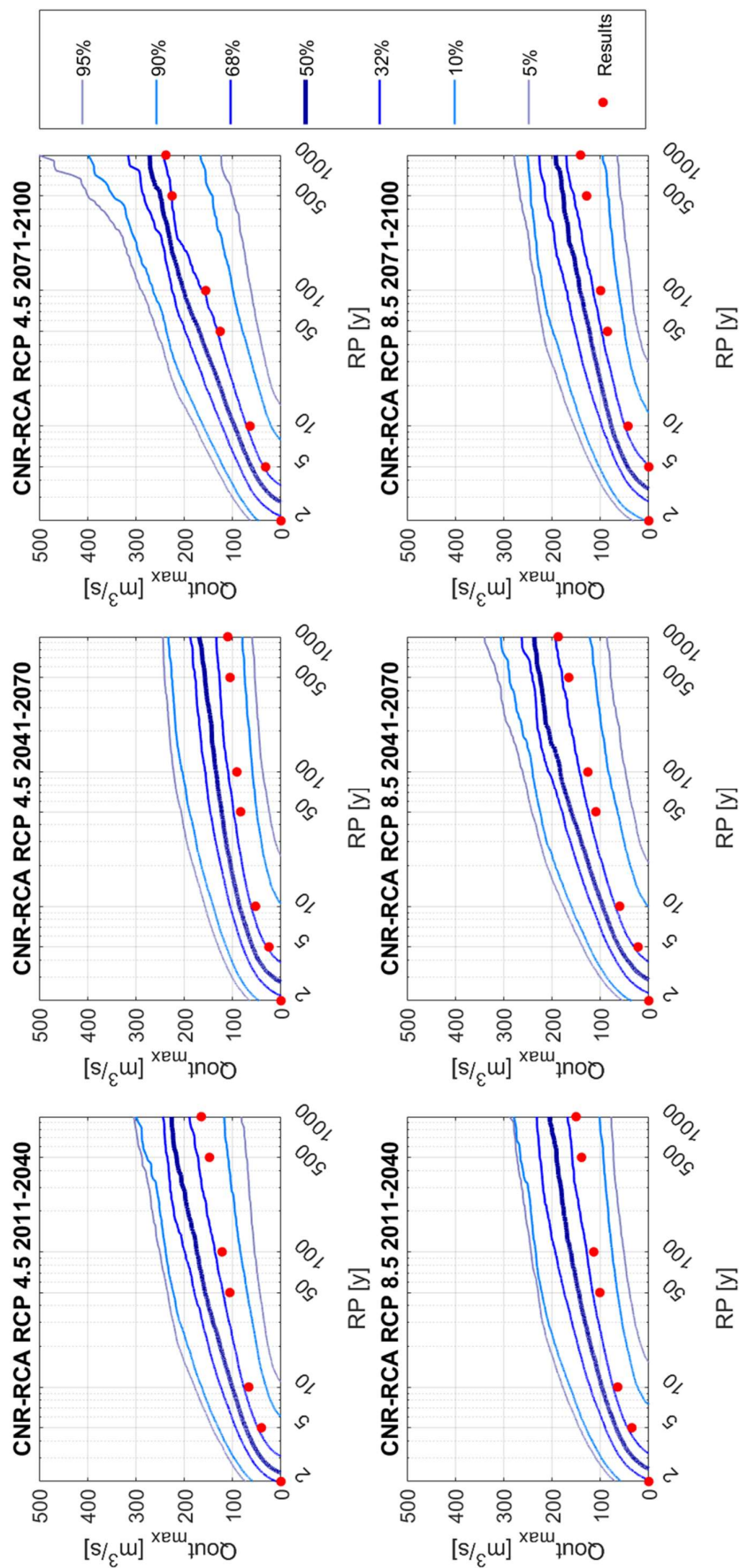


Figure E11: Expected maxima outflow discharge in the future for the CNR-RCA climate model considering uncertainty. The first row includes the results for RCP 4.5 and the second row includes the results for RCP 8.5. Columns present results by time windows in the future. The thickest blue line represents the median values. Thinner light blue lines represent the results without considering uncertainty. Red points represent the results for the seven return periods.